Nearby Supernova Factory : Calibration of SNIFS data and spectrophotometric Type Ia supernovae light curves.

Rui da Silva Pereira

THÈSE DE DOCTORAT DE L'UNIVERSITÉ PARIS.DIDEROT (Paris 7)

Spécialité

Astrophysique et Méthodes Associées

Présentée par

M. Rui DA SILVA PEREIRA

en vue de l'obtention du grade de

DOCTEUR de L'UNIVERSITÉ PARIS.DIDEROT (Paris 7)

Nearby Supernova Factory :

Étalonnage des données de SNIFS et courbes de lumière spectrophotométriques de supernovæ de type Ia.

Calibration of SNIFS data and spectrophotometric Type Ia supernovæ light curves.

Soutenue le 5 décembre 2008 devant le jury composé de :

Pierre ANTILOGUS	*Directeur de thèse*
James BARTLETT	*Président du jury*
Ariel GOOBAR	*Rapporteur*
Ana MOURÃO	*Examinateur*
Mário PIMENTA	*Examinateur*
James RICH	*Rapporteur*

(. . .)
E aqueles que por obras valerosas
Se vão da lei da Morte libertando,
Cantando espalharei por toda parte,
Se a tanto me ajudar o engenho e arte.

Luís de Camões

iv

Acknowledgements

In no particular order, I would like to thank:

- First of all, Pierre Antilogus, for his flawless supervision. It was a pleasure to work with him during the last 3 years, and I'll miss his bursts of laughter echoing around the lab :)

- Jim Bartlett, for accepting to be the president of my thesis defense committee, Ariel Goobar and Jim Rich for having the patience and the availability to referee my thesis in such a short time frame, and Ana Mourão and Mário Pimenta for also accepting to be members of the defense committee;

- All the members of the SNfactory collaboration, the folks of the Lyon and Berkeley teams, and especially the ones which whom I worked most closely in Paris, Gabriele Garavini, Sébastien Gilles, Stephen Bailey and Chao Wu;

- The Supernovæ group at the LPNHE, particularly Nicolas Regnault, Pierre Astier and Julien Guy, for their patience and availability to answer my questions about `poloka` or SALT;

- The people of the LPNHE, Ursula Bassler and José Ocariz, two perfect thesis "god-mother/father", and all the "jeunes" who came and went during these years and shared meals, doubts, laughs or brain-dead emails: Delphine Guide, Bruno Marcos, Guillaume Thérin, Emmanuel Busato, Emannuel Hornero, Claire Juramy, Sylvain Baumont, Diego Terront, Luz Guevara, Alejandro, Henso, Homero, Andrés and all the other members of the Venezuelan troupe, Florent Fayette, Jérome Glisse, Andrzej Siódmok, Taia Kronborg, Nicolas Fourmanoit, Marc Dhellot and of course, my two favorite italians, Pietro and Stefania;

- The guys of the Meudon M2 2004 promo, Arnaud, Benoit(s), Marc, Fabio, Ferras and Xavier(s), for all the shared beers and good moments; and Jacqueline Plancy: I would still be wrestling with university bureaucracy if it wasn't for her;

- All of those who I (momentarily) forgot to include in this list.

E por último um agradecimento especial: aos meus pais, que sempre me apoiaram nas minhas escolhas, mesmo que isso quisesse dizer mudar de país e fazer carreira a "olhar para as estrelas", e que possivelmente já se arrependeram várias vezes de me terem oferecido um telescópio quando era pequeno; e à Aurélie, minha estrela de referência num céu que pareceu muitas vezes demasiado escuro.

ACKNOWLEDGEMENTS

Résumé en français

La dernière décade a été une époque marquée par de nombreux changements en cosmologie. De nouvelles méthodes observationnelles, avec une précision grandissante, ont changé notre vision de l'univers et la façon dont nous l'étudions. Un modèle en accord avec les observations est donc apparu (§ 1): un modèle où l'univers subit une expansion accélérée, emportée par une énergie sombre d'origine inconnue, et où la majeure partie de la matière est sous la forme d'une matière sombre invisible. Actuellement, environ 95% du contenu total en énergie de l'univers est d'origine incertaine.

Les supernovæ de type Ia (SNe Ia) (§ 2.3) représentent un des outils observationnels à notre disposition. Généralement acceptées comme étant l'explosion thermonucléaire d'une naine blanche, ayant atteint sa masse critique après accrétion de masse à partir d'un compagnon dans un système binaire, les SNe Ia sont des évènements extrêmement lumineux visibles à des distances cosmologiques. Les SNe Ia ont aussi une luminosité remarquablement homogène; c'est pourquoi des méthodes d'étalonnage ont été développées, pour permettre leur utilisation comme outils pour la mesure de distances (des chandelles standards), permettant de sonder la géométrie et la dynamique de l'univers et de ses composants. Les SNe Ia sont un des piliers de la cosmologie observationnelle moderne, avec les mesures du fond diffus cosmologique et de la formation de grandes structures dans l'univers.

L'analyse cosmologique à partir des SNe Ia doit s'appuyer sur l'observation d'objets mesurés à grands et petits décalages vers le rouge (z). La détermination des paramètres cosmologiques est basée sur une comparaison entre des échantillons de ces deux types d'objets, cependant tandis que le nombre d'objets mesurés à grands décalages vers le rouge a augmenté progressivement dans les dernières années, la quantité d'objets proches mesurés de façon consistante est toujours faible. Ceci constitue actuellement l'une des plus grandes sources d'erreurs systématiques dans les analyses de cosmologie basées sur les SNe Ia.

Le cadre de travail

Cette thèse s'inscrit dans le cadre de l'expérience SNfactory (Partie II), une collaboration franco-américaine, qui a pour objectif l'observation d'environ 200 SNe Ia proches ($0.03 < z < 0.08$) issues d'une recherche propre et suivies grâce à un spectrographe de champ intégral spécialement conçu pour l'étude de SNe Ia, SNIFS (§ 4). Les séries temporales de spectres de SNe Ia, étalonnées de manière absolue en flux, sont des données uniques appropriées à une analyse soit spectroscopique, soit spectrophotométrique. Cet ensemble de données est également fondamental pour un usage plus précis des SNe Ia dans un cadre cosmologique, et aussi pour une meilleure compréhension de la physique des explosions de supernovæ.

Le travail effectué pendant cette thèse a porté d'une part sur l'étalonnage de la voie photométrique de SNIFS, et d'autre part sur l'analyse scientifique en cours avec les données spectrophotométriques les plus récentes.

Résumé du travail et résultats

La voie photométrique de SNIFS (§ 4.2) est constituée des caméras (CCD) qui permettent l'observation du champ autour de la supernova, en parallèle avec l'acquisition des spectres. Ces caméras permettent d'acquérir des données essentielles pour la calibration absolue en flux des spectres, dans la mesure où elles permettent la détermination de l'atténuation atmosphérique différentielle entre nuits non-photométriques.

La première partie de ce travail a été consacrée à l'étalonnage des données brutes issues de la voie photométrique (§ 8), de la mise en place de procédures de "nettoyage" de lumière parasite jusqu'à la caractérisation des divers paramètres de la caméra photométrique. L'objectif de ces études est d'obtenir des *rapports photométriques* (§ 9) entre nuits. Cette première partie a abouti à la création d'une chaîne de traitement et d'extraction des rapports photométriques, qui a été intégrée dans le traitement centrale de SNfactory. La qualité des rapports photométriques produits a été évaluée, et ses erreurs systématiques ont été estimées comme étant inférieures à 2%.

Par la suite, les images d'acquisition issues du pointage du télescope (un sous-produit de la voie photométrique) ont été utilisées pour la création de courbes de lumière d'une seule couleur (§ 10). Ces courbes de lumière ont été ajustées avec SALT, le programme d'ajustement de courbes de lumière crée par la collaboration SNLS, qui est utilisé pour la standardisation des observations de SNe Ia à grands et petits décalages vers le rouge. Des courbes crées, 73 on été utilisées dans une première étude des distributions de phase (la date de découverte de la supernova par rapport au maximum de sa courbe de lumière) et de "stretch" (le facteur d'étirement utilisé par SALT pour décrire la relation *plus brillant – plus lent* trouvé sur les courbes de lumière des SNe Ia). Les deux distributions sont en accord avec des données précédemment publiées, ce qui démontre que cet échantillon d'objets est approprié pour une analyse cosmologique. Un biais dans les résultats de SALT a cependant été observé, pour les courbes de lumière ne possèdent pas des mesures avant le maximum de luminosité.

Avec les rapports photométriques calculés précédemment, la chaîne d'étalonnage en flux a été mise en oeuvre sur les spectres de six étoiles standards spectrophotométriques (§ 11.2). Les courbes de lumière en résultant ont permis de déterminer la précision actuelle de l'étalonnage en flux de SNfactory dans les nuits non-photométriques ($\sim 5\%$) et aussi de confirmer la consistance en couleur des spectres extraits. Les courbes de lumière de 30 supernovæ on été par la suite synthétisées et ajustées avec SALT. Ces courbes de lumière représentent ainsi les premières courbes de lumière jamais issues de données spectrophotométriques (§ 11.3).

Finalement, ces courbes de lumière on été utilisées dans la création du premier diagramme d'Hubble proche spectrophotométrique (§ 12), qui présente une dispersion 15% (quadratiquement) plus petite que celui fait avec des données publiques. Ceci démontre l'amélioration significative dans la qualité de l'étalonnage en utilisant des données issues d'un seul instrument. La qualité des données nous permet ainsi d'explorer l'origine de la dispersion intrinsèque des SNe Ia, notamment leur variabilité spectroscopique, ce qui est confirmé par l'observation d'un objet spectroscopiquement particulier comme étant un objet hors échelle du diagramme d'Hubble. Les mêmes données ont aussi permis pour la première fois un ajustement cosmologique de SNe Ia sans $\mathcal{K}$-correction (§ 12.2); c'est-à-dire un ajustement qui est insensible aux interactions entre les particularités spectrales des SNe Ia et les limites des bandes passantes des filtres utilisés, en fonction du décalage vers le rouge. L'ajustement cosmologique dans ces conditions présente une réduction quadratique de 5% dans la dispersion des résidus du diagramme d'Hubble, et nous pouvons conclure que la $\mathcal{K}$-correction (jusqu'à maintenant inclue dans la "dispersion intrinsèque des SNe Ia") combinée à la description de SALT2 de la variabilité spectrale des SNe Ia, induit

une dispersion du même ordre de grandeur dans les ajustements cosmologiques "standards". Un entraînement de SALT2 avec le lot de données de SNfactory pourra certainement réduire cette dispersion due à la $\mathcal{K}$-correction dans les analyses cosmologiques avec SNe Ia. Un étude exploratoire pour l'identification et la compréhension d'objets particuliers, par l'utilisation de courbes de lumière de filtres étroits placés sur des particularités spectrales, a aussi été effectuée (§ 12.3). Nous pouvons conclure que la qualité actuelle de l'extraction des spectres et le nombre d'objets disponibles ne permettent pas la construction d'une méthode robuste de rejet de points aberrants, nécessaire pour une étude de ce genre. Néanmoins une étude qualitative de certaines courbes de lumière étroites a suggéré l'existence possible de sous-familles inclues dans la famille particulière des SNe Ia 91T-like (surlumineuses).

Après un important effort technique par un petit nombre de personnes, l'analyse de données de SNfactory est bien lancée et commence à justifier l'investissement fait. L'étude d'un lot de données deux fois plus grand que celui présenté dans cette thèse a commencé cet automne. Des développements continus dans l'extraction de données, étalonnage et méthodes d'analyse nous permettront d'extraire encore plus d'informations de cet lot de données de valeur inestimable, du point de vue soit des ajustements cosmologiques, soit de la physique à la base de la diversité observée des SNe Ia.

Contents

Introduction

The last decade has been an eventful one for cosmology. New observational methods, with ever increasing precision, changed our vision of the universe and the way we study it.

An observationally consistent model has emerged. One of an universe in accelerated expansion, driven by a dark energy due to an elusive cosmological constant, and where most of the matter is in the form of an invisible dark matter. Such is the scenario cosmology faces today: roughly 95% of the total energy distribution of the universe is of uncertain origin. These are interesting times indeed!

One of the observational tools at our disposal, is the Type Ia supernovæ (SNe Ia). Commonly accepted as the thermonuclear explosion of a white dwarf star, who reached its critical mass due to matter accretion from a binary companion, these events are extremely bright, making them visible up to cosmological distances. They are also remarkably homogeneous: standardization methods have been developed that effectively allow their usage as a distance ruler (a standard candle) to probe the geometry and dynamics of the universe, and hence its constituents. They are one of the cornerstones of modern observational cosmology, along with measurements of the cosmic microwave background radiation and large scale structure.

The last years have seen the establishment of several supernovæ surveys, which aim to collect the biggest possible dataset of SNe Ia observations, from nearby and distant events (at low or high redshift). The determination of the cosmological parameters rests on a comparison between these two samples, hence the interest of having high quality, well sampled data on both distance ranges. That is not however the case. Nearby supernovæ (at distances where their observed luminosity is independent of the cosmological model), are more difficult to find, due to the larger areas of sky that need to be scanned. Therefore, while the statistics of high redshift SNe Ia increase, the number of well observed, consistent datasets of nearby supernovæ is still small. They represent today one of the main sources of systematic errors on the cosmological analysis using supernovæ.

Among the current low redshift surveys built to tackle this problem, is the SNfactory project. It aims to observe around 200 nearby SNe Ia with high quality spectral data, originated from a dedicated integral field unit spectrograph, SNIFS. The resulting dataset is unique in the sense that it consists of spectral time series of SNe Ia, suitable either for spectroscopic or spectrophotometric analysis. It is at the same time a fundamental dataset for an higher precision usage of SNe Ia as dark energy probes, and for a better understanding of the physics behind supernovæ explosions.

I joined the SNfactory collaboration on September 2005, and this manuscript aims to group the ensemble of the work and the contributions to the project made during my thesis. It was mainly focused on the development and implementation of a calibration and extraction pipeline for the SNIFS' photometric channel data, essential for the flux calibration of the spectra. I also took part on the ongoing scientific analysis effort, for which I contributed with a novel way of using SNIFS' unique dataset on a cosmological fit point of view.

This manuscript is divided into 4 parts and 12 chapters.

Part I consists in an introduction to cosmology. In Chapter 1 the fundamental equations of cosmology will be presented, as well as the cosmological parameters and observables, leading up to the current standard cosmological model. Chapter 2 will then introduce the three main axis of observational cosmology: the cosmic microwave background and large scale structure measurements are briefly described, while bigger emphasis is given to the supernovæ. Their classification, origins and photometric and spectral homogeneity *vs.* peculiarity are discussed, as well as their current usage as dark energy probes.

Part II presents the SNfactory project and its unique observational approach. In Chapter 3, the scientific goals of SNfactory and the spectrophotometry concept are introduced. Chapter 4 describes the SNIFS instrument, the integral field spectrograph built by the collaboration for dedicated SNe Ia observations, its division into spectroscopic and photometric channels, and the remote data taking procedure. In Chapter 5 the different components of the project are detailed: the supernovæ search survey using the QUEST-II camera, and subsequent screening and spectroscopic followup made using SNIFS. Statistics from the current SNfactory sample are shown as well as a number of interesting (peculiar) objects observed by SNfactory.

Part III details the data acquisition and calibration procedures for SNIFS, with special focus on the photometric channel data calibration, extraction and its usage on the spectra flux calibration scheme. In Chapter 6 a typical (remote) observation night is explained, as well as the different kinds of data acquired by SNIFS during each run. Chapter 7 describes the full SNIFS spectral calibration procedure, starting from the raw spectral data up until the flux calibrated spectra, and on the role of the photometric channel on the flux calibration of non-photometric nights, using between nights' photometric ratios. In Chapter 8 all the different aspects of the calibration of the raw photometric channel exposures are detailed. Chapter 9 explains the full pipeline work-flow for the extraction of the photometric ratios from the photometric channel data, and presents quality benchmarks.

Part IV consists on the analysis of photometric and spectrophotometric data, issued or calibrated using data from the photometric channel pipeline, presented on the previous Part. In Chapter 10, results from the light curves made using the acquisition images from a sub-sample of 73 SNe Ia are shown. Phase and stretch distributions for a representative SNfactory dataset are derived, and compared to the published nearby supernovæ datasets. In Chapter 11 the gray extinction hypothesis is tested using photometric ratios data from the photometric pipeline, and SNfactory's first spectrophotometric light curves are shown, both for fundamental standard calibrators as well as for a sub-sample of ~ 30 SNe Ia. Chapter 12 details the cosmological analysis performed using the dataset presented in the previous chapter, notably the first ever nearby Hubble diagram produced from spectrophotometric data. A novel way for the creation of light curves is shown, $\mathcal{K}$-correction-free light curves that take advantage of this unique dataset, and present a reduced scatter of the nearby Hubble diagram residuals. Finally, light curves from synthetic bands centered on particular features or wavelength regions are also investigated, with an emphasis on their utility in photometric subclassification.
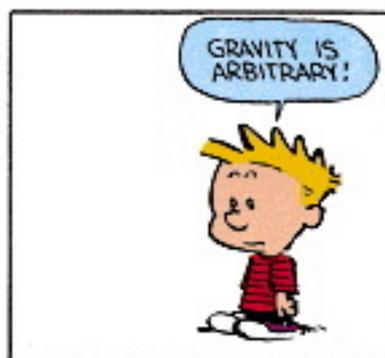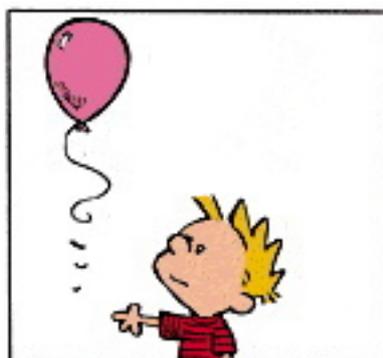
Part I

Observing the Universe

Chapter 1

Big Bang cosmology

There is a theory which states that if ever anyone discovers exactly what the Universe is for and why it is here, it will instantly disappear and be replaced by something even more bizarre and inexplicable.
There is another which states that this has already happened.

Douglas Adams

Cosmology is the science of the *universum*, the "combination of all things into a whole". It aims to explain the origin and evolution of the entire contents of the universe and the underlying physical processes.

Throughout history, mankind saw the accumulation of astronomical evidences contradicting further and further its anthropocentric beliefs. They took us from being in the center of the "creation" up to inhabiting an average-sized planet orbiting an average-sized star in the periphery of a average-sized rotating galaxy. A galaxy flying towards an unknown goal in the middle of billions of similar galaxies, in an universe with a center which is everywhere and nowhere at the same time, where no location is more special than any other.

Such accumulated evidences formed thus our current understanding of the universe: an evolving entity whose birth, in a singular moment of infinite density, pressure and spacetime curvature, and growth is explained by the hot Big Bang theory. This theory lies itself on the theoretical framework of Einstein's general relativity and on well established observational evidences.

1.1 Homogeneity and isotropy

Inherent in the foundations of this cosmological theory is the *cosmological principle*, first stated by Copernicus. It hypothesizes that the universe is spatially homogeneous and isotropic, that is, spatially invariant under translation and rotation, thus making all positions fundamentally equivalent.

Specifically, by homogeneous we mean that (at large scales, bigger than 100 Mpc[1]) the universe looks the same at every point and by isotropic that it looks the same in all directions. These assumptions are nowadays well confirmed respectively by the large-scale distribution of galaxies (§ 2.2) and the near-uniformity of the CMB temperature (§ 2.1).

---

[1] 1 Mpc = 3.26×10^8 light years

Imposing these symmetries[2] to the universe at large scale, we can thus study its evolution.

1.2 FLRW models in general relativity

1.2.1 Robertson-Walker (RW) metric

Under the assumption of the cosmological principle, our spacetime metric can be written in terms of an invariant four dimensions geodesic metric $g_{\mu\nu}$ which follows

$$ds^2 = g_{\mu\nu}dx^\mu dx^\nu \ , \tag{1.1}$$

that is, relates length measurements ds to a chosen coordinate system dx (and thus is an intrinsic description of space), as the so-called *Robertson-Walker* metric

$$ds^2 = dt^2 - a^2(t)\left[\frac{dr^2}{(1-kr^2)} + r^2\left(d\theta^2 + \sin^2\theta d\phi^2\right)\right] \ . \tag{1.2}$$

We are assuming the speed of light is equal to unity ($c = 1$) and: t is the proper time, r, θ, ϕ are comoving (spherical) spatial coordinates, $a(t)$ is the scale factor (normalized by $a(t_0) \equiv 1$)[3], and the constant k characterizes the spatial curvature of the universe. $k = \{-1, 0, 1\}$ correspond respectively to open (saddle-like), spatially flat and closed (3-sphere) universes.

1.2.2 Einstein equations

The cosmological equations of motion are derived from the Einstein (1917) field equations

$$\mathcal{R}_{\mu\nu} - \frac{1}{2}g_{\mu\nu}\mathcal{R} = 8\pi G T_{\mu\nu} - \Lambda g_{\mu\nu} \ , \tag{1.3}$$

where G is Newton's gravitational constant, and which relate the curvature, represented by the Ricci tensor $\mathcal{R}_{\mu\nu}$ to the energy-momentum tensor $T_{\mu\nu}$[4]. The $\Lambda g_{\mu\nu}$ term is the cosmological constant (Λ) term and was added by Einstein since he was interested in finding static solutions, both due to his personal beliefs and in accordance to the astronomical data available at the time, but which his initial formulation did not allowed. This effort however was unsuccessful: the static universe described by this theory was unstable, and both de Sitter's solution of (1.3) for empty universes with $\Lambda > 0$, and measurements of the radial velocities of distant galaxies using the redshift (§ 1.3.1) of their spectra by Slipher (1924), showed that our universe is in fact not static, which led Einstein to abandon the cosmological constant.

Despite Einstein's misguided motivation for introducing the cosmological constant term, there is nothing wrong (*i.e.* inconsistent) with the presence of such a term in the equations. We will see in § 1.2.4 what this term may represent in modern cosmology.

---

[2]The homogeneity and isotropy are symmetries of *space* and not of *spacetime*. Homogeneous, isotropic spacetimes have a family of preferred three-dimensional spatial slices on which the three-dimensional geometry is homogeneous and isotropic.

[3]Throughout this document, this normalization will be implicit and the $_0$ subscript will always represent the present epoch.

[4]Or in other words, matter and energy are the source of the curvature of spacetime.

1.2.3 Perfect fluid approximation

The cosmological principle gives rise to the picture of the universe as a physical system of "cosmic fluid" whose fundamental particles are galaxies. We thus assume that the matter content of the universe is a perfect fluid with energy-momentum tensor

$$T_{\mu\nu} = (p + \rho) u_\mu u_\nu - p g_{\mu\nu} , \qquad (1.4)$$

where the metric $g_{\mu\nu}$ is described by (1.2), ρ is the energy density, p the isotropic pressure and $u = (1, 0, 0, 0)$ the velocity 4-vector for the isotropic fluid in comoving coordinates.

1.2.4 Friedmann-Lemaître (FL) equations of motion

By substitution of the perfect fluid energy-momentum tensor (1.4) and the RW metric (1.2) on Einstein's equations (1.3), we can obtain the so-called Friedmann-Lemaître equations

$$H^2 \equiv \left(\frac{\dot{a}}{a}\right)^2 = \frac{8\pi G\rho}{3} - \frac{k}{a^2} + \frac{\Lambda}{3} \qquad (1.5)$$

$$\frac{\ddot{a}}{a} = -\frac{4\pi G}{3}(\rho + 3p) + \frac{\Lambda}{3} , \qquad (1.6)$$

which relate the dynamics of the universe (the time variation of the scale factor, $\dot{a}$) with the pressure and energy density of its constituents. $H(t)$ is the Hubble parameter. Nowadays the Λ term is commonly thought as a measure of the *energy density of the vacuum*[5], or more generally of a *dark energy*, so it can be represented with the other pressure and density terms[6], as

$$\Lambda = 8\pi G\rho_\Lambda = -8\pi G p_\Lambda . \qquad (1.7)$$

Eq. (1.5) has a classical mechanical analog if we assume $\Lambda = 0$. Looking at $-\frac{k}{a^2}$ as a "total energy", then we see that the evolution of the universe is governed by the relation between the potential energy ($\frac{8\pi G\rho}{3}$) and the kinetic ($\frac{\dot{a}}{a}$) terms, making it expand or contract up to a fate determined by the curvature constant k. For $k = 1$ the universe recollapses in a finite time, whereas for $k = \{0, -1\}$ it expands indefinitely. These conclusions can be altered when $\Lambda \neq 0$ (or more generally with some component with $(\rho + 3p) < 0$).

From equations (1.5) and (1.6) one can obtain the conservation equation (in agreement with the first law of thermodynamics), for the components of the universe

$$\begin{aligned} \dot{\rho} &= -3H(\rho + p) \\ &= -3H\rho(1 + w) , \end{aligned} \qquad (1.8)$$

which expresses the evolution of energy density with time (its a-dependence). $w_i \equiv \frac{p_i}{\rho_i}$ is the equation of state parameter for any i component of the universe (*cf.* § 1.3.3).

Armed with this theoretical background we are now able to apply our knowledge to study the evolution of the universe.

---

[5]However this, as some (Kolb 2007) authors prefer to call it, *cosmoillogical* constant, is still one of the unresolved puzzles in fundamental physics, in view of the incredible fine-tuning problem which represents the several orders of magnitude difference between its present value and the value predicted by quantum field theory (Zel'Dovich 1967; Carroll 2001; Bousso 2008).

[6]Throughout this document, the x subscript will be used to represent a general dark energy term, not just the cosmological constant one.

1.3 The expanding universe

1.3.1 Cosmological redshift

Most methods of measuring the composition of the universe rely on various observations of electromagnetic radiation. It is therefore important to discuss how the properties of light detected from a source are connected to a certain cosmological model.

By observing the spectra of starlight of nearby galaxies we can identify known emission lines and compare their wavelengths λ to the (known) emitted ones. These may appear displaced towards the blue or the red part of the spectrum, respectively *blushifted* or *redshifted*, in what may be interpreted as a Doppler effect in flat spacetime. That means that these galaxies are moving towards or away from us, with a velocity v related to the shift in wavelength $\Delta\lambda$ by the Doppler formula

$$z \equiv \frac{\Delta\lambda}{\lambda} \simeq \frac{v}{c} \ , \tag{1.9}$$

where z is the *redshift* and the second equality is valid for objects in our "neighborhood" ($v \ll c$).

If we have now a particle moving in a spacetime geometry described by the time dependent RW metric (1.2), its energy will change, similarly as it would if it moved in a time-dependent potential. For a photon whose energy is proportional to frequency, that change in energy is the *cosmological redshift*. We consider a photon emitted from a galaxy at comoving coordinate $r = R$ at time t. It will travel in a geodesic $ds^2 = 0$, so that in the time between emission and reception the photon traveled a spatial coordinate distance (in the spatially flat case)

$$R = \int_t^{t_0} \frac{\mathrm{d}t}{a(t)} \ . \tag{1.10}$$

If we suppose instead that a series of pulses are emitted with frequency $\omega = \frac{2\pi}{\delta t}$, the time interval between the pulses at reception δt_0 can be calculated from (1.10) since all pulses travel the same spatial coordinate separation R:

$$\int_{t+\delta t}^{t_0+\delta t_0} \frac{\mathrm{d}t}{a(t)} = R = \int_t^{t_0} \frac{\mathrm{d}t}{a(t)} \ , \tag{1.11}$$

and consequently

$$\frac{\delta t_0}{a(t_0)} - \frac{\delta t}{a(t)} = 0 \ , \tag{1.12}$$

which means

$$\frac{\omega_0}{\omega} = \frac{\lambda}{\lambda_0} = \frac{a(t)}{a(t_0)} \ . \tag{1.13}$$

Using (1.9) and $a(t_0) \equiv 1$ we can write the definition of cosmological redshift

$$\frac{1}{1+z} \equiv a(t) \ , \tag{1.14}$$

and the redshift is thus a direct probe of the scale factor at the time of emission. While this relation was derived for a spatially flat model, it holds for any homogeneous and isotropic model.

1.3.2 Hubble's discovery

By 1929, Hubble had obtained the distance to 18 nearby spiral galaxies (his "nebulæ") and combined his results with the velocities measured by Slipher (1924). He found out that they were receding away from us with velocity given by $v = cz$, which increased linearly with distance (Fig. 1.1)

$$v = H_0 r \ . \tag{1.15}$$

This is the *Hubble's law*, with H_0 the Hubble constant (the present value of the Hubble parameter, introduced in § 1.2.4). Its message is that *the universe is expanding* and a static universe, where the galaxies should move about randomly is ruled out. The expanding universe, in this comoving coordinates' frame where all galaxies rush away from each other, is interpreted not by a change in position coordinates but by an ever-increasing metric – the expansion of space itself.
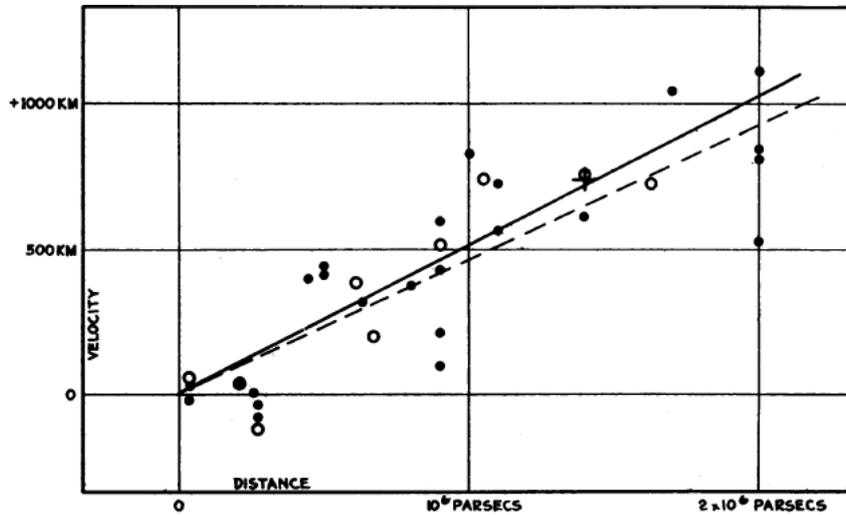
Figure 1.1: Hubble's original diagram relating the recession velocity of the "nebulæ" with their distance from us. The two lines use different corrections for the Sun's motion. He found $h \sim 0.5$. From Hubble (1929).

Hubble's constant can be written as

$$H_0 \equiv 100 \ h \ \mathrm{km \ s^{-1} Mpc^{-1}} \ , \tag{1.16}$$

with recent measurements (Freedman et al. 2001) finding

$$h = 0.72 \pm 0.08 \ .$$

1.3.3 Universe composition evolution

In order to discover how the universe might evolve, we need some idea of what is in it. In a cosmological context this is done by specifying the equation of state for each of the components of the universe.

From (1.8) and for a w_i constant, we can write the time evolution of the energy density

$$\frac{\dot{\rho}_i}{\rho_i} = -3\frac{\dot{a}}{a}(1+w_i) \tag{1.17}$$

$$\rho_i = \rho_{i_0}\left(\frac{a}{a_0}\right)^{-3(1+w_i)} \tag{1.18}$$

$$\rho_i \propto a^{-3(1+w_i)} \tag{1.19}$$

$$\propto (1+z)^{3(1+w_i)} \ , \tag{1.20}$$

and using (1.5), (1.19) and the fact that, since at early times a is small and the curvature term can be neglected, we write the time evolution of the scale factor for a single component universe as

$$a(t) \propto t^{\frac{2}{3(1+w_i)}} \ . \tag{1.21}$$

So, for the three most common barotropic (with pressure linearly proportional to density) fluids present in the universe, we can divide the history of the universe (Fig. 1.2) into three epochs:
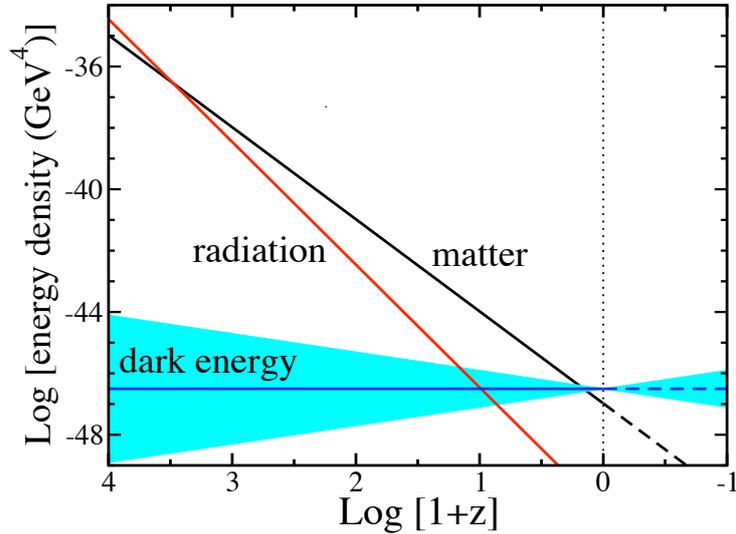
Figure 1.2: Evolution of radiation, matter, and dark energy densities with redshift. From Frieman et al. (2008a).

Radiation-dominated In the early hot and dense universe, it is appropriate to assume an equation of state corresponding to a gas of radiation (or relativistic particles) for which $w_r = \frac{1}{3}$, leading to

$$\rho_r \propto a^{-4} \ ; \ a(t) \propto t^{\frac{1}{2}} \ . \tag{1.22}$$

We can see that the radiation density decreases with the forth power of the scale factor. Three of these powers are accounted for by the volume increase during the expansion, while the forth one comes from the cosmological redshift.

Matter-dominated At relatively late times, non-relativistic matter eventually dominates the energy density over radiation. It's a pressureless gas of particles with temperatures much smaller than their mass for which $w_m = 0$, and

$$\rho_m \propto a^{-3} \ ; \ a(t) \propto t^{\frac{2}{3}} \ . \tag{1.23}$$

Vacuum energy-dominated If there is a dominant source of vacuum energy that acts as a cosmological constant according to (1.7), its equation of state is $w_x = w_\Lambda = -1$, so

$$\rho_\Lambda \propto \text{constant} \; ; \; a(t) \propto e^{Ht} \; , \tag{1.24}$$

and the universe expands exponentially. However the vacuum equation of state does not need to be the $w = -1$ of Λ, neither it needs to be constant. That's the more general possibility of a dynamical vacuum energy (§ 1.4.1) of the type

$$w_x(a) = w_0 + (1-a)w_a \; . \tag{1.25}$$

Recent measurements (Komatsu et al. 2008), constraint respectively the dark energy constant and time-dependent equations of state (for a flat universe) by

$$-0.11 < 1 + w < 0.14 \; (95\% \text{ CL})$$
$$-0.38 < 1 + w_0 < 0.14 \; (95\% \text{ CL})$$

(For the sake of completeness, assuming (against all the major evidences (§ 2.1)) that our universe has $k \neq 0$ and we have a null dark energy parameter, we would have instead a curvature-dominated epoch, with

$$a(t) \propto t \; . \tag{1.26}$$

)

1.3.4 Cosmological parameters

We can now define a set of parameters which will describe the contents and their changes throughout the expansion history of the universe.

Energy densities

From the Friedmann equation (1.5), for any value of the Hubble parameter H there is a critical value of the density that would be required in order to make the spatial geometry of the universe flat, $k = 0$:

$$\rho_c \equiv \frac{3H^2}{8\pi G} \; , \tag{1.27}$$

which corresponds on the present epoch to

$$\begin{aligned}
\rho_c(t_0) &= 1.88 \; h^2 \times 10^{-26} \text{ kg m}^{-3} \\
&= 2.78 \; h^{-1} \times 10^{11} \text{ M}_\odot / \left(h^{-1}\text{Mpc}\right)^3 \\
&= 11.26 \; h^2 \text{ protons m}^{-3} \; ,
\end{aligned}$$

or ~ 6 protons per cubic meter, a rather dilute fluid. Since that the observed typical mass for a galaxy is in the order of $10^{11} \sim 10^{12} \; M_\odot$ (solar masses), and their separations in the order of a Mpc, we can see that the universe cannot be far away from the critical density. Beyond this critical density, the universe's geometry becomes closed, and the amount of matter provides enough gravitational attraction to stop and reverse the expansion.

The critical density can be used to set a natural scale for the density of the universe, by defining the *density parameter*

$$\Omega \equiv \frac{\rho}{\rho_c} \; . \tag{1.28}$$

We can thus rewrite the Friedmann equation as

$$\Omega - 1 = \frac{k}{a^2 H^2} \ , \tag{1.29}$$

with (for the i components, radiation, matter and dark energy)

$$\Omega = \sum_i \Omega_i = \sum_i \frac{8\pi \mathrm{G} \rho_\mathrm{i}}{3H^2} \ . \tag{1.30}$$

It is interesting to note the direct relation given by (1.29) between energy content and curvature of the universe: $\Omega \ \{> 1, < 1, = 1\}$ gives us respectively closed, open or spatially flat universes. Specifically stating the different contributions to the energy density today, we can write the "cosmic sum" which determines the overall sign of the curvature[7]

$$\Omega_0 = \Omega_r + \Omega_m + \Omega_x = \frac{k}{H_0^2} + 1 \ . \tag{1.31}$$

Deceleration parameter

Looking now at the second Friedmann equation (1.6), we can define a new parameter, the so-called *deceleration*[8] *parameter*

$$q_0 \equiv -\frac{\ddot{a}}{a_0 H_0^2} = \frac{1}{2} \sum_i \Omega_{0_i}(1 + 3w_i) \tag{1.32}$$

$$= \Omega_r + \frac{\Omega_m}{2} + \frac{\Omega_x}{2}(1 + 3w_x) \ , \tag{1.33}$$

which relates the dynamics of the universe with its contents. $q_0 = 0$ would represent a static universe, whether a positive or negative value means the expansion is decelerating or accelerating. For a flat universe, w_x has to be $< -\frac{1}{3}$ for the latter case to happen.

Hubble parameter

The (time dependent) Hubble parameter already introduced in § 1.2.4 can be related to its present day value (Hubble's constant). Substituting (1.28) on (1.18) we obtain

$$\rho_i = \rho_c \Omega_0 a^{-3(1+w_i)} \ , \tag{1.34}$$

which applied with (1.27) and (1.31) on the Friedmann equation (1.5), gives us the a-dependent Hubble parameter

$$H(a) = H_0 \sqrt{\Omega(a) + (1 - \Omega_0)a^{-2}} \ , \tag{1.35}$$

with

$$\Omega(a) = \sum_i \Omega_{0_i} a^{-3(1+w_i)}$$

$$= \Omega_r a^{-4} + \Omega_m a^{-3} + \Omega_x a^{-3(1+w_x)} \ . \tag{1.36}$$

An equivalent redshift-dependent Hubble parameter can easily be found using (1.14)

$$H(z) = H_0 \sqrt{\Omega(z) + (1 - \Omega_0)(1 + z)^2} \ . \tag{1.37}$$

---

[7]Some authors also define a curvature "density" parameter, as $\Omega_k \equiv -\frac{k}{H_0^2}$, and thus $\Omega_0 + \Omega_k = 1$.

[8]The reason for the name is historical, since it was believed that the universe should be decelerating.

Lookback time and age of the universe

From the definition of Hubble parameter (1.5) we can derive the expression of the *lookback time*, *i.e.* the time interval between the present epoch and the time t of an event that happened at redshift z

$$\int_0^{t(a)} dt' = \int_1^a \frac{da'}{a'H(a')}$$

$$H_0 t = \int_0^{\frac{1}{1+z}} da \left[(1 - \Omega_0) + \Omega_r a^{-2} + \Omega_m a^{-1} + \Omega_x a^{-(1+3w_x)} \right]^{-\frac{1}{2}} , \qquad (1.38)$$

where we used (1.35). By setting $z \rightarrow \infty$ one obtains the present age of the universe as a function of the densities parameters. Recent measurements (Komatsu et al. 2008) find

$$t_0 = 13.73 \pm 0.12 \text{ Gyr} .$$

The $(\Omega_\Lambda, \Omega_m)$ plane
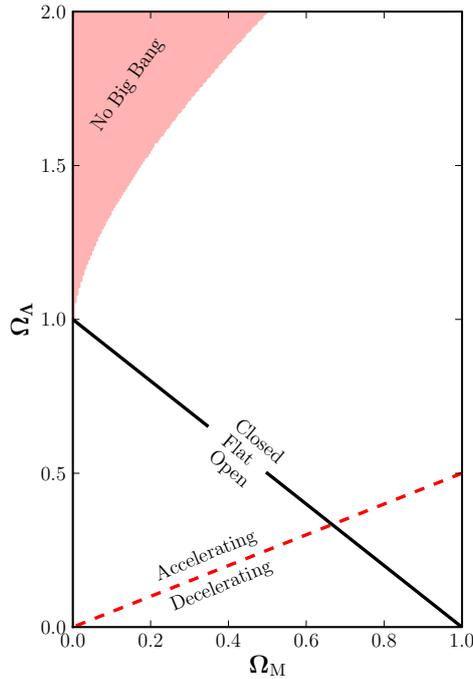
Figure 1.3: The $(\Omega_\Lambda, \Omega_m)$ plane.

In the present day, where the radiation density is very small, we can reduce equation (1.31) to a very simple relation between the energy densities of two components, matter and dark energy. This gives rise to a typical way of plotting our observational constraints, which can be directly compared with predictions from the cosmological models.

A plot of the $(\Omega_\Lambda, \Omega_m)$ space can be seen in Fig. 1.3, where we use $w_\Lambda = -1$. The accelerating/deceleration line is given by $q = 0$, the closed/open one by $k = 0$, and the shadowed region for no Big Bang is delimited by $H_0 t = \infty$.

1.3.5 Cosmological observables

All the introduced cosmological parameters depend on a certain number of observables, of which we already introduced the redshift. We will now introduce another one: distances.

Proper distance

In the comoving frame at which we are at the origin, the distance from us to an object is not an observable. That's because a distant object can only be observed by the light it emitted at an earlier time, where the universe had a different scale factor, none of which observable either.

We need then to define a relationship between the physical distance and the redshift, as a function of the dynamics and the contents of the universe.

The *proper distance* d_P is defined so that $4\pi d_\mathrm{P}^2$ is the area of the sphere over which light from a far emitting source spreads in the time it travels to us. It can be derived using the metric for a null geodesic

$$\int_0^{d_\mathrm{P}} \frac{\mathrm{d}r}{\sqrt{1-kr^2}} = \int_0^{t_0} \frac{\mathrm{d}t'}{a} = \int_0^z \frac{\mathrm{d}z'}{H(z')} = \int_a^1 \frac{\mathrm{d}a'}{a'^2 H(a')} \ . \tag{1.39}$$

Evaluating the left hand side integral and using (1.37) we get

$$d_P = \frac{1}{H_0 \sqrt{|\Omega_k|}} \mathcal{X}\left[\sqrt{|\Omega_k|}\int_0^z \mathcal{Z}(z')\mathrm{d}z'\right] \ , \tag{1.40}$$

with $\Omega_k = \Omega_0 - 1$ (see footnote 7),

$$\mathcal{X}[x] = \begin{cases} \sin x & \text{if } k > 0 \\ x & \text{if } k = 0 \\ \sinh x & \text{if } k < 0 \end{cases} \ , \tag{1.41}$$

and

$$\mathcal{Z}(z') = \left[\Omega_r(1+z')^4 + \Omega_m(1+z')^3 + \Omega_x(1+z')^{3(1+w_x)} + \Omega_k(1+z')^2\right]^{-\frac{1}{2}} \ . \tag{1.42}$$

If we now have $k \sim 0$, (1.40) reduces to (*cf.* Fig. 1.4)

$$d_\mathrm{P} = \frac{1}{H_0}\int_0^z \frac{\mathrm{d}z'}{\sqrt{\Omega_r(1+z')^4 + \Omega_m(1+z')^3 + \Omega_x(1+z')^{3(1+w_x)}}} \ . \tag{1.43}$$

Luminosity distance

The main method to calculate distances to any stellar objects is to estimate its true luminosity and compare that to the observed flux (inversely proportional to the square distance).

The measured flux f is connected to the intrinsic luminosity L by

$$f = \frac{L}{4\pi d_\mathrm{L}^2} \ , \tag{1.44}$$

where d_L is the *luminosity distance*. In an expanding universe, this relation does not hold: the observed flux is reduced by $(1+z)^2$ due to the cosmological redshift. From (1.13) we see that one
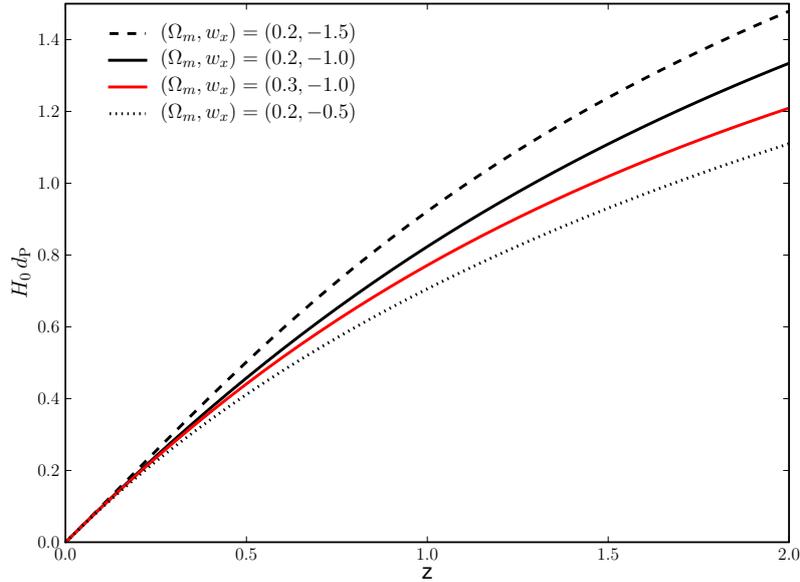
Figure 1.4: Proper distance relation with redshift for different cosmological parameters, in a flat universe.

power of $(1+z)$ comes from the energy reduction due to wavelength lengthening, and another due to the decreasing frequency on reception, so that

$$f = \frac{L}{4\pi d_{\mathrm{P}}^2 (1+z)^2} \; , \tag{1.45}$$

where d_{P} is the proper distance (1.40). We have thus

$$d_{\mathrm{L}} = d_{\mathrm{P}}(1+z) \; . \tag{1.46}$$

In astronomy the brightness of an object is typically expressed in terms of magnitudes. This logarithmic measure of relative flux is so, that the *apparent magnitude m* of an object is related to its flux f as

$$m - m_* = -2.5 \log_{10} \frac{f}{f_*} = -2.5 \log_{10} \frac{L}{L_*} \frac{d_{\mathrm{L}_*}^2}{d_{\mathrm{L}}^2} \; , \tag{1.47}$$

and becomes an absolute scale if the object with flux f_* is used as standard reference. This reference is an object whose intrinsic luminosity L_* is such, that if its luminosity distance d_{L_*} is 10pc, its apparent magnitude m_* is equal to 0. We can thus define the *distance modulus μ*

$$\begin{aligned} \mu \equiv m - M &= 5 \log_{10} \frac{d_{\mathrm{L}}}{10} \\ &= 5 \log_{10} [d_{\mathrm{P}}(1+z)] - 5 \; , \end{aligned} \tag{1.48}$$

with the *absolute magnitude*

$$M \equiv -2.5 \log_{10} \frac{L}{L_*} \; . \tag{1.49}$$

These definitions imply $L_* \approx 78.7 L_\odot$, which is the case for Vega (α Lyr), historically used as a reference for the magnitude system (nowadays, filter dependent zero-points are used instead).

We thus introduced a new observable, the received flux of a distant source. The astronomical object for which we are able to infer its intrinsic luminosity independently of the observed flux is called a *standard candle*. That's the case of the Cepheids (used by Hubble for the distances determination), which are variable stars who present a correlation between their period and luminosity, as well of other standardizable objects like globular or galaxies clusters (*cf.* Roos (2003)).

One important standard candle, observable up to distances where the cosmological redshift effects dominates (and thus for which we can use (1.48) to study the composition of the universe), are the type Ia supernovæ (SNe Ia). They are the main study object of this thesis, and thus the luminosity distance will be our most important observable. The SNe Ia will be further presented in § 2.3.

Angular-diameter distance

The usage of objects of known intrinsic size, the *standard rulers*, allows us to measure the proper distance in a similar fashion of the luminosity distances, although now in a "orthogonal" direction of the metric. The diameter of a source of light at comoving distance d_{P} is defined by (1.2) as

$$D \equiv a(t)\theta d_{\mathrm{P}} \ . \tag{1.50}$$

We can then define the *angular-diameter distance* as

$$\begin{aligned} d_{\mathrm{A}} \equiv \frac{D}{\theta} &= a(t)d_{\mathrm{P}} \\ &= \frac{d_{\mathrm{P}}}{1+z} \ , \end{aligned} \tag{1.51}$$

where θ is the measured angular diameter. It relates to the luminosity distance (1.46) as

$$d_{\mathrm{A}} = \frac{d_{\mathrm{L}}}{(1+z)^2} \ .$$

A key application of the angular-diameter distance is in the study of features in the cosmic microwave background radiation (§ 2.1).

Other observables

Other observables which I will not detail, include the number of objects (galaxies, quasars) within a *comoving volume* element, which relates d_{P}^2 and $H(z)$; and the mass power spectrum from the distribution of galaxies at very large scales, which depends on the initial spectrum of inhomogeneities and their evolution with time. They are mainly used by redshift surveys of large scale structure (§ 2.2).

1.4 The ΛCDM concordance model

We arrive thus at the consensus cosmological model, the so-called ΛCDM (cosmological constant and cold dark matter) model. Considered as the nowadays "standard model" for cosmology, it tells us that:

- the geometry and dynamics of the expanding universe are described by the general relativity FLRW models (§ 1.2 and 1.3);

- the universe is flat ($k = 0$, $\Omega_o = 1$) and had nearly scale-invariant inhomogeneities in the initial density perturbations (§ 2.1 and 2.2), which are responsible for the structure formation, as predicted by the inflation theory (Guth 2004);

- the total energy density of the universe is accounted for at:

    - $\sim 4\%$ by the baryon energy density, constraint by the big bang model of primordial nucleosynthesis (Burles et al. 2001);
    - $\sim 23\%$ by a cold, nonbaryonic and collisionless matter (cold dark matter);
    - $\sim 73\%$ by a cosmological constant (Λ) type of dark energy ($w_\Lambda = -1$), which accelerates the expansion (§ 2.3).

This model's predictions and assumptions are currently well constraint by observational data (*cf.* Chap. 2). There's still however some theoretical animosity towards this model, namely about the cosmological constant. While correctly explaining today's observations of the accelerated expansion, there is no underlying physics associated to it nor to its constant equation of state. The tentative explanation by means of the vacuum energy (*cf.* footnote 5), struggles with a 120 orders of magnitude difference between the predicted and measured values. Another problem is the so-called *coincidence problem*: why is $\Omega_m + \Omega_\Lambda \simeq 1$ precisely today when we are here to observe it, after an expansion of several billion years? If Ω_m decreases with time and Ω_Λ remains constant, why has the cosmological constant begin to dominate the sum only now?

Other than an explanation based on the untestable anthropic principle[9], a few modifications to the standard model are proposed to try to solve these and other problems, although they still remain observationally indistinguishable from a cosmological constant model.

1.4.1 Extension models

Most extension models to explain the expansion acceleration can be divided into three categories (Roos 2008) according to their modifications:

dynamical which modify the right hand side of Einstein's equations (1.3). These *quintessence* models (Martin 2008) assume a slowly evolving scalar field, with negative pressure, having a potential with an energy density behaving like a decaying cosmological constant.

geometrical which modify the left hand side of (1.3). Changes can by made to obtain a new version of the Friedmann equation which defines $a(t)$, or else to the equations that govern the growth of the density perturbations. These modifications must reduce to the standard GR at very small (solar system), and very large (early times) distances to be compatible with observations.

new spatial conditions by removing the cosmological principle assumption that the universe is spatially homogeneous at large scales. These *back-reaction* models assume we are at the center of a nearly spherical large scale under-dense region. The non-linear gravitational effects of these spatial density perturbations, averaged over large scales, would give a distance-redshift relation similar to that of an accelerating universe.

---

[9]Which states that the universe is as it is because otherwise we would not be here to observe it.

Chapter 2

Observational cosmology

As seen on the previous chapter, the cosmic expansion (and acceleration, which we will see shortly), and the role played by dark energy are one of the most intriguing problems that physics faces today. Recent years have seen a new wealth of experiments arrive, that try to bring answers to these questions, in an unprecedented program to determine the nature of dark energy with high precision.

I will now present the three major axis of experiments that probe the expansion history of the Universe.

2.1 Cosmic Microwave Background

After the Big Bang, the universe was radiation-dominated. In this hot and dense plasma of matter and radiation in thermal equilibrium, photons scattered freely of electrons and prevented the formation of neutral nuclei. With the expansion, the temperature gradually decreased until the photons' energy was not enough to ionize hydrogen ($T \sim 3000$ K), and the neutral light elements appeared. The universe thus became transparent to radiation and the photons were allowed to travel free. This epoch of the last scattering of photons, when the universe had around 380,000 years ($z \sim 1100$), is called the *photon-decoupling* or *recombination*[1] time, and the cosmic microwave background (CMB) is the leftover radiation from this moment.

The CMB was first detected by Penzias and Wilson (1965), and its predicted blackbody spectrum was measured with high accuracy by the COBE (Smoot et al. 1992; Fixsen et al. 1996) space-borne experiment. The measured temperature of the CMB nowadays is

$$T_{\mathrm{CMB}_0} = 2.725 \pm 0.002 \text{ K} .$$

COBE's observational breakthrough was the measurement of angular variations in the temperature maps of the CMB. These very small *anisotropies*

$$\frac{\Delta T}{T} \sim 10^{-5} ,$$

are an expected effect of the inflationary phase, and the key to understand the origin of structure on the universe, since they reflect the departure from homogeneity at the recombination epoch. The anisotropies form from the density perturbations that propagated as acoustic waves in the initial plasma of matter and photons. After decoupling, these perturbations no longer oscillate and the CMB photons have imprinted a snapshot of the state of the fluid at that time.

---

[1]Which might be a misleading name, since the baryons and electrons were never combined before.

By analyzing the anisotropies map (Fig. 2.1a), one can extract the fundamental oscillatory mode and corresponding harmonics, and obtain its power spectrum (Fig. 2.1b). The exact form of the peaks of the power spectrum depends on the matter content of the universe, thus the measurement of its shape (a standard ruler), yields precise information about many cosmological parameters. These measurements, while not probing dark energy directly, provide constraints like the flatness (Ω_k), or the baryon (Ω_b) and dark matter densities (Ω_c), that can be used to infer Ω_Λ.
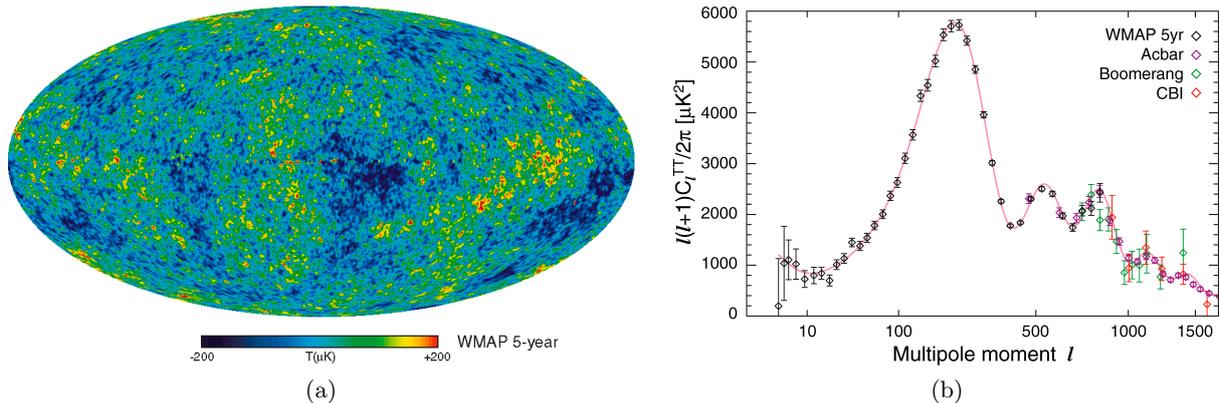
Figure 2.1: (a) WMAP 5 year CMB temperature anisotropies map from Hinshaw et al. (2008); (b) CMB temperature power spectrum from the WMAP 5 year dataset (Nolta et al. 2008), along with results from ACBAR (Reichardt et al. 2008), BOOMERANG (Jones et al. 2006) and CBI (Readhead et al. 2004). The red curve is the best-fit ΛCDM model to the WMAP data.

The most recent CMB measurements come from the WMAP satellite (Komatsu et al. 2008), whose 5 year results for a few ΛCDM parameters, combined with BAO (§ 2.2) and SNe (§ 2.3) data, are expressed in Table 2.1. In the near future, a new generation of ground and space (like the Planck satellite (The Planck Collaboration 2006)) experiments will further study the CMB with even higher accuracy, searching *e.g.* for the imprint of primordial gravitational waves in its polarization power spectrum.

Parameter	WMAP+BAO+SN
t_0	13.73 ± 0.12
H_0	70.1 ± 1.3
Ω_b	0.0462 ± 0.0015
Ω_c	0.233 ± 0.013
Ω_Λ	0.721 ± 0.015
Ω_0	1.0052 ± 0.0064

Table 2.1: Some ΛCDM parameters inferred from the 5 year WMAP+BAO+SN. From Komatsu et al. (2008).

2.2 Large Scale Structure

The various forms of structures (stars, galaxies, clusters of galaxies) we observe today in the universe (Fig. 2.2), are collectively referred to as the large-scale structure (LSS). They are the

result of slight overdensities in the initial baryon-photon plasma, that grew through gravitational instability throughout the expansion.
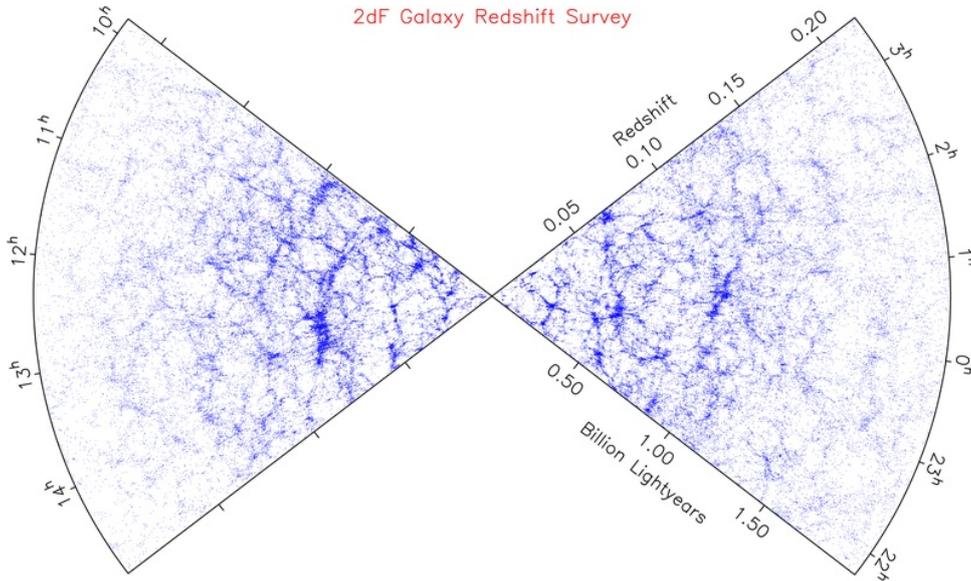
Figure 2.2: The 2dFGRS map, showing the redshift distribution of the full sample of ~ 240000 observed galaxies up to $z \sim 0.2$. From Colless et al. (2003).

There are several methods which use the LSS to probe for different observables, of which the most promising for dark energy measurements are:

Baryon acoustic oscillations In the same way as the density fluctuations in the primordial photon-baryon plasma show up in the temperature power spectrum of the CMB, they can also be seen in the large scale spatial distribution of baryons. Their manifestation is a spike at ~ 150 Mpc separation in the matter distribution correlation function, an effective standard ruler and hence a dark energy distance-redshift probe. In the recent years, wide field redshift surveys like the 2dFGRS (Colless et al. 2003) and the SDSS (Adelman-McCarthy et al. 2008), provided us with 3D maps of the galaxy distribution in the nearby universe. Since galaxies trace the evolution of (dark) matter, these surveys can be used to find the characteristic BAO scale (Eisenstein et al. 2005; Percival et al. 2007).

Weak gravitational lensing The observed shapes of distant galaxies become slightly distorted as light from them passes through foreground mass structures. The "distortion" pattern depends then on the distances to the source and lens as well as its mass, being thus both a geometrical (distance-redshift) and mass distribution probe. This lensing signal that induces an observable ellipticity (the cosmic *shear*) in the background galaxies has been detected (Bacon et al. 2000; Hoekstra et al. 2006), and wide field galaxy surveys are being carried (Fu et al. 2008) to further improve the quality of this cosmological probe.

Galaxy cluster counts Galaxy clusters are the largest gravitationally-collapsed objects in the universe, and "mark" the locations that had the highest density fluctuations in the early universe. The measurement of the spatial density and distribution of galaxy clusters is sensitive to dark energy through its effect on a combination of the angular-diameter distance-redshift relation, the time evolution of the expansion rate and the growth rate of structure. Several different observables are used, either separately or combined (Bergé et al.

2008), to infer the galaxy cluster mass function: direct counting, x-ray flux/temperature, the Sunyaev-Zeldovich effect or weak gravitational lensing.

2.3   Supernovæ

A supernova explosion is the energetic display of a star's transition to a new phase of its evolution, or its death. This is one of the most energetic events in the universe, creating a new short-lived object in the sky, that outshines its host galaxy during a time-frame of a few weeks. Their extreme intrinsic luminosity make supernovæ observable up to cosmological distances, and thus standardizable probes of dark energy.

I will first present the divisions of the broad supernovæ "label" and corresponding origins, and then detail the present usage of supernovæ in cosmology.

2.3.1   Classification and origins

Historically, supernovæ classification has been based on their spectral features. Minkowski (1941) divided them into two groups, depending on the existence of hydrogen lines on their spectra at maximum light: type I supernovæ do not show H lines, whether type II do. This division was later extended (Filippenko 1997), as it became noticeable that there were more spectral and photometric differences inside each group.

The type I group is divided into 3 sub-families: the type Ia supernovæ (SNe Ia) with strong Si II absorption lines; and the Ib and Ic, both without Si II and respectively with or without He I. The type II divides into: II-l and II-p, based on their light curve[2] shapes (*linear* or with a *plateau*); II-n distinguished by *narrow* emission lines and slowly decreasing light curves; and II-b which represent a special type of supernova whose early time spectra is similar to type II and late time to Ib/c. This classification and corresponding spectra and light curve examples can be seen in Fig. 2.3 and 2.4.

Despite what one could think from this "standard" classification, type Ib/c supernovæ are closer to type II than to type Ia. This can be seen from the similar late time spectra (Fig. 2.4a), and from measurements of the explosion rates per host galaxy (Cappellaro et al. 1999): we do not observe any Ib/c or II supernovæ on elliptical galaxies, whether Ia are observed in all galaxy types. Furthermore, SNe Ia present an overall homogeneous spectroscopic and photometric behavior, contrary to the other types. These evidences (as well as the observation of the cross-over II-b type, linking SNe II with SNe Ib/c), reflect the different physical mechanisms, and hence the different origins, between the SNe Ia and all the other SNe.

Assuming a supernova originates from a single stellar object, only two physical mechanisms can explain the observed energy output: either through the release of the nuclear energy by an explosive reaction (thermonuclear supernovæ); either through the release of the gravitational binding energy when a star collapses to a compact object (core-collapse supernovæ).

Thermonuclear supernovæ

The homogeneity of the class of SNe Ia, allied to the facts that no hydrogen or helium exists in their spectra, and no remaining object is found in its remnants, provides a strong hint that their progenitor may be a carbon-oxygen white dwarf (WD) star (Woosley and Weaver 1986).

A WD is the "residual after-life" of stars whose main-sequence mass is lower than $10M_\odot$. During the main part of its life, the star burns hydrogen transforming it into helium. The

---

[2] A light curve is the representation of the supernova's brightness variation with time.
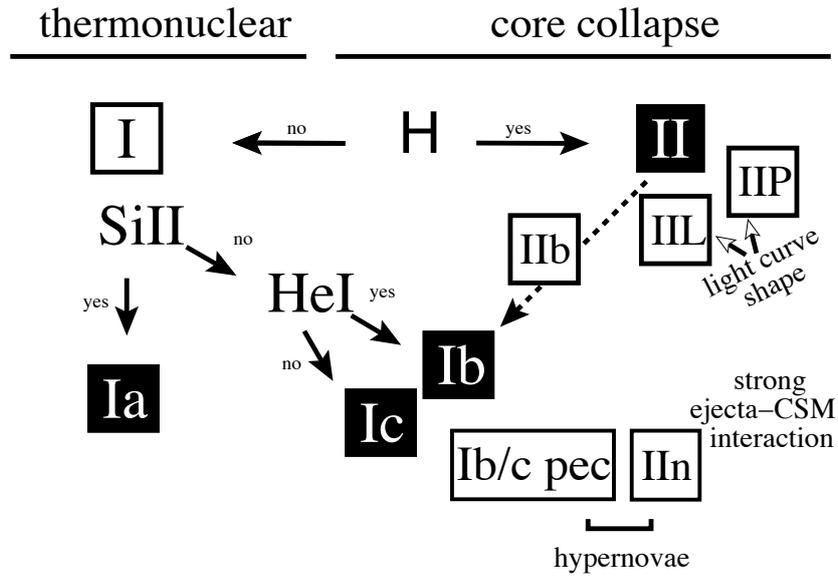
Figure 2.3: Supernovæ classification into different sub-groups. Remark the different origin of the SNe Ia with respect to all the other types. From Turatto (2003).
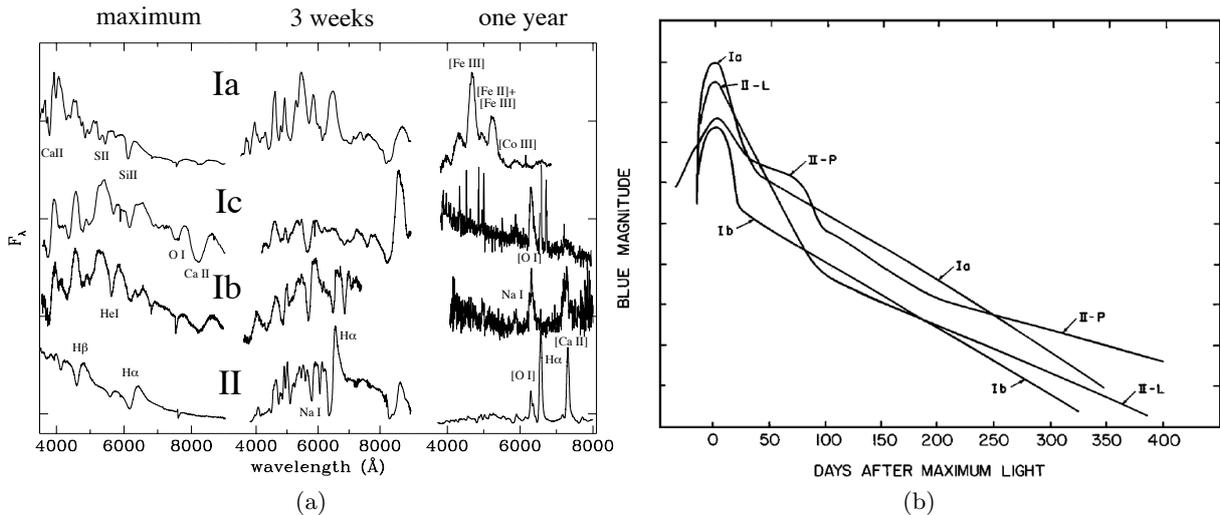
Figure 2.4: (a) Spectra of the main types of supernovæ at three different epochs and characteristic lines; (b) Typical (blue) light curves for the main types of supernovæ. Notice the higher luminosity at maximum of the SNe Ia with respect to all the other types. From Turatto (2003), Filippenko (1997).

thermonuclear reactions in the core stop when the hydrogen is exhausted, making the newly formed helium core contract, and the fusion of hydrogen "drift" towards the shell. As the outer layers are gradually heated, the star's envelope expands and its luminosity increases, attaining the *red giant* phase. During this phase, the core gradually contracts and its density becomes so great that the electrons become a degenerate gas, ruled by the Pauli exclusion principle. This degenerate gas pressure only depends on the density, not on temperature, and is enough to balance the gravitational force, even though no fusion reactions occur. As the core continues to contract, the temperature increases until being enough to ignite the helium, the *helium-flash*. This out of control process (in the degenerate core, the increase in temperature does not make it

expand, instead fueling even more the helium burning), increases the temperature continually, and as it approaches the Fermi temperature the electrons become once again non-degenerate and the helium-flash stops.

The star then burns quietly all the helium in the core, creating carbon and oxygen until (as in earlier phases), the core fuel ends and the reactions continue in an outer shell of helium. Once again the star expands, and since the helium burning reaction (triple-alpha) is very sensitive to temperature, the star will enter a pulsating phase, where the balance between internal pressure and gravity changes as the star expands (and the temperature decreases) or contracts (and the temperature increases). These pulsations generate a very strong outflow of mass from the stars surface, which will gradually scatter its envelope in the form of an expanding shell heated by the hot core, a planetary nebula[3]. The core, constituted of a degenerate carbon and oxygen gas, continues to contract and cool, and a WD is formed.

The WD's exotic constitution makes it a strange object: the more massive it is the smaller it gets (a WD with the mass of the Sun would be roughly the size of the Earth). Besides, a WD is only stable up to a specific mass, the Chandrasekhar mass (Chandrasekhar 1931) of $\sim 1.4 M_\odot$, above which the degenerate electron gas pressure cannot counter the gravitational collapse.

That is the key behind the SNe Ia: if we have a WD in a binary system (the *single-degenerate* scenario), accreting matter from a companion (Fig. 2.5), its mass will steadily increase up to the Chandrasekhar limit. At that moment, the density in the core is such that carbon fusion ignites, leading to the production of ^{56}Ni. As we have already seen, thermonuclear fusion is unstable in the degenerate matter, in the sense that it does not allow the moderation of the burning by expansion. A nuclear instability ensues, followed by a nuclear burning front that propagates through the star and explodes it completely.

A new SNe Ia then appears in the sky and its luminosity peaks in just a few days. The consequent decrease of the light curve over several months cannot be powered by the explosion itself, since temperature decreases too fast, and is explained instead by the radioactive decay of the ^{56}Ni produced during the carbon fusion, into its daughter nucleus: ^{56}Ni $\rightarrow^{56}$ Co $\rightarrow^{56}$ Fe.

While accounting for the relative SNe Ia homogeneity (related to the limit imposed by the Chandrasekhar mass), not all the physical processes behind this model are yet fully understood. Several flame propagation and explosion scenarios are proposed (Hillebrandt and Niemeyer 2000), and despite the huge improvement in recent years, numerical hydrodynamical simulations of SNe Ia explosions are still incapable of providing an accurate enough description of observations (Roepke 2008).

Core-collapse supernovæ

The fact that type II or Ib/c supernovæ are absent from the elliptical galaxies, which contain only old, low-mass stars, makes a strong point on their origin as the gravitational collapse of a massive star. In the core of their progenitors (stars with mass higher than ~ 10 M$_\odot$), the hydrostatical equilibrium holds as long as the fusion reactions burn the available hydrogen and form heavier and heavier elements, up to iron. The star has then an "onion-layer" structure, with layers of different composition, from the iron in the core to the hydrogen[4] in the envelope. Since no further exothermic reactions are possible, as the iron core mass continues to increase, it reaches the Chandrasekhar mass and the internal (degenerate electron) pressure can no longer counterbalance gravity. The star collapses until the core attains a large enough density and

---

[3]Historically called this way, since it looks like a planet when viewed through a small telescope.

[4]In the case of SNe II. SNe Ib progenitors are thought to have lost their hydrogen layer due to strong stellar winds or interaction with a binary companion, while SNe Ic would lose their helium layer as well.

Figure 2.5: Artist impression of a SNe Ia caused by the explosion of a WD accreting matter in a binary system. By D. Hardy (http://www.astroart.org).

temperature, where the iron nucleons are photo-dissociated into helium nuclei and free electrons, which (through inverse β decay) combine with protons to form neutrons and neutrinos. A neutron star[5] is formed. The sudden increase in pressure, due to the strong-force bounded neutrons, make the collapsing layers rebound, and the radiation pressure of the huge neutrino flow from the core would then be responsible for the displacement of the outer remaining layers of the star, which is then observed as a supernova.

The observation of supernova remnants with neutron stars in their center further supports this model.

2.3.2 SNe Ia homogeneity - standard candles

Visible up to great distances (the furthest observed until today has $z = 1.75$), supernovæ are a good candidate for a cosmological probe. Contrary to SN II and Ib/c, whose energy output is heavily dependent on the (wide-ranging) mass of the progenitor, SNe Ia have a similar evolution and explosion process (the thermonuclear disruption of a WD near the Chandrasekhar mass), and we can thus expect them to show a small scatter around their intrinsic peak luminosity. If this assumption is correct, SNe Ia explosions provides us with a good standard candle for distances way beyond the Cepheids. So, how good is this homogeneity?

Photometrically

The most common (and less telescope-time consuming) way to observe supernovæ is by photometric followup of their evolution. This is done by measuring on consecutive nights its luminosity (apparent magnitude), thus obtaining light curves in different filters[6]. The light curves for a typical SN Ia are shown in Fig. 2.6a.

---

[5]Under certain conditions, this neutron star can further collapse into a black hole.
[6]The Johnson-Cousins (Bessell 1990) UBVRI or the Fukugita et al. (1996) SDSS ugriz photometric systems are commonly used.
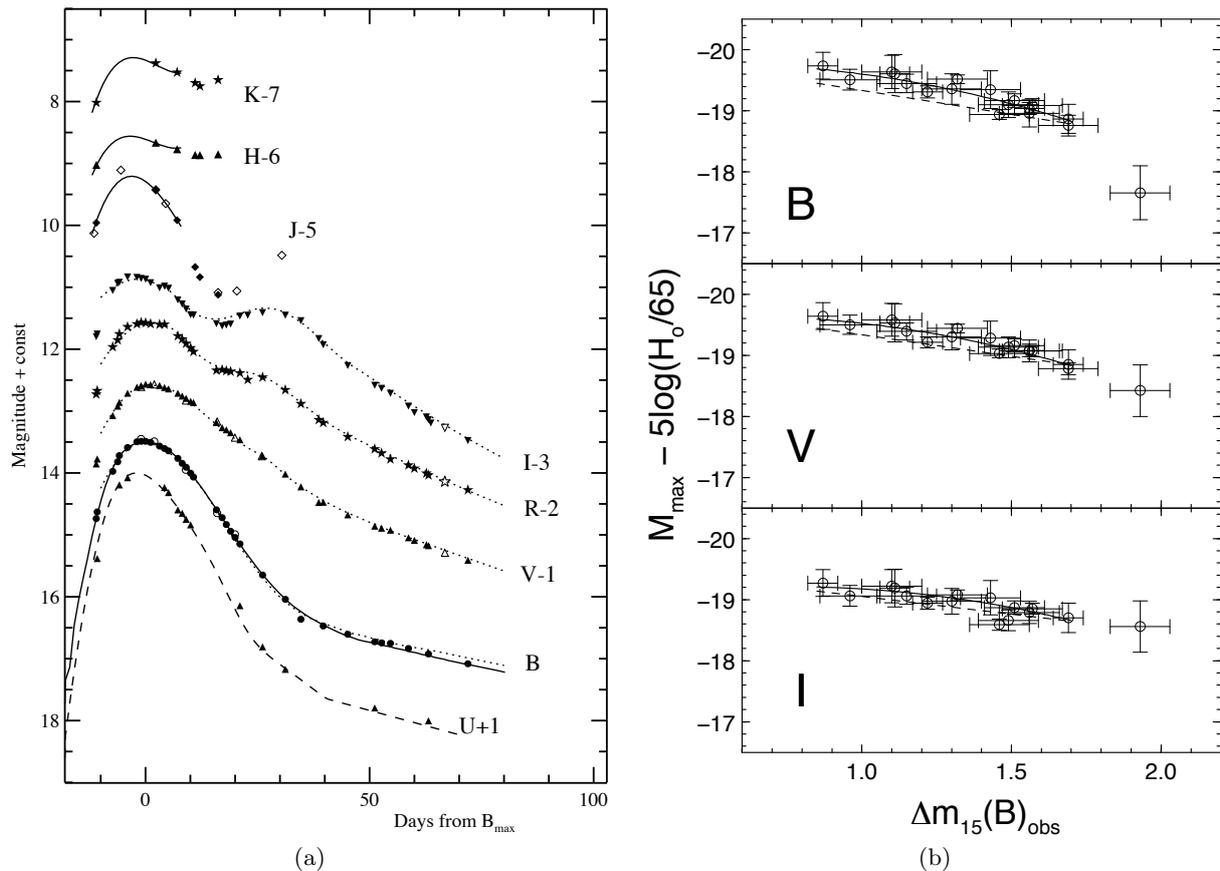
Figure 2.6: (a) Light curve in several bands (Johnson-Cousins UBVRI and near-infrared) from a typical SN Ia (SN2003du). Phase is with relation to B maximum. Adapted from Stanishev et al. (2007); (b) Brigther-slower correlation for SNe Ia light curves. Adapted from Phillips et al. (1999).

On the other hand, if one wants to know their absolute magnitude (to test our standard candle assumption), the case is somewhat different, since we need to have a measure of its distance. Hamuy et al. (1996) observed a number of nearby supernovæ in the *smooth Hubble flow*[7], for which the distance can be estimated via the host galaxy redshift and Hubble's law. The found (uncorrected - see next paragraph) values present some dispersion (Fig. 2.7a): scatters of 0.38 and 0.26 magnitudes for M_B and M_V (the absolute magnitude in the B and V bands respectively) were found. These scatters are compatible with results from several teams, which have been using observations of SNe Ia on galaxies with distances known through different techniques, like Cepheids measurements, for the determination of the Hubble constant: Sandage et al. (2006) observes mean absolute magnitudes M_{BV} between -19.3 and -19.55, compatible with the 0.3 magnitudes *range* span of the M_B measured by other teams, depending on calibration techniques and observational methods (see Table 2 in Gibson et al. (2000)).

Despite the existence of this scatter (thought to be mainly due to the amount of ^{56}Ni produced during the explosion (Timmes et al. 2003)), it is remarkably small: SNe Ia seem indeed to be good standard candles.

The first step in the SNe Ia standardization was made when, as new supernovæ started

---

[7]Where they are far enough ($z > 0.02$) so that intrinsic velocities are negligible, and near enough ($z < 0.08$) so that the cosmological expansion acceleration effects are negligible and Hubble's law is valid in first approximation.

to be systematically observed, it became clear that a linear correlation exists between the peak luminosity and the decline rate of their light curve. This "brighter-slower" (*i.e.* brighter objects' light curves seem to decline slower, see Fig. 2.7a) relation was introduced by Phillips (1993), in the form of the parameter Δm_{15}, which is the difference in magnitudes between the maximum and 15 days after it (Fig. 2.6b). By applying this empirical correction model to the absolute magnitudes, Hamuy et al. (1996) found the scatter reduced by a factor of 2, which entails a distance determination precision of $7 - 10\%$.

Several other standardization methods followed, notably: the MLCS (Riess et al. 1996) and stretch (Perlmutter et al. 1997b; Goldhaber et al. 2001) (Fig. 2.7b) methods, using supernovæ light curve shape templates; the ΔC_{12} (Wang et al. 2005) method for the "brighter-bluer"[8] correlation; the MLCS2k2 (Jha et al. 2007) and SALT[2] (Guy et al. 2005; Guy et al. 2007) methods, using both light curve shape and color parameters. In this work we will be mostly interested in the SALT approach, further detailed in § 2.3.4.
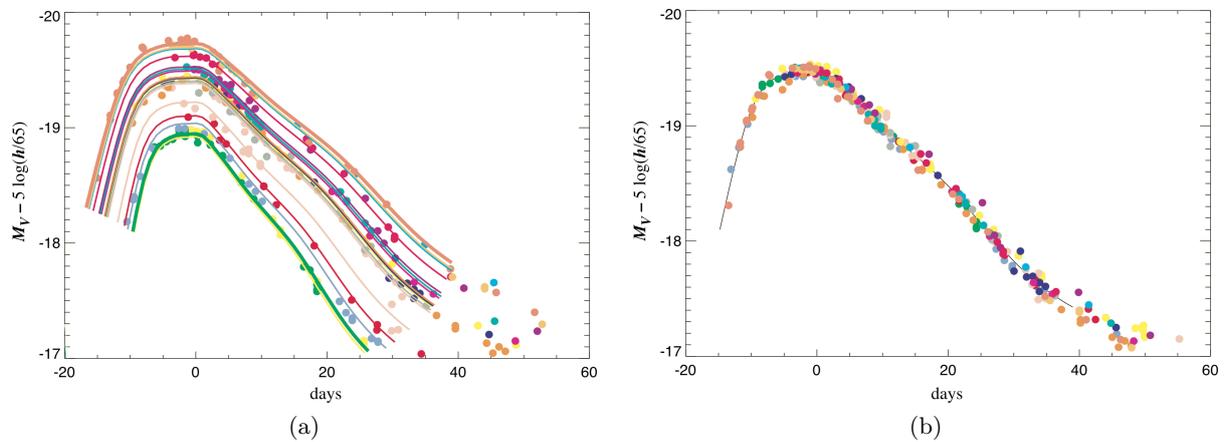
Figure 2.7: Cálan/Tololo nearby supernovæ absolute magnitudes in V band, (a) as observed and (b) after correction using the *stretch* parameter. Adapted from Perlmutter et al. (1997a).

It should be noticed that all these methods are mainly empirical. They correlate a distance-dependent parameter with one or more distance-independent parameters, and are applied on the single evidence that they improve the fit around the Hubble line in the Hubble diagram (*cf.* § 2.3.4). This approach is valid for a cosmological analysis, where we are interested in the *relative* distances between nearby and distant supernovæ sets, both standardizable by the most recent methods.

Spectroscopically

"Branch-normal" (Branch et al. 2006) SNe Ia optical spectra (Fig. 2.8a) present a remarkable homogeneity, as can be seen in Fig. 2.8b. The most identifiable spectral characteristic of a SN Ia (and its defining feature) is the prominent absorption around 6100Å, due to the Si II doublet ($\lambda\lambda$6347Å and 6371Å). Other observable lines near maximum light are Ca II ($\lambda\lambda$3934Å, 3968Å, and λ8579Å), Si II (λ3858Å, λ4130Å, λ5051Å, λ5972Å), Mg II (λ4481Å), S II (λ5468Å and $\lambda\lambda$5612Å, 5654Å) and O I (λ7773Å). The spectrum is also scattered with low-ionization Ni, Fe, and Co lines which increase in later times.

---

[8]Using the B-V color variation in the same sense as the Δm_{15} for magnitude.
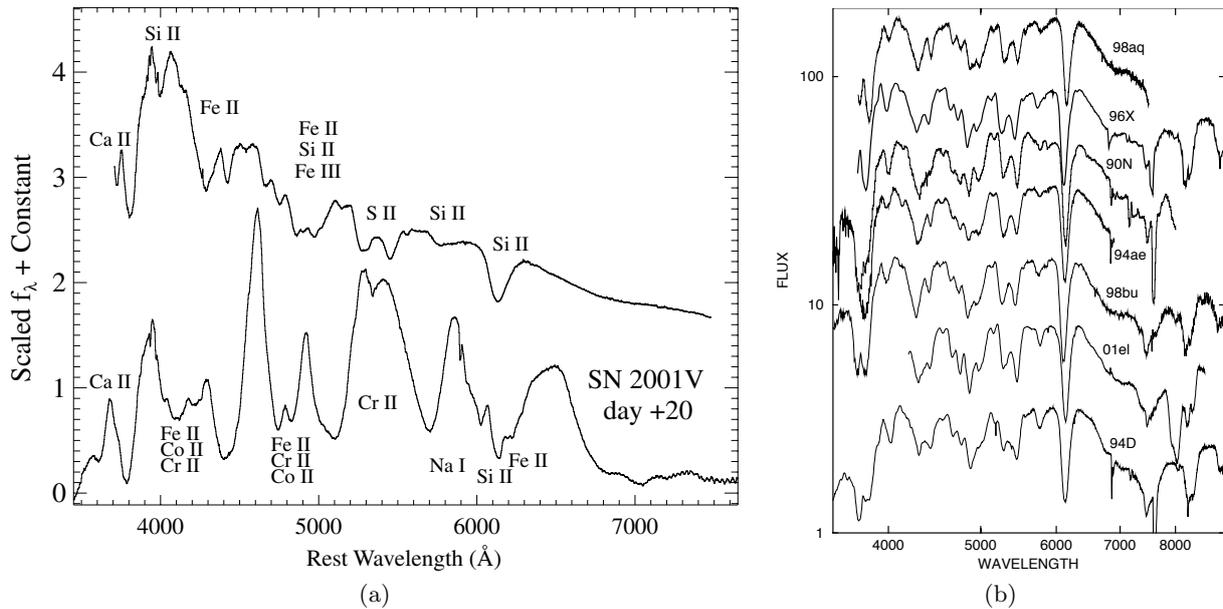
Figure 2.8: (a) Spectrum and characteristic lines at maximum (up) and 20 days later (bottom) for a typical SN Ia (SN1998aq). From Matheson et al. (2008). (b) Spectra at maximum luminosity for several "Branch-normal" SNe Ia. From Branch et al. (2006).

The analysis of SNe Ia spectral evolution divides their lifetime into two phases: the early *photospheric* phase, where the outer layers are opaque to radiation and we observe their constitution in the form of absorption lines, that change as the layers expand and become transparent; and the *nebular* phase, several weeks after maximum, when the environment has become transparent and we observe the emission lines of the inner layers, that can be attributed to Co and Fe transitions. The nebular phase is dominated by the changing strength of these individual lines multiplets. Despite the overall uniformity, subtle differences exist in lines strengths and velocities between different SNe Ia (Hachinger et al. 2006).

Deserving to be placed in a category apart, are a lot of peculiar SNe Ia presenting very different light curves and spectra from the "typical" ones. These will be presented in § 2.3.3.

While this photometric/spectroscopic division was made for easier presentation, they are obviously intrinsically connected: a light curve point is nothing more than the integration of a supernova spectrum by a bandpass filter. It is then clear that we could easily study the homogeneity and standardization of the SNe Ia class by simply using absolutely flux calibrated spectra. We will see in § 3 how the SNfactory project intends to do this.

2.3.3 SNe Ia heterogeneity - peculiar objects

Not all supernovæ fall into the "Branch-normal" category, as the ones already introduced. Some are substantially different, enough to place them into two distinct categories: underluminous and overluminous. They are connected to two objects observed in 1991 and used as the "reference" for each subclass: SN1991bg (under-) and SN1991T (overluminous) respectively. Typical light curves and spectra for these supernovæ are presented in Fig. 2.9.
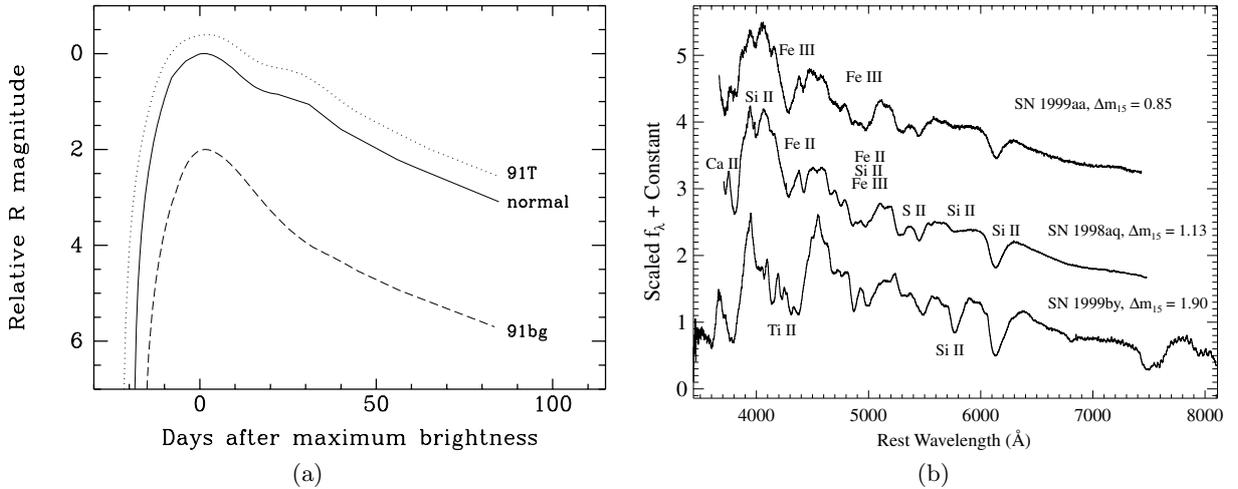
Figure 2.9: (a) Reconstructed light curves for under-, overluminous and normal SNe Ia in the R band, from Li et al. (2001); (b) Typical spectra for under- (SN1999by) and overluminous (SN1999aa) with relation to "Branch-normal" (SN1998aq) SNe Ia. From Matheson et al. (2008).

Underluminous

Photometrically, SN1991bg-like (Filippenko et al. 1992a) supernovæ are mainly identifiable by their redder color (cooler), and lower than normal luminosity (SN1991bg was 2.5 mag subluminous in B at maximum), the lack of the second peak in R and I bands and a fast decaying light curve. Their spectra has an accentuated absorption through around 4000Å, attributed to Ti II and very narrow nebular lines.

They are suggested to be the result of an explosion that underproduces ^{56}Ni with respect to a normal SNe Ia, having in the ejecta a large fraction of the mass of the progenitor unburned.

Overluminous

Photometrically, SN1991T-like (Filippenko et al. 1992b) supernovæ are slightly more luminous (SN1999T was 0.6 mag brighter), although their light curve is similar to normal SNe Ia. The main feature of their early spectra is that they do no present the typical Si II absorption, which is a lot shallower. They are instead dominated by Fe III and become very similar to typical SNe Ia spectra in the nebular phase.

They may originate from a double detonation of a WD originated at the boundary layer of the C+O core and the helium envelope, or from a delayed detonation which synthesizes ^{56}Ni in the outer part of the exploding WD.

Several others peculiar events have been observed in recent years. Branch et al. (2006) proposes their division into different sub-categories, identifiable by the equivalent width relations of certain absorption lines. Under and overluminous would then be *cool* and *shallow silicon* supernovæ.

It should be pointed out that, as we will see in next section, underluminous objects are not used for the cosmological analysis, whether overluminous are, since we are able to standardize them using the same approach as for normal SNe Ia.

2.3.4   SNe Ia as a dark energy probe

In the end of last decade, two teams used supernovæ to study the expansion history of the universe, opening a new era for cosmology. The results[9] of the High-z (Riess et al. 1998) and SCP (Supernova Cosmology Project) (Perlmutter et al. 1999) teams were stunning: the greater than expected dimming of faraway supernovæ led to the conclusion that, not only the universe expansion is *accelerating*, but the responsible for this acceleration seems to be a cosmological constant type of dark energy, which accounts for $\sim 70\%$ of the energy content of the universe.

Both teams used on their analysis (explained later on) the nearby supernovæ sample from the Cálan-Tololo survey (Hamuy et al. 1996), and respectively 16 and 42 high-redshift supernovæ up to $z \sim 0.8$, issued from the corresponding search programs. The low statistical sample and the systematic uncertainties, resulting from the need to inter-calibrate different telescopes used on their observation, led to the creation of a second generation of experiments to study high-redshift supernovæ.

I'll succinctly present these experiments and the way the cosmological analysis using supernovæ is performed.

High-z supernovæ surveys

Two experiments have recently searched for a large statistic of high-redshift supernovæ: the SNLS (SuperNova Legacy Survey) (Astier et al. 2006) and ESSENCE (Equation of State: SupErNovæ trace Cosmic Expansion) (Wood-Vasey et al. 2007) projects. Both used dedicated search and followup instruments/pipelines[10], to obtain consistent photometric calibration. These (deep) wide-field surveys consisted in the observation of several predetermined patches of the sky with a certain cadence. The subtraction of consecutive observations of the same field allowed the identification of new or variable objects, whose most promising SNe candidates were sent for spectroscopic identification (and redshift determination of the host galaxy) on 8m-class telescopes, necessary due to the low luminosity of these distant supernovæ. The confirmed SNe Ia light curves are then extracted from the sequence of observations (on different bands) of the field. They are photometrically calibrated (to obtain accurate *observed* magnitudes), using secondary or tertiary standard stars[11] from the same field.

For its first 3 years of data taking, SNLS collected ~ 250 SNe Ia, while ESSENCE has published ~ 60, which by themselves already represent more then five times the combined sample of SCP+High-z. We can also compare this number to the set of 133 nearby SNe Ia compiled (Jha et al. 2007) from several sources, from which *e.g.* Wood-Vasey et al. (2007) only uses 45 in its analysis.

Apart from these two "high-volume" supernovæ surveys, the Higher-z Supernova Search project (Riess et al. 2007), as we can deduce from its name, is observing supernovæ at higher redshifts than we can observe from the ground, by using the Hubble Space Telescope observations of the GOODS (Great Observatories Origins Deep Survey) fields. Their observations, which go up to $z \sim 1.55$ (being SN1997ff the furthest supernova observed by the HST, at $z = 1.75$ (Gilliland et al. 1999)), can probe both the dark energy-dominated and (dark) matter-dominated epochs. The results show directly, for the first time, that the universal expansion rate has

---

[9]Despite preliminary analysis (Perlmutter et al. 1996) that seemed to indicate otherwise.

[10]SNLS used data from the Canada-France-Hawaii Telescope Legacy Survey issued from the one square degree Megacam, installed on the CFHT 3.6m telescope on the top of Mauna Kea, Hawaii; ESSENCE used the 0.36 square degree MOSAIC II camera, installed on the 4m Blanco telescope at CTIO/Cerro Tololo, Chile (Miknaitis et al. 2007).

[11]The *primary* standard stars are usually from Landolt (1992) or Smith et al. (2002).

changed over time: the universe was indeed decelerating at $z > 1$ and the acceleration phase has started only during the second half of the universal history.

In the future, several projects (some of them nothing more for now than propositions) will observe high-z supernovæ in combination with other probes (like BAO and galaxies weak-lensing). These may be ground-based like Pan-STARRS (Kaiser et al. 2002), ALPACA (Corasaniti et al. 2006), LSST (Tyson 2002), or space-based like SNAP (SNAP Collaboration: G. Aldering et al. 2004) or DUNE (Refregier et al. 2008), and shall provide us with thousands of new SNe Ia at even greater redshift ranges.

Low and intermediate-z supernovæ surveys

As we will see later, a nearby sample of supernovæ is essential for the cosmological analysis, since they fix the Hubble diagram zero point. Several projects observe (or observed) nearby or intermediate redshift supernovæ, and they can be divided into the ones that have dedicated search pipelines or not.

The first group comprises the SNfactory (*cf.* § II), the Lick Observatory Supernova Search[12] (LOSS), the SDSS Supernova Survey (Frieman et al. 2008b)[13] (SDSS-SS) and the Texas Supernova Search[14] (TSS). LOSS uses the 0.75m KAIT robotic telescope at Lick, and from 1998 to 2006 discovered 231 confirmed SNe Ia. The SDSS-SS is a blind survey that uses time on the SDSS 2.5m telescope, and focus mainly on intermediate redshift ($0.1 < z < 0.3$) events. ~ 500 spectroscopically confirmed SNe Ia were observed over the course of three 3-months campaigns. The TSS is a blind search using the ROTSE-III 0.45m telescope. In the 2004–2007 period it has found 29 nearby SNe Ia.

Other projects that do not have dedicated searches, focus on the followup of publicly announced SNe Ia. These include the Harvard-Smithsonian Center for Astrophysics[15] (CfA), the Carnegie Supernova Project[16] (CSP) and the European Research Training Network[17] (RTN). The CfA group uses telescope on the FLWO, and published many of the SNe Ia light curves used for cosmology (Jha et al. 2007), and also a number of SNe Ia spectra originated from different instruments/telescope (Matheson et al. 2008). The CSP follows SNe using telescopes from the Las Campanas Observatory. Several tenths of SNe Ia were followed, with a small number of them on the smooth Hubble flow. The RTN was a network focused on the study of the physics of supernovæ explosions through detailed comparison of models and observations. Their campaigns studied in detail 9 nearby SNe Ia.

All of these projects are based on the photometric measurement of supernovæ light curves, while some of them also do spectral observations, for identification and measurement of the host redshift.

Light curve fitter

For their usage in the cosmological fit, supernovæ light curves must be put into the same "reference" for comparison, as already explained in § 2.3.2. Since it will be later used in this work, I will focus on the SNLS approach, which uses SALT[2] as light curve fitter and distance estimator.

---

[12]http://astro.berkeley.edu/~bait/kait.html

[13]http://sdssdp47.fnal.gov/sdsssn/sdsssn.html

[14]http://grad40.as.utexas.edu/~quimby/tss/

[15]http://cfa-www.harvard.edu/supernova/

[16]http://csp1.lco.cl/~cspuser1/PUB/CSP.html

[17]http://www.mpa-garching.mpg.de/~rtn/

SALT2 (Guy et al. 2007) is the evolution of SALT (Guy et al. 2005), used on the first year SNLS cosmological analysis (Astier et al. 2006). It relies on an evolution model for the spectral energy distribution (SED) of a supernova, and differs from the SALT approach in the sense that spectra (contrary to photometric points only) and high-redshift supernovæ are now used for model training. Each supernova is then treated as the departure from an "average" SN spectral sequence, with possible variations of luminosity, color and spectral features.

The flux model for a supernova is of the type

$$F_{\mathrm{SN}}(p,\lambda) = x_0 \times [M_0(p,\lambda) + x_1 M_1(p,\lambda) + \ldots] \times \exp\left[c\, CL(\lambda)\right] \;, \qquad (2.1)$$

where the flux at a certain phase p (relative to B maximum) and at rest-frame wavelength λ depends on: $M_i(p,\lambda)$, an average spectral sequence (similar in concept to the SN templates by Nugent et al. (2002)) for $i = 0$, with additional components ($i > 0$) to account for SNe Ia variability; $CL(\lambda)$, an average color correction law[18]; c, a color offset at maximum with respect to the average, $c = (B-V)_{\mathrm{max}} - \langle B-V \rangle$; x_0, a normalization factor, allowing standardization without knowledge of distances; and x_i which are the intrinsic parameters for the SN, in practice behaving equivalently to the *stretch* or Δm_{15} (§ 2.3.2) parameters.
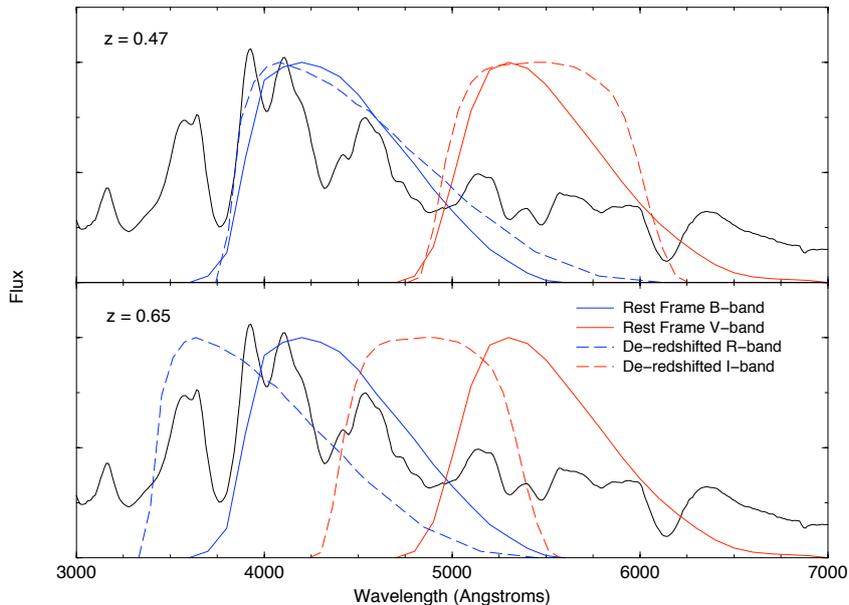
Figure 2.10: $\mathcal{K}$-corrections for the same supernova SED at two different redshifts. The blue and red filled lines correspond to both B and V rest-frame filters, and the dashed ones to de-redshifted R and I filters. The agreement is good for the smaller redshift, but on higher z the need to use multiple observation filters to describe the rest-frame ones arises. The requirement for a set of filters that extends well into the redder part of the optical window, when observing very high redshift supernovæ, is obvious. From Nugent et al. (2002).

This parametrization implicitly takes into account the so-called $\mathcal{K}$-corrections (Fig. 2.10). The need for this correction issues from the purely technical effect that occurs when we are doing photometry, and trying to observe a continuous supernova SED redshifted through fixed

---

[18]The fact that SALT[2] implicitly includes into a single term the supernovæ intrinsic color variation and the color from the host galaxy, is criticized by Wood-Vasey et al. (2007), who separate both components in their fitter. They however agree that the SALT2 approach seems to work rather well, and gives comparable results to MLCS2k2.

bandpass filters. Supernovæ magnitudes are traditionally compared on *rest-frame* B filter. The spectral features (and thus the integrated flux) that are "seen" on earth through that B filter will not be the same, since the SED appears to us redshifted. Thus, depending on the redshift of the object, different combinations of filters and associated $\mathcal{K}$-corrections (calculated from spectral templates) need to be used for conversion of the observed magnitude to that which would be observed in the rest frame in another filter. This correction has been a typical source of photometric errors, and by modeling together both light curves and spectral features (and knowing the observation filters bandpasses), SALT2 deals with $\mathcal{K}$-corrections intrinsically.

The SALT2 model is trained on a SNe Ia dataset composed of light curves and spectra (not necessarily coincident in phase), of nearby objects issued from different surveys and SNLS high-redshift objects. Each object should have at least one measurement before the date of maximum for good peak luminosity estimation. Underluminous objects are left out, since their very different spectroscopic features and color evolution won't be properly described by the average spectral template being modeled (and besides they are not observed at high redshifts, due to their low luminosity). For details and results of the training procedure see Guy et al. (2007) and Fig. 2.11.

In practice, the found model is able to describe most of the variability with $i \leq 1$, so that a SN is characterized (relative to the fiducial average M_i and CL models) by four parameters: date of B maximum, a x_0 normalization, a x_1 *stretch*-equivalent parameter and a color.

Cosmological analysis

The SNe Ia cosmological fit is fundamentally a comparison between low and high redshift supernovæ, whose observed magnitude should vary with redshift according to the luminosity distance, in the standard candle assumption. It can be performed using the found parameters for each supernova by SALT2. The distance estimator is of the type

$$\mu_B = m_B^* - M + \alpha_x \times x_1 - \beta \times c \ , \tag{2.2}$$

where m_B^*, the apparent magnitude at maximum on the rest-frame B filter, is derived from the light curve fit (from the phase and overall flux normalization estimates) together with x_1 and c; and α_x, β and M are fitted by minimizing the residuals in the Hubble diagram. A function of the type

$$\chi^2 = \sum_i \frac{\left(\mathbf{V}^{\mathrm{T}}\mathbf{X}_i - M - 5\log_{10}(d_L(\theta, z)/10 \text{ pc})\right)^2}{\mathbf{V}^{\mathrm{T}}\ \mathbf{C}(\mathbf{X}_i)\ \mathbf{V}} \ , \tag{2.3}$$

is used, with

$$\mathbf{X}_i = \left(\begin{array}{c} m_B^* \\ x_1 \\ c \end{array} \right) \ , \ \mathbf{V} = \left(\begin{array}{c} 1 \\ \alpha_x \\ -\beta \end{array} \right) \ ,$$

where d_L is the luminosity distance dependent on the θ cosmological parameters, and $\mathbf{C}(\mathbf{X}_i)$ is the covariance matrix of the parameters $\mathbf{X}_i$, which accounts for errors in m_B^*, due to the SNe Ia intrinsic dispersion and peculiar velocities of nearby objects.

Guy et al. (2007), using the same dataset as Astier et al. (2006) finds

$$\Omega_m = 0.240 \pm 0.033$$
$$\alpha_x = 0.13 \pm 0.013$$
$$\beta = 1.77 \pm 0.16$$

(a)

(b)

(c)

(d)
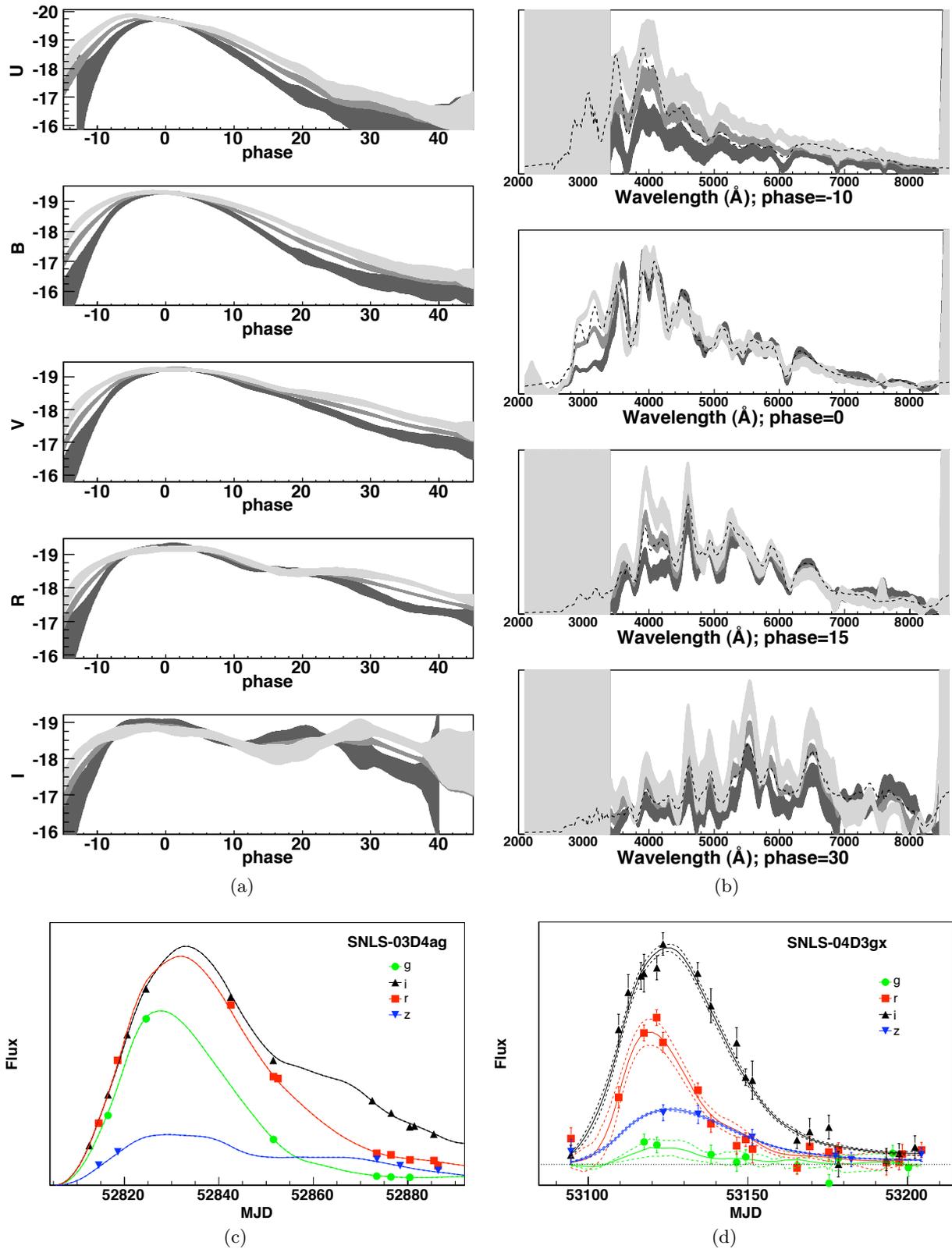
Figure 2.11: SALT2 models and results: (a) UBVRI template light curves for x_1 of -2,0,2 (dark to light curves); (b) template spectra for x_1 of -2,0,2 (dark to light curves), compared to Nugent et al. (2002) templates (dashed line); (c)–(d) photometric measurement points for SNLS' SNe Ia at $z = 0.285$ and $z = 0.91$ respectively, and derived light curves from the SALT2 model. From Guy et al. (2007).

for a flat ΛCDM cosmology, with RMS scatter around the best fit Hubble relation of 0.161 mag (compare with the pre-standardization typical values presented in § 2.3.2).

The results of the cosmological analysis from both high-z surveys together with the most recent compilation of 307 SNe Ia (Kowalski et al. 2008) (including the ones from Riess et al. (2007)), are shown in Table 2.2 and Fig. 2.12. The combination with other probes improves notably the accuracy of the measurements, by breaking the SNe Ia data degeneracy between Ω_Λ, w and Ω_m, as can be seen in Fig. 2.12b–2.12c.

Parameter	SNLS+BAO[†]	ESSENCE+BAO[‡]	SNe Ia +BAO+CMB[*]
Ω_m	0.271 ± 0.021	$0.274\,^{+0.032}_{-0.020}$	$0.274\,^{+0.016+0.013}_{-0.016-0.012}$
w	-1.023 ± 0.087	$-1.047\,^{+0.125}_{-0.124}$	$-0.969^{+0.059+0.063}_{-0.063-0.066}$

[†] Astier et al. (2006) using SALT
[‡] Wood-Vasey et al. (2007) using MLCS2k2
[*] Kowalski et al. (2008) using SALT

Table 2.2: Flat ΛCDM parameters inferred from the most recent high-z SNe Ia datasets and a combination of other probes.

Supernovæ can also be used for determination of the Hubble constant H_0. In practice, the interception at $z = 0$ of the expansion line in the Hubble diagram, gives us a relation between H_0 and the absolute magnitude of a SN Ia. This absolute magnitude can be obtained from supernovæ observed on galaxies which have distances measured by other means like Cepheids. See *e.g.* Gibson et al. (2000), Riess et al. (2005), Sandage et al. (2006), van Leeuwen et al. (2007).

2.3.5 The need for nearby SNe Ia

From what we've seen on the previous sections, it is clear the importance of the nearby supernovæ sets in the cosmological analysis.

They anchor the low redshift Hubble diagram and play a fundamental role in the training of light curve/distance fitters. Being closer and brighter, they also have smaller measurement uncertainties and provide a well characterized sample to search for systematic departures from homogeneity, through comparison of subsamples. We can thus expect both reduced statistical and systematical uncertainties on the cosmological analysis, with a better quality nearby sample, instead of the current heterogeneous one issued from different sources with different calibration issues.

Statistical improvements

Currently the number of available high-z supernovæ is already higher then the low-z one, and this difference will continue to increase (*e.g.* SNLS is expected to provide > 500 SNe Ia by the end of the project). This difference makes the current low-z sample a determining factor on the precision with which we can measure the cosmological parameters, in the way they can constraint the nuisance parameter relating the Hubble constant and the SNe Ia intrinsic luminosity in the cosmological fits.

Linder (2006) shows that the lack of a large sample of nearby supernovæ (300 SNe centered around $z = 0.05$), reduces the constraints on the dark energy equation of state by a factor of two (Fig. 2.13).

(a)

(b)

(c)
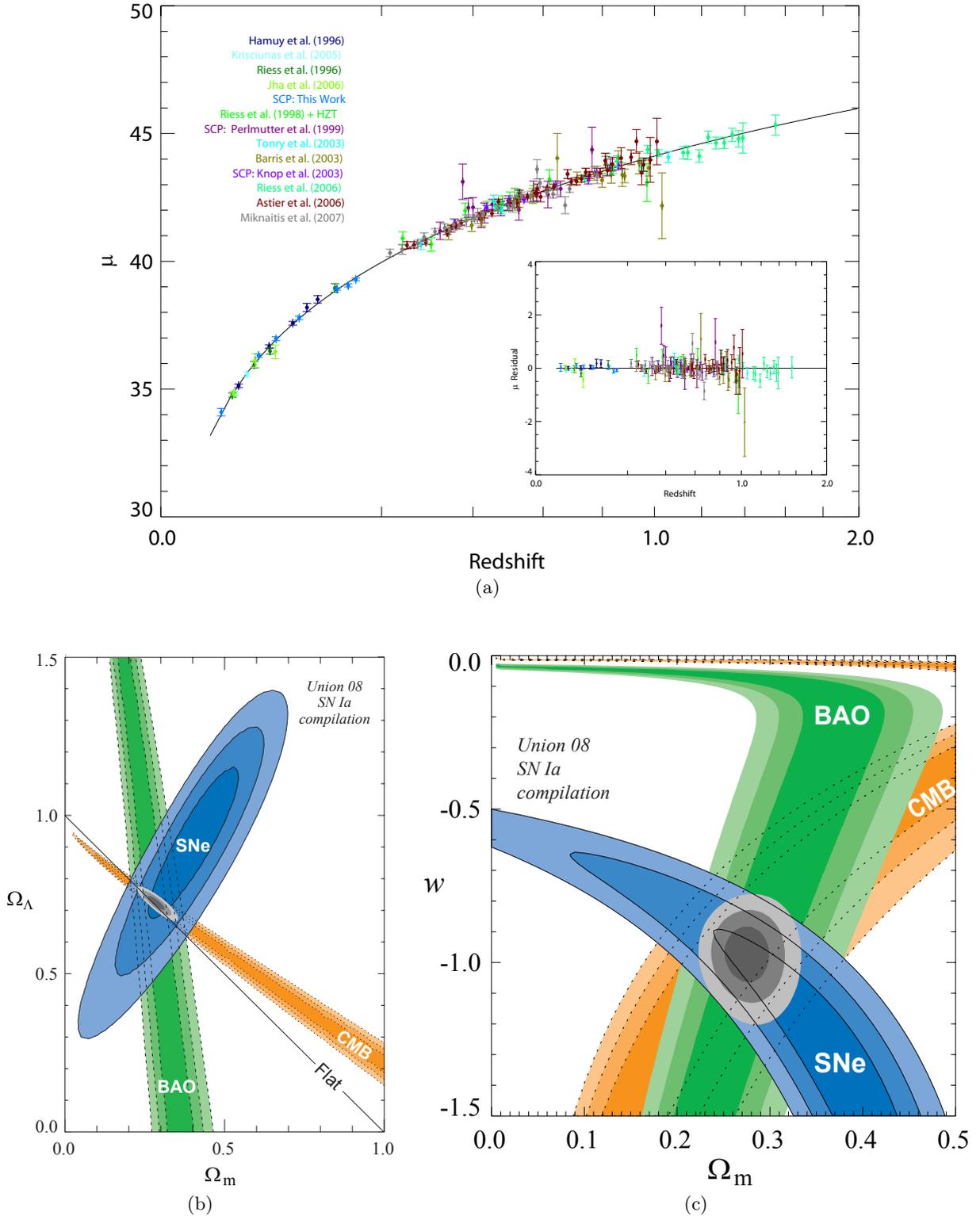
Figure 2.12: (a) Hubble (magnitude-redshift) diagram and best-fit flat cosmology, for the full Union SNe Ia dataset. The supernovæ distance modulus are obtained from the light curve fitters (SALT in this case) and the redshifts are measured from the supernova host galaxy; (b) confidence contours of $(\Omega_m, \Omega_\Lambda)$ and (c) of (w, Ω_Λ) from the combination of SNe Ia, BAO and CMB data. From Kowalski et al. (2008).
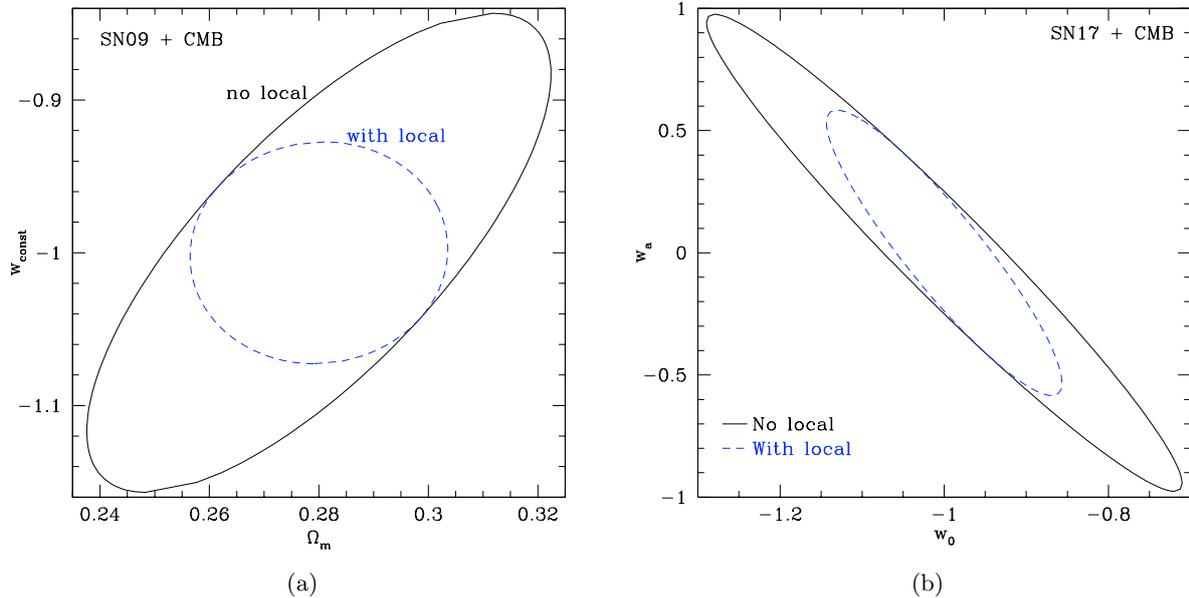
Figure 2.13: Confidence contours for (a) (w, Ω_m) from a SNLS-like dataset of 500 SNe Ia uniformly distributed between $0.2 < z < 0.9$ and (b) (w_a, w_0) from a SNAP-like dataset of 2000 SNe Ia distributed between $0.2 < z < 1.7$, both with and without a nearby sample of 300 SNe Ia centered at $z = 0.05$. On both cases the leverage on the dark energy equation of state parameters is a factor of two better when using the nearby SNe sample. From Linder (2006).

Systematics improvements

As the statistical high-z sample increases, the results of surveys like SNLS are dominated by systematic uncertainties. Table 2.3 shows the current systematic errors on the dark energy equation of state parameter for a 3 year SNLS analysis. We can see that more than half of the uncertainty can be reduced by a new well-calibrated low-z sample.

Systematic effect	σ_w
Color of Vega on Landolt system[†]	0.0391
SNLS zero-points[†]	0.0311
SNLS bandpasses	0.0286
SN model[†]	0.0278
Evolution of β	0.0242
Landolt bandpasses[†]	0.0146
Local flows	0.0137
SED of Vega	0.0131

[†] Can be improved by new low-z SNe Ia sample

Table 2.3: Systematic effects accounting for the dark energy equation of state error, for a SNLS 3 year analysis. From Conley and Supernova Legacy Survey (2007).

Furthermore, the Dark Energy Task Force in their recent report (Albrecht et al. 2006), notes that our inability to forecast systematic error levels reliably is the biggest impediment to judging the future capabilities of the techniques to probe dark energy, and that assessments of

effectiveness could be made more reliably with detailed spectroscopic and photometric observations of about 500 nearby supernovæ, to study the variety of peak explosion magnitudes and any associated observational signatures of effects of evolution, metallicity, or reddening, as well as improvements in the system of photometric calibrations.

They further remark that changes in the population of SNe Ia events and foreground extinction over time will bias dark energy parameters, unless they can be identified by signatures in the colors/spectra/light curves of individual events. Estimating the systematic errors that will affect given surveys are very difficult in the absence of a quantitative understanding of the diversity of supernovæ events and their foreground extinction, and the ways in which this diversity is manifested in the spectral/temporal observables of each event.

It is to answer this need for a large sample of nearby SNe Ia, with high-accuracy photometry/spectra, that the SNfactory project was designed.

Part II

The SNfactory project

Chapter 3

A new approach to SNe observation

The SNfactory project (Aldering et al. 2002) was born in 2000, with the objective of studying in detail a large sample of SNe Ia in the nearby smooth Hubble flow ($0.03 < z < 0.08$), in order to refine their cosmological use as calibrated standard candles. The SNfactory consortium is composed of ~ 40 scientists and technical staff of laboratories from France (LPNHE, CRAL and IPNL) and the United States (LBL, Yale University), which designed and built a dedicated instrument for supernovæ observation (see § 4), and are responsible for the implementation and exploitation of the supernovæ search/followup (§ 5) and calibration (Part III) pipelines.

The main project goals can be summarized into:

- observe a large number of low-redshift supernovæ with small statistical and systematic uncertainties, such that the uncertainties in the cosmological parameters determination techniques that combine low and high-redshift supernovæ are significantly reduced;

- $\mathcal{K}$-correction-free light curves with wavelength coverage spanning the optical window and corresponding multi-epoch spectral indicators, in order to directly test the effects and proper formulation of dust extinction correction and existing empirical luminosity indicators;

- perform detailed spectral and photometric studies, as a mean to develop improved luminosity indicators, and to serve as input to computational supernova models designed to complete our understanding of the physics of supernova explosions.

3.1 Improving our knowledge of SNe Ia

As already seen, today's projects that use high-redshift supernovæ to study the evolution history of the universe rely on the possibility of using SNe Ia as standard(izable) candles. The standardization methods (§ 2.3.4) depend heavily on accurate photometric and spectroscopic measurements of a large sample of supernovæ, for proper modeling of the spectral features *vs.* luminosity/color parameters' evolution, and better understanding of the origin of the observed empirical correlations between light curve shape and those parameters. Several factors like the intrinsic luminosity dispersion, supernovæ evolution, explosion mechanisms, galaxy type, dust extinction on the host galaxy or spectral subclasses may play a role in this correlations, and the usage of supernovæ on cosmology will benefit from improvements on our understanding of each one of them.

For this purpose, SNfactory intends to provide data that will directly address some of these issues, by providing spectrophotometric (see § 3.2) temporal (each 3–4 days) sequences for a

larger number ($\sim$ 200) of nearby supernovæ, not so far ($z < 0.08$) as to require excessive amounts of telescope time, yet far enough ($z > 0.03$) so that host galaxy peculiar velocities will contribute little to the error budget. The fact that this data is all issued from the same telescope/instrument, allows systematic uncertainties to be well controlled since there's no need for intercalibration between different observation methodologies. Besides, the spectrophotometric approach makes $\mathcal{K}$-corrections unnecessary, further reducing the systematics.

With this data, SNfactory wants in particular to scrutinize the SNe Ia closely enough so that we can find second-order differences that are not yet parameterized by the current relations. Well-observed nearby SNe Ia, especially in host galaxies spanning a wide range in star-formation histories, are essential for hunting for such possible second-order systematic trends, and the observables that could constrain them. In addition, further study of nearby SNe will allow refinement of the known luminosity indicators, and perhaps the discovery of more accurate or economical indicators: new exclusion criteria and standardization methods, based on light curve shapes, color and/or spectral features can be developed having a denser sample of high quality supernovæ observations. Guy et al. (2007) notes this, by stating that a more robust approach on standardization could be made if we had a more homogeneous and denser set of observations per supernova, namely one spectrophotometric spectrum every 4–5 days.

In terms of supernovæ astrophysics, the large sample of SNfactory's SNe Ia will be important in recognizing the signature of any new supernova sub-types, which could in turn signal the existence of multiple progenitor scenarios. A series of key supernova features (Nugent et al. 1995; Hoeflich et al. 1998) responds to differences in the underlying physics. By measuring these features for each supernova one can tightly constrain the physical conditions of the explosion, making it possible to recognize sets of supernovae with matching initial conditions. The current theoretical models of SNe Ia explosions are not sufficiently complete to predict the precise luminosity of each supernova, but they are able to give the rough relationships between changes in the physical conditions of the supernovæ (such as opacity, metallicity, fused nickel mass, and nickel distribution) and changes in their peak luminosities. SNfactory's data can then play a key role in empirically calibrating these relationships, between changes in the physical conditions of the supernovae (as seen in the light curve and spectral features) and observed luminosities.

The resulting SNfactory dataset will then allow detailed exploration of SNe Ia properties never before possible, which will almost certainly lead to a better understanding of supernovæ physics, and possibly allow improved luminosity estimates. Notably it will enable us to better study:

- the intrinsic luminosity and color functions of SNe Ia;

- new relations between light curve shapes and spectral diagnostics;

- supernovæ properties in different host galaxy environments.

A well sampled spectral archive of SNe Ia of this type also represents a major legacy value for future experiments, being *e.g.* a valuable input for the modeling of SNe Ia photometrical identification algorithms or for increasing accuracy on photometric redshifts determination, both important for experiments like LSST, which intend to observe photometrically a great number of supernovæ and galaxies.

3.2 Integral field spectrophotometry

A defining characteristic of SNfactory is its observational approach. An Integral Field Unit (IFU) spectrograph is used, the first of its kind designed specially for supernovæ observations: the SuperNova Integral Field Spectrograph (SNIFS § 4).

This technique departs from the typical supernovæ surveys, which follow photometrically a supernova light curve during its lifetime, with only one or two spectroscopic exposures for type confirmation. Instead, by dividing the instrument's field-of-view into an array, we obtain simultaneously multiple spectra that map the field (sky+supernova +host galaxy) and allow to collect all the light from the supernova in the (x, y, λ) space. This represents a major advantage over traditional slit-spectrographs, where the fraction of light entering the instrument is a function of wavelength and the accuracy of centering in the slit, and where host galaxy light can only be removed by spatial interpolation or subtraction of galaxy templates.

The IFU approach, by collecting all the light from the object, allows us thus to *absolutely* flux calibrate the obtained spectra, using spectrophotometric standard stars (see § 7 for details). This opens up a whole new range of studies that can be performed using this spectral data, like absolute flux comparison of spectral features to supernovæ composition models and respective evolution with phase, flux-calibrated supernovæ SED for fitters like SALT2 and light curves obtained on *any* filter we wish, directly synthesized from the spectra (Fig. 3.1). The latter is the *spectrophotometric* approach for supernovæ light curves: flux calibrated spectral temporal sequences can provide synthetic photometry points/light curves, by the convolution of any bandpass filter. This represents an advantage over the traditional methods, in the sense that it eliminates the need for significant corrections, like $\mathcal{K}$-corrections, extinction-dependent filter bandpasses in the UV or host galaxy contamination of spectral indicators.

(a)   (b)
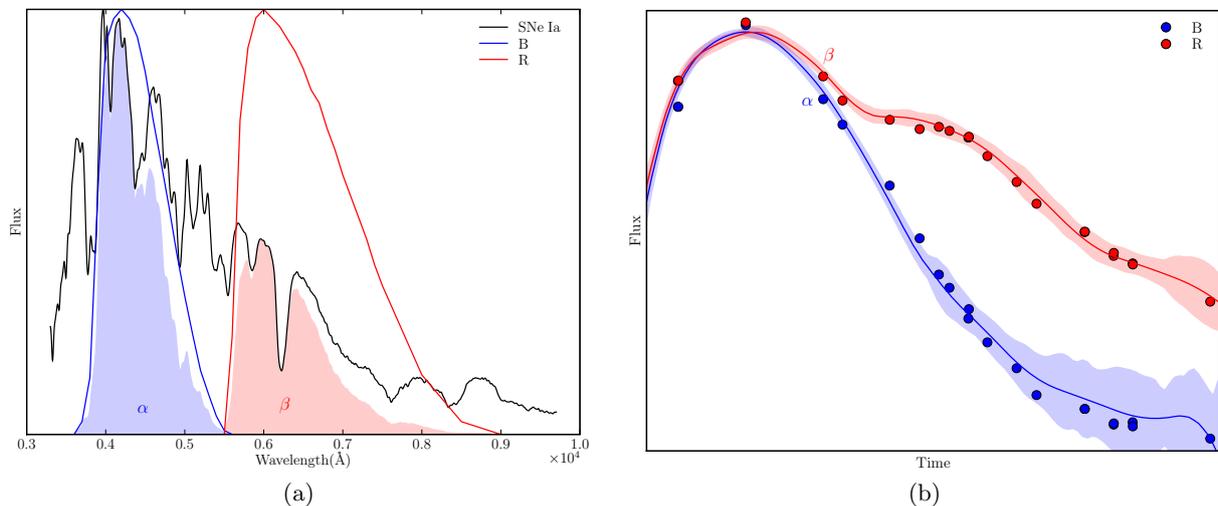
Figure 3.1: Spectrophotometry concept: (a) by convolving any filter (here Bessell B and R are shown) with each flux calibrated spectrum from a SNe Ia temporal sequence, we can obtain (b) the corresponding light curve points for that filter, without any $\mathcal{K}$-corrections involved. The light curve line fitted using SALT2 is given for reference.

Chapter 4

The SuperNova Integral Field Spectrograph

SNIFS ([Lantz et al. 2004](#)) is the instrument designed, built and used by the SNfactory collaboration for supernovæ observation. It is a two-way optical spectrograph equipped with TIGER-like ([Bacon et al. 1995](#)) integral field units, and represents a technological milestone, in that it is the world's premier fully-integrated instrument specifically designed for semi-autonomous observation of point sources on a diffuse background at moderate spectral resolution. It is permanently mounted at the bent-Cassegrain port of the University of Hawaii 2.2m (Fig. 4.1a) telescope[1] on Mauna Kea, Big Island, Hawaii.

(a)   (b)
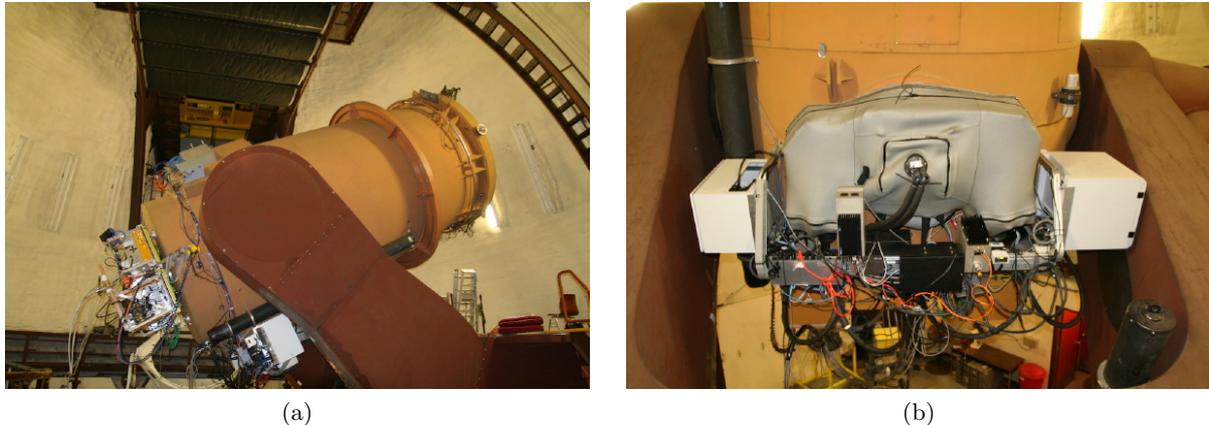
Figure 4.1: (a) University of Hawaii 2.2m (UH88) telescope; (b) SNIFS mounted on the bent-Cassegrain port of UH88. The main instrument is in the center under the neoprene cover, used to isolate it from external light and keep the internal temperature and humidity from large changes, besides all the support electronics.

SNIFS (Fig. 4.1b) includes two spectroscopic channels, together providing wavelength coverage from 3200 to 10000Å, a photometric channel for acquisition, guiding and monitoring of field stars adjacent to the spectroscopy targets for night-to-night extinction monitoring and a calibration unit. Both spectroscopic and photometric channels use the same shutter, so that observations with both channels are guaranteed to have identical observing conditions. An opto-mechanical schematic of SNIFS can be seen in Fig. 4.2.

---

[1]Also known as UH88 – a Cassegrain reflector tube telescope with an f/10 focal ratio, on an open fork equatorial mount – http://www.ifa.hawaii.edu/88inch.
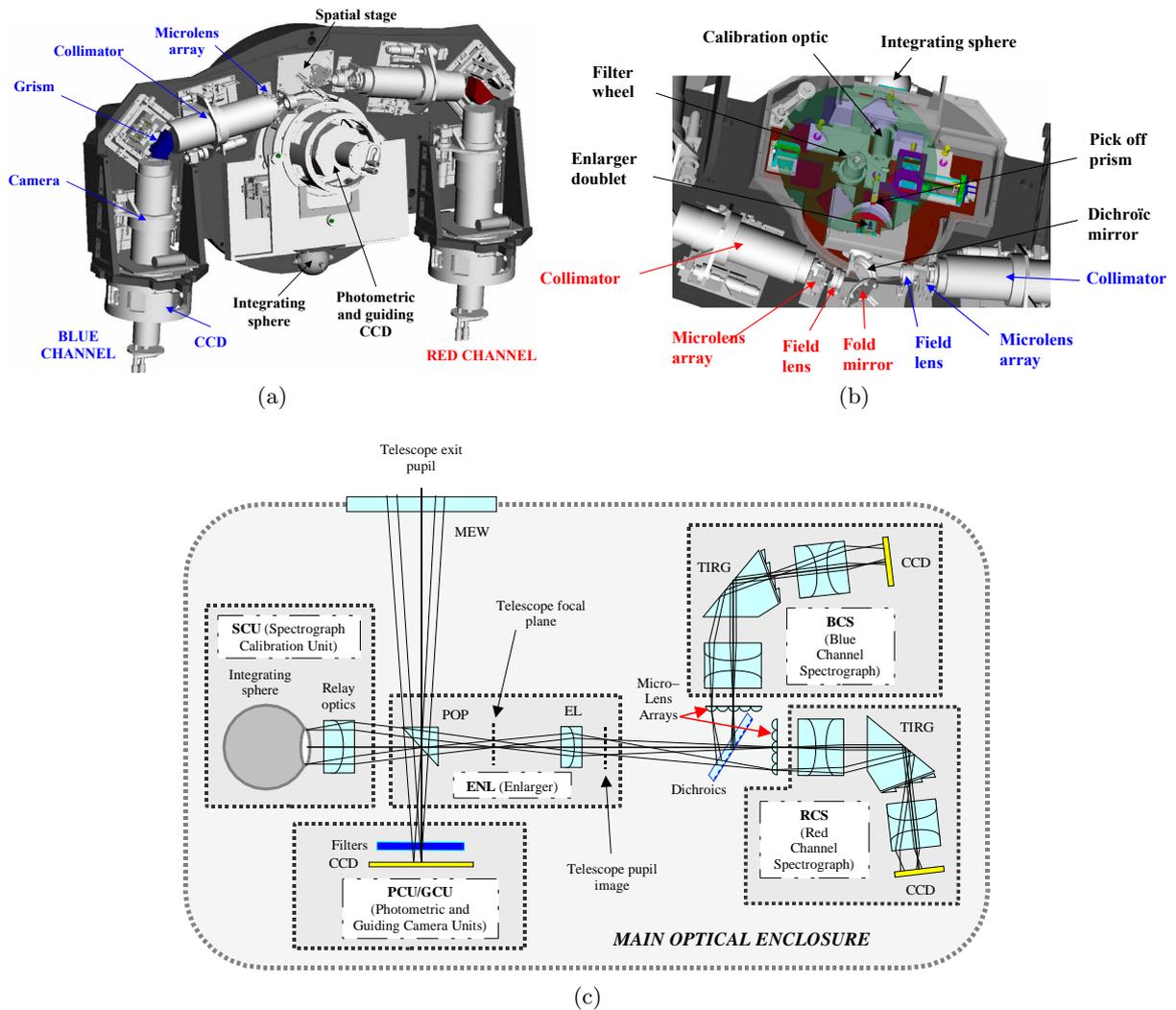
Figure 4.2: SNIFS (a) general mechanical schematic; (b) zoom of the central part of the instrument; (c) general optical schematic.

4.1 Spectroscopic channels

SNIFS has two (blue/B and red/R) channels, each equipped with a 15×15 microlens-array (MLA) IFU, which split an enlarged image of the telescope focus into several spatial samples, continuously covering a $6'' \times 6''$ field-of-view with a sampling of $0.4''$. Each of the 225 samples has its spectra decomposed by a classical spectrograph, on E2V CCDs[2] (thinned for the blue channel and thick for the red channel) with 2046×4096 pixels of 15μm, at (σ) resolutions of 2.4Å and 3.2Å respectively. The blue channel covers $3200 - 5400$Å at a fixed dispersion of ~ 2.5Å/pixel, while the red channel covers $5200 - 10000$Å at a fixed dispersion of ~ 2.9Å/pixel.

---

[2]Charge-Coupled Device, used nowadays as the standard detector on optical wavelengths. Built from silicon wafers, its storage and information retrieval method is dependent on the containment and manipulation of electrons and holes produced by photoelectric effect. They are stored in the depletion region of metal insulator semiconductor capacitors, which form a large array. During readout the accumulated charges are manipulated in a way that makes them flow from one capacitor to another (hence the name), then transformed by the read-out electronics into a digital number per capacitor (counts per pixel) and stored in the computer memory. See *e.g.* Howell (2006).

The two channels can be operated together or separately.

In its path towards the CCDs, the light collected by the telescope is reflected by the primary and secondary mirrors, reflected again by a tertiary mirror which sends it through the SNIFS entrance window on the side of the tube, and once inside SNIFS it passes through a series of optical components (Fig. 4.2c):

Pick-off prism (POP) which reflects the light of a small field-of-view ($6'' \times 6''$) centered on the target to the spectroscopic channels' entrance enlarger. The light of the other objects of the field proceeds straight to the photometric channel (§ 4.2). A prism was chosen over a flat mirror due to its higher efficiency in the ultraviolet spectral domain;

Enlarger (EL) which expands the field-of-view up to a reasonable size (21×21mm) where the microlens-array can be placed. Together with a field lens compensates the spherical and chromatic aberrations introduced by the POP and the entrance window;

Dichroic which splits the beam into the blue (reflected) and red (transmitted) wavelengths for each spectrograph channel (Fig. 4.3). Its nominal half-power point if ~ 5150Å[3]. The optical components that follow are similar between both spectrographs (BCS & RCS);

| (a) | (b) |
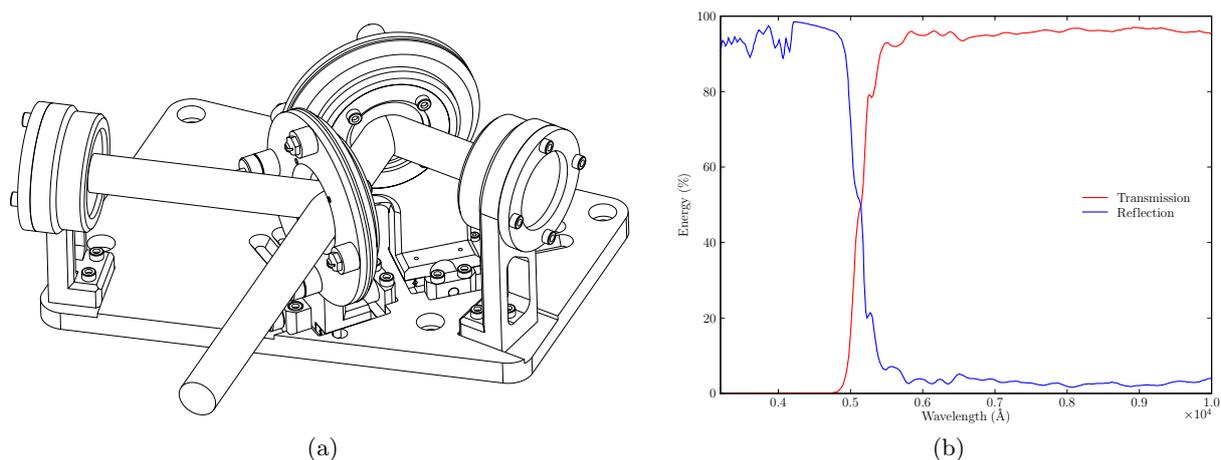
Figure 4.3: (a) Spatial stage schematic. The dichroic is visible at the lower center, and splits the entrance beam for the blue (left) and red (right) spectrographs; (b) Dichroic transmission for the blue and red wavelengths.

Microlens-array (MLA) which splits the field into 225 squared samples or *spaxels*. Each MLA (Fig. 4.4) is made of fused silica and composed of two crossed cylindrical lenses with an air space of 100μm between them. They are tilted in order to distribute all the spectra in the detector without overlapping;

Colimator which transforms the beam coming from the focal plane of the microlens into a parallel beam, before feeding it into the dispersive element;

Grism a total internal reflection grism (grating+prism) disperser, which reflects the beam at $50°$ incidence and disperses most of the light in its first diffraction order;

---

[3]During the first year of observations, the dichroic bandpass was discovered to vary noticeably, due to a sensitivity of the multilayer coating to humidity. In the impossibility to replace the dichroic, a software correction for this problem was implemented in the data processing pipeline.

<div align="center">(a)   (b)</div>
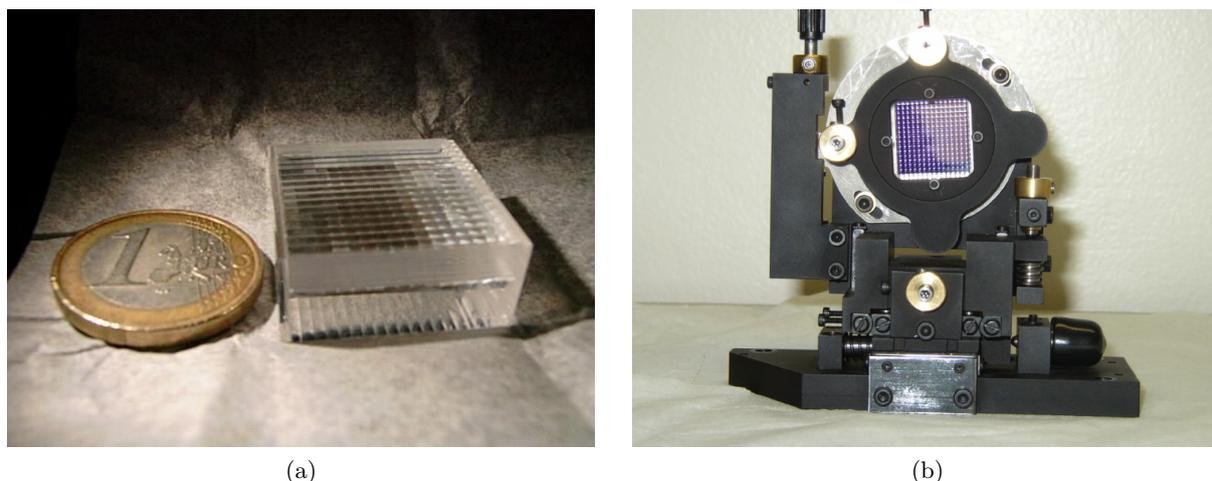
Figure 4.4: One microlens-array (21mm × 21mm) (a) next to an 1€ coin for scale; (b) in its support mount during assembly.

Camera composed of several optical elements for correction and re-imaging of the parallel beam on the CCD;

CCD detector where the spectra are acquired, inside a dewar for low-temperature ($-120°$C) operation.

SNIFS also contains a calibration unit (before the enlarger) for the spectrograph channels, with an integration sphere and specific optics, that simulates the primary mirror of the telescope illuminated homogeneously. It includes continuum and spectral lamps for flat-field, spectral and spatial calibration of the spectrographs.

The overall telescope and spectrograph channels transmission (basically the efficiency to transform a photon in the atmosphere to an electron in the CCD), computed for a night of 2005 is shown in Fig. 4.5.
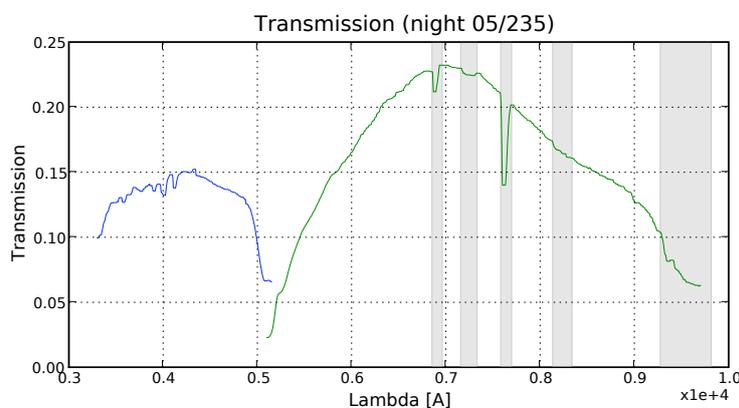
Figure 4.5: SNIFS blue (blue line) and red (green line) spectrographs transmissions.

4.2 Photometric channel

The light that enters SNIFS and is not deflected by the POP passes through a filter wheel and then illuminates the photometric (P) channel.

It is constituted by the photometry and guiding cameras, placed on the telescope focal plane. The first is used in conjunction with a special (§ 4.2.1) multiple-band filter, which allows the monitoring of relative atmospheric extinction during the spectroscopy observations. The second is illuminated by off-axis light and is used for telescope guiding during spectroscopy and for focusing or offsetting between exposures. Both cameras are placed side by side (Fig. 4.6a), and can be used together for unguided photometric exposures. They are deep depleted (40μm) E2V CCD detectors with 2046×4096 15μm pixels, as the red spectrograph CCD. Their field-of-view is $\sim 4.5' \times 9'$ with spatial resolution of $0.137''$/pixel.

(a)   (b)

(c)   (d)
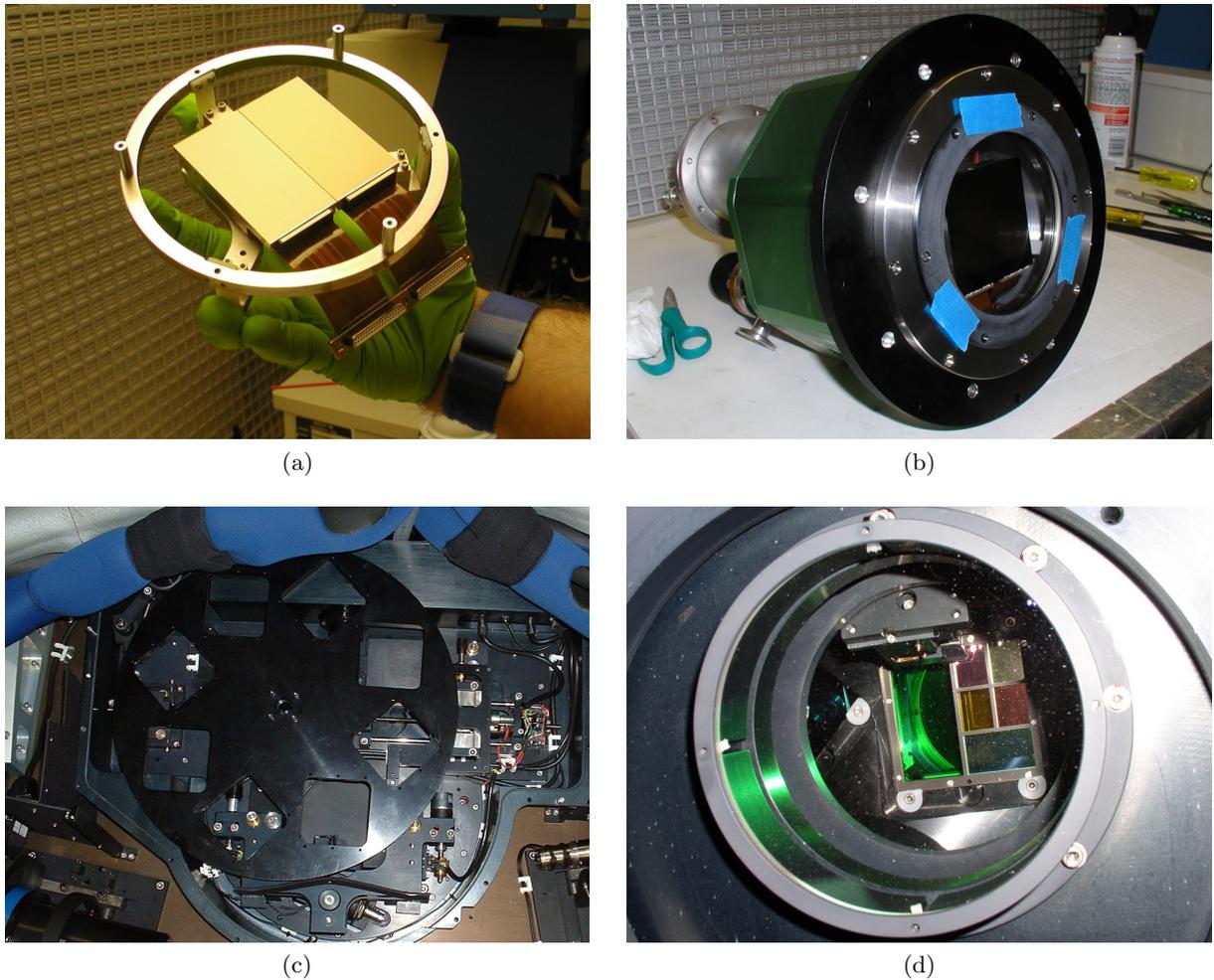
Figure 4.6: Photometric channel during assembly: (a) both photometric and guiding cameras' CCDs are placed inside a dewar (b) and kept under vacuum and low temperatures provided by a liquid nitrogen cryogenic system. (c) Filter wheel during assembly: the final placement of the CCDs is beneath the lower/right hole; (d) Photometric channel covered by the multi-filter, as seen through the SNIFS entrance window: the multi-filter mosaic is seen on the right, with the guider V filter on the left.

The photometric channel is equipped with a filter wheel (Fig. 4.6c), containing V (Bessell)

and *ugriz* (SDSS) filters, as well as a pinhole filter and a special multi-filter mosaic.

4.2.1 Multi-filter

We've seen that the goal of SNfactory is to record full spectroscopic information for each object, many times over the course of a few months. However to accurately measure intrinsic spectral changes in the supernova, spectral changes due to day-to-day fluctuation in the atmospheric extinction must be independently determined.

With the advent of CCDs, imaging followup of variable events such as supernovæ has exploited the fact that, over small fields of view non-photometric conditions (meaning, when the atmospheric transmission varies during the night) tend to uniformly depress the flux from all objects in the field. Thus, non-variable objects in the field can be used as comparison objects, and once the brightness of such comparison objects is determined under photometric conditions, the relative brightness between the target object and comparison objects can be converted to an absolute flux. In the case of SNIFS, the small field-of-view of the spectrograph does not allow for simultaneous spectral observations of more than one object, so the photometric channel is used for this task. Field stars around the supernovæ are imaged on each night, simultaneously and under the same conditions as the spectra. By monitoring the flux variations of these stars between non-photometric and photometric nights (where the absolute flux of the supernova is calibrated using spectro-photometric standards, *cf.* § 7), we can thus calculate a relative flux correction that should be applied to the spectra.
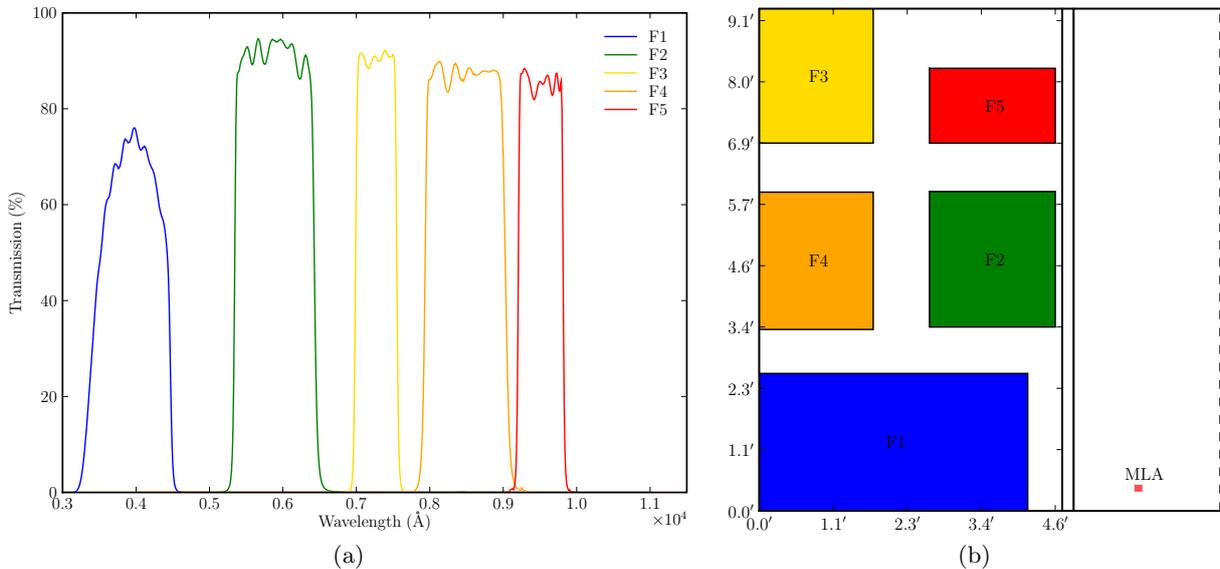
Figure 4.7: (a) Transmission of each filter of the multi-filter mosaic and (b) spatial distribution of the respective effective areas, not accounting for shadows of the support and other optical elements. MLA represents the relative position and effective field-of-view of the microlens-array. The physical separation between both CCDs is also represented.

For this purpose, the photometric channel is equipped with a special multi-filter (MF) mosaic. It is composed of several narrow-band filters, each one intended to probe different components of the atmosphere (Rayleigh diffusion, ozone layer, aerosols and water vapor). The transmission curves of the five filters used can be seen in Fig. 4.7a, which will be referenced throughout this manuscript as F1 to F5, in relation to their increasing effective wavelengths: 400, 590, 725, 850

and 950nm. Their relative positions and effective areas on the images formed on the photometric CCD (and hence flipped from the filter positions seen in Fig. 4.6d) are represented in Fig. 4.7b. Apart from the inter-filter areas with shadows from the MF support, the top of F5 is cut due to the shadow of an optical element (the enlarger) of the spectrograph channel, while the small area lost at the right of F1 is due to the shadow of the POP when in place.

The measured atmospheric extinction by SNIFS on a night of January 2006, using bright standard stars[4], is shown in Fig. 4.8a. Represented are the different components that form the (blue) extinction curve, the Rayleigh, ozone and aerosol contributions. Fig. 4.8b represents the so-called telluric lines, meaning the absorption lines on the redder part of the optical window (and infrared) due to the water vapor and molecular oxygen present in the Earth's atmosphere (Stevenson 1994).
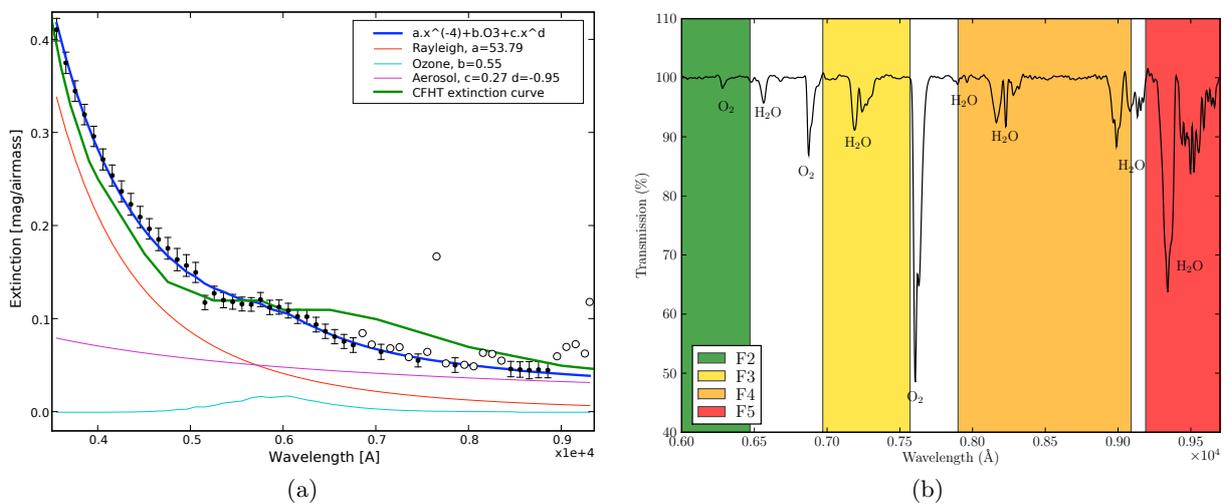
Figure 4.8: (a) Measured extinction curve (blue) by SNIFS for a night of January of 2006. This measurement is made using several bright standard stars observed on different airmasses. The individual Rayleigh, ozone and aerosol contributions are represented. For comparison, the green curve is the assumed "standard" extinction curve at Mauna Kea, obtained from the CFHT (Bèland et al. 1988); (b) Telluric absorption lines due to molecular oxygen (O_2) and water vapor (H_2O), obtained from a continuum-normalized average of three spectra from EG131 (a WD spectrophotometric standard star), observed with SNIFS on specially high humidity nights, and divided by its reference spectrum. The wavelength ranges of four MF filters are over-plotted.

By comparing the transmission curves for the MF filters, we can see that each one will be sensitive to different components of the extinction: Rayleigh for F1, ozone for F2 and water vapor especially for F5 (F3 and F4 also coincide with water absorption bands, but they are usually very weak and negligible on normal observation conditions). For further details on the usage of the photometric channel data for spectral flux calibration see § 7.

4.3 Data taking

Due to a large effort on automation and software development, SNIFS together with the telescope can be controlled from anywhere in the world via broadband Internet connection.

---

[4]It is not the purpose of this manuscript to describe in detail the spectrum analysis and extinction determination. For more information see Gilles (2006), Buton (2009).

SNIFS operations are heavily scripted to keep the need for human interaction to a minimum. At the lowest level, interacting directly with the instrument are the five software "agents", one per channel (blue channel is controlled by DETCOM, red and photometric by OTCOM), one for SNIFS itself, and one for interacting with the UH88 telescope via the TCS (Telescope Control System). At higher level, the scripts that perform sequences of tasks involving multiple agents (like focus, target acquisition or science exposures) are controlled by the AIC (Automated Instrument Control) environment, which validates observation sequences against specifications, launches and monitors scripts execution for specific failure modes.

On a typical night (a shift) the observer (shifter) will ensure that the AIC observation schedule is performed without incidents, ensures data quality, verifies acquisition of each target, and can take control over AIC in case of problems (like bad weather or SNIFS agents crashes). As of the end of 2007, with the accumulated experience and support software a shift can be almost fully run by AIC without need for human intervention.

A shift is divided into four main parts, US0/3 and FR1/2. Before sunset, the US0 shifter (from LBNL) prepares SNIFS, takes calibration data, calls the TO (telescope operator) in Hawaii, and takes control of the telescope, zeroing and focusing it. The FR1 shifter (which rotates through the french institution in proportion to available personnel), takes over at around 7h CET[5] until the middle of the night. He is then changed for another shifter (FR2), which will continue observations until sunrise around 17h30 CET, when the dome is closed, the telescope stopped and the TO relieved from service. US3 then takes over to perform more calibration runs and put SNIFS to standby until the next shift.

The control of SNIFS and UH88 is made entirely through two VNC[6] connections to the summit computers, the *director* (Fig. 4.9a) and *analysis* (Fig. 4.9b) VNCs. All the shifters are in permanent contact between them in a specific chat room through instant messenger, and call the TO directly to solve any problem or make specific requests about the telescope or dome systems. A collaborative TWiki webpage is also maintained, which *e.g.* regroups all the available information about the summit weather evolution. A network webcam, SNIFSTV, is also installed inside the dome, allowing for monitoring of the instrument, telescope and dome lights.

From mid-2005 to mid-2007 I contributed actively for the data taking shifts and the formation/support of new shifters, totaling around 60 half-nights of observation, which accounts for more than 300h of SNIFS usage.

4.4   Problems with SNIFS

During its data taking period, SNIFS suffered from a few unexpected mechanical problems, that prevented data acquisition or crippled the instrument during some time. The main problems occurred in:

December 2005 - January 2006 the SNIFS cooling system lines were severely damaged during the installation of the LIPS instrument on UH88, preventing observations during one month;

August - September 2006 due to a bigger than expected worn out of the POP motor gear, it failed in the beginning of August, preventing the placing of the POP in position and thus the usage of the spectroscopic channels during one month;

---

[5]Depending on the time of the year, there is a 11/12h difference between CET and Hawaii Standard Time.
[6]Virtual Network Computing

mid-October 2006 an earthquake off the coast of the Big Island caused damage to the dome enclosure and prevented reliable data taking using the UH88 TCS during one week;

mid-November 2006 - March 2007 the filter wheel lock mechanism started to present random failures, making the MF mosaic not completely align to the photometric channel on several exposures. A software solution was implemented and the problem was fixed in the March 07 intervention.

SNIFS is subject to an annual mechanical maintenance intervention for instrument revision and substitution of warn out components, as well as to possible non-planned interventions to fix some major issue as the ones presented previously. During these interventions the instrument is dismounted and parts replaced which will entail changes in the configuration (*e.g.* the relative positioning of the CCDs and optical components). These changes should be taken into account later when analyzing the data and comparing exposures taken far from each other in time.

Date	Cause	Specific changes
March 2005	Maintenance	
June 2006	Maintenance	Phot. channel baffling / SNIFS not dismounted
September 2006	POP intervention	POP motor, baffling
March 2007	Maintenance	Filter wheel lock mechanism, baffling
March 2008	Maintenance	SNIFS not dismounted

Table 4.1: SNIFS Hawaii interventions.

The interventions made to SNIFS since its installation in 2004 are shown in Table 4.1. The different (approximate) epochs they represent, and corresponding notation used in this manuscript are detailed in Table 4.2.

Epoch notation	Julian date period (+2453000)	Intervention
$\mathcal{A}$	installation – 453	March 2005
$\mathcal{B}$	453 – 907	June 2006
$\mathcal{C}$	907 – 990	September 2006
$\mathcal{D}^{\dagger}$	990 – 1185	March 2007
$\mathcal{E}$	1185 – present	

† A sub-period $\mathcal{D}2$ is distinguished between 1013 and 1101 when a falling baffle of the P channel obscured slightly F1.

Table 4.2: Epoch separation between interventions on SNIFS, for later reference.
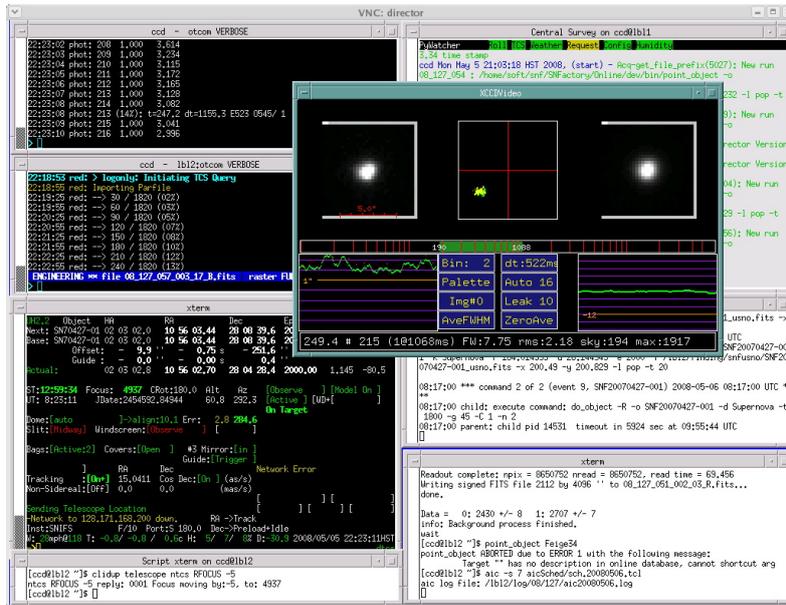
(a)
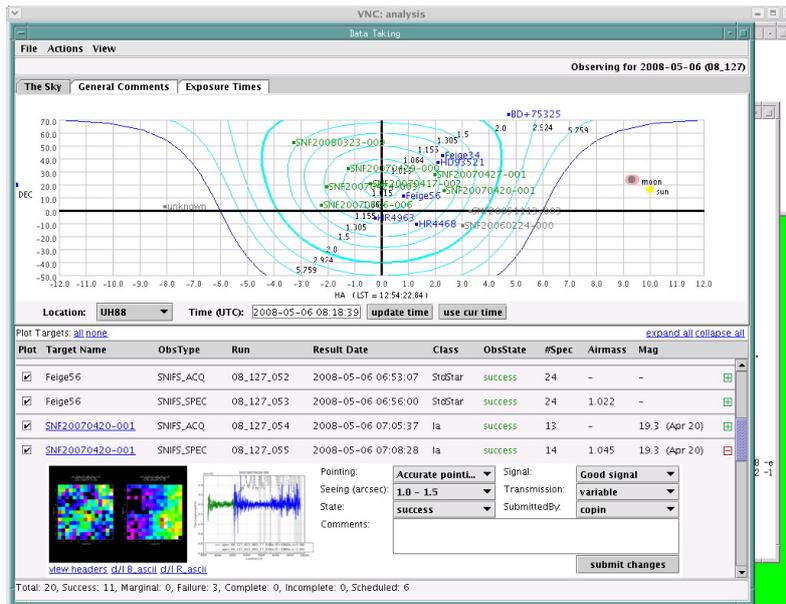
(b)

Figure 4.9: (a) The *director* VNC is divided into several small windows: on the top left, two windows monitor the low level agents, which in the shown case are performing a spectrum exposure. On the lower left the TCS windows monitors every parameter related to the telescope and dome. On the right a "central survey" watcher logs every status or failure message issued from the different scripts. On the lower right is visible the log window for AIC and a window that allows the shifter to launch or manually override AIC. The superposed window shows the guide star used during the exposure, and monitors its seeing (FWHM) and flux variations. It is also used by the shifter to monitor the quality of the focus of the telescope and compensate for small deviations during the night, without the need for a full focus run; (b) The *analysis* VNC is used for data analysis on-the-fly and hosts the Data Taking interface, developed at LBNL, which shows the night schedule and is automatically updated with the observed data, allowing the shifter to tag its quality and leave useful comments for future reference.

Chapter 5

The observational implementation

The objects in the SNfactory dataset are either issued from the specific search pipeline of the collaboration (the biggest part), or are supernovæ whose discovery is made public via IAUC[1] (International Astronomical Union Circulars) or specific diffusion lists. These public supernovæ may be discoveries from amateurs astronomers or from specific surveys, like LOSS, TSS or SDSS-SS.

After spectroscopic confirmation of the unidentified targets, they are followed spectroscopically using SNIFS. I will present these different steps and associated statistics as of the end of 2007.

5.1 Search

Contrary to high redshift supernovæ surveys, a nearby survey needs to search a wider area of the sky due to the lesser rate per square degree of expected events (*e.g.* SNLS observes ~ 100 supernovæ per year on a continuously monitored patch of the sky, with 2 square degrees). The SNfactory survey is based on a blind search approach: a wide-field telescope scans the sky and any transients are considered as candidate SNe, regardless of whether an associated host galaxy is detected. This method allows for an unbiased search, contrary to other nearby "galaxy-searches", which monitor galaxies from a specific pre-determined catalog for new supernova explosions, and are systematically biased against SNe in low-luminosity, low-metallicity galaxies since these catalogs are generally flux-limited.

The SNfactory supernova search pipeline is performed by the LBL group, on data issued from the 1.2m Samuel Oschin Schmidt telescope[2] (Fig. 5.1a) at Palomar Observatory, owned and operated by the California Institute of Technology (Caltech). The data are taken by other collaborations, and we search for supernovæ in those data that are deemed useful, contrary to a dedicated search facility which cost and schedule did not allow. During the search testing phase in the beginning of the project, the imaging data were obtained by the NEAT (Near Earth Asteroid Team) using the "3-banger" camera, covering 3.75 square degrees and with a pointing cadence mostly designed for detection of the motion of asteroids in certain fields. From mid-2003, a new camera was installed by the QUEST (Quasar Equatorial Survey Team) collaboration, and the overall effort was recast as the Palomar-QUEST Survey[3], which divides the observation time between NEAT, QUEST and Caltech. The QUEST-II camera (Rabinowitz et al. 2003) consists

---

[1]http://cfa-www.harvard.edu/iau/cbat.html
[2]http://www.astro.caltech.edu/palomar/sot.html
[3]http://www.astro.caltech.edu/~george/pq/

of 112 CCDs which cover 16 square degrees every two pointings. The new camera posed data processing difficulties for all users, whose identification and solving, while scaling the old software for the new multi-CCD approach took until around mid-2005. The first confirmed SN Ia issued from the Quest-II pipeline was observed by SNfactory in May 2005. Several further changes were made with time, especially during a forced stop of the search between March and May 2006 for reassessment of both infrastructure and software efficiencies and needed improvements, and the search pipeline attained "maximum luminosity" in mid-2007 (Fig. 5.3a), meaning that its cadence of detected candidates is in par with the capacity of SNIFS to confirm (§ 5.2) and follow (§ 5.3) candidates during a single night.

(a)   (b)
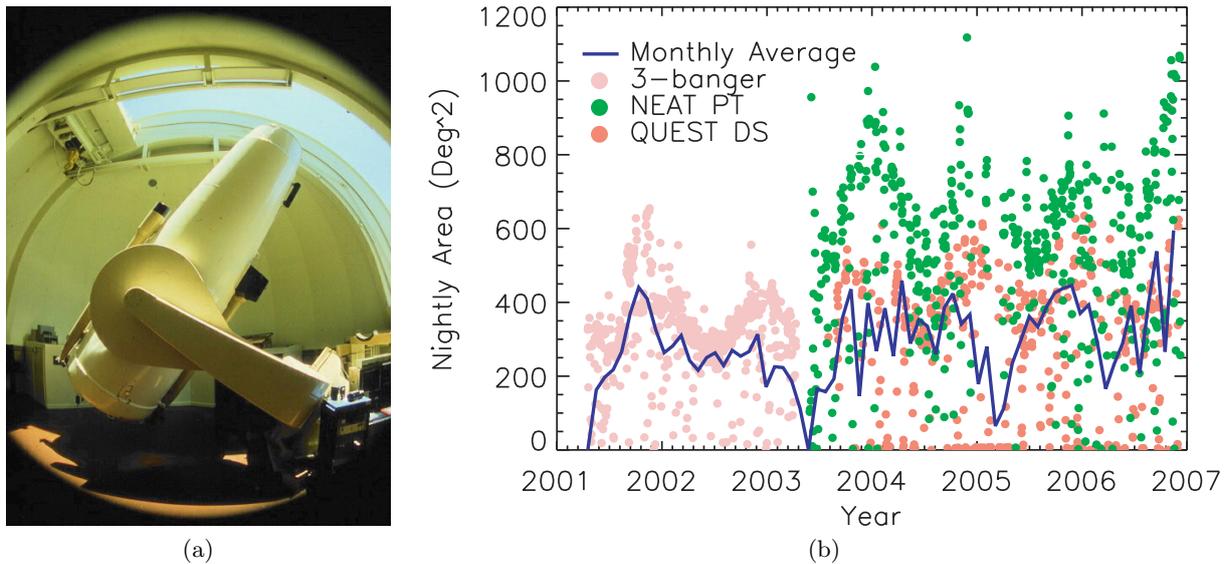
Figure 5.1: (a) Mt. Palomar's 1.2m Samuel Oschin Schmidt telescope; (b) Sky area coverage at Palomar for each of the observation modes: 3-banger, QUEST-II point-&-track (NEAT data), and QUEST-II camera drift-scan (QUEST data). The line shows the sky coverage averaged over each lunar month.

All images are transferred from Mt. Palomar using a high-speed wireless datalink to NERSC (National Energy Research Scientific Computing Center). There they are processed and subtracted from reference images, and the residual sources that pass a set of image parameter cuts (Bailey et al. 2007) are automatically identified and passed on to human scanners, for vetoing.

5.2   Screening

Based on historical data for the same field (to easily distinguish variable stars or similar transients from supernovæ) a candidate may be sent directly to the SNIFS observation queue by a scanner, for spectroscopic identification. If the supernova is positively identified to be a SN Ia on an early enough phase, and with a redshift $\lesssim 0.08$, it is marked for subsequent followup. While the distinction between the different sub-types of supernovæ is easily made by looking at the spectral features of the screened target, its phase determination, using only one observation (and thus without the possibility to obtain a light curve), relies on software that compares the spectrum with a database of SNe Ia spectra like SUSPECT (Richardson et al. 2001), with known redshifts and phases. This type of software will also greatly benefit from the SNfactory

dataset.

When insufficient vetting constraints are available, imaging data is attempted to be obtained from other sources. Both the Lick 1m and the OHP (Observatoire de Haute Provence) 1.2m telescopes were used for photometric screening of candidates, however this work was not pursued, since it is labor intensive and the classical telescope scheduling means that candidates might wait several days before they are screened. Instead, a procedure was implemented in SNIFS, which makes a quick 60s unguided exposure using the photometric channel, to check for luminosity increase with relation to the discovery image. This is quite fast and allows for several photometric screens during one night with small loss of followup time. Furthermore, in the case a candidate is deemed worthwhile by the shifter, it can be added to the night schedule and spectred immediately. The opposite may also happen: in the case which a candidate is sent directly for spectroscopic confirmation, the shifter is adverted and may judge from the acquisition image that the object is too dim or not anymore there, and it can be dropped.

Fig. 5.2 shows the statistics as of the end of 2007 for the number of targets screened by SNIFS, as well as the redshift and types of the confirmed supernovæ. The SNe Ia whose redshift is inside the SNfactory intended observational range, and whose phase is before or close to maximum are added to the SNIFS queue of spectroscopic followup.
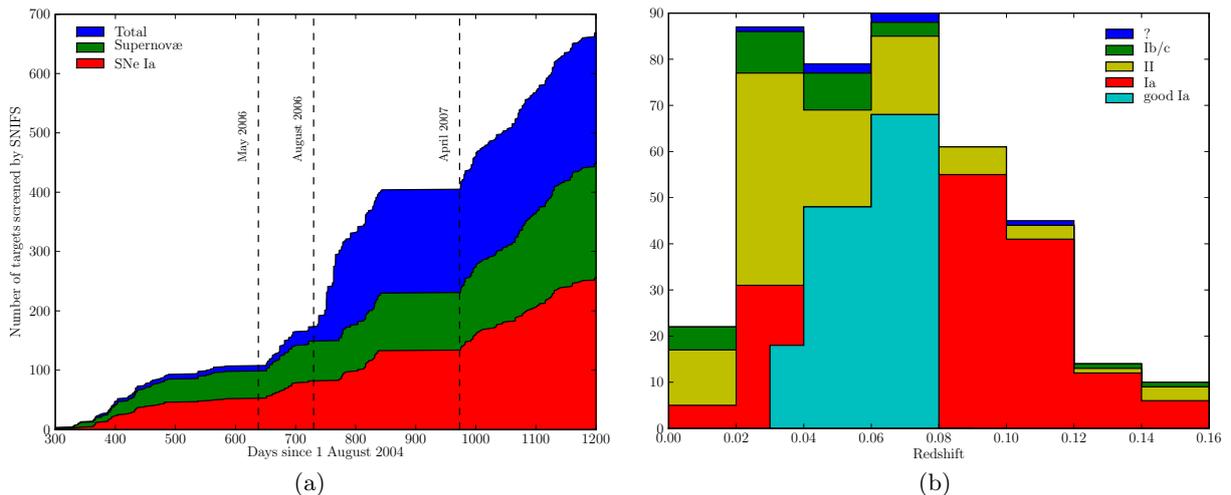
Figure 5.2: (a) Time evolution of the number of targets issued from the SNfactory search pipeline and screened photometrically and/or spectroscopically by SNIFS. Spring 2006 corresponds to the real take off of the project, both due to the passage into full night operations and the improvement of the search yield. A problem with the POP motor on August 2006 prevented the usage of the spectrograph during one month, hence the big increase in photometric screening at that time; (b) Redshift and type distribution for the supernovæ found by the SNfactory search pipeline and screened by SNIFS, as of the end of 2007. ? represents either Ia?, Ib/c? or II? supernovæ whose identification is not certain, and the *good* sample are the SNe Ia with $0.03 < z < 0.08$. 408 screened targets for which there is a redshift measurement are represented. We can see that SNe Ia represent more than half of the screened targets.

5.3 Spectroscopic followup

A followup observation is one that is made when a target was already previously identified as SN Ia. Since it is a time consuming observation (a typical pointing + spectrum exposure + related calibration can take around 30 minutes), the number of supernovæ that can be observed

during a night is limited, and the observation schedule is optimized in order to have spectral sequences of the same object with no more than 3 or 4 days between them (which may be further affected by unpredictable events like bad weather).

After the start of operations, the 20% time share agreement between University of Hawaii and SNfactory for the usage of the UH88 telescope, allowed SNIFS to be used during three alternating half-nights each week (or more precisely, the first and third half-night for each sequence of five). Since May of 2006 the time share was increased to 30%, allowing now for SNIFS to use the UH88 exclusively all of the night (representing ~ 10 hours for science operation and ~ 4 hours for calibration and setup), three times per week, 8.5 months per year[4], which increased the number of supernovæ susceptible to be followed per shift.

Fig. 5.3 shows the statistics as of the middle of 2008 for the targets followed by SNIFS. To be considered as followed, a target must be observed on more than 5 epochs, which currently amounts to around 167 SNe Ia, totaling more than 2500 spectra. That accounts for around 1000h of open shutter time of the spectrograph, 2/3 of the total open time if we consider spectroscopic screening and standard stars used for calibration. This already represents the biggest archive of nearby SNe Ia spectra currently available.

SNIFS will continue to acquire data regularly until the end of 2008, and will be used to collect spectral final references in 2009.
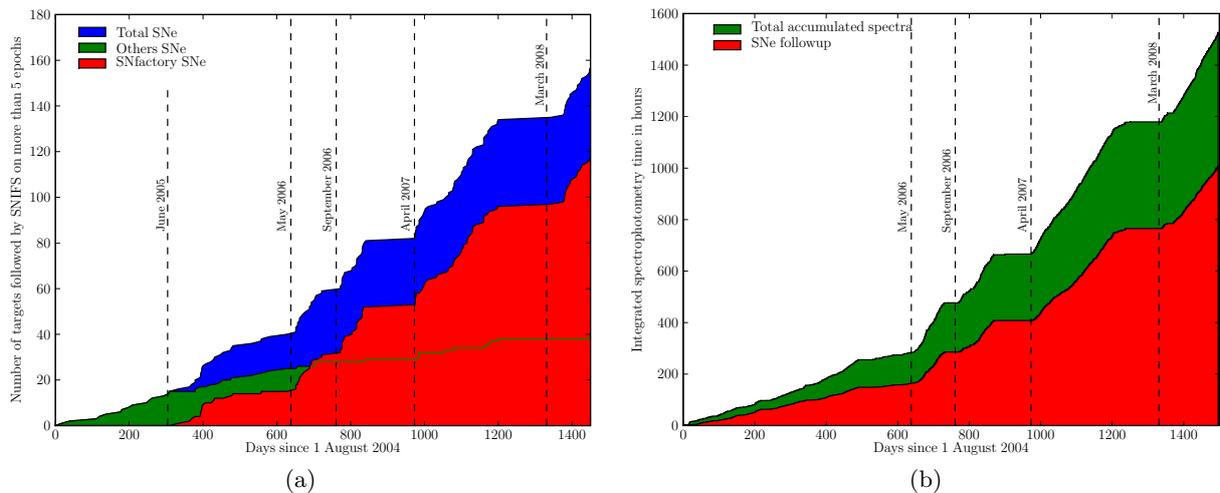
Figure 5.3: (a) Time evolution (up to mid 2008) of the number of targets followed spectroscopically by SNIFS on more than 5 epochs, and distribution with relation to the discoverer. The observation of the first target issued from the SNfactory search survey was carried in June 2005. The survey debated with infrastructure and software scaling problems up until the spring of 2006, which coincided with the change for full night observations. Since September 2006 the number of followed SNfactory targets overcome the IAUC ones. The plateau around this time is due to the POP motor failure. After the 2007 winter pause, the yield of the search attained "maximum luminosity"; (b) Hours of open shutter time for SNe Ia followup with relation to total open time (accounting for screening and calibration). The steep increase after May 2006 is accounted for the change to full night observations.

---

[4]The data taking is stopped for 3.5 months during winter, which is a period of typical bad weather conditions, that impact a lot the search and are also a problem for the followup.

5.4 Interesting SNfactory objects

From the supernovæ sample observed by SNfactory up until now, a few peculiar objects were followed with particular interest. Two of them have already been subject of publications, that represent important contributions to our understanding of the progenitors and environments of SNe Ia, as well as the physics of how SNe Ia explode.

I will detail these objects here, which on top of their scientific interest, consist an example of the observational power of the SNfactory program.

5.4.1 SN2005gj

The SN2005gj (Aldering et al. 2006) supernova is the second confirmed case of interaction between the ejecta of a supernova and the circumstellar medium (CSM). Like SN2002ic (Wood-Vasey et al. 2004), it is an hybrid SN Ia/II-n: at the time of the screening observation by SNIFS, it presented a narrow Hα emission superimposed on a broader component, making it indistinguishable from a classical SN II-n and prompting its removal from the SNIFS observational queue. However, later on (Prieto et al. 2005) it was found to also present spectral features characteristic of a SN Ia, which lead to more spectral followup by SNIFS.

This type of event is important in the study of SNe Ia progenitors. The two most favored scenarios, both involving the thermonuclear disruption of a WD, are the *single-degenerate* model where the WD accretes matter from a less evolved companion star until it reaches the Chandrasekhar mass and explodes (see § 2.3.1), and the *double-degenerate* model where a binary system of WD spirals-in and coalesces. The detection of circumstellar hydrogen in the spectrum of an SN Ia would be interpreted as support for the single-degenerate scenario.

Early phase photometry and spectroscopy (Fig. 5.4) shows a more intense and earlier interaction with the CSM than in the SN2002ic case. It was found that the light curve and measured velocity of the unshocked CSM imply a very recent period of mass loss, in contrast to SN 2002ic, for which an inner cavity in the CSM was inferred. A flat radial density profile for the CSM describes well the early light curve, however a decomposition of the spectra into SN Ia and shock emission components allows for little obscuration of the supernova, suggesting an aspherical or clumpy distribution for the CSM.

The host galaxy low metallicity inferred from ground- and space-based photometry, and Keck spectroscopy, as well as the fact that this galaxy is undergoing a significant star formation event that began $\sim$ 200 Myr ago place the strongest constraint to date on the age of a SN Ia progenitor.

It is also of interest to know how a supernova of this kind could be mistakenly included as a SN Ia in a cosmological analysis. From a spectral point of view, a high redshift event could be considered has an overluminous type II SN in an early phase, whether on later times it could be wrongly classified as an SN Ia. Photometrically, the flat light curve of SN2005gj would exclude it, but in the case of SN2002ic and its weaker interaction we need late (> 40 days) data to make a proper selection, which is possible with the current high redshift rolling search surveys like SNLS or ESSENCE. The fact that also both SN2005cj, SN2002ic and other candidates for CSM interaction all appear on low luminosity hosts, confirm the importance of blind search on surveys how which to study SNe Ia physics.

5.4.2 SN2006D

Early SNIFS spectra of SN2006D include the strongest signature of unburned material at photospheric velocities observed in a SN Ia to date (Fig. 5.5). This observation is important
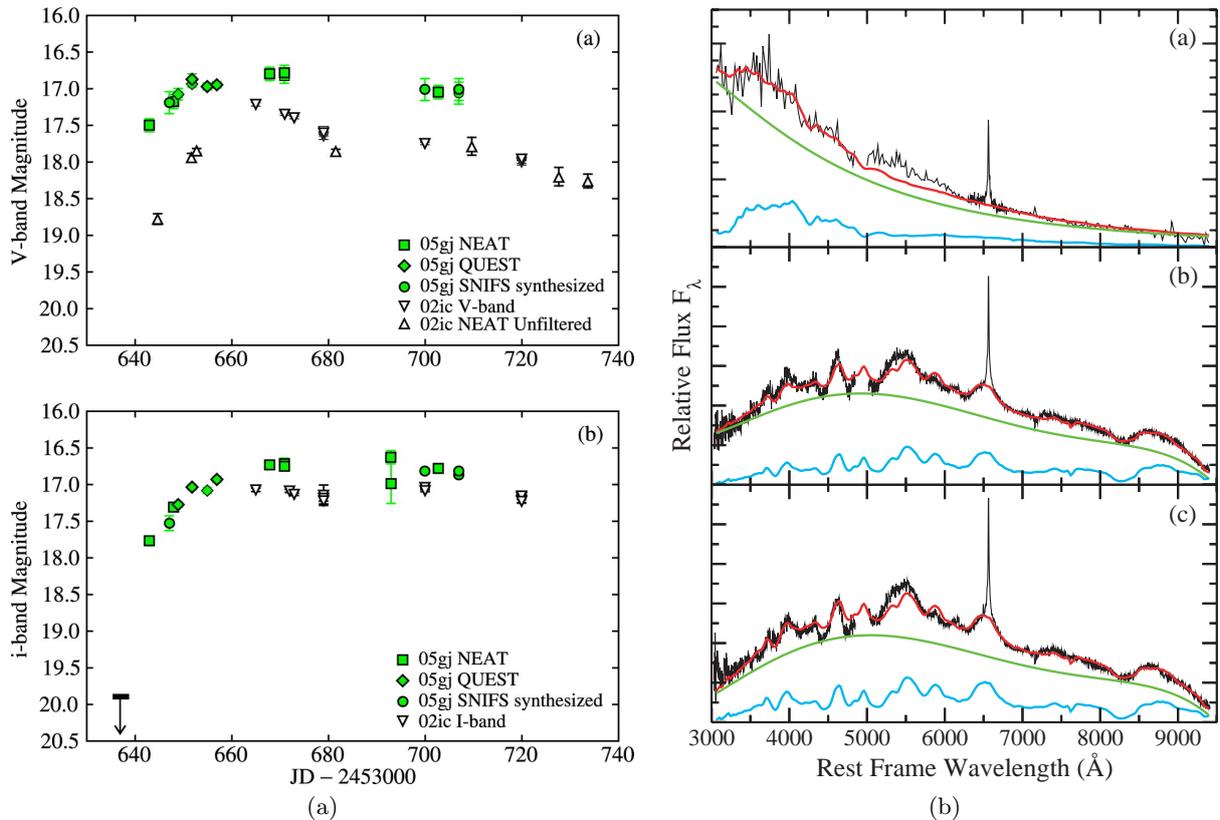
Figure 5.4: (a) Light curves of SN2005g and SN2002ic in V band (top) and i band (bottom). SN2002i's time axis has been shifted to match the explosion date of SN2005gj. (b) Decompositions of the SN2005g j spectra: (a) comparison of the spectrum from 11 days after explosion to a blackbody plus a 91T-like template spectrum from the same rest-frame phase; (b, c) decomposition of the day 64 and day 71 spectra in terms of a smooth polynomial (representing the contribution to the spectrum from the CSM interaction) plus a 91T-like template at 60 and 66 rest-frame days after explosion, respectively. From Aldering et al. (2006).

in the sense that the current state of the art in hydrodynamical supernova explosion models are characterized by differing distributions of unburned and synthesized material. Therefore, the amount and spatial distribution of unburned ejecta, specifically carbon, is an important constraint on explosion models from observations.

SNIFS earliest spectrum exhibits C II absorption features below 14,000 km s^{-1}, including a distinctive C II $\lambda6580$Å absorption feature, which dissipate as the supernova approaches peak brightness.

In addition to discussing implications of photospheric-velocity carbon for white dwarf explosion models, Thomas et al. (2007) outline some factors that may influence the frequency of its detection before and around peak brightness: depopulation of the C II optical levels by non-LTE effects (a new effect that could explain the relatively sporadic detection of carbon in SN Ia spectra in general), and line-of-sight effects resulting from a clumpy distribution of unburned material with low volume-filling factor. Some degree of clumpiness in the distribution of unburned material may be present in SNe Ia, to some degree – a theory which must be addressed by white dwarf explosion and SN atmosphere modelers.
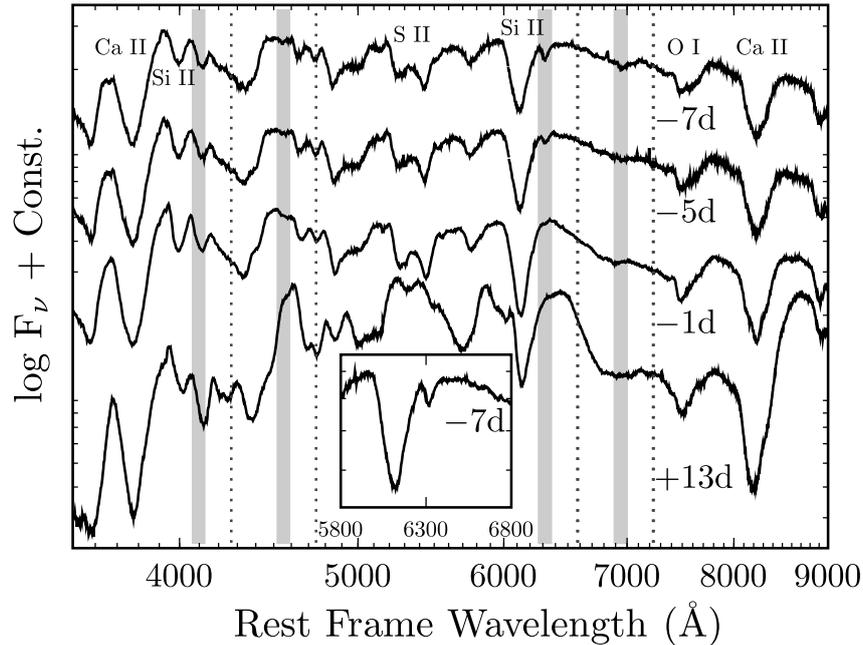
Figure 5.5: SNIFS spectral time series of SN2006D. Dotted vertical lines mark rest wavelengths of C II lines $\lambda\lambda$4267Å, 4745Å, 6580Å, and 7234Å. Shaded bands indicate blueshifts between 10,000 and 14,000 km s^{-1} with respect to these lines, typical of the velocity at the photosphere at these phases. Inset is a zoom of the region around the 6320Å notch in the -7 day spectrum. This is the strongest constraint on unburned white dwarf material from optical spectra to date. From Thomas et al. (2007).

5.4.3 SNF20070803-005

The supernova SNF20070803-005 was discovered by the SNfactory in August 2007 around 8 days before maximum. It is a SN1991T-like overluminous supernova, as can be seen from its spectral time series (Fig. 5.6a): the Si II feature around 6100Å is very shallow, and the spectra are dominated by the Fe III lines.

5.4.4 SNF20070825-001

The supernova SNF20070825-001 was discovered by the SNfactory in August 2007 and followed spectroscopically during 20 epochs. A spectral time series comprising half of these epochs can be seen in Fig. 5.6b. With redshift ~ 0.07, its light curve is abnormally bright, peaking at 17.5 mag in B, which gives an absolute magnitude of $M_B \approx -19.9$ (an average SN Ia has $M_B \approx -19.1$).

This object is similar to SNLS-03D3bb (Howell et al. 2006) (Fig. 5.6c–5.6d), a SN Ia originating from a *super*-Chandrasekhar-mass white dwarf. The inferred mass of ^{56}Ni that could account for the brightness of SNLS-03D3bb, is not possible if the progenitor is limited by the Chandrasekhar mass. The observed low ejecta velocities are also incompatible with the Chandrasekhar mass model, by implying a bigger progenitor binding energy, and thus a larger total mass. Such high mass WD have been shown to be possible in the case of a rapidly rotation star (Yoon and Langer 2005). SNF20070825-001 is thus the second observation ever of such kind of events.

Another supernova, SNF20080723-012 was recently discovered, and a first analysis shows it to be spectrally similar to SNF20070825-001.

Figure 5.6: (a) Spectral time series for the SN1991T-like supernova SNF20070803-005; (b) Spectral time series for the SNLS-03D3bb-like supernova SNF20070825-001; (c) SNIFS spectrum of SNF20070825-001 near maximum light; (d) Spectrum of SNLS-03D3bb near maximum light, compared to a normal SN Ia (top) and a SYNOW fit to the data (bottom). It shows the typical lines seen on SNe Ia, but with a velocity lower than usual. From Howell et al. (2006).

5.4.5 SNF20080720-001

The supernova SNF20080720-001 was discovered by SNfactory in July 2008. It presents typical SN Ia spectral features, but a strong red continuum (Fig. 5.7b), possibly derived from dust on the host galaxy: its acquisition image shows an edge-on galaxy with a clear dust-lane visible (Fig. 5.7a).

Such object can in principle be used to constraint the source of the dust extinction, and to extract the host galaxy reddening law, by comparing its colors with the ones from another non-extincted supernova, with similar spectral features. That would allow us to obtain an extinction law from another galaxy and compare it to the standard Milky Way one.

(a)   (b)
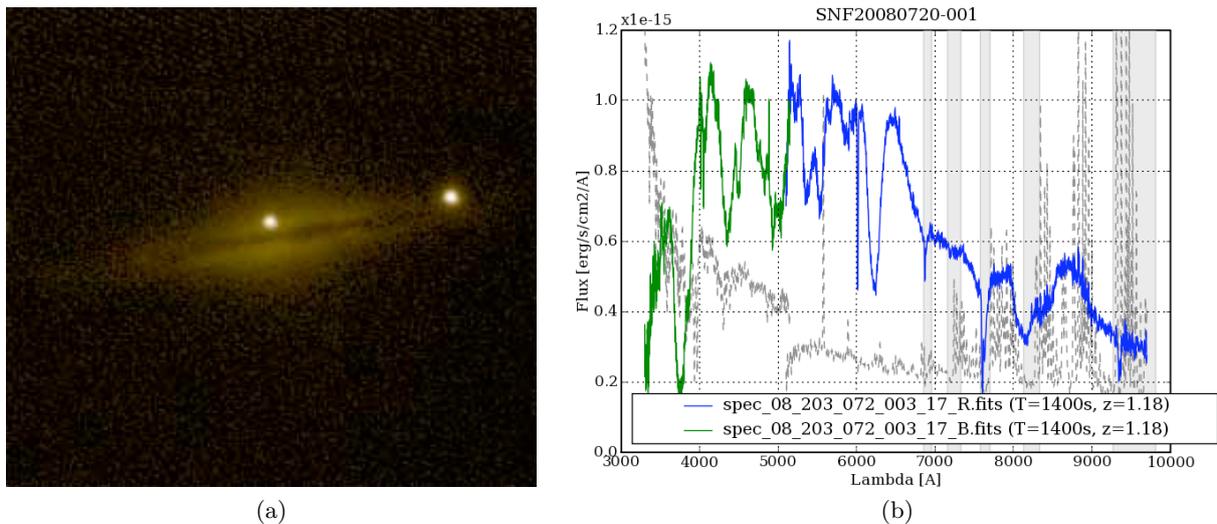
Figure 5.7: (a) Acquisition image for SNF20080720-001, with the host galaxy dust-lane clearly visible; (b) SNF20080720-001 spectrum near maximum light.

Part III

From photons to bits - SNfactory's data acquisition & calibration

Chapter 6

Data acquisition rationale

A typical night of observation using SNIFS is composed of several operations, mostly consisting on the acquisition of science (§ 6.2) and related calibration (§ 6.3) exposures, using the spectroscopic and photometric channels, in conjunction or separately.

6.1 A night's run schedule

A night can be divided into three main parts: before sunset (US0 shift), dark time (FR1/2 shifts) and after sunrise (US3 shift). US0/3 acquire mostly calibration data, while FR1/2 acquire both calibration and science data from the targets to be observed, as dictated by the night schedule.

The observation schedule is compiled at LBL, and takes into account the supernovæ which are on queue for followup, as well as the ones arriving from the search pipeline for photometric or spectroscopic screening. The scheduler allocates during the night the biggest possible number of targets, whose priority depends on several parameters, like the time since last observation and current phase for the followup targets and probability to be a SN Ia for the screened ones.

A full night is roughly composed of the following operations:

- up to 15 SNe Ia and candidate supernovæ spectrophotometry exposures;

- up to 4 photometric screenings;

- 3 spectrophotometric standard stars during dark time;

- 8 spectrophotometric standard stars during evening and morning twilight;

- sky and dome flats at the start and end of night;

- arc and continuum calibrations for each spectroscopic exposure.

An example of a night schedule, composed of several screening and followup targets, is shown in Fig. 6.1.

6.2 Science exposures

A science exposure will be defined as being every exposure, on any channel, of a target on the sky (supernova or standard star), either being screened or followed.
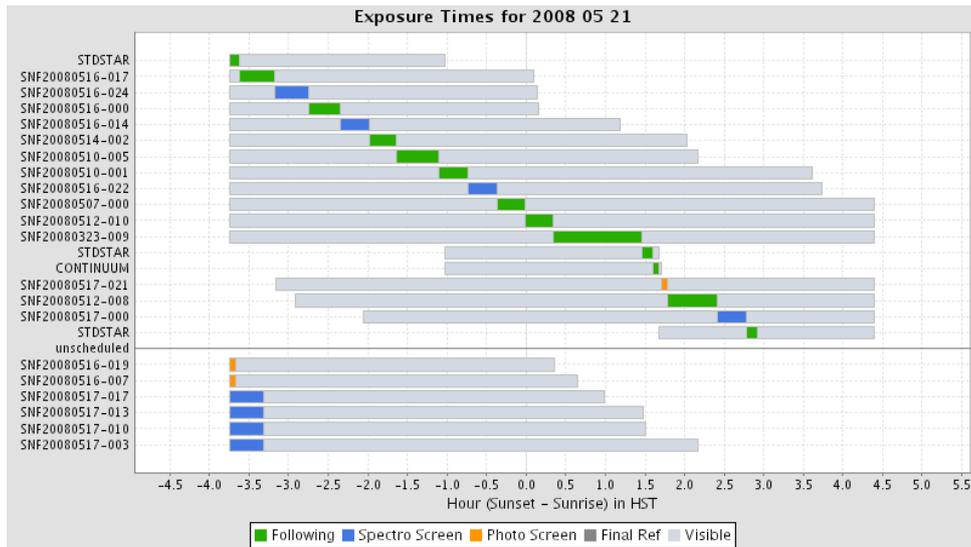
Figure 6.1: SNIFS schedule/visibility chart for a night of May 2008.

6.2.1 Spectrum datacube

A datacube is produced for each spectroscopic exposure, and is basically a (x, y, λ) "cube" containing the ensemble of spectra formed at each of the 225 (x, y) *spaxels* in which the MLA divides the spectrograph field of view (Fig. 6.2a). To create the datacubes from the raw images (Fig. 6.2b), each spectrum is extracted from the CCD with the help of the arc and continuum exposures (§ 6.3), and an optimized extractor is then used to combine the multiple spectra from the object and obtain one single spectrum, separated from the sky and host galaxy ones. Not being part of my work in SNfactory, I'll leave the details of this (highly non trivial) process to Gilles (2006), Buton (2009), Bongard (2009).

6.2.2 Acquisition exposure

An acquisition exposure (from which a small part can be seen on the left panel of Fig. 6.2a, for more details see § 9.2.1), is a small exposure taken using the photometric channel with the POP removed. It is taken right before the multi-filter exposure, and allows to fine tune the pointing of the telescope. In this image, the target and the brightest stars around it will be visible, and thus it can be compared to a finding chart star catalog, and the object precisely re-centered on the position where the POP will be placed. A guider star is also selected, to be used during the subsequent long spectral exposure, from the stars observed by the guider CCD.

6.2.3 Multi-filter exposure

Acquired exactly at the same time of the spectra, due to the common shutter, the MF exposure images the stars surrounding the observed target, on the wider field of view of the photometric channel (Fig. 4.7b). A raw image (Fig. 6.2c) will then be calibrated (§ 8) and processed (§ 9) in order to obtain the necessary correction factors, applied during the spectrum flux calibration (§ 7) to compensate for the atmospheric attenuation.

70

(a)

(b)

(c)
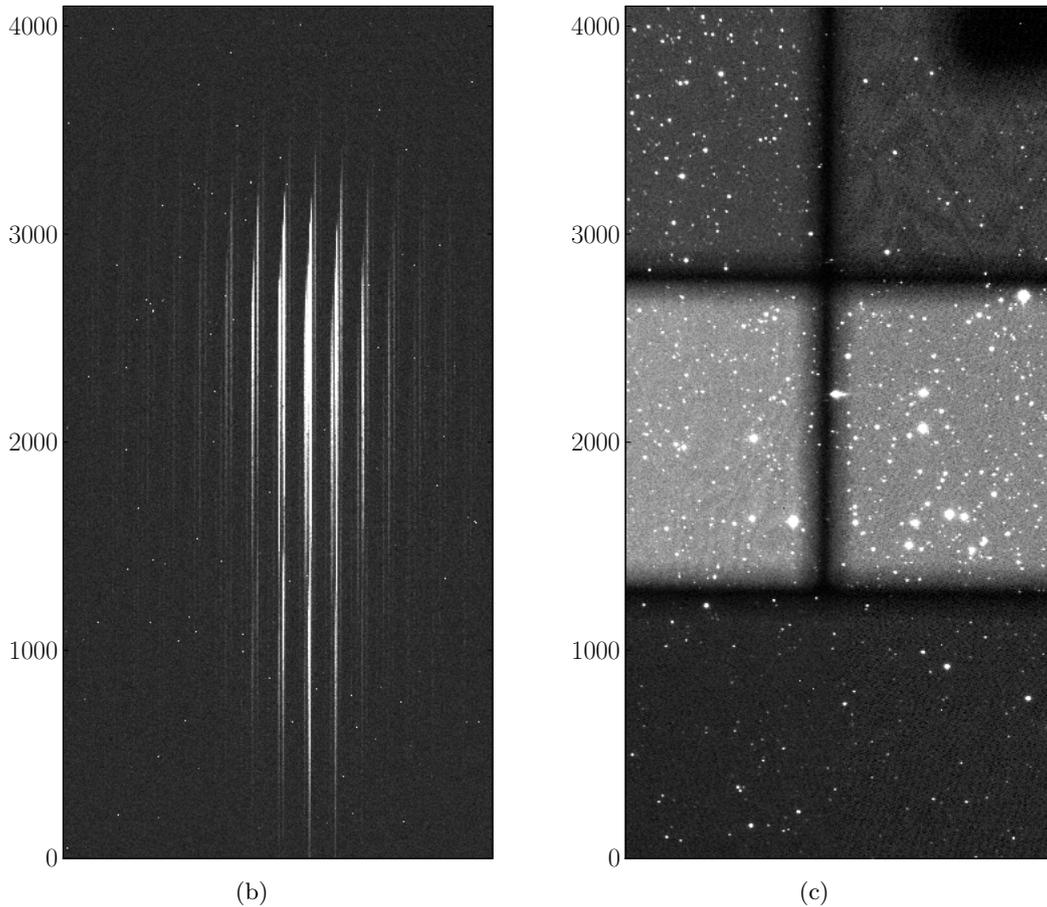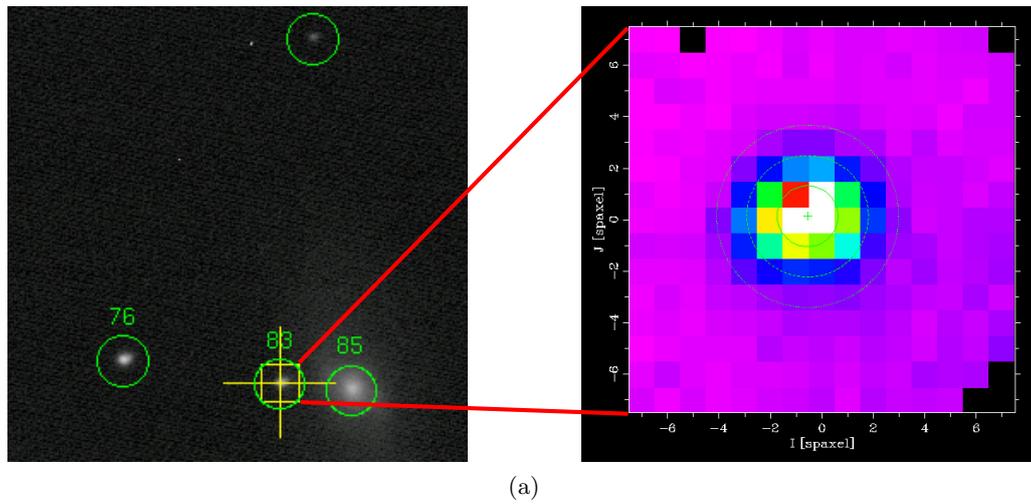
Figure 6.2: (a) The MLA $6'' \times 6''$ field of view is mapped into 225 spaxels, and a (b) spectrum for each one of them is registered on the spectroscopic channels' CCDs; (c) A raw exposure of the surrounding stars of a supernova field, using the photometric channel CCD with the multi-filter (F1 to F5 are visible). A pixel corresponds to $0.137''$. For comparison, the MLA (yellow) square on (a) is 45 pixels wide.

71

6.3 Calibration exposures

A calibration exposure will be defined as being every exposure, on any channel, that is used to calibrate the science ones. They can be taken during the night in parallel to the science ones, or on any other time.

6.3.1 Bias

A bias exposure is a 0s exposure on any CCD, which will only consist of noise added by the readout electronics, used to convert the charges on the CCD to a digital signal. Several exposures are taken during the US0/3 shifts on all channels, and a mean stack is them subtracted from the science raw exposures, to remove any residual charges added during readout.

6.3.2 Dark

The darks have a typical exposure time of 1h and are made with the instrument shutter closed, by the US0/3 shifts and between data taking days, on a continuous loop. They will mostly consist of thermal noise and are thus dependent on the temperature. For SNIFS, the CCDs are kept at ~ 150K, and the dark current typically consists of a few electrons per hour.

6.3.3 Flat field

A flat field image is used in order to flatten the relative response of each pixel of the CCD to the incoming radiation, so that the full array response is uniform and each pixel count is comparable to its neighbors. Ideally, a flat field image is spectrally and spatially flat. Once such an image is obtained, we can divide our science images by it to remove all the pixel-to-pixel intrinsic response variations. Two kinds of flat fields for the photometric channel are taken by US0/3: dome flats, by pointing the telescope to the interior of the (closed) dome which is illuminated with a special lamp; and sky flats, by pointing the telescope to the evening or morning (uniform) twilight skies. For more details see § 8.2. The flat fielding procedure of the spectroscopic channels uses a different kind of exposures, from internal spectral continuum lamps.

6.3.4 Continuum

A continuum exposure is specific to the spectroscopic channel. During the pointing sequence of the telescope performed with the help of the photometric channel, the spectroscopic channels observe the output of a smooth black body-like spectral lamp out of the calibration unit of SNIFS. A small raster image is obtained for monitoring of possible dichroic bandpass changes. At the beginning, middle and end of night, full continuum exposures are also taken, which will be used for low frequency flat field correction of the throughput of each lens of the MLA.

6.3.5 Arc

An arc exposure is also specific to the spectroscopic channel, and are made after the spectral science exposure, and before moving the telescope to another target. A very stable spectral lamp (present in the calibration unit) is observed, and the position of its (known) spectral distribution on the spectrograph CCDs is used as seed to precisely localize on the CCD the spectra of each spaxel (sensitive to mechanical flexure), and for wavelength calibration of the science spectra.

Chapter 7

Spectra flux calibration

In this chapter I will describe the photometric calibration scheme of the spectral data acquired by SNIFS, which special emphasis on the role of the photometric channel.

The baseline requirement for spectrophotometry for the SNfactory, is an internally consistent extra-atmospheric flux calibration with systematic accuracy better than 1% under photometric conditions, and better than 3% under non-photometric conditions.

7.1 Atmospheric extinction and photometricity

Together with the telescope and instrument throughputs, the correction for atmospheric extinction is a central aspect of the flux calibration scheme. At a given time t it can be divided into two components with different airmass[1] z dependencies

$$T_{\mathrm{atm}}(\lambda, z, t) = A^z(\lambda, t) \times A_{\oplus}^{z^{\alpha}}(\lambda, t) \ , \tag{7.1}$$

where the $A_{\oplus}$ component is non-unity only on some very restrict wavelength ranges, the telluric lines (see Fig. 4.8b). Rewriting the extinction terms in magnitudes we get

$$T_{\mathrm{atm}}(\lambda, z, t) = 10^{-0.4[K(\lambda, t) + K_{\oplus}(\lambda, t)]} \ , \tag{7.2}$$

where the K extinction curves can be decomposed in the contribution by the several physical components (Fig. 4.8a):

$$K(\lambda) = \sum_i k_i(\lambda) \tag{7.3}$$

Rayleigh scattering

$$k_R(\lambda) = a_R \lambda^{-4+\epsilon} \ , \text{with } \epsilon \sim 0.04 \tag{7.4}$$

It dominates the extinction at most wavelengths under photometric conditions. a_R depends on the molecular scale height which depends on altitude, and on weakly varying parameters like temperature and pressure.

Aerosol scattering

$$k_A(\lambda) = a_A \lambda^{-\gamma} \ , \text{with } -1 \lesssim \gamma \lesssim 4 \tag{7.5}$$

---

[1]The airmass is the atmosphere path length through which an observation is made, defined as the secant of the zenith angle (the angle between the point right above an observer and the object being observed), and is thus 1 at zenith by definition.

Generally the second greatest contributor. γ depends on the particle size distribution of the aerosols, which shows variation with the source of a given mass of air. Scattering by suspended water droplets is generally included in the aerosol scattering budget.

Ozone absorption

$$k_{O_3}(\lambda) = a_{O_3} P_{O_3}(\lambda) \tag{7.6}$$

Generally smaller than Rayleigh scattering over most of the optical spectrum. P_{O_3} has a spectral shape which is well known, but it's amplitude has seasonal variations and it is also reported to vary on timescales of hours. O_2 also produces narrow absorption telluric lines.

Water vapor k_{H_2O} is generally absent or weak except at a few wavelength intervals (telluric lines) in the red part of the optical window. It may vary over the course of a few days or during a single night, especially if clouds are present and passing through the field of view. It is spectrally neutral due to the large number of random scatters in large water droplets or ice crystals.

A night is said to be *photometric* if the extinction curves K are time-independent, and *non-photometric* for the opposite case. In the current implementation of the SNfactory calibration pipeline, $K_\oplus$ is also assumed to not be time-dependent, even on non-photometric conditions.

As we can see, the flux calibration approach will depend on the photometricity of the night, and thus we need a measurement of the transmission stability of each night. For this, SNfactory uses the output of SkyProbe[2] (Cuillandre et al. 2002), a real-time sky transparency monitor installed at the CFHT, that observes standard stars on a wide field-of-view centered on the instantaneous pointing of the telescope. Using the data issued from SkyProbe, and taking into account that the pointings of both UH88 and CFHT are not the same, each night is graded according to the evolution and scatter of the atmospheric transmission throughout the observation run. Nights with an RMS scatter of the SkyProbe data lower than 0.02 mags are assumed to be photometric (see Figure 7.1 for examples).

It is obvious that the flux calibration scheme should differ for each of theses cases. The following description is based on the internal SNfactory calibration reference schema, and the notation used will be the following:

S, s generic name for a supernova and associated secondary sources observed on the photometric channel;

F, f generic name for a faint standard star (exposure time $\gtrsim$ 100s) and associated secondary sources observed on the photometric channel;

B generic name for a bright standard star (exposure time $\sim$ 1s);

X intrinsic spectrum/flux of the object type X;

$\overline{X}$ tabulated spectrum (standard star);

$\widetilde{X}$ observed spectrum/flux;

$\widehat{X}$ flat-fielded spectrum.

On a given night, several observations can be made by both channels:
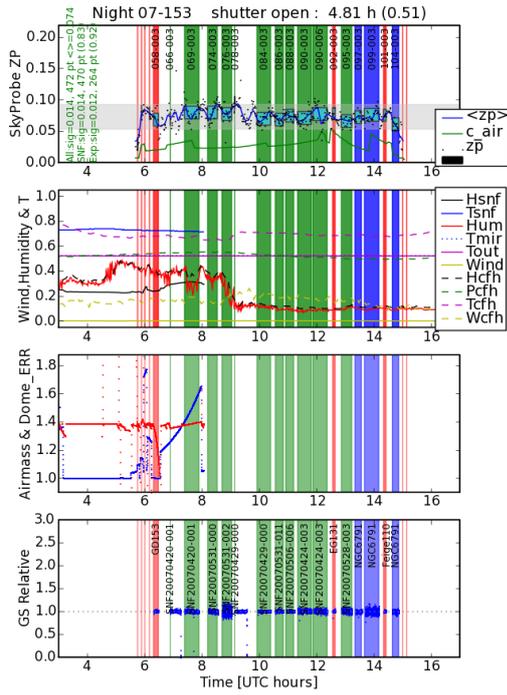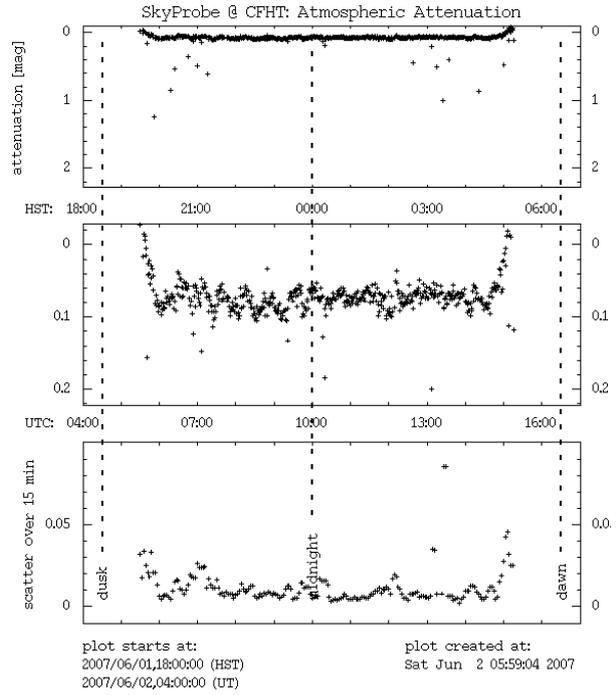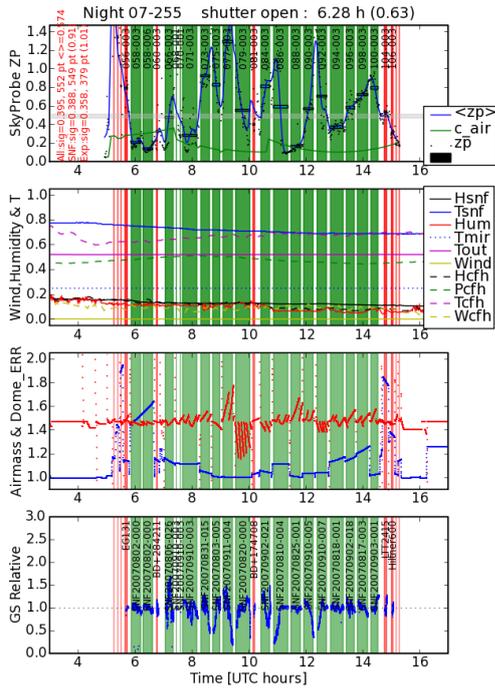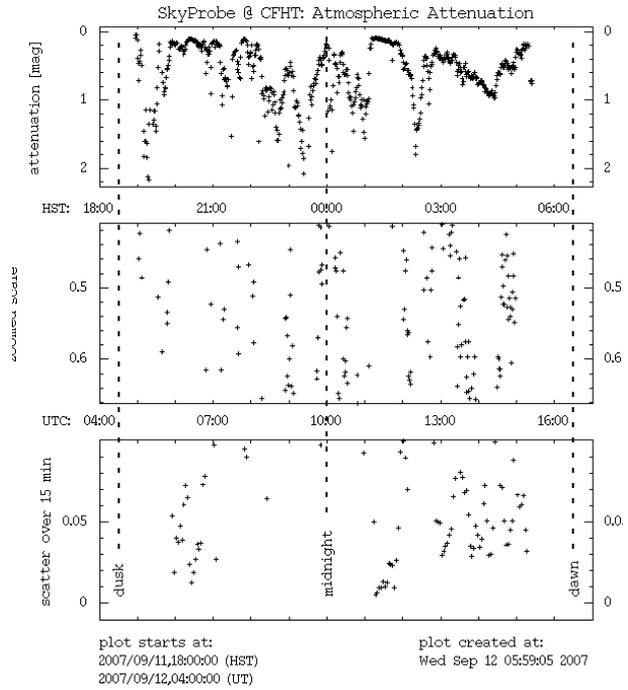
Figure 7.1: Examples of SkyProbe data for both photometric (07_153) and non-photometric (07_255) nights. (a) and (c) represent a "nightplot" analysis of the observing run: the top panel shows the SkyProbe zero point trend and each observed target (vertical bars - red for standard stars, green and blue for SNe) throughout the night; the other panels show respectively the variation in weather conditions (temperature, humidity, pressure, *etc*), dome alignment and pointing airmass, and the guide star flux variation. (b) and (d) are the "raw" SkyProbe data issued from CFHT. The difference in the atmospheric attenuation stability during both nights is noticeable.

75

7.1.1 Spectroscopic channel

Continuum lamp Spatially uniform, with a smooth black body-like spectrum $C(\lambda)$ and including the transmission of the instrument:

$$\widetilde{C}_l(\lambda) = C(\lambda) \times T_l(\lambda) \; ; \tag{7.7}$$

Target Observed at airmass z with an intrinsic spectrum $X(\lambda)$, and including the transmission of the instrument, telescope and atmosphere:

$$\widetilde{X}_l(\lambda) = X(\lambda) \times T_l(\lambda) \times T_{\text{tel}}(\lambda) \times T_{\text{atm}}(\lambda, z) \; . \tag{7.8}$$

After spectro-spatial flat-fielding by the same continuum exposure, we have, independently of the night photometricity and assuming that the overall spectrograph transmission is stable between both observations

$$\widehat{S}(\lambda) = S(\lambda) \times \frac{\widehat{F}(\lambda)}{F(\lambda)} \frac{{}^{[S]}T_{\text{atm}}(\lambda, z_S)}{{}^{[F]}T_{\text{atm}}(\lambda, z_F)} \; , \tag{7.9}$$

where ${}^{[S]}T_{\text{atm}}$ and ${}^{[F]}T_{\text{atm}}$ are the effective atmospheric transmissions during object and standard star observations.

7.1.2 Photometric channel

Secondary source Observed at airmass z through a specific MF filter with transmission T_{MF}, and including the transmission of the telescope (no other optical components apart from the SNIFS entrance window are crossed by the light path) and atmosphere. Its measured flux is:

$$\widetilde{x} = \int x(\lambda) \, T_{\text{MF}}(\lambda) \, T_{\text{tel}}(\lambda) \, T_{\text{atm}}(\lambda, z) \, \mathrm{d}\lambda \; . \tag{7.10}$$

We will then see how these observations can be used for the purpose of flux calibration on each night.

7.2 Photometric night

By definition, when conditions are photometric ${}^{[p]}$ the atmospheric extinction T_{atm} is isotropic in the sky and has no time dependence

$$^{[S]}T_{\text{atm}} \equiv {}^{[F]}T_{\text{atm}} \equiv {}^{[p]}T_{\text{atm}} \; . \tag{7.11}$$

It can be derived using a set of bright standard stars:

$$^{[p]}\widehat{B}_i(\lambda) = \frac{B_i(\lambda)}{{}^{[p]}C(\lambda)} \times {}^{[p]}T_{\text{tel}}(\lambda) \times {}^{[p]}T_{\text{atm}}(\lambda, z_i) \; , \tag{7.12}$$

where

$$^{[p]}T_{\text{atm}}(\lambda, z_i) = {}^{[p]}A^{z_i}(\lambda) \times {}^{[p]}A_{\oplus}^{z_i^{\alpha}}(\lambda) \; . \tag{7.13}$$

The telluric lines correction is made by calculating an effective continuum shape for B outside of their wavelength domains, with posterior application inside the domain (for details see Buton (2009)). Outside the telluric domains, $A_\oplus \equiv 1$ and

$$\frac{^{[\mathrm{p}]}\widehat{B}_i(\lambda)}{\overline{B}_i(\lambda)} = \frac{^{[\mathrm{p}]}T_{\mathrm{tel}}(\lambda)}{^{[\mathrm{p}]}C(\lambda)} {^{[\mathrm{p}]}A^{z_i}(\lambda)} \tag{7.14}$$

$$\log \frac{^{[\mathrm{p}]}\widehat{B}_i(\lambda)}{\overline{B}_i(\lambda)} = \alpha(\lambda) + z_i \times \log {^{[\mathrm{p}]}A(\lambda)} \,, \tag{7.15}$$

and we can thus get $^{[\mathrm{p}]}A$ by means of a linear regression of (7.15) with the maximum number of B stars possible. Together with $^{[\mathrm{p}]}A_\oplus$ we calculate $^{[\mathrm{p}]}T_{\mathrm{atm}}$, which can be used to obtain the flux calibration spectrum $^{[\mathrm{p}]}\mathcal{F}$ from a faint standard star F (with secondary sources f observed by the photometric channel), observed on the same night at airmass z_F

$$^{[\mathrm{p}]}\mathcal{F}_F(\lambda) = \frac{^{[\mathrm{p}]}\widehat{F}(\lambda)}{\overline{F}(\lambda)} \frac{1}{^{[\mathrm{p}]}T_{\mathrm{atm}}(\lambda, z_F)} \tag{7.16}$$

$$= \frac{^{[\mathrm{p}]}T_{\mathrm{tel}}(\lambda)}{^{[\mathrm{p}]}C(\lambda)} \,. \tag{7.17}$$

The supernova spectrum $\widehat{S}(\lambda)$ observed at airmass z can then be flux calibrated using

$$S(\lambda) = \frac{^{[\mathrm{p}]}\widehat{S}(\lambda)}{^{[\mathrm{p}]}\mathcal{F}_F(\lambda)} \frac{1}{^{[\mathrm{p}]}T_{\mathrm{atm}}(\lambda, z)} \,. \tag{7.18}$$

7.3 Non-photometric night

On a non-photometric night $^{[\mathrm{n}]}$, the atmospheric extinction changes with time and thus the approach taken on the photometric night is not valid, since T_{atm} will change between the observation of the supernova and the faint standard star.

A set of bright standard stars can be used, described in the same way as (7.12), as well as a faint standard star described in a similar fashion

$$^{[\mathrm{n_F}]}\widehat{F}(\lambda) = \frac{F(\lambda)}{^{[\mathrm{n}]}C(\lambda)} \times {^{[\mathrm{n}]}T_{\mathrm{tel}}(\lambda)} \times {^{[\mathrm{n_F}]}T_{\mathrm{atm}}(\lambda, z_F)} \,, \tag{7.19}$$

with the flux of each corresponding secondary sources in the photometric channel being

$$^{[\mathrm{n_F}]}\widetilde{f} = \int f(\lambda) \, {^{[\mathrm{n}]}T_{\mathrm{MF}}(\lambda)} \, {^{[\mathrm{n}]}T_{\mathrm{tel}}(\lambda)} \, {^{[\mathrm{n_F}]}T_{\mathrm{atm}}(\lambda, z_F)} \, \mathrm{d}\lambda \,, \tag{7.20}$$

where $^{[\mathrm{n_F}]}$ represents a different period of the night $^{[\mathrm{n}]}$, with different transmission conditions.

The supernova spectrum observed at airmass z is

$$^{[\mathrm{n}]}\widehat{S}(\lambda) = \frac{S(\lambda)}{^{[\mathrm{n}]}C(\lambda)} \times {^{[\mathrm{n}]}T_{\mathrm{tel}}} \times {^{[\mathrm{n}]}T_{\mathrm{atm}}(\lambda, z)} \,, \tag{7.21}$$

and the corresponding secondary sources in the photometric channel have flux

$$^{[\mathrm{n}]}\widetilde{s} = \int s(\lambda) \, {^{[\mathrm{n}]}T_{\mathrm{MF}}(\lambda)} \, {^{[\mathrm{n}]}T_{\mathrm{tel}}(\lambda)} \, {^{[\mathrm{n}]}T_{\mathrm{atm}}(\lambda, z)} \, \mathrm{d}\lambda \,. \tag{7.22}$$

The flux of a secondary source on a MF filter can be approximated (by carrying a Taylor development of the atmospheric transmission to first order in the filter's effective wavelength[3] λ_{eff}) with

$$\widetilde{x} \simeq T_{\text{atm}}(\lambda_{\text{eff}}, z_x) \int x(\lambda) \, T_{\text{MF}}(\lambda) \, T_{\text{tel}}(\lambda) \, \mathrm{d}\lambda \, . \tag{7.23}$$

λ_{eff} is dependent on the unknown spectrum x of the secondary source, and we will assume that it is approximately constant for all secondary sources and that it does not vary with time. We can thus write

$$\widetilde{x} \simeq \overline{x} \times \overline{T_{\text{MF}} T_{\text{tel}}} \times T_{\text{atm}}(\lambda_{\text{eff}}, z_X) \, , \tag{7.24}$$

with

$$\int x(\lambda) \, T_{\text{MF}}(\lambda) \, T_{\text{tel}}(\lambda) \, \mathrm{d}\lambda \simeq \overline{x} \times \overline{T_{\text{MF}} T_{\text{tel}}} \, . \tag{7.25}$$

Equations (7.20) and (7.22) can now be approximated respectively by

$$^{[\text{nF}]}\widetilde{f} \simeq \overline{f} \times \overline{^{[\text{n}]}T_{\text{MF}} {}^{[\text{n}]}T_{\text{tel}}} \times {}^{[\text{nF}]}T_{\text{atm}}(\lambda_{\text{eff}}, z_F) \tag{7.26}$$

$$^{[\text{n}]}\widetilde{s} \simeq \overline{s} \times \overline{^{[\text{n}]}T_{\text{MF}} {}^{[\text{n}]}T_{\text{tel}}} \times {}^{[\text{n}]}T_{\text{atm}}(\lambda_{\text{eff}}, z) \, . \tag{7.27}$$

For the derivation of the atmospheric extinction that will be used to flux calibrate a given target X, the telluric component (that is still assumed constant) can be derived in the same way as for the photometric night, and we will use the ratios of fluxes from the secondary sources.

7.3.1 Photometric channel ratios

The *photometric ratio* of a certain secondary source in a specific filter of the MF, is defined as the ratio of its flux (7.24) when observed on both a photometric and non-photometric nights by the photometric channel

$$^{[\text{np}]}q_X(\lambda_{\text{eff}}) \triangleq \left\langle \frac{^{[\text{p}]}\widetilde{x}}{^{[\text{n}]}\widetilde{x}} \right\rangle \tag{7.28}$$

$$\simeq \frac{^{[\text{n}]}T_{\text{atm}}(\lambda_{\text{eff}}, {}^{[\text{n}]}z_X)}{^{[\text{p}]}T_{\text{atm}}(\lambda_{\text{eff}}, {}^{[\text{p}]}z_X)} \, , \tag{7.29}$$

where we are assuming that the overall transmission of the photometric channel $(\overline{T_{\text{MF}} T_{\text{tel}}})$ is stable between nights $^{[\text{p}]}$ and $^{[\text{n}]}$ (see § 8.6). We can rewrite (7.29) as

$$^{[\text{np}]}q_X(\lambda_{\text{eff}}) = \frac{^{[\text{n}]}T_{\text{atm}}(\lambda_{\text{eff}}, {}^{[\text{n}]}z_X)}{^{[\text{p}]}T_{\text{atm}}(\lambda_{\text{eff}}, {}^{[\text{n}]}z_X)} \times \frac{^{[\text{p}]}T_{\text{atm}}(\lambda_{\text{eff}}, {}^{[\text{n}]}z_X)}{^{[\text{p}]}T_{\text{atm}}(\lambda_{\text{eff}}, {}^{[\text{p}]}z_X)} \tag{7.30}$$

$$= \left[\frac{^{[\text{n}]}A_{\text{atm}}(\lambda_{\text{eff}})}{^{[\text{p}]}A_{\text{atm}}(\lambda_{\text{eff}})} \right]^{^{[\text{n}]}z_X} \times {}^{[\text{p}]}T_{\text{atm}}(\lambda_{\text{eff}}, {}^{[\text{n}]}z_X - {}^{[\text{p}]}z_X) \, , \tag{7.31}$$

since $T_{\text{atm}}(\lambda, z) \equiv A_{\text{atm}}^z(\lambda)$.

The differential atmospheric extinction term

$$^{[\text{np}]}\Delta A_{\text{atm}}(\lambda) \triangleq \frac{^{[\text{n}]}A_{\text{atm}}(\lambda)}{^{[\text{p}]}A_{\text{atm}}(\lambda)} \, , \tag{7.32}$$

---

[3]$\lambda_{\text{eff}} = \frac{\int \lambda \, x(\lambda) \, T_{\text{MF}}(\lambda) \, T_{\text{tel}}(\lambda) \, \mathrm{d}\lambda}{\int x(\lambda) \, T_{\text{MF}}(\lambda) \, T_{\text{tel}}(\lambda) \, \mathrm{d}\lambda}$

is *a priori* dependent on λ, however this chromaticity is weak, as can be seen by decomposing the atmospheric extinction in its physical components, where only aerosol scattering has a significant yet weak time-dependence. We can then approximate (7.32), by a smooth interpolating function between the i effective wavelengths of the different filters of the MF

$$^{[\mathrm{np}]}\Delta T_{\mathrm{atm}}(\lambda) \mathrel{\widehat{=}} \left[^{[\mathrm{np}]}\Delta A_{\mathrm{atm}}(\lambda)\right]^{[\mathrm{n}]z_X} \simeq \left\lfloor \frac{^{[\mathrm{np}]}q_X(\lambda_i)}{^{[\mathrm{p}]}T_{\mathrm{atm}}(\lambda_i, {}^{[\mathrm{n}]}z_X - {}^{[\mathrm{p}]}z_X)} \right\rfloor_{\lambda-\mathrm{interpolated}} . \qquad (7.33)$$

Finally the effective atmospheric transmission for target X in non-photometric conditions $^{[\mathrm{n}]}$ can be estimated using

$$^{[\mathrm{n}]}T_{\mathrm{atm}}(\lambda, {}^{[\mathrm{n}]}z_X) = {}^{[\mathrm{p}]}T_{\mathrm{atm}}(\lambda, {}^{[\mathrm{n}]}z_X) \times {}^{[\mathrm{np}]}\Delta T_{\mathrm{atm}}(\lambda) . \qquad (7.34)$$

Overall, if $^{[\mathrm{p}]}$ and $^{[\mathrm{p}']}$ are photometric nights (not necessarily the same), during which the supernova S and the faint standard star F were observed, we can flux calibrate the supernova spectrum

$$S(\lambda) = {}^{[\mathrm{p}]}\widehat{S}(\lambda) \frac{F(\lambda)}{^{[\mathrm{n_F}]}\widehat{F}(\lambda)} \times \frac{^{[\mathrm{n_F}]}T_{\mathrm{atm}}(\lambda, {}^{[\mathrm{n_F}]}z_F)}{^{[\mathrm{n}]}T_{\mathrm{atm}}(\lambda, {}^{[\mathrm{n}]}z_S)} \qquad (7.35)$$

$$= \frac{^{[\mathrm{n}]}\widehat{S}}{^{[\mathrm{n_F}]}\mathcal{F}_F} \frac{1}{^{[\mathrm{n}]}T_{\mathrm{atm}}(\lambda, {}^{[\mathrm{n}]}z_S)} , \qquad (7.36)$$

with the flux calibration spectrum

$$^{[\mathrm{n_F}]}\mathcal{F}_F(\lambda) \mathrel{\widehat{=}} \frac{^{[\mathrm{n_F}]}\widehat{F}(\lambda)}{\overline{F}(\lambda)} \frac{1}{^{[\mathrm{n_F}]}T_{\mathrm{atm}}(\lambda, {}^{[\mathrm{n_F}]}z_F)} , \qquad (7.37)$$

and

$$^{[\mathrm{n}]}T_{\mathrm{atm}}(\lambda, {}^{[\mathrm{n}]}z_S) = {}^{[\mathrm{p}]}T_{\mathrm{atm}}(\lambda, {}^{[\mathrm{n}]}z_S) \times {}^{[\mathrm{np}]}\Delta T_{\mathrm{atm}}(\lambda) \qquad (7.38)$$

$$^{[\mathrm{n_F}]}T_{\mathrm{atm}}(\lambda, {}^{[\mathrm{n_F}]}z_F) = {}^{[\mathrm{p}']}T_{\mathrm{atm}}(\lambda, {}^{[\mathrm{n_F}]}z_F) \times {}^{[\mathrm{n_F}\mathrm{p}']}\Delta T_{\mathrm{atm}}(\lambda) . \qquad (7.39)$$

7.3.2 The gray hypothesis

Since, as already seen, $\Delta T_{\mathrm{atm}}(\lambda)$ (7.32) is only weakly dependent on λ, we can constraint it even further than in (7.33) if we assume the *gray hypothesis*: approximating it by an (achromatic) constant which can be estimated from a single filter λ_{eff} of the MF

$$^{[\mathrm{np}]}\Delta T_{\mathrm{atm}}(\lambda) \simeq {}^{[\mathrm{np}]}\Delta T_{\mathrm{atm}}(\lambda_{\mathrm{eff}}) = \frac{^{[\mathrm{np}]}q_X(\lambda_{\mathrm{eff}})}{^{[\mathrm{p}]}T_{\mathrm{atm}}(\lambda_{\mathrm{eff}}, {}^{[\mathrm{n}]}z_X - {}^{[\mathrm{p}]}z_X)} , \qquad (7.40)$$

which is equivalent to assume that the differential atmospheric extinction between conditions $^{[\mathrm{n}]}$ and $^{[\mathrm{p}]}$ from different nights is *a*chromatic

$$^{[\mathrm{n}]}T_{\mathrm{atm}}(\lambda, z) = {}^{[\mathrm{np}]}g \, {}^{[\mathrm{p}]}T_{\mathrm{atm}}(\lambda, z) , \qquad (7.41)$$

and

$$^{[\mathrm{np}]}\Delta T_{\mathrm{atm}}(\lambda) = {}^{[\mathrm{np}]}g . \qquad (7.42)$$

This is the current implementation of the flux calibration pipeline of SNfactory: we place ourselves on the gray hypothesis over different nights, and an extinction template is used, together with the photometric ratios from F2 on the non-photometric nights. The next step on the implementation of the proposed calibration scheme is under development (Buton 2009): the gray hypothesis requirement is limited per single night, for which an extinction template is calculated, using all the available standard stars.

Chapter 8

Photometric channel calibration

The only uniform CCD is a dead CCD.

Craig Mackay

Each raw science image issued from the photometric channel of SNIFS must be calibrated, so that we are able to flux-compare exposures taken at very different epochs.

In this chapter I'll detail some steps of this calibration and the problems associated to it.

8.1 Pickup noise

The images made using the photometric channel have a distinct incoherent pickup noise structure. This "herring-bone" pattern noise (Fig. 8.1a) is particularly visible on short exposures or bias images. It adds to the typical shot and readout noises, manifesting itself as a "tail" of a few tenths of photo-electrons (Fig. 8.1b), on the otherwise gaussian noise distribution.

(a)   (b)
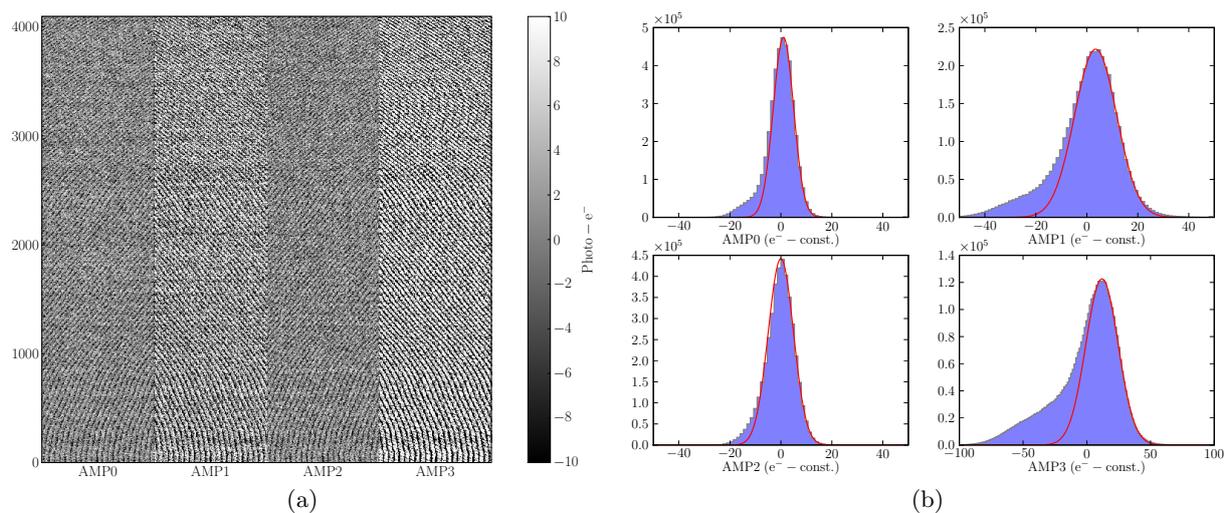
Figure 8.1: Pickup noise pattern (a) on a bias exposure from the middle of 2005 and (b) pixel distribution histograms per amplifier. The red line is a gaussian fit to the histogram peak, representing the readout noise distribution.

Since this tail is always present in the lower part of the distribution, it means we are measuring lower counts than expected from a simple gaussian readout noise, in a large number of pixels. The pattern is symmetrically-correlated between each of the amplifiers of each CCD, and between CCDs, which points to a noisy common component, somewhere in the electronics chain responsible for the readout, amplification and analog-to-digital conversion of the CCD accumulated charges (power supply, cablings, video boards, *etc*).

The pickup pattern has an intrinsic spatial frequency, which is a combination of the readout frequencies of the CCD serial and parallel registers and possibly some other unknown component, like an AC-like frequency, and is modulated in amplitude. This frequency and amplitude changes make the pattern different even on two consecutive images. That makes it possible to stack multiple images to average it out (on bias images without any objects), but on the other hand prevents us from creating a reference subtraction mask. The other possible approach is then frequency-space analysis.

A tentative approach using an FFT procedure developed for the HST STIS spectrograph (Jansen et al. 2002), led to some promising results (Fig. 8.2a), but was abandoned due to one important reason: the image for detection of the pattern must be completely empty of bright objects. While this is possible with a bias image, it is not practical on any of the science exposures, for which we cannot produce "data models".
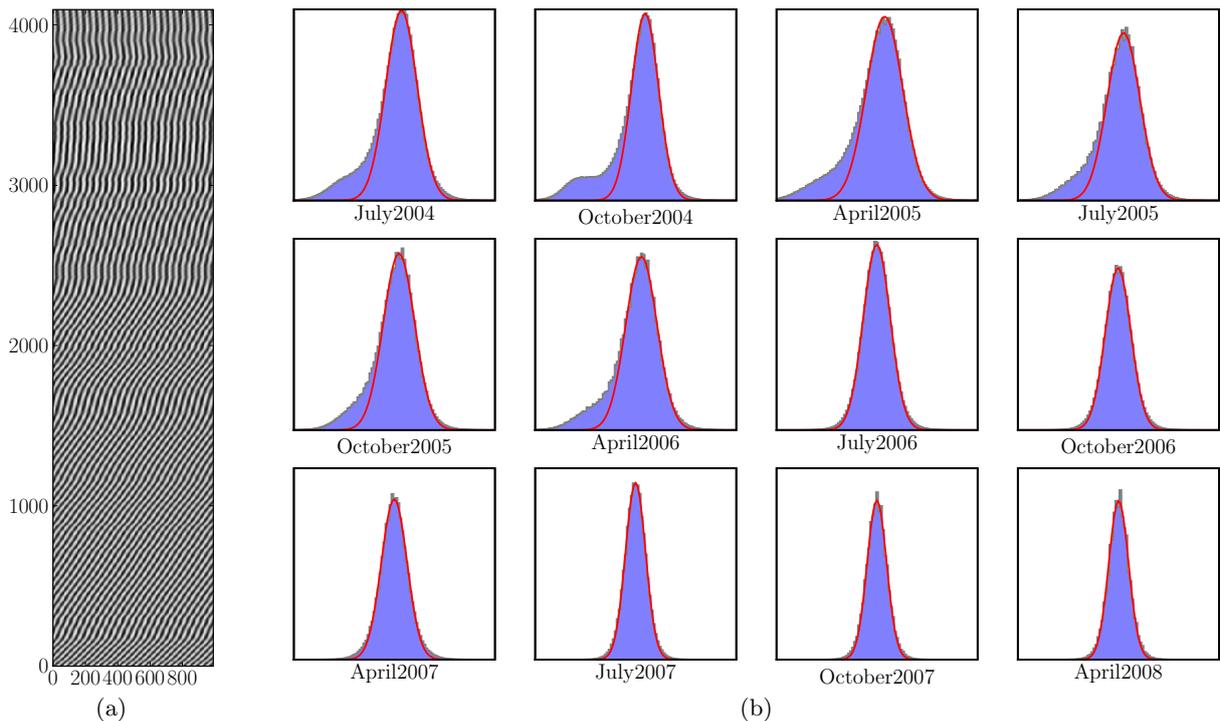
Figure 8.2: (a) "Herring-bone" noise pattern extracted by the Jansen et al. (2002) procedure; (b) Pickup noise evolution for AMP1 (second amplifier of the science camera). The X axis range is the same as in Fig. 8.1b.

During the Hawaii intervention in June 2006, a swapping of power supplies considerably reduced the noise (almost completely in the science CCD) for all the data since then (Fig. 8.2b). Due to this improvement and to the fact that the effective value of the noise is quite small (~ 30 photo-electrons), making it negligible when compared to the sky/objects flux on the pre-2006

science exposures, it is left as-is in the rest of the calibration chain, without any correction applied.

8.2 Flat fielding

In a CCD, each pixel has a slightly different gain and quantum efficiency value when compared with its neighbors. In order to flatten the relative response of each pixel to the incoming radiation, a flat field image is traditionally used. This image is obtained by observing an uniformly lit field, which is usually either the interior of the dome (a dome flat) or the twilight sky (sky flat), and is ideally spectrally and spatially flat. Such (normalized) image is then used to divide the (same night) science exposures to remove the pixel-to-pixel gain and quantum efficiency variations.

There are three kinds of flats that can be obtained using the photometric channel:

Dome flats taken during the day shifts, by illuminating the interior of the dome with a spectral lamp attached to the telescope tube, and whose intensity can be controlled remotely. In 2005 (night 114[1]), a special reflective screen was installed in the dome and started to be used for the dome flats, in order to improve the flux in the bluest part of the spectrum. Unfortunately it was shredded due to high winds in the beginning of 2006 and never replaced, obliging to go back to standard dome flats. Since the advent of full night shifts, US0/3 takes dome flats pointing at two different areas of the dome, whose reflected spectrum is slightly different even at the same lamp intensity;

Sky flats which started to be acquired on night 141 of 2005. A special script is used, which adjusts the exposure time in order to compensate the continuously changing sky brightness during dusk or dawn twilight, and obtain a stable number of counts throughout the run;

Super flats are obtained by a median filtering of spatially offseted exposures of the night sky, in order to remove the stars. Since the switch to full nights, SNIFS observes at least 10 different fields (with large exposure time) per night, so super flats can be obtained easily.

The "final" flat field image for each of the cases is usually a median stack of all the single exposures. In Fig. 8.3 are represented each of the flat field cases for a night in the end of 2007.

The first thing one notices is the huge non-uniformity of the flats, especially in the filters closer to the borders. These gradients, which can amount to more than a 10% difference in the received flux throughout the surface of a single sub-filter (Table 8.1), are due to extra light that attains the CCD (§ 8.3), and unfortunately make the flats useless for their intended purpose: by dividing a raw exposure by one of these flats, we would not be correcting for inter-pixel gain variations, but instead "masking" an additive component of the flux, by normalizing instead of subtracting it as an extra background. We can also remark the different patterns in F1 between the dome and the other flats: the almost nonexistent flux in the bluer part of the dome spectrum (Fig. 8.3d), with relation to the sky and night spectra, makes it susceptible of light leaks from the adjacent filters in the dome flat. On the other flats, however, we can see a "grid" pattern coming from the fact that the smaller wavelength photons are absorbed near the surface of the CCD. On the super flats (Fig. 8.3c) we can also see the presence of fringing patterns in the redder filters (§ 8.3.3).

---

[1]The main temporal unit used when dealing with SNIFS events, is the night number counting from the 1st of January of each year.
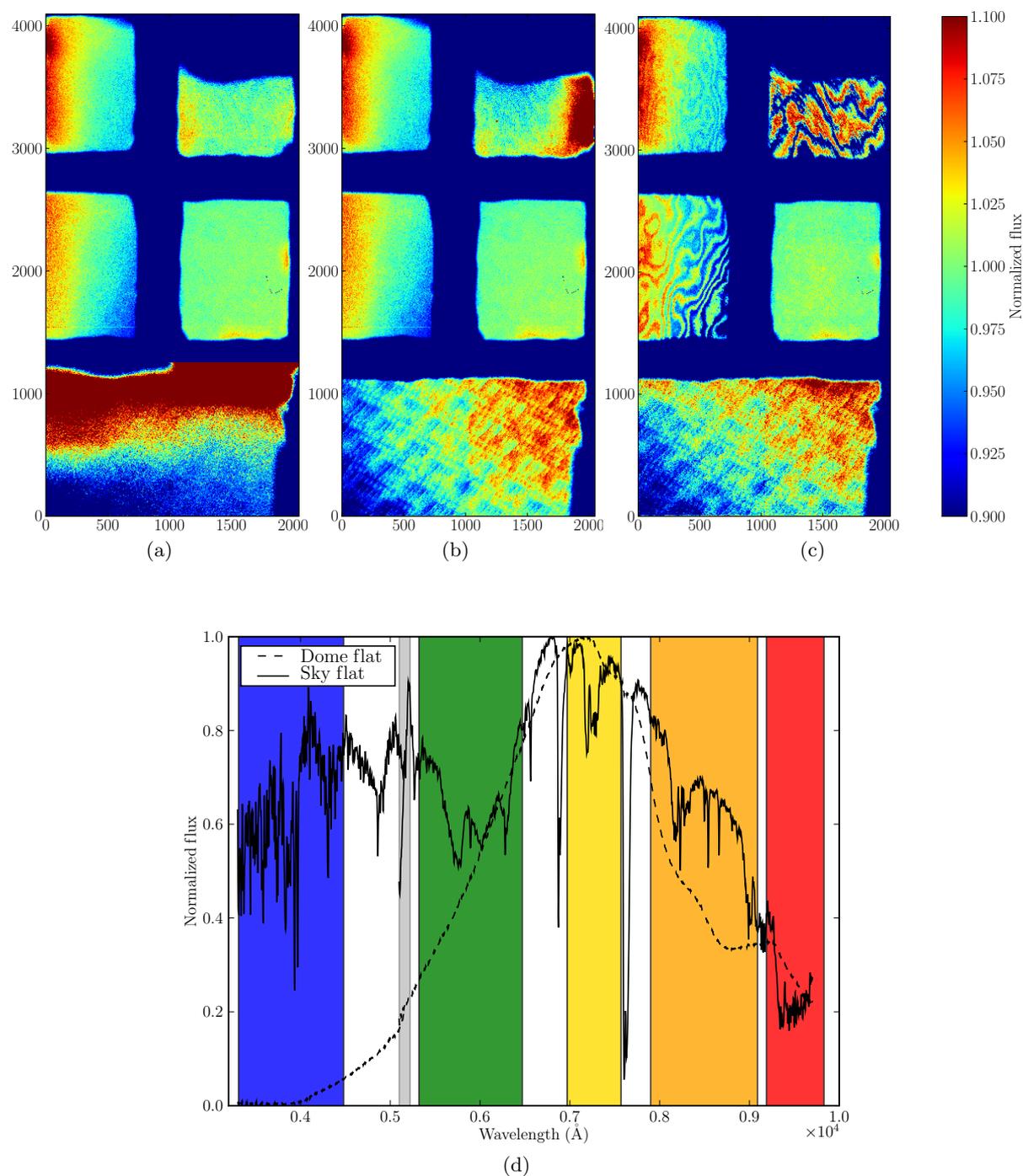
Figure 8.3: Three different MF flat fields for the same night (07_320) created by median stacking several independent exposures: (a) dome, (b) sky (twilight) and (c) super flats. Each filter from the MF is normalized independently. (d) represents the normalized typical spectra of a dome flat (from the dome lamp) compared to a sky flat (a sun-like spectrum). The colored shaded areas represent the wavelength span of each MF filters F1 through F5, whilst the gray one represents the dichroic transition from the B to R channels.

	F1	F2	F3	F4	F5
Dome flat	0.180	0.010	0.032	0.032	0.018
Sky flat	0.045	0.011	0.033	0.032	0.044
Super flat	0.049	0.012	0.036	0.042	0.074

Table 8.1: Normalized flux RMS for the flats present in Fig. 8.3, in each filter of the MF.

8.3 Extra light and light leaks

The extra light present in the MF flats may have several possible origins:

- it is passing between the filter support and the filter wheel, being thus *unfiltered*;

- it is due to a non-uniform coating of the filters;

- it is due to reflections somewhere inside SNIFS or on the border of the filter support, before or after being filtered;

- it is leaking from a nearby filter.

| (a) | (b) |
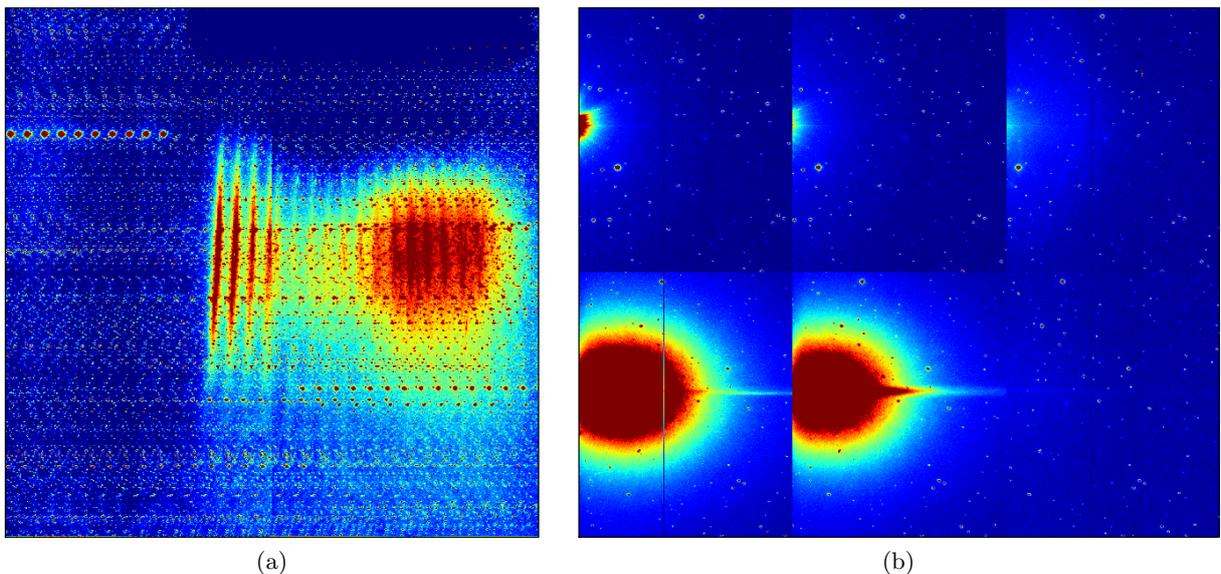
Figure 8.4: (a) Stack of all the images from the scan of the enlarger (whose shadow can be seen on the top) made with a bright star. The abnormal reflection glow, over 3 of the amplifiers of the photometric camera, is due to the successive reflections of the star on the enlarger; (b) Sequence of 6 images (left-right, top-bottom) of a scan using a star which is moved towards the outside of the CCD. Right after the star leaves the field (3rd image) and crosses the edge between the filter and its support, a very strong halo appears (4th image), due to a reflection outside of the CCD FOV.

A closer look at the flats seems to rule out the first case: if one was to assume that unfiltered light was leaking and attained the borders of the CCD, that would mean that we should see a "border pattern" with a flux value independent of the filtered light, which is not the case (F1 has no obvious leak on the left side, and non-normalized flat fields do not present any constant "leaky" border effect). We can also confirm the second hypothesis: it explains the isolated "hot

spots" in the middle of the right and bottom borders of F2 and the right border of F5, seen *e.g.* in Fig. 8.3a.

To test the third hypothesis, two simple experiments were made, where a bright star was placed over the enlarger location and near the edge of the CCDs and its position successively shifted, in order to scan respectively, reflections on the enlarger and on the transition between the filter and its support. The results confirm clearly both of the areas as origins for extra light in the CCD: Fig. 8.4a stack shows the huge reflection pattern created by the enlarger, whereas on the sequence of Fig. 8.4b we can see the light halo that appears right after the star leaves the FOV of the CCD. The X displacement between the first and forth images of the sequence is equivalent to a 4.5mm displacement over the CCD, meaning that the reflection origin is very close to the border of the CCD – the transition between the filter and its (metallic) support.

While the reflection due to the enlarger has been properly masked during a SNIFS intervention (§ 8.3.1 and Fig. 8.5), the border reflections were never completely solved and represent the most important source of extra light on F3 and F4, as can be seen by the halos present near their left edges.

The last hypothesis is confirmed by the (already mentioned) case where the flux passing through F1 in the dome flats is very low, and all the detected light in that area is coming from the nearby F2 and F4 filters. Furthermore, using filtered dome flats (Fig. 8.5) to limit the dome lamp spectrum to a single filter of the MF, one can see a large halo light that affects the surrounding filters, although at a very small scale (lower than 0.5%).
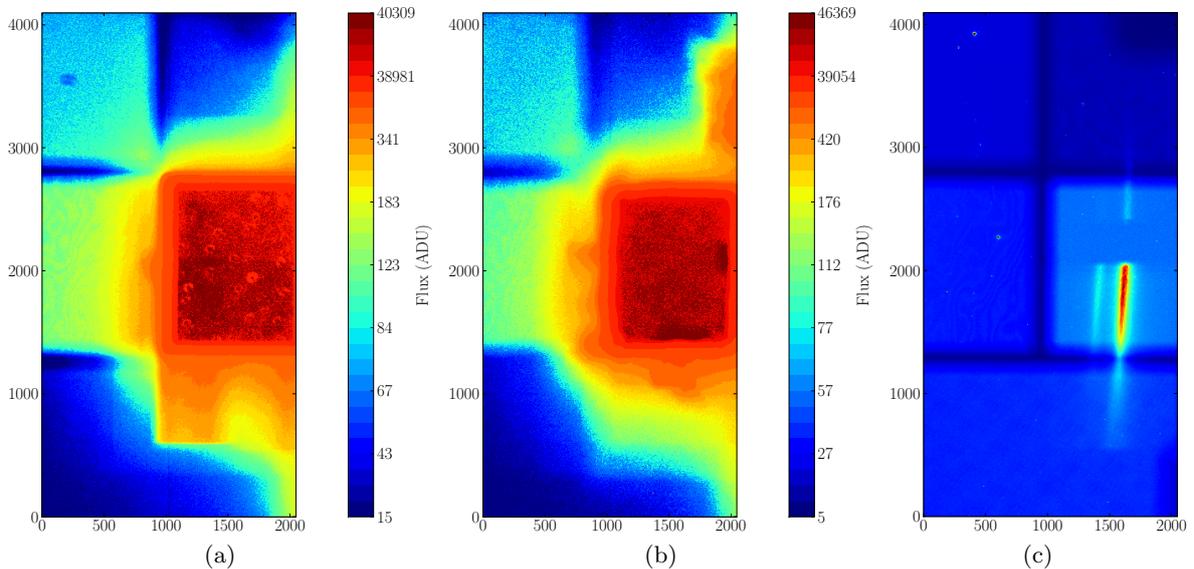
Figure 8.5: Filtered dome flats using a narrow band filter with effective wavelength ~ 5500Å (close to F2): (a) is a median stack of multiple exposures taken during the June 2006 SNIFS intervention, where the square reflection due to the enlarger is clearly seen (the light coming at an angle with relation to the filters plane, crosses F2 and "illuminates" the area of F1), in contrast with (b), the stack made in September 2006, where the enlarger was already properly masked. A large halo of leaked light from F2 can be seen all around the filter, although its flux is weak – notice the non-linearity of the flux scale. (c) MF exposure of the field around the standard star HZ21: a very bright star which falls exactly on the enlarger produces a reflexion over F2, which disappears completely on exposures taken after the SNIFS intervention.

The sources of extra light on the photometric channel are then, by order of importance, the reflexions on the filter borders, non-uniform coating of the filters and leaking from nearby filters. All of these cases will be obviously more extreme on the case of the uniform flux flat fields, than with the science exposures, and as seen before, that makes the flat fields useless for their main intended purpose (high frequency pixel-to-pixel response uniformization).

Such low frequency "extra" flat should not pose a problem to the science exposures, in the sense that we expect it to be relatively stable between nights and the same star flux will be measured at the same location, to a few pixels difference. Besides, in their case the extra light will be dealt with by the fringing correction procedure (§ 8.3.3), as well as the background subtraction part of the image processing pipeline (§ 9.2.4). However that still leaves us with the inter-pixel response variation unaccounted for. No method has yet been devised to try to recover that information from the flat fields, *e.g.* using the "defringing" procedure also on the flats. Such effect is thus not corrected for the moment, but its impact is expected to be very small if not negligible, in the output images of the photometric channel.

8.3.1 Hawaii intervention

During the SNIFS intervention on June 2006, in which I took part, special care was taken to try to minimize the extra light problem, notably by covering all the reflective metallic components in the light path and effectively baffling the entry of SNIFS. A swapping of power supplies for the readout video boards of the photometric channel was also performed, in order to reduce the pickup noise.

Figure 8.6: Working inside the UH88 tube. The baffling of SNIFS was made by covering different internal components using a black felt-like paper, and tested by making consecutive exposures using the photometric channel, controlling SNIFS directly from inside the tube.

The efficacy of the baffling to reduce the reflected light has already been shown on the filtered dome flats (Fig. 8.5b), and can be further seen in the case of the field of the standard star HZ21, where a bright star falls on top of the enlarger, and whose reflexion disappears on exposures

taken after the intervention (Fig. 8.5c). Nonetheless, the border reflexions, although partially attenuated on this and subsequent interventions, were never completely solved.

8.3.2   Moon

Due to the fact that SNIFS is used throughout all the month, with no stopping even on bright time (when the moon phase is close to full), it is clear that the presence of this extra source in the sky will pose further issues to the light leaks control. Indeed, and despite the fact that the observation schedules are made in such a way to prevent observation of objects too close to the moon, there are a fair amount of exposures where the photometric channel is highly affected by the moon if it is close-by: rectangular patches with larger than normal background counts are visible in each sub-filter of the MF. The shadows of the MF support and the slightly off-axis position of the moon with relation to the object being observed, create a non-uniform illumination with some very sharp transitions (Fig. 8.7), which will be an issue for the background estimation routine later on in the pipeline (§ 9.2.4).
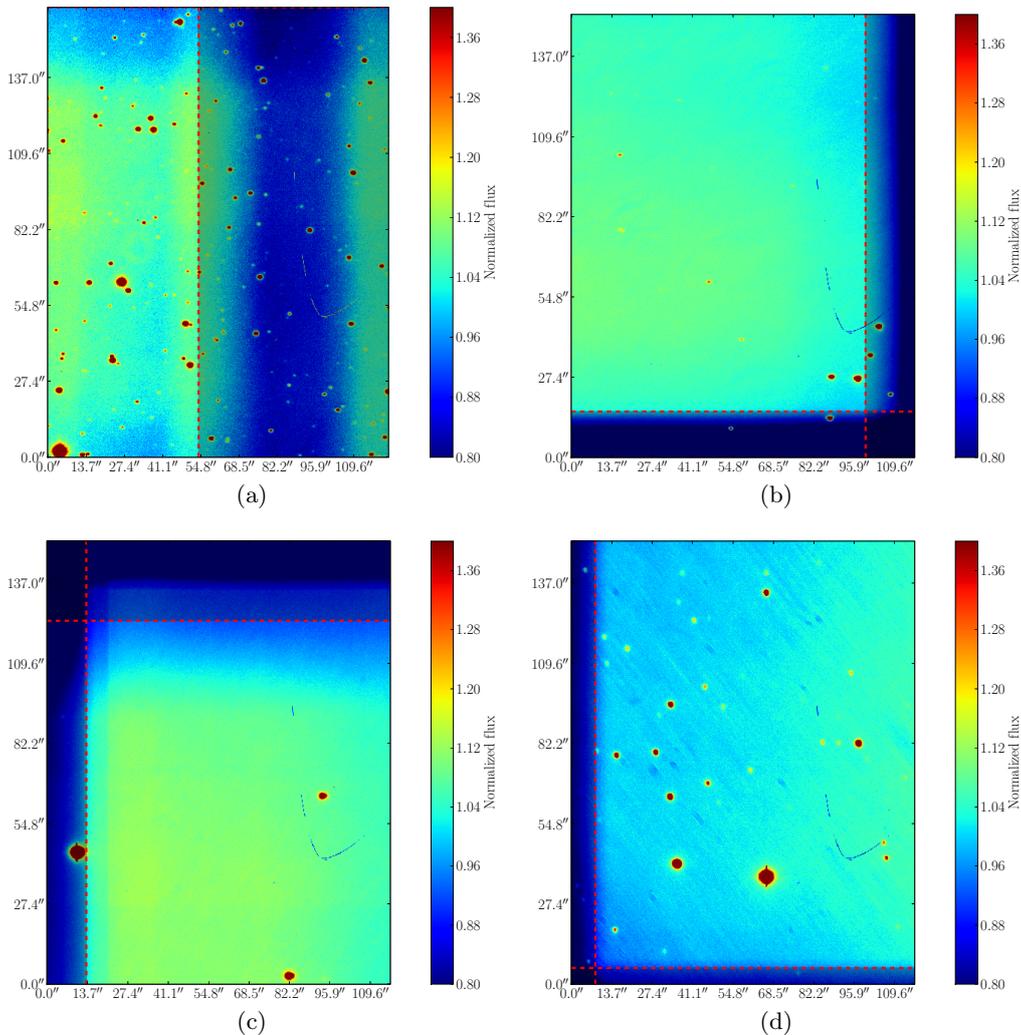
Figure 8.7: Results of the automatic moon "border detector" on F2 for the four different cases: (a) $[+,+]$, (b) $[+,-]$, (c) $[-,+]$ and (d) $[-,-]$. The kept part after the cut is defined by the red dashed lines.

To mitigate this problem, an automatic routine was implemented in the image processing part of the pipeline. It analyzes the raw exposures and tries to identify the borders that delimit the "good" area, where the background due to the moon is most uniform and can be best subtracted, and then cuts accordingly.

The procedure is the following: the image array (with the stars masked) is summed in the right ascension (RA) and declination (DEC) directions, and each one of them convolved with a step function (an $[1, 1, \ldots, -1, -1]$ Heaviside-type function). The maximums of the convolved array are then identified, based on some *a priori* about the relative position of the moon[2], to give the estimated positions where the cut should be made.

This approach is not optimal, in the sense that it may fail to find the borders or find false positives, and is affected by other sources of extra light, especially in the external sub-filters. It was tested in a group of ~ 200 images of F2, F3 and F4 for objects observed closer than $30°$ of the moon: about 75% of the images were correctly handled, either by not cutting when no sharp borders are present, either by selecting the correct area for cutting. Although this far from perfect efficacy, it helps nonetheless to minimize the problem of the moon, on otherwise useless exposures. Fig. 8.7 shows the results of this procedure on four different cases for F2.

8.3.3 Fringing

Another source of extra light on the redder filters of the MF are the fringes, an interference pattern (essentially Newton's rings) between light waves that reflect within the CCD, or long wavelength light that passes through the array and is reflected back. They are due to the strong narrow emission lines of the night sky in the redder part of the optical spectrum, whose intensity will change from night to night or even during the same night. In the case of MF science exposures, fringing patterns are visible on F4 and F5 (and more faintly on F3).

`poloka`'s (*cf.* § 9.1) defringing implementation is based on a principal components analysis (PCA). In brief, a PCA may be thought as a way to identify patterns in data, and express the data in such a way as to highlight their similarities and differences. For this, super flats were created for every dark (no moon) night with SNIFS observations of at least 5 different fields. Around 200 flats were created accounting for data until mid-2007, cutted into the 5 sub-filters and separated according to the different epochs between interventions. The PCA is performed in each of these subsets: a $n \times n$ covariance matrix is created from the n images, where each entry is the scalar product between each pair of images. The matrix's eigenvalues are calculated, the corresponding normalized eigenvectors images created, and the fringes isolated as the main eigenvectors of the created basis (Fig. 8.8). During the defringing process, each of the fringes map of the appropriate subset will be properly renormalized and subtracted from the raw image.

The created fringes maps will also contain extra light due to the already explained cases of light leaks. In this sense, the defringing procedure will also accomplish a further background subtraction. That is why all raw images from sub-filters of the MF are "defringed", even though typically they do not present fringes. Fig. 8.9 shows the result of the defringing procedure on a crowded field exposure.

---

[2]Four cases are possible, depending on the relative positions on the sky of the moon and target: $[+, +]$, $[+, -]$, $[-, +]$, $[-, -]$ for positive/negative $[\Delta RA, \Delta DEC]$, with $\Delta = $ target $-$ moon.
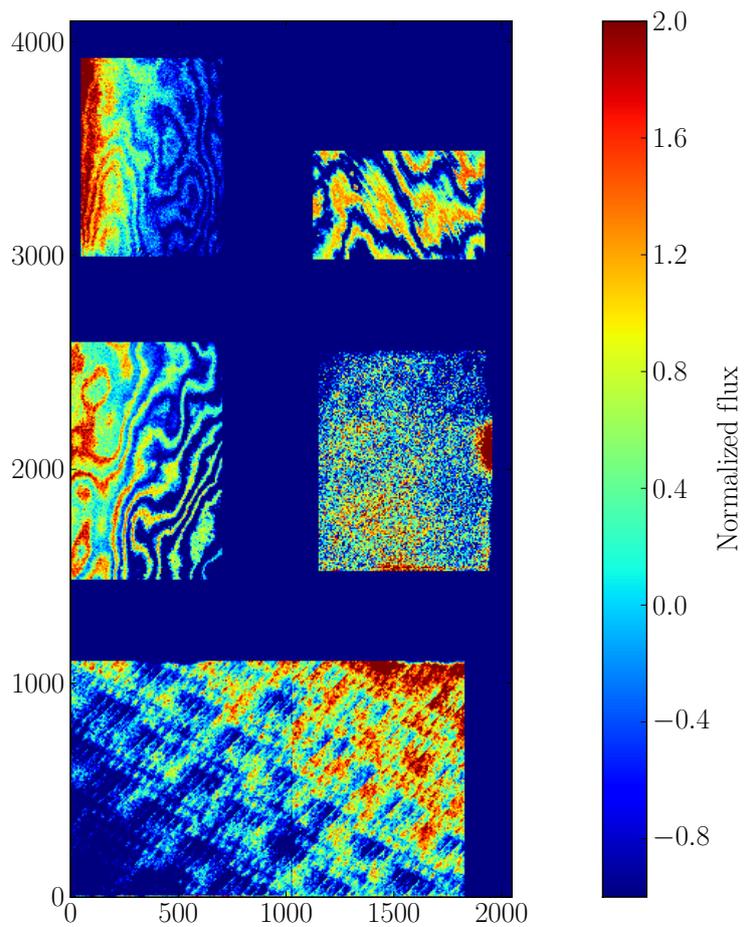
Figure 8.8: Fringes map for each of the sub-filters of the MF, for the epoch $\mathcal{E}$. Besides the fringe interference patterns visible on F3 through F5, extra background gradients due to light leaks are visible on all the filters.
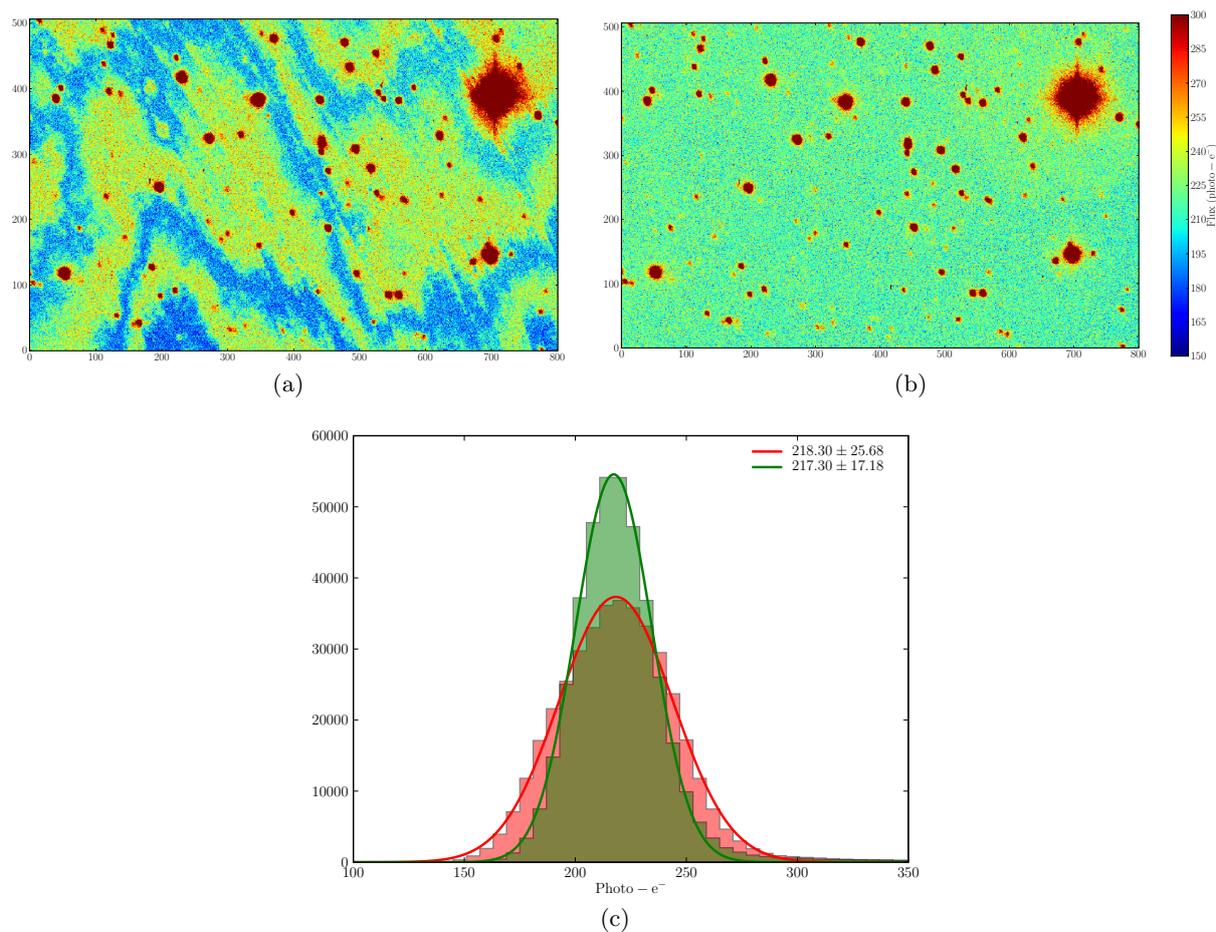
Figure 8.9: (a) F5 image of EG131, with visible fringes whose amplitude is $\sim 25\%$ of the background value; (b) the same F5 exposure after defringing, showing an uniform background without the fringing spatial pattern; (c) Background pixel's distribution before (red) and after defringing (green). Notice the reduced RMS (up to near poissonian noise levels), after the removal of the fringes.

8.4 Shutter latency

Due to the way the main shutter of SNIFS opens (Fig. 8.10), parts of the photometric channel CCDs will have a slightly bigger exposure time when compared to the rest. While this sub-second increased exposure time will be negligible on long exposures, it will be important for very short exposures of a few seconds, which is the case for the HR/HD standard stars or some flat fields.
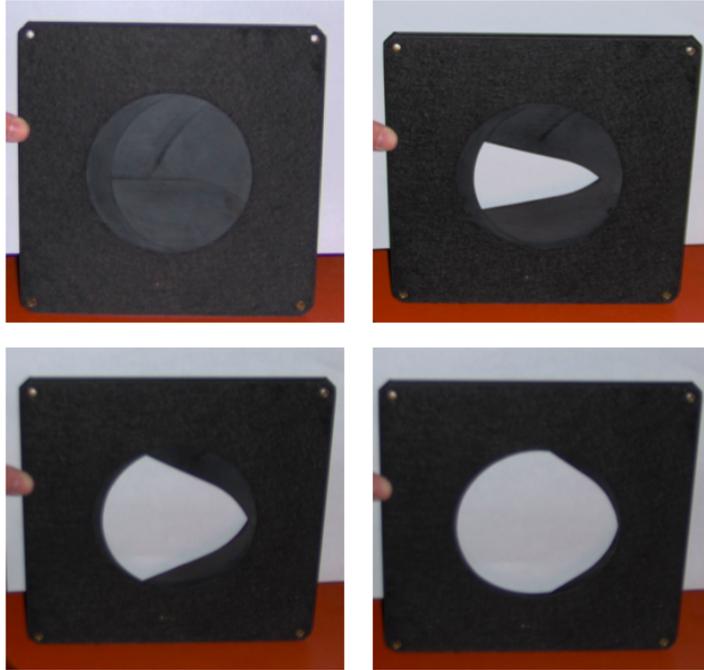
Figure 8.10: Shutter opening sequence. The four "petal-like" components open in such a way, that the resulting extra illumination map will be quite different from the radial ones (more illuminated at the center than at the borders), typically created by an iris diaphragm.

We thus want to model this illumination component, in terms of a extra exposure time map of the P channel CCDs. Let $[\alpha, \beta]$ be bias-corrected and median-stacked dome flats on a specific filter, with different exposure times $t_{[\alpha,\beta]}$. The number of photo-electrons per pixel ij will be

$$[\alpha, \beta]_{ij} = n_{ij} \, g_{ij}(t_{[\alpha,\beta]} + \delta t_{ij}) \; , \tag{8.1}$$

where n_{ij} is the number of measured ADUs[3] per pixel per time unit (directly connected to the dome lamp flux), and g_{ij} the gain (*cf.* § 8.5) of each pixel. δt_{ij} is the 2D map of the extra exposure time due to the shutter latency. Being α and β respectively high and small exposure time flat fields, and assuming that the dome lamp flux, the pixel gain map and the shutter latency time are constant during the period in which α and β are taken, we have

$$\delta t_{ij} = \frac{\beta t_\alpha - \alpha t_\beta}{\alpha - \beta} \; . \tag{8.2}$$

This approach was applied to data from the night 08_178: a sequence of V flat fields with the same dome lamp intensity and two exposures times, 50 and 1 seconds. Each group was

---

[3]One ADU or Analog/Digital Unit, corresponds to one resolution unit of the analog to digital converter used to digitize the CCD signal. These are the units used when we are referring to "raw" image counts.

overscan-subtracted and median stacked ($t_\alpha = 50.007$s and $t_\beta = 1.007$s). The resulting δt_{ij} latency map obtained using (8.2) is shown in Figure 8.11a, from which we can see that, for a small (1s) exposure, certain parts of the CCDs will measure $\sim 10\%$ more flux when compared with the borders. A smooth model (Figure 8.11b) was also derived by fitting each column of the latency map by a 5th order polynomial and convolving the result by a median filter with a box 30 pixel wide.

(a)   (b)
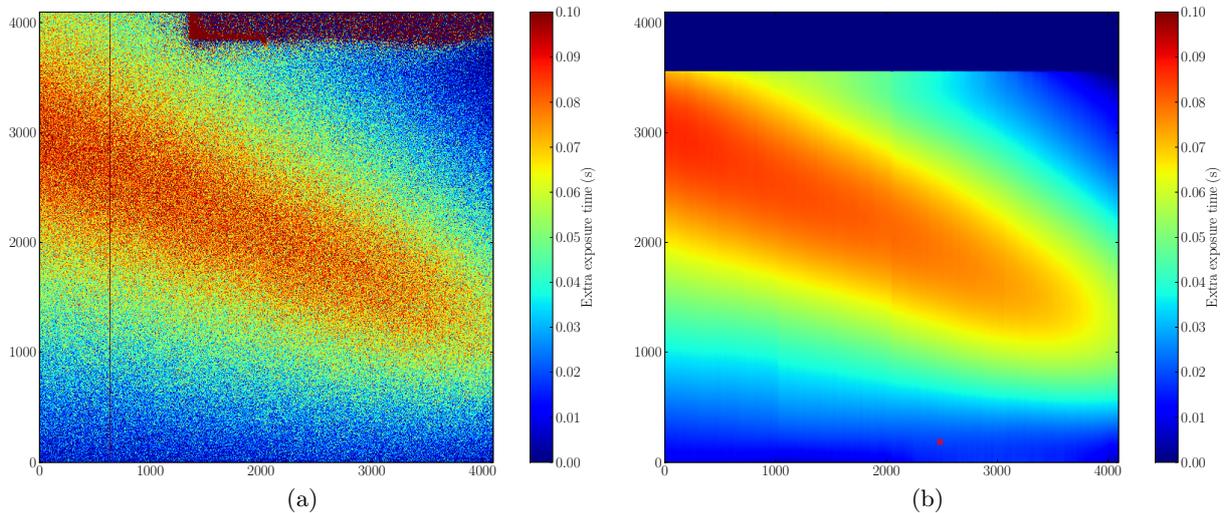
Figure 8.11: Shutter latency map (a) and smooth model (b). One can clearly see the overexposure diagonal pattern, due to the asymmetric opening sequence of the shutter (which is not mounted parallel to the CCDs). The enlarger shadow was masked on the latency model, and the MLA area is represented as a red square.

Assuming that the latency map δt_{ij} remains constant in time[4], it can be used to correct any exposure γ by simply doing

$$\gamma'_{ij} = \frac{\gamma_{ij}}{t_\gamma + \delta t_{ij}} t_\gamma \ . \tag{8.3}$$

The correction was tested on a stack of five V flat fields with average exposure time 1.0035 s, from night 07_243, and the results are shown in Figure 8.12. We can see that the overexposure pattern disappears completely after being corrected by the latency model. The remaining extra light on the borders is due to light leaks (§ 8.3) on the filter support.

This latency model can also be used to calculate the necessary correction on the exposure time for very short exposures of bright HR/HD standard stars. A first analysis done in 2005 was only using the center of the guiding CCD to estimate the shutter latency, and didn't reflect its value at the POP position. Measuring the mean δ_{ij} on the latency model around the POP position (2485,185), the obtained value with this approach is 0.0192s, in agreement with what is obtained when comparing flux calibrated short and long exposure standard stars: 0.0197$\pm$0.004s.

8.5   Gain variation

The gain of a CCD is set by the readout electronics and determines how the accumulated charge in each pixel will be converted to a digital number (ADU) in the output image. Each of

---

[4]A quite strong assumption, which is tested on an yearly basis using V dome flats special runs, available since 2006. A 2008 check is still to be done.
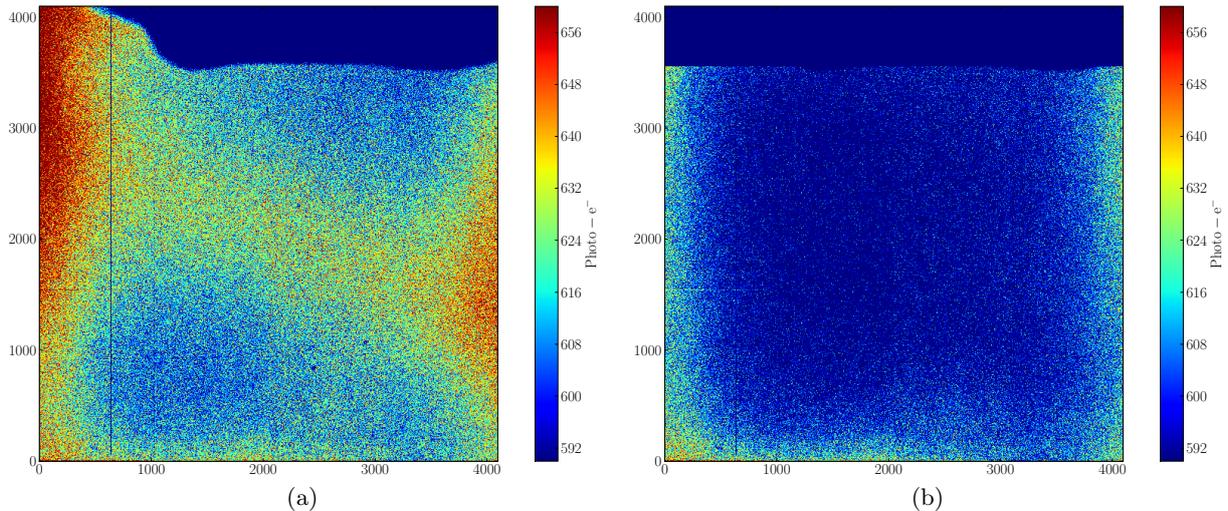
Figure 8.12: Stack of 1 second flat fields (a) before and (b) after correction using the latency model.

the four pre-amplifiers of the photometric channel (two per CCD chip) has an independent gain setting, defined by a conjugation of their intrinsic (by construction) gain and the settings of the video boards.

The gain values for the photometric CCDs that were measured in the laboratory prior to the assembly of SNIFS, using ^{55}Fe X-ray sources, are listed in Table 8.2. These are the values that are used during the preprocessing stage of the image processing pipeline (*cf.* § 9.2), to transform the raw image counts in ADU into the received photo-electrons, and are assumed has a reference value prior to calibration of the photometric channel.

AMP0	AMP1	AMP2	AMP3
1.618	1.576	1.510	1.520

Table 8.2: Measured gains (e^-/ADU) for the photometric channel CCDs using ^{55}Fe X-ray sources.

An hypothetical absolute or relative (between pre-amplifiers) variation of the gain with time, may lead to inaccuracies in the measured flux, when comparing observations of the same object which are several months or years apart. We have thus the interest in finding a way to properly monitor any possible gain variations.

8.5.1 Gain determination

The method for determination of the gain is based on the one proposed by Janesick (2001), which uses uniform flat fields and the fact that at high flux levels (S_{ADU}) the shot noise ($\sigma_{S_{\mathrm{ADU}}}$) due to photon statistics dominates over the readout noise of the CCD, satisfying

$$S_{\mathrm{ADU}} \equiv \frac{N_{e^-}}{\mathcal{G}} \tag{8.4}$$

$$\sigma_{S_{\mathrm{ADU}}} = \frac{\sqrt{N_{e^-}}}{\mathcal{G}} \, , \tag{8.5}$$

and hence the gain can be calculated using

$$\mathcal{G} = \frac{S_{\mathrm{ADU}}}{\sigma^2_{S_{\mathrm{ADU}}}} \ . \tag{8.6}$$

To avoid large scale flux variations in the flat fields, and pixel-to-pixel non-uniformities of the gain, pairs of exposures taken at the same flux level are used. In this approach, we will then have

$$\mathcal{G} = \frac{\overline{F_1} + \overline{F_2} - (\overline{B_1} + \overline{B_2})}{\sigma^2_{\Delta F} + \sigma^2_{\Delta B}} \ , \tag{8.7}$$

where $\overline{F_i}$ is the mean counts measured on each flat field exposure, $\overline{B_i}$ the mean bias level, and $\Delta[F, B] = [F, B]_1 - [F, B]_2$. In our case, we will be using (binning 1) V dome flat fields with corresponding bias level measured on the overscan strips of each image.

8.5.2 Absolute variation and correlation with flux

Each sequence of dome flats taken by SNIFS is composed of three exposures, hence measurements of the signal and variance will be made for the 3 different combinations of pairs of images and their mean used to estimate the gain. The results of the gain determination on the photometric science CCD (amplifiers 0 and 1) since the beginning of 2006 up to mid-2008 are shown in Table 8.3 and Fig. 8.13a.

Epoch	AMP0	AMP1
January – June 2006	1.614 ± 0.006	1.550 ± 0.007
September 2006 ↓	1.630 ± 0.006	1.568 ± 0.003
March 2007 ↓	1.620 ± 0.014	1.552 ± 0.014
June 2007 ↓	1.614 ± 0.006	1.546 ± 0.007
March 2008 – present	1.614 ± 0.006	1.546 ± 0.006
2006–2008	1.615 ± 0.009	1.548 ± 0.010

Table 8.3: Median gain values and associated MAD (Median Absolute Deviation) for the two amplifiers of the photometric channel science CCD.

Despite the fairly accurate value obtained for the gain on the ensemble of the epochs compared with the tabulated values measured in the laboratory, it is clear that if we look at each epoch individually the gain value seems to change by a considerable amount: between September 2006 and March 2007, its value differs by $\sim 1\%$ from the median gain. Apart from a possible correlation with the CCD temperature (which was tested and is non-existent), the other external parameter that can present fluctuations with time is the dome lamp flux, either due to aging, due to the different reflexion properties of the dome in the evening *vs.* morning dome flat positions, or simply due to the consecutive changes of the dome flats acquisition scripts with different flux selections. By plotting the measured gain *vs.* the mean accumulated flux per pixel (Fig. 8.13b), it is clear the existence of a correlation between gain and flux.

The observed correlation is basically a measurement artifact, and not really a gain change. Downing et al. (2006) identified a similar problem while characterizing E2V 44-82 CCDs (the same used in SNIFS photometric channel), which present a non-linear photon transfer curve (variance *vs.* signal in ADUs) while having a perfect linearity (counts/second *vs.* signal). A. Sørensen[5] observes the same behavior on the E2V 44-82 CCD from DFOSC at the Danish telescope.

---

[5] http://www.astro.ku.dk/~ijaf/ccd/ringo.ps.gz
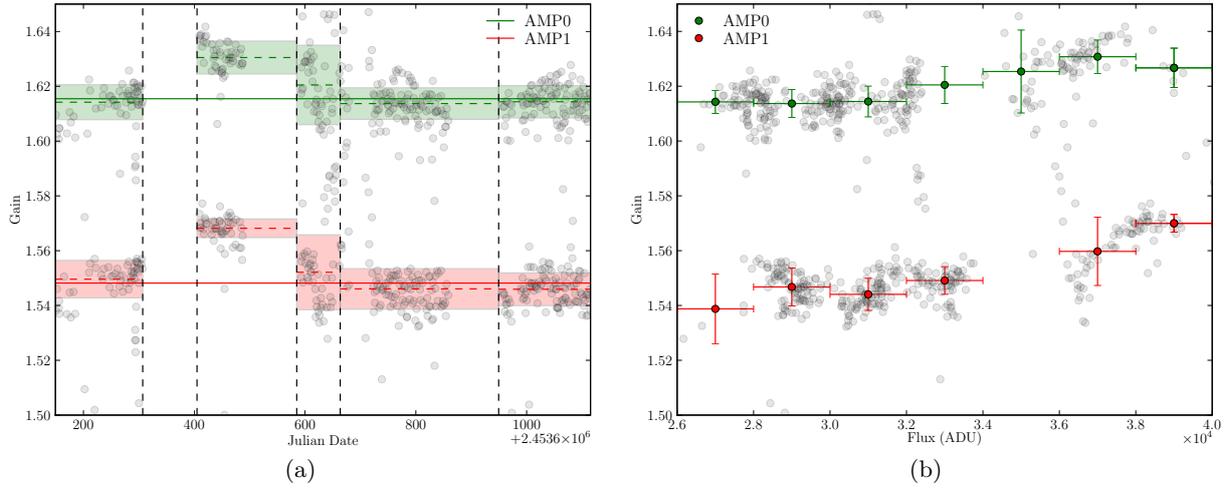
Figure 8.13: (a) Median gain (horizontal dashed line) and MAD (shaded area) for both amplifiers of the photometric channel science CCD, for different epochs. The vertical dashed lines correspond respectively to: June 2006, September 2006, March 2007, June 2007 and March 2008; (b) Gain correlation with mean flux.

A sequence of V flat fields, with increasing exposure time and the same fixed dome lamp flux, was obtained on the night 178 of 2008 to further study this effect in the photometric channel. As can be seen in Fig. 8.14, the SNIFS photometric channel science CCD suffers from the same problem: while its linearity is extremely good (after correction for shutter latency, the median absolute deviation of the counts per second up to 40000 ADU is around 0.06%), the photon transfer curve is non-linear and a correlation (Fig. 8.14d) between measured gain and mean flux is still observed.

The explanation for this problem proposed by Downing et al. (2006), is that the observed non-linearity is due to spreading or sharing of charge between the potential wells of the pixels in the image area, which increases with signal level and affects the variance determination. This can be tested by measuring the correlation of adjacent pixels on a difference of two uniformly lit flat fields $\Delta F_{i,j}$, using the spatial autocorrelation

$$R_{m,n} = \frac{\sum_{i,j} \Delta F_{i,j}\ \Delta F_{i+m,j+n}}{\sum_{i,j} \Delta F_{i,j}^2}\ . \tag{8.8}$$

The summed correlation of a central pixel with the four adjacent ones is shown in Fig. 8.14c and indeed it is higher for higher signal levels. The proposed solution is to use the autocorrelation variance instead of the normal variance, or if possible binned flat fields. Using the autocorrelation variance

$$\sigma_{\text{AC}}^2 = \sum_{m,n} \frac{\sum_{i,j}(\Delta F_{i,j} - \overline{\Delta F_{i,j}})(\Delta F_{i+m,j+n} - \overline{\Delta F_{i+m,j+n}})}{I\,J - 1}\ , \tag{8.9}$$

where $(m,n) \in [(-1,0),(0,0),(1,0),(0,-1),(0,1)]$, the obtained value for the gain is no longer dependent on the flux (Fig. 8.14e), which validates the hypothesis of pixel flux correlation with the nearby neighbors.

The measured gain using this procedure, is compared to the one obtained using binned (binning 2) V flats, taken during the 2006 up to mid-2008 period, in Table 8.4.
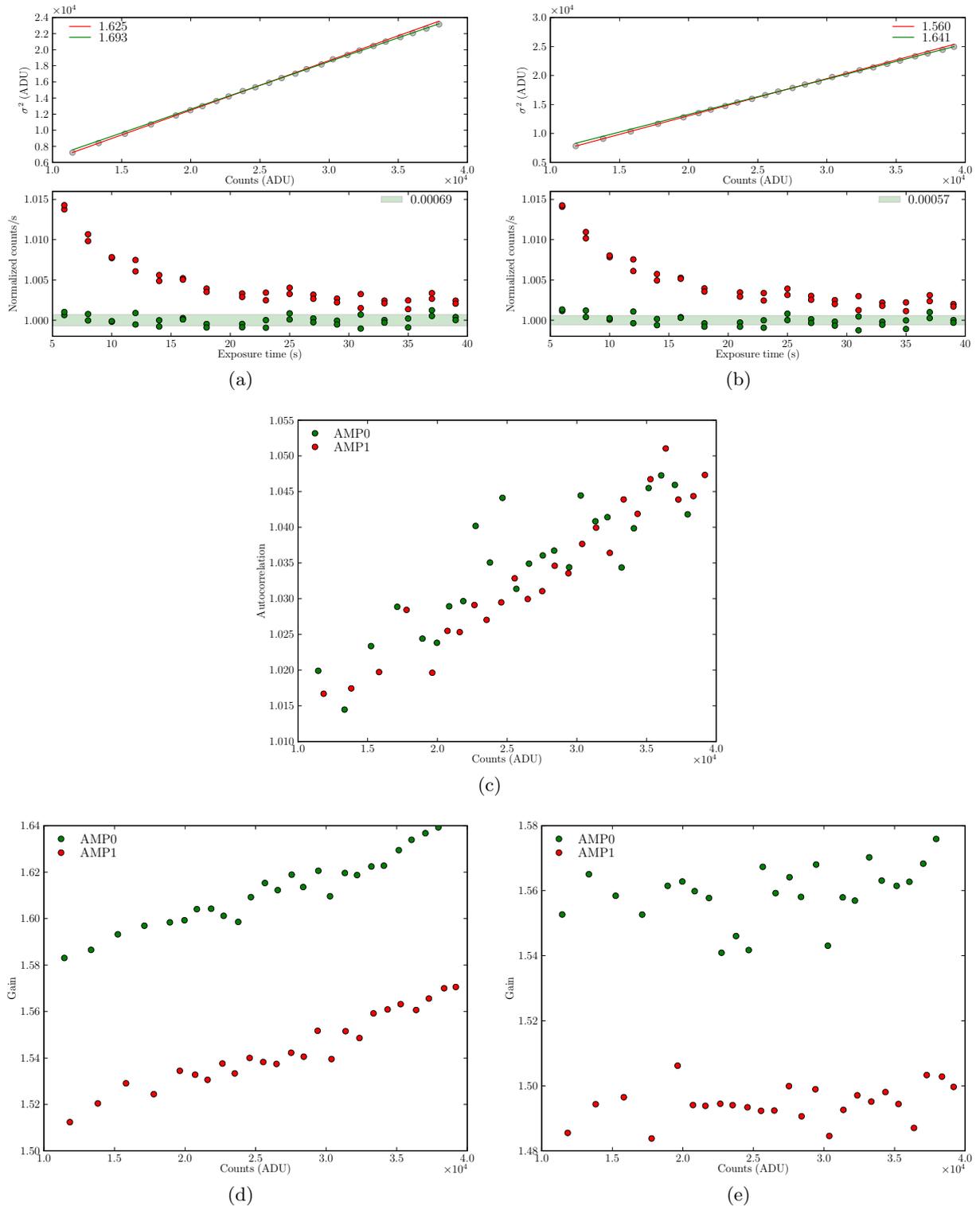
Figure 8.14: (a)–(b) Photon transfer curve (top panel) and linearity (bottom panel) plots respectively for the AMP0 and AMP1 of the photometric channel science CCD, using binning 1 V flat fields. On the top panel, two linear fits of the gain are shown, using the points with counts < 25000 ADU (red) and > 25000 ADU (green). On the bottom panel, the normalized counts per second are shown, on a raw exposure (red) and after correction for the shutter latency (green). The shaded area represents the MAD around 1; (c) Sum of the autocorrelation with the four adjacent pixels in a difference image of two flats; (d)–(e) Gain variation with mean counts using respectively normal and autocorrelation variances.

Epoch	AMP0		AMP1	
	σ^2_{AC}	Binning 2	σ^2_{AC}	Binning 2
January – June 2006	1.561 ± 0.010	1.562 ± 0.005	1.498 ± 0.006	1.503 ± 0.006
September 2006 ↓	1.557 ± 0.010	1.560 ± 0.007	1.500 ± 0.006	1.494 ± 0.011
March 2007 ↓	1.554 ± 0.015	1.553 ± 0.016	1.490 ± 0.011	1.491 ± 0.012
June 2007 ↓	1.550 ± 0.011	1.555 ± 0.008	1.488 ± 0.008	1.489 ± 0.006
March 2008 – present	1.554 ± 0.010	1.559 ± 0.007	1.491 ± 0.006	1.493 ± 0.006
2006–2008	1.554 ± 0.011	1.558 ± 0.009	1.492 ± 0.009	1.492 ± 0.008

Table 8.4: Median gain values and associated MAD (Median Absolute Deviation) for the two amplifiers of the photometric channel science CCD, obtained using the autocorrelation variance or binning 2 V flats.

Both methods give very similar results. The retained method for gain measurement will be the binned flat fields, due to their smaller size (faster I/O on disk) and slightly faster computational method. Fig. 8.15 shows the equivalent plots of Fig. 8.13 using the binned flats. As expected, the correlation between gain and mean flux is no longer present.
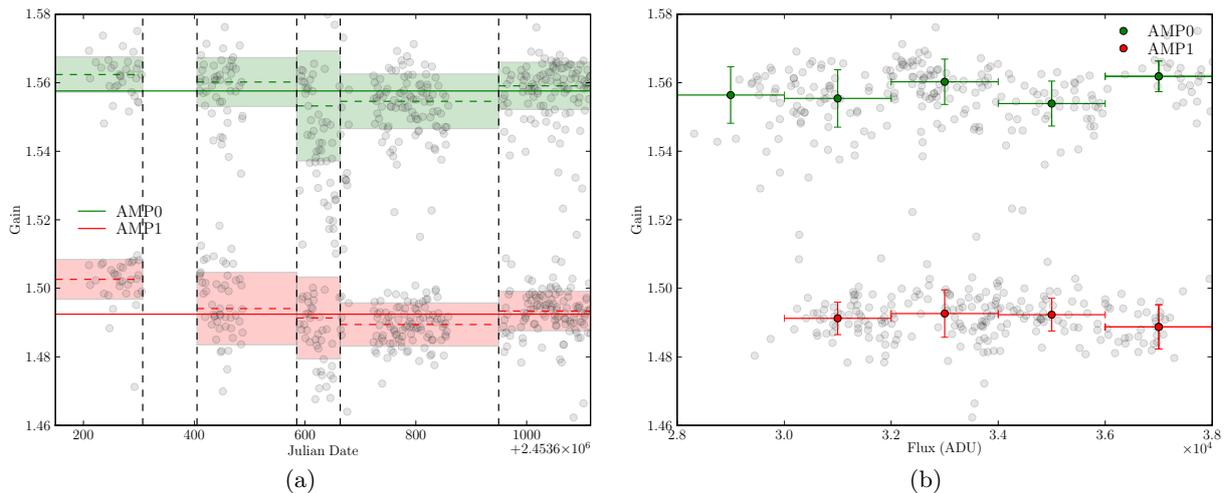
Figure 8.15: (a) Median gain (horizontal dashed line) and MAD (shaded area) for both amplifiers of the photometric channel science CCD, for different epochs, using binned V flats. The vertical dashed lines correspond respectively to: June 2006, September 2006, March 2007, June 2007 and March 2008; (b) Gain correlation with mean flux, for binned V flats.

In conclusion, the photometric channel science CCD gain seems stable in the long run, with a median absolute deviation in the order of 1% and variations lower than 0.5% of the median gain between consecutive epochs. We can see that the measured values are quite different from the ones show in Table 8.2. This will not affect in first order the intended usage of the photometric channel data, since that we will be making relative photometry of sources which are always observed on the same amplifier, hence the used constant gain value will cancel out, and for the moment no gain correction is applied on the photometric channel science exposures. It is however a small source of errors for the photometric ratios and a correction will be implemented for future productions.

8.5.3 Relative variation

As important as a global drift of the gain is a possible relative variation between the gains of AMP0 and AMP1. Since the filters of the MF are divided in such a way that F3 and F4 are on AMP0, F2 and F5 on AMP1 and F1 on both, an independent gain variation between both amplifiers would mean a possible "color term" on the photometric ratios for different sub-filters, in objects observed during a large time-frame, as is the case of the standard stars.

This can be easily monitored by measuring the mean flux, on a flat field corrected for shutter latency, in two small boxes 20 pixels wide, right before and after the separation between AMP0 and AMP1, and comparing both fluxes: the ratio of the fluxes should be the inverse gain ratio. Fig. 8.16 show the results of this procedure using the binned V flats. The obtained median ratio (in green) is the same as the one obtained using the independently measured gains (in red), but with a much smaller dispersion: a relative drift during the 2+ years period can be observed between the gains of AMP0 and AMP1, in the order of $\sim 0.1\%$.

Once again the observed variation is very small compared to the photometric ratios extraction errors and hence not accounted for at the moment.
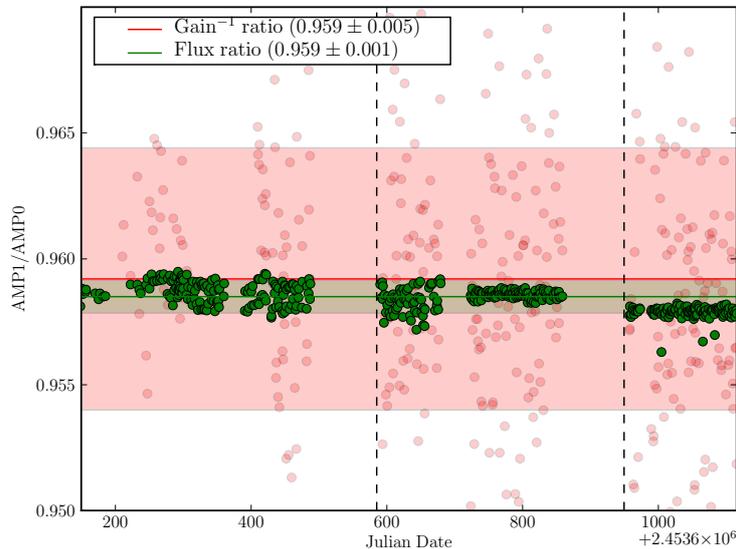
Figure 8.16: Relative gain drift between AMP0 and AMP1, measured using flux ratios (in green) and gain ratios (in red) on binning 2 V flats. The shaded areas represent the MAD about the median value. The vertical dashed lines correspond respectively to March 2007 and March 2008.

8.5.4 Guiding CCD gain

Less important than the science CCD, the guiding CCD will be used nonetheless for acquisition images and subsequent acquisition light curves. The same procedures as the shown on the last sections were used to try to measure the gain of AMP2 and AMP3, however the results are not fully conclusive.

Linearity plots for the four amplifiers are shown in Fig. 8.17a, where the difference to the bottom panels of Fig. 8.14a– 8.14b is that the exposures are here ordered by the time they were taken (the exposures were not taken with increasing exposure time, in order to de-correlate a possible lamp flux variation with the exposure time). We are restricting ourselves to the time frame where the dome lamp flux is stable, as can be seen by the stability of AMP0 and 1, and even so the number of measured counts per second on the AMP2 and 3 still continue to increase

up until the middle of the run. The only possible explanation for this behavior is an independent gain fluctuation of both amplifiers of the guiding CCD. It should be noticed that this data run was taken on a night when the photometric channel had not been used for more than 4h, so one could then argue that the guiding CCD takes longer to "warm up" than the science CCD. Further evidence for this possibility is present in Fig. 8.17b, which shows the time evolution of the flux ratio (in a similar way as in Fig. 8.16) between the pairs of amplifiers of both CCDs. We can see that while the flux ratio is very stable on the science CCD, it is abnormal during most of the run for the guiding CCD, taking around 1h to stabilize.
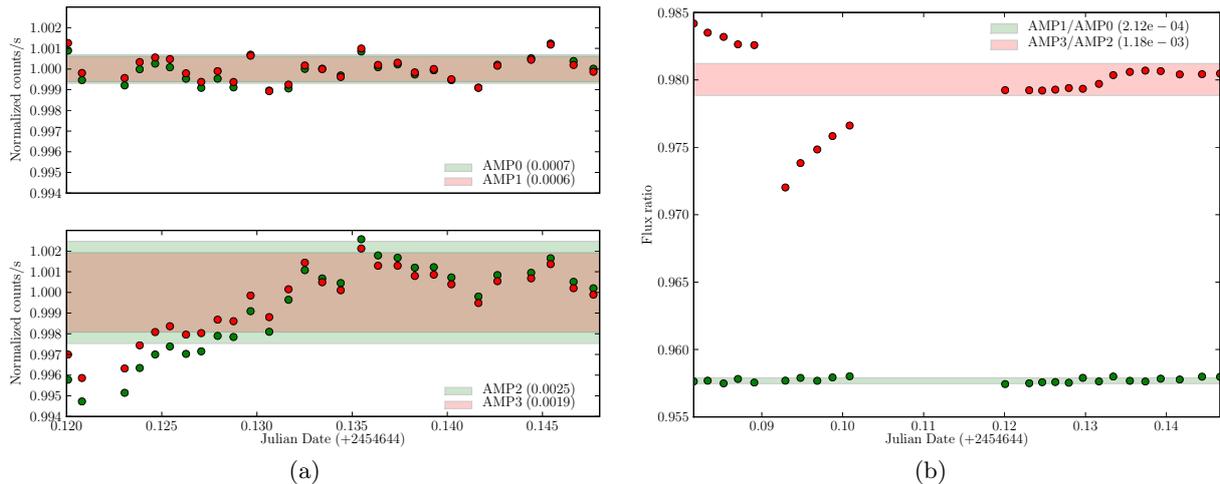
Figure 8.17: (a) Linearity plots of the four amplifiers of both cameras of the photometric channel from the flat run of night 08_178. The shaded areas represent the MAD; (b) Flux ratio between adjacent amplifiers for the flat run of night 08_178.

One would then expect to have different gain values, depending on how long SNIFS has been used before the acquisition of the flat fields for the gain measurement, meaning, if we use the binned flats taken before the start of the night (evening flats) or the ones at the end (morning flats). The measured gain using either evening or morning binned V flats is detailed in Table 8.5, and Fig. 8.18 shows the measured flux ratios between AMP2 and AMP3. Indeed we can see clearly different gains and ratios using the evening flats or the morning ones. The median flux ratio for the evening flats is in accordance with the one found previously using the exposures from night 08_178, after stabilization (Fig. 8.17b).

	AMP2		AMP3	
Epoch	Evening	Morning	Evening	Morning
September 2006 ↓	1.435 ± 0.010	1.429 ± 0.015	1.413 ± 0.013	1.390 ± 0.016
March 2007 ↓	1.426 ± 0.014	1.408 ± 0.017	1.391 ± 0.021	1.362 ± 0.016
June 2007 ↓	1.435 ± 0.006	1.411 ± 0.020	1.405 ± 0.008	1.364 ± 0.028
March 2008 – present	1.441 ± 0.008	1.406 ± 0.009	1.410 ± 0.006	1.353 ± 0.007
2006–2008	1.437 ± 0.009	1.410 ± 0.015	1.407 ± 0.010	1.359 ± 0.016

Table 8.5: Median gain values and associated MAD for the two amplifiers of the photometric channel guiding CCD, obtained using binning 2 V flats from the start of night (evening) and end of night (morning).
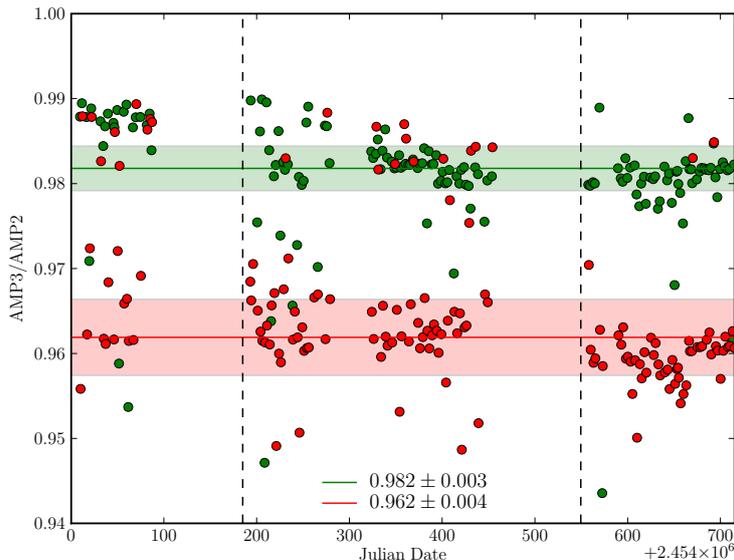
Figure 8.18: Relative gain drift between AMP3 and AMP2, measured using flux ratios on evening (green) and morning (red) binning 2 V flats. The shaded areas represent the MAD about the median value. The vertical dashed lines correspond respectively to March 2007 and March 2008.

It is unclear what is the cause of the observed gain variations in the guiding CCD. While it is obvious that its gain takes longer to stabilize after SNIFS has not been used for a long time, it also looks like that the gain drifts during the observation night, which may come from an increase in temperature of the CCD and associated electronics. Until further clarification of this issue, no gain correction is applied to the guiding CCD exposures.

8.6 Spectro/photometric channels intercalibration

The validity of the assumption made on (7.29) (page 78), that the photometric channel transmission with relation to the spectroscopic channel is stable during a certain period of time, can (in principle) be tested using the dome flats. For that task, we need absolute flux calibrated dome flat spectra, whose convolution with each of the transmissions from the MF sub-filters can be integrated, and compared with the measured flux on the photometric exposure done in parallel. Such study was however not done for the moment.

8.7 Filter zero points

No two detectors are the same, and if we also take into account all the different mirrors, lens or filters that a photon crosses in its path until being detected, measurements of the flux of the same object by two different instruments are intrinsically different. Thus, in order to make two measurements comparable, they have to be calibrated in relation to one of the standard photometric systems (Bessell 2005), by means of photometric transformations calculated for a given set of filters.

As a way to check the throughput of the P channel set of filters, and since we will intend later (§ 9.2.11) to do absolute magnitude measurements on the V filter, a photometric transformation was derived for each one of them. It is of the type:

$$m_x = M_x + a + b(\mathrm{X} - 1) + c\,\mathrm{CI}\;,\tag{8.10}$$

with instrumental magnitude

$$m_x = -2.5 \log_{10}(f_x) + 2.5 \log_{10}(t_x) \ , \tag{8.11}$$

absolute magnitude M, airmass X, color[6] CI, flux f and exposure time t on the filter x. The parameters a, b and c are respectively the filter zero points (which can be seen as the magnitude of an object that will produce 1 photo-e$^-$/sec in the detector), the first-order extinction coefficient and the color coefficient.

During August of 2006, SNIFS observed some Landolt (1992) fields, that can be used for the determination of the photometric transformation parameters. For good results, they have to be observed during a photometric night and with large airmass coverage. The fields observed in these conditions are shown on Table 8.6.

Field	Night	Airmass range
SA113	06_231	1.08–1.62
	06_244	1.55–1.73
SA114	06_231	1.05–1.78
	06_244	1.05–1.55
PG0231	06_234	1.03–1.23
PG1633	06_234	1.04–1.79

Table 8.6: Landolt standard star fields used for the determination of photometric parameters of the P channel filters.

Each of the exposures was processed and the stars fluxes measured by PSF photometry using `poloka` (§ 9.2.10). Each field WCS was properly set by matching to the USNO catalog (Monet et al. 2003), thus allowing for determination of accurate right ascension and declination coordinates of the field stars. The absolute magnitudes of the field objects are obtained from standard star catalogs: for the V filter, Stetson (2000) observations of both PG fields[7] were used, which have the advantage of extending Landolt's catalogs with several hundreds more standard stars; for the *ugriz* filters, the SA fields were used, since they coincide with the SDSS observational surface and calibrated object magnitudes can be obtained from their Sky Server[8].

It should be mentioned that we do not intend here to obtain highly accurate absolute photometry from these exposures (which besides is not the main usage of the P channel). The main intent is to find a reasonable throughput estimation of each filter. That is why higher order extinction and color coefficients are not used. Furthermore, same night observations of different fields will be average together, and ideally one should take into account *e.g.*, the directional non-uniformity of the extinction or the position of the stars in the CCD (Stetson 2005). A least square minimization of

$$\chi^2 = \sum_i^n \frac{[M_i + a + b(X_i - 1) + c\, CI_i - m_i]^2}{\sigma_{m_i}^2 + \sigma_{M_i}^2 + \sigma_{CI}^2} \ , \tag{8.12}$$

was performed, and the obtained parameters are shown in Table 8.7.

The throughput of the filters, approximated by a top-hat function with central wavelength λ and width $\Delta\lambda$, can be calculated using

$$10^{0.4(-a-16.852)} \frac{\lambda}{\pi r^2 \Delta\lambda} \ , \tag{8.13}$$

---

[6]Defined as the difference between the absolute magnitude of the star in two different filters, *e.g.* B-V.

[7]Obtained from http://www2.cadc-ccda.hia-iha.nrc-cnrc.gc.ca/community/STETSON

[8]http://skyserver.sdss.org

Filter	a	b	c (CI)	# stars	χ^2/dof	Residuals RMS (mag)
V	-25.24	0.08	0.10 (B-V)	205	11.39	0.05
u	-24.29	0.31	-0.11 (u-g)	73	101.17	0.19
g	-25.75	0.11	0.02 (g-r)	123	22.62	0.05
r	-25.59	0.02	0.05 (r-i)	117	8.25	0.05
i	-24.93	0.03	0.02 (i-z)	161	13.85	0.07
z	-24.03	0.01	0.76 (i-z)	105	46.64	0.17

Table 8.7: Photometric parameters for the full filter set of the photometric channel.

where the 16.852 term comes from the AB magnitude system zero point (on which the *ugriz* magnitudes are based) in photo-electrons, and r is the telescope mirror radius (110cm). The obtained values are on Table 8.8 and plotted in Fig. 8.19, where for comparison it was added each filter throughput, convolved with the full P channel throughput (SNIFS entrance, three reflections in aluminized mirrors, dewar window and CCD quantum efficiency) and a blackbody at 5700K, representing an average star SED. The dashed lines correspond to the ideal throughput when all the mirrors are freshly aluminized. However, the throughput changes rapidly after aluminization, so a correction factor was derived using flux ratios between flat fields, taken right before and after the UH88 primary mirror aluminization that was performed in mid-2007. The full lines represent then the throughput when all the mirrors have not been aluminized recently, which was the case when the data was taken.

For comparison, the spectrograph channel throughput can be seen in Fig. 4.5, page 50. The calculated throughputs are compatible with the "theoretical" ones obtained from the convolution of transmission curves, except for u and z, whose zero point seems to have been over estimated, and which already presented the biggest residual scatters.

Filter	λ	$\Delta\lambda$	Throughput
u	3592	476	0.19
g	4743	1349	0.34
r	6234	1392	0.37
i	7619	1490	0.23
z	8758	997	0.17

Table 8.8: Throughput of the *ugriz* SNIFS filter set. The filter effective wavelength (λ) and width ($\Delta\lambda$) are in Å.

8.8 MLA object position determination

For optimum spectrum extraction it is needed a good estimation of the object's position in MLA, which can be provided by the P channel. Invisible in the science exposure (since the POP is in place, to send the object light into the spectrograph), the object's coordinates have to be derived from its position in the acquisition exposure and propagated to MLA coordinates. This will be done in three steps:

1. measurement of the (pixel) barycenter of the object and the guide star in the acquisition exposure (before telescope pointing fine tuning), and determination of their relative positions. In the case it is possible, and for better accuracy, the object position derived from
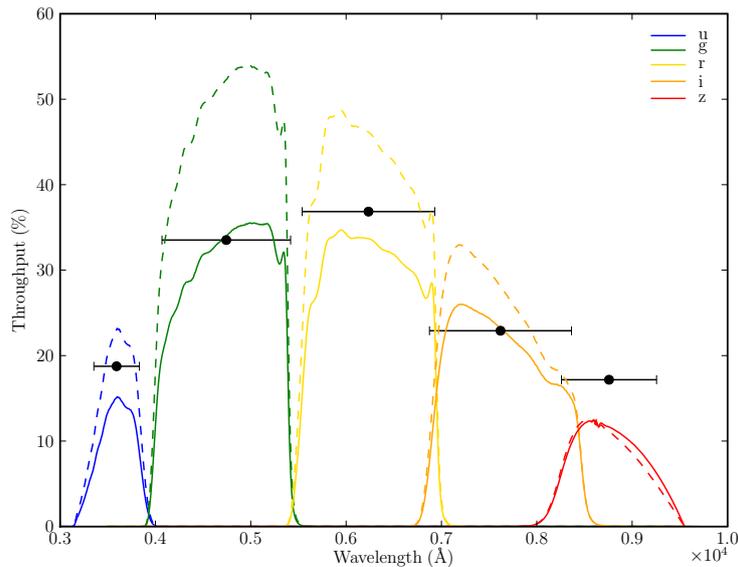
Figure 8.19: Throughput of the SNIFS *ugriz* filter set, calculated using the measured zero points and a top-hat function (in black), compared with each throughput convolved with the full P channel throughput (lines). The dashed lines assume that the telescope mirrors are perfectly aluminized.

V filter light curves (§ 9.2.11) is used;

2. estimation of the object position on the science exposure, from the guide star coordinates and their relative positions derived on the previous step;

3. conversion from P channel pixel coordinates to MLA spaxel coordinates on the spectrograph channel.

The first step can be performed with sub-pixel accuracy. The position seeds of both object and guide star are taken from the SNfactory database (which in turn are issued from the acquisition scripts' logs), and while mostly accurate they are not perfect: a test comparison of 32 acquisition exposures for Feige110 presents an average distance of 3 pixels between the ones given by the DB and the ones measured directly on the raw images. The second step uses the guide star coordinates directly from the database (calculated from the output logs of the guider algorithm), and they are not refined since that due to the fast continuous readout of the guiding CCD, only faint "ghosts" are visible in the final image.

The transformation matrix between both channels is of the kind

$$
\begin{bmatrix} x'_S \\ y'_S \end{bmatrix} = \begin{bmatrix} k_x \cos\phi & k_x \sin\phi \\ -k_y \sin\phi & k_y \cos\phi \end{bmatrix} \begin{bmatrix} x_P - x_0 \\ y_P - y_0 \end{bmatrix} , \tag{8.14}
$$

where S and P stand respectively for spectroscopic and photometric channel coordinates and $k_{x,y}$ is a scale factor, and accounts for a translation and a rotation of ϕ about a point (x_0, y_0), the MLA center coordinates on the photometric channel. For the determination of the five unknown parameters, a least square minimization of the function

$$
\chi^2 = \sum_i^n (x'_S - x_S)^2 + \sum_i^n (y'_S - y_S)^2 , \tag{8.15}
$$

is performed, where x'_S and y'_S are the functions from (8.14) and the $x_{S,P}$, $y_{S,P}$ coordinates come from a "scan" performed on night 07_352: a star was placed on different relative positions

inside the MLA, and both photometric and spectroscopic channels used to acquire exposures, thus mapping the different displacements of the star on the MLA field of view. The centroid of the star on the B and R channels was obtained from the reconstructed images by the spectrum extraction code, using an ADR correction to 5250Å, and the corresponding positions in the P channel were directly measured from the raw images using a barycenter estimator.

Parameter	B		R	
k_x	0.323	$\pm$ 0.017	0.324	$\pm$ 0.017
k_y	-0.315	$\pm$ 0.017	-0.310	$\pm$ 0.017
ϕ	0.048	$\pm$ 0.037	0.069	$\pm$ 0.037
x_0	2487.883	$\pm$ 0.663	2485.443	$\pm$ 0.648
y_0	184.343	$\pm$ 0.672	183.266	$\pm$ 0.679
(x_S, y_S) RMS	(0.327, 0.405)		(0.319, 0.390)	

Table 8.9: Fitted transformation parameters. The RMS is in spectroscopic channel coordinates (spaxels), ϕ in radians and (x_0, y_0) in photometric channel pixels.

The minimization results, performed separately on the B and R channels can be seen in Table 8.9, and the residuals of the fit in Fig. 8.20.
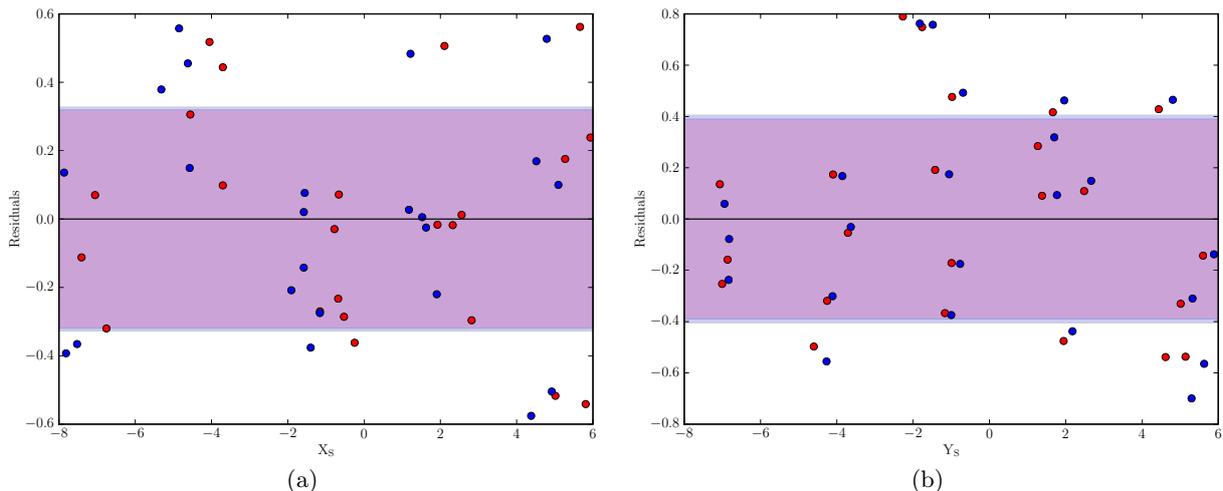
Figure 8.20: Residuals of the found transformation between photometric and spectroscopic (blue and red) channels coordinates, in (a) X and (b) Y.

The scale parameter is close to the predicted one, since 1 spaxel $\sim 0.4''$ and 1 pixel $\sim$ $0.137''$, thus $k \sim 0.343$ (the negative k_y is due to the inverted RA axis between both channels). The rotation of the order of $3°$ is small as expected (due to the mechanical configuration of SNIFS), and the found (x_0, y_0) is compatible with the previously measured value for the POP position, (2485.0, 185.0). However, the found transformation has an RMS scatter of around 0.4 spaxels, which is higher than what was expected from the precision of the measurements on both spectroscopic and photometric channels, and not accurate enough as a centering seed for "blind" spectrum extractions.

It is unclear what is the origin of the large residuals' RMS. It may be due to a non appropriate choice of the transformation model, which could improve if we take into account other geometrical parameters, e.g. due to mechanical flexures between both channels (and thus de-

pendent on the telescope position), or fluctuations on the POP position or inclination relative to the P channel. These extra parameters are however still possibilities, and were not thoroughly tested. The slightly different parameters found using B or R data could suggest an ADR induced effect, coming from a difference between the ADR correction wavelength, and the effective central wavelength of the guiding V filter, 5370Å. The correction of the measured positions on the S exposures to the new reference wavelength, make however almost negligible improvements, reducing the residuals RMS of 2% at best.

Chapter 9

Photometric ratios extraction

The photometric ratios, used for the flux calibration of non-photometric nights as seen in § 7, are the result of a dedicated extraction pipeline built specifically for the photometric channel. I will now detail this pipeline and further assess the quality of its output.

9.1 Pipeline implementation

The low level handling of the raw images issued from SNIFS, is made using a derived version of `poloka` (previously known as `TOADS`, TOols for Analysis and Detection of Supernovæ). It is a `C++` toolbox for image processing, developed, maintained and used by elements of the SNLS group at LPNHE, for supernova light curve extraction and photometric calibration. A clean CVS HEAD[1] version of `poloka` was imported to the SNfactory CVS[2] on the 22nd of May 2007, over which all the needed changes (to deal with the SNIFS images and different pipelining constraints) were subsequently implemented.

The pipeline itself is a `python` script called `SnfPhot`. It uses extensively the (built from scratch) `SnfPhotPipeline` package, consisting of wrappers for low-level `poloka` calls, and several other convenience tools to deal with every aspect of the pipeline, like input/outputs, database interaction, image handling, data fitting and plotting, *etc*. For details see Appendix A.

9.2 Pipeline flow

The most basic input that can be given to `SnfPhot` is a list of photometric channel exposures (which are ordinary FITS[3] files), ordered so that the first one will be taken as reference for all the alignment and flux comparison operations. The exposures can be raw ones (Fclass 17) or ones which have already been preprocessed (Fclass 18), meaning that: the overscan (a positive offset value introduced by the CCD amplifier electronics to avoid negative numbers in the output image) was subtracted, and the pixels of each amplifier multiplied by the corresponding gain (to transform ADU into photo-electrons). Since all the multi-filter science exposures (and related acquisition exposures, see § 9.2.1) from the photometric channel have been preprocessed and stored in the SNfactory archive, these are the preferred input (`SnfPhot` by itself will not subtract the bias map when preprocessing). For flexibility, `SnfPhot` can also accept simply the name of the target we which to produce, and then searches the appropriate images in the archive database.

---

[1] https://cvs.in2p3.fr/snovae-toads/poloka/
[2] https://cvs.in2p3.fr/snovae-SNFactory/poloka/
[3] Flexible Image Transport System - http://fits.gsfc.nasa.gov

9.2.1   ACQ *vs.* MF

Each time the telescope is pointed to a new target, an acquisition (ACQ) exposure is taken. Typically these exposures use both science and guiding cameras with binning[4] 2 (2048×2048 pixels), with an exposure time of ~ 20s using the Bessell V filter. They are made without the presence of the POP on the field of view, and are the only ones where the target is directly observed by the photometric channel. They are used to refine the pointing of the telescope, by comparison with a finder chart, so that the target is correctly centered in the POP for the subsequent spectrum exposure.
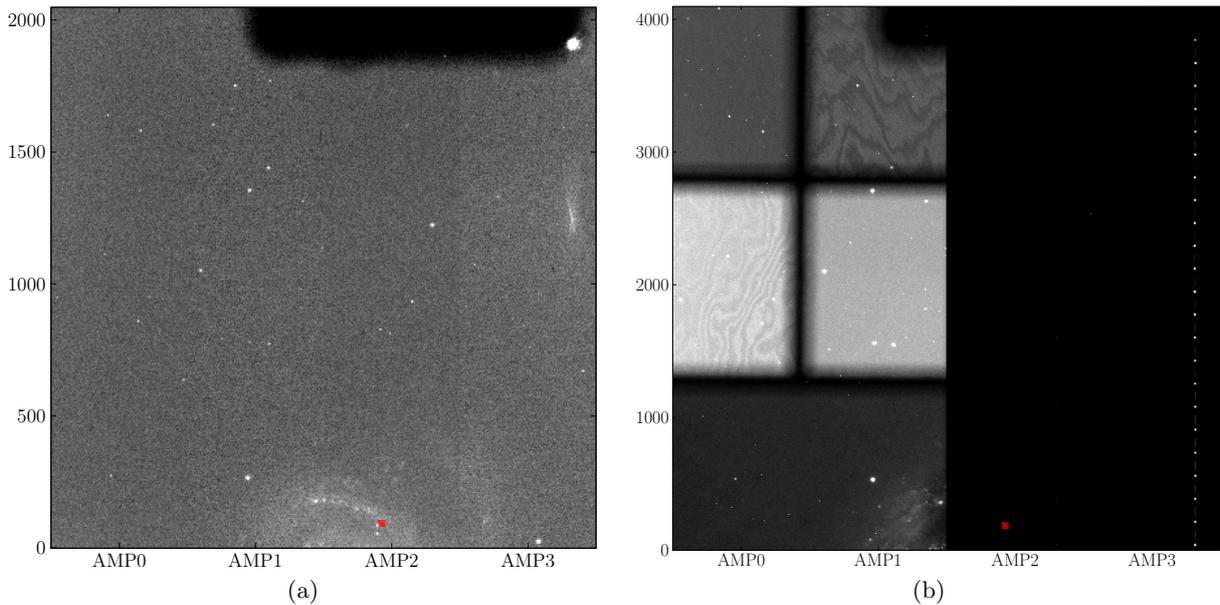
Figure 9.1: (a) Acquisition and (b) multi-filter exposures for SN2006X. The red square represents the field of view of the spectrograph (MLA). The target is easily seen on the acquisition image, right next to the MLA square (before re-centering) with the (very big) host galaxy in the background. We can also see that the multi-filter images the left side of the field seen by the acquisition image, while the guiding camera at right shows some flux residuals of the guiding process. The orientation is North on the bottom and East on the left.

SnfPhot can deal with ACQ or MF exposures, but separately. There are slight differences in the way each image type is dealt and their final purposes: the photometric ratios are computed from the MF exposures, while the ACQ ones are used for object positioning (§ 8.8) and rough V filter light curves (§ 9.2.11) of the supernovæ.

9.2.2   Filter cutting

Each individual sub-filter of the MF will be treated independently as if it was a single exposure, by cutting it from the image. The specific area to be cut is chosen to avoid any shadow due to the MF support or other elements (like the POP), so it has to be epoch dependent (see Table 4.2 on page 55). Changes after the SNIFS interventions in the relative position of the CCD

---

[4]A binned CCD exposure is such that the charges of a group of neighboring pixels is collected together as a single pixel. A binning of 2 means that the pixels are summed two by two in either rows and columns, effectively reducing the number of readout pixels (and thus readout time) by 4, while losing spatial resolution.

and MF support, and increased shadows due to the addition of baffling and/or black silicon to fight the light leaks, will usually reduce the effective area of each filter.

Filter	$\mathcal{A}$	$\mathcal{B}$–$\mathcal{C}$	$\mathcal{D}^{\ddagger}\mathcal{E}$
F1	(0,1)–(1814,1121)	(0,1)–(1825,1106)	(0,1)–(1825,1106)
F2	(1150,1500)–(2000,2605)	(1114,1442)–(2005,2627)	(1149,1522)–(1954,2552)
F3	(0,3000)–(770,4096)	(0,2946)–(795,4096)	(45,2993)–(710,3923)
F4	(0,1480)–(770,2600)	(0,1442)–(795,2627)	(0,1482)–(700,2593)
F5	(1150,3000)–(2000,3610)	(1109,2946)–(2015,3599)	(1119,2979)–(1920,3486)

† for $\mathcal{D}2$ F1 limits are (1024,400)–(1825,1106), all the others remain the same.

Table 9.1: Epoch dependent MF cuts. The (x,y) coordinates are shown for the lower left – upper right points of each filter rectangle in a 4096×4096 binning 1 image. The epochs where there was no notable change in the coordinates are grouped together. One pixel represents $0.137''$.

In the case of acquisition exposures, a cut is made to remove the shadow of the enlarger on the top, and an extra group of columns is added between AMP1 and AMP2, so that the physical separation between both CCDs on the P channel (~ 77.1 pixels), is taken into account. That allows us to obtain an accurate "on the sky" relative positioning of the stars, essential when performing matches to star catalogs. The number of columns added is 77 or 38, for binning 1 or 2 respectively[5], and their value is set to the mean background level of the exposure.

A previously constructed image representing the dead pixels of the photometric CCD is also cutted. This image gives basically the position of 3 dead columns in the AMP0, that should be taken into account later when searching for objects and measuring their flux.

9.2.3 DbImage

To keep `poloka` compatibility, the same approach is used in terms of image storage: the DbImage. This is nothing more than a directory per sub-filter, which contains the main exposure file and related data (FITS image maps and ASCII catalogs mainly). The most important files inside a DbImage are:

calibrated.fits the main file derived from the raw exposure;

back.fits background subtracted from calibrated.fits;

weight.fits weight map;

satur.fits saturation map;

dead.fits dead pixels map;

se*.list SExtractor object catalog;

aperse*.list aperture fluxes catalog derived from the SExtractor one;

9.2.4 Object identification

The identification of the objects present in an image (previously defringed and cleaned of moon border effects), is made by `poloka` using an embedded version of SExtractor (Bertin and Arnouts 1996). The procedure has a great deal of intermediate steps.

---

[5] Notice the small error in position introduced by ignoring the decimal part of the separation. Being an image a discrete array of pixels, it would oblige to recalculate the flux distribution of all the pixels if we were to use a further 0.1 pixel shift. Besides, the $0.014''$ loss in precision is negligible.

- the sky background flux is measured by calculating a clipped mean over 10000 pixels of the image. A weight map of the same size of `calibrated.fits` is then created, each pixel value being the inverse of the sky variance. In case we were using a flat field, it would be also taken into account by the weight map. A temporary bad pixels map (pixels with zero flux) is created, to serve as input to SExtractor;

- SExtractor is run using some predefined detection thresholds (3σ from the background), and uses the weight, bad and (previously made) dead pixels maps to identify the objects in the exposure. A saturation map is created with all the saturated pixels[6] and the affected stars are flagged in the catalog;

- the sky background contribution is calculated, by masking all the objects present in the field and dividing the exposure into several patches 200 pixels wide. The measured background flux on each patch is then used to build a smooth background map, that is subtracted from the raw exposure;

- a seeing[7] estimate is made, using the FWHM of the found objects. The weight map is updated to take into account the background changes and pixels of very low flux;

- the final object catalog is written. It is a typical SExtractor catalog, with several positional and flux parameters per object. For a detailed description of each one of them, see the SExtractor documentation[8].

Notice that this procedure will identify all objects, including false positives due to cosmetic defects or CCD non-uniformities not previously corrected, present on the image. SExtractor tries to distinguish between galaxies or stars automatically, but a more refined filtering of the catalog is done later on.

9.2.5 Aperture photometry

Although SExtractor already performs aperture photometry (the object flux is the sum of all the background-subtracted pixels inside a certain circular area centered on it), `poloka` has a specific procedure to do it in a more robust way. It takes into account the weight and saturation maps, and is able to account for sub-pixels in the border of the apertures, by oversampling them.

A number of different aperture measurements are made, with seeing dependent radius: the seeing (in σ pixel units) is calculated from the star cluster locus in object shape (the a and b semi-major and semi-minor axes of an ellipse) space, and then multiplied by several factors (1.175, 2.0, 2.5, 3.0, 3.5, 4.0, 5.0, 7.5, 10. and 15.), thus giving ten different flux measurements. In case the seeing calculation fails (mostly due to a small number of objects), the code was changed so that the seeing is set as the one calculated from the guide star and stored in the SNfactory database. This is slightly less accurate since the guide star (GS) is observed in the Bessell V filter and the seeing is wavelength dependent (§ 9.3.2). In the uncommon case of the GS seeing not being available, we resort to the seeing calculated previously by SExtractor. The

---

[6] The CCDs are read using 16bit ADCs, so a pixel charge will not be able to be measured if after conversion it is higher than the ADC's 65536 ADU limit.

[7] The seeing can be though as a measurement of the atmospheric turbulence and the perturbations it induces in any ground-based observation. It is usually defined as the FWHM of the PSF (*cf.* § 9.2.10) of a point source (star) observed by the instrument. A lower value means a more stable atmosphere – the typical seeing of SNIFS observations is $\sim 1''$, *cf.* § 9.3.2.

[8] http://terapix.iap.fr/soft/sextractor

flux measurement error is set as the (statistical) photon noise, which follows a Poisson law, and thus

$$\sigma_{\text{flux}} = \sqrt{\sum_i (f_i + \sigma_{S_i}^2)} \,, \tag{9.1}$$

where the summation of the fluxes f is made over the i background-subtracted pixels inside the aperture circle, and σ_S^2 is the sky variance, obtained from the weight map.

9.2.6 Image alignment

After the previous processing steps, all the DbImages are aligned to the reference one, which for consistency is set to be the photometric night with the best seeing.

For this purpose, the object lists previously created will be cleaned using $[5, 3, N]$[9] and matched by finding a geometric transformation which accounts for translation, scaling and rotation (for more technical details of the inner working of `poloka`, *cf.* Fabbro (2001), one of the creators of `TOADS`). The found transformation is then applied to the "to be transformed" image and corresponding weight and saturation maps, as well as its SExtractor object list. The transformed image will have the same physical size of the reference one, so any transformed area that now falls outside the reference field will be cut, while any new empty area will be padded with zeros (Fig. 9.2).
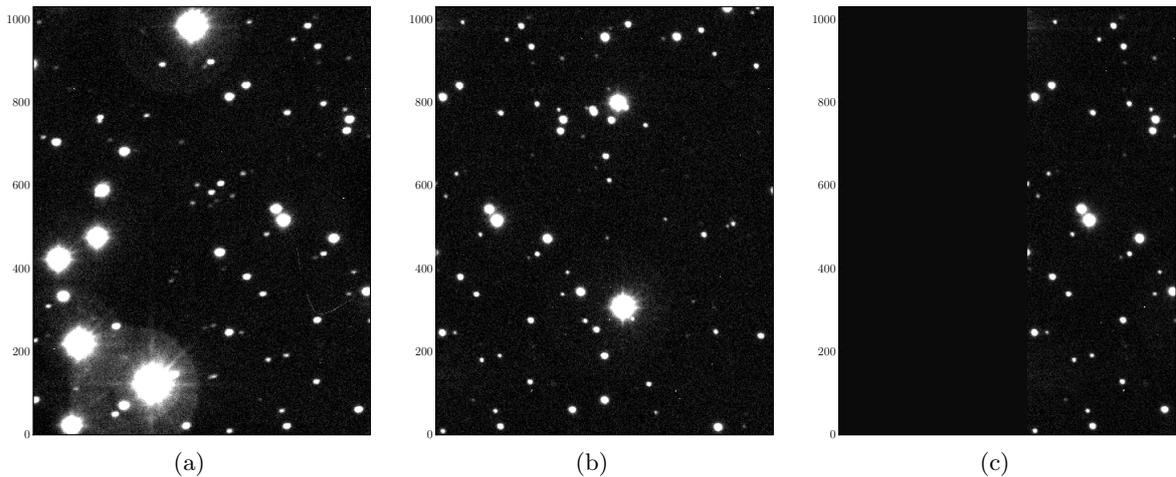
Figure 9.2: Two exposures of the same field, with a telescope shift between them: (c) is the result of the alignment procedure applied to (b) with relation to the reference (a).

9.2.7 Stacking and reference catalog

The next step of the pipeline is to compare the catalogs of each aligned image to a reference catalog previously made. This is done in order to prevent the inclusion of undesired objects (like galaxies) in the catalogs, that may not be automatically rejected (*e.g.*, in the case the

---

[9]All the list cleaning/refinements done in any `poloka` function called by the pipeline were changed, so that they can now be centrally controlled. For reference purposes, the main selection cuts applied will be identified by the $[a, b, c]$ notation, where a stands for minimum signal to noise ratio, b for the SExtractor extraction flag maximum value (detailed in the documentation), and c for the usage or not of seeing related FWHM cuts (Y/N).

telescope is out of focus, the stars' PSF will be elliptical, making them difficult to automatically distinguish from the galaxies).

For the creation of this reference catalog, stacks of all the fields observed by SNIFS were made for each filter of the MF. For each field, exposures taken on dark nights (without Moon) are searched, fully processed, aligned and median stacked. The resulting image goes deeper (fainter objects are better resolved) than a typical exposure and has higher SNR (signal to noise ratio).

A total of 175 supernovæ (followed until mid-2008) and 27 standard stars were stacked and their catalogs produced. Each of these catalogs was verified by "human scanners", using a purposely created GUI interface between the image viewer DS9 and specific poloka catalog cleaning procedures. The scanner cleans the catalog using the default [30,0,Y] parameters and visually checks the quality of the selected objects. Bad objects are removed, the others which were wrongly rejected are added, and the final (reference) catalog is saved (Fig. 9.3). These steps can be easily remade for each new target observed by SNIFS, after enough exposures (~ 5) are available, and before it is fed into the full analysis chain.
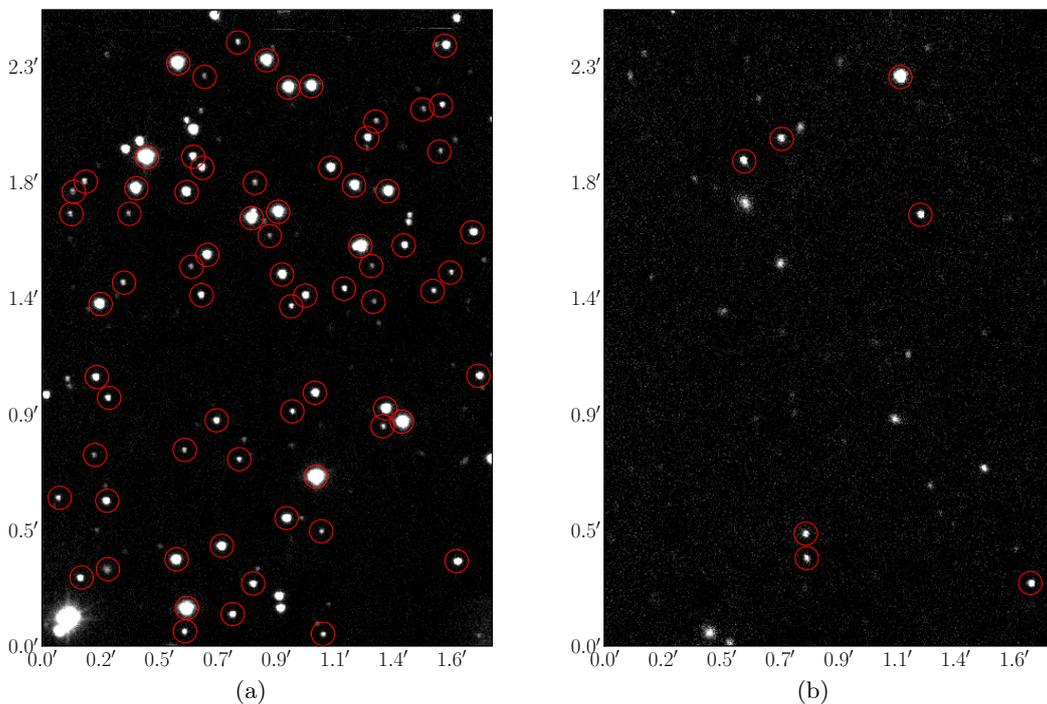
Figure 9.3: Examples of stacks for two F3 fields: (a) crowded (GD71) and (b) uncrowded (SN2005M). The red circles represent the stars which will be used as the reference catalog.

There are a few stacks which were impossible to be made due to a very small number of bright stars in a specific filter, which prevents the determination of the alignment transformation between different exposures. They are detailed on Table 9.2. One could in those cases try to use the alignment transformation of the nearby filters to derive a proper alignment, however that would be of no interest, since the photometric ratios would be impossible to compute due to the lack of stars. Having a reference catalog is not a determining point for the flow of the pipeline: ACQ images do not have reference catalogs, and the pipeline will try to automatically clean the objects list on the fly.

It should be pointed out that even though this reference catalog could have been used on the previous alignment step, it is only being used to select the "good" stars for the next step

MF filter	field
F1	LTT377
	SNF20050927-005
	SNF20061109-002
F2	HZ21
	SN2005bg
F3	BD+75325
	Feige34
F5	BD+75325
	Feige34
	Feige56
	HZ44
	LTT1020
	LTT377
	SN2005ag
	SN2005bg
	SN2005bl
	SN2005cc
	SN2005M
	SN2005ki
	SNF20050929-005
	SNF20061020-000
	SNF20070802-000
	SNF20070810-004
	SNF20070817-003
	SNF20070818-001
	SNF20070825-001
	SNF20070902-018
	SNF20070912-000
	SNF20071001-005
	SNF20071003-004
	SNF20071003-016
	SNF20071108-009
	SNF20080507-000
	SNF20080510-005
	SNF20080514-002

Table 9.2: MF fields for which stacking was impossible to be made due to the lack of enough bright stars for alignment between exposures.

(photometric ratios calculation). The `poloka` alignment algorithm is robust enough, and for that purpose we don't care if we use galaxies, besides the stars.

9.2.8 Image subtraction - photometric ratios

Once all the images are properly aligned, their star catalogs filtered with relation to the stack reference one, and cleaned with $[10, 3, N]$, we can proceed to the last and most important step, the calculation of the photometric ratio between each of the images and the reference one (to not be mistaken with the stack reference – this reference image is defined once for each run of the pipeline, and as already said, is set to be the photometric night with best seeing).

They are a by-product of a `poloka` procedure which we will be using partially, that subtracts[10] the reference image from every other image and returns the photometric ratio for each of those pairs, using two separate methods.

Convolution kernel

The default implementation of the `image_sub` procedure is such that the pair of images to be subtracted are first homogenized, to make them comparable flux-wise. This homogenization consists in the search of a convolution kernel that will be used to convolve the best quality image (the reference one, with better seeing), in order to bring it to the "photometric frame" of the worst quality one. The kernel will take into account the the variations in seeing, and differences in instrumental/atmospheric transmission between both observations.

A convolution kernel K between the best seeing (B) and worst seeing (W) images is estimated, so that

$$B(x, y) \otimes K(u, v) = W(x, y) \ , \tag{9.2}$$

where the kernel is decomposed into a base of gaussian functions multiplied by polynomials, and is determined by a least squares fit on vignettes of the brightest objects of the reference image. For the technical details refer to Alard and Lupton (1998), Alard (1999), Fabbro (2001).

The convolution kernel is made such that its integral is constant all over the image, for photometric conservation. This integral is the so-called *photometric ratio*, which as already seen, will account mainly for the differences in transmission between both observations (as well as differences in exposure time, since the exposures are not corrected for it, and we should take that into account later).

This method however presents two major inconveniences: it performs poorly when the number of available objects in the field is small, and does not produces an estimate of the error on the ratio (*cf.* § 9.3). That is why the following method is also used.

Aperture photometry

Another estimator of the flux ratio between two nights is based on the aperture fluxes already measured for each of the stars of the field. If we have N stars with aperture fluxes measured on both the reference (B) and another night (W), we want to estimate the photometric ratio $\mathcal{P}$ which minimizes

$$\chi^2 = \sum_{i}^{N} \frac{(W_i - \mathcal{P} \, B_i)^2}{\sigma_{W_i}^2 + (\mathcal{P} \, \sigma_{B_i})^2} \ . \tag{9.3}$$

---

[10]I recall that the origins of `poloka` are connected with the detection and/or photometry of supernovæ in search images for SCP and later SNLS.

`poloka`'s least square fit implementation uses the equivalent formulation

$$\chi^2 = \sum_i^N \frac{(W_i - \mathcal{P}\,\mathcal{Z}_i)^2}{\sigma_{W_i}^2} + \frac{(B_i - \mathcal{Z}_i)^2}{\sigma_{B_i}^2} \ , \tag{9.4}$$

where

$$\mathcal{Z}_i = \frac{\mathcal{P}\,W\,\sigma_{B_i}^2 + B_i\,\sigma_{W_i}^2}{\sigma_{W_i}^2 + (\mathcal{P}\,\sigma_{B_i})^2} \ , \tag{9.5}$$

whose minimization by least squares with outliers clipping leads to an estimator with a very small bias and almost optimal. It has the advantage of working better than the convolution kernels when the number of objects is smaller, and besides, a (photon statistics) error of $\mathcal{P}$ can be estimated from the minimization.

Both methods will be further compared in § 9.3.4.

9.2.9 Photometric ratios parsing

The last step of the pipeline consists in the final parsing of the photometric ratios raw output files, in order to provide an input file for the spectra flux calibration pipeline (§ 7). The ratios are corrected for differences in the exposure time of each pair of exposures, which is included in the raw ratios, by simply making

$$\mathcal{P}' = \mathcal{P}\frac{t_B}{t_W} \ . \tag{9.6}$$

The output file resembles something like

```
08_134_096_003 05_126_022_001  1.129  1.149   97      0.995      0.001
08_137_076_003 05_126_022_001  1.129  1.149  113      1.010      0.002
08_139_099_003 05_126_022_001  1.129  1.149   90      0.986      0.001
```

where each line accounts for a $[W, B]$ exposure pair, with respective observation event numbers, airmasses, number of stars used for the ratio calculation, $\mathcal{P}'$ and $\sigma_{\mathcal{P}'}$.

9.2.10 PSF photometry

Besides the already presented aperture photometry, a more robust procedure of flux measurement is also implemented in `poloka`: PSF (Point Spread Function) photometry. A PSF can be seen as the representation of a point source by the instrument, and covers both instrumental optical effects (like focus and field distortion), with atmospheric turbulence effects. The determination of the PSF for an exposure, sometimes far from the circular shape assumed by the aperture photometry, allows thus an optimal extraction of the flux of the objects in the field.

The procedure is based on the one from `DAOPHOT` (Stetson 1987) and uses cleaned ($[10, 3, N]$) star catalogs previously filtered with relation to the stack reference. A Moffat function (a modified Lorentzian with variable power law index) is first fitted to all the stars (Fig. 9.4a), and a subset is used to calculate an interpolated residual (Fig. 9.4b), which is added to create the final PSF model (Fig. 9.4c), then used for flux and positions fitting of the stars from the catalog. As with the convolution kernels, no 2D spatial variation of the PSF's analytic and residual parameters is allowed: since a single sub-filter of the MF has a small field-of-view, any optical distortion is assumed to be constant over all its surface.

Being an intrinsically better measure of fluxes, the PSF photometry will be used for benchmarking of the quality of the aperture photometry, which it cannot replace, since it faces similar
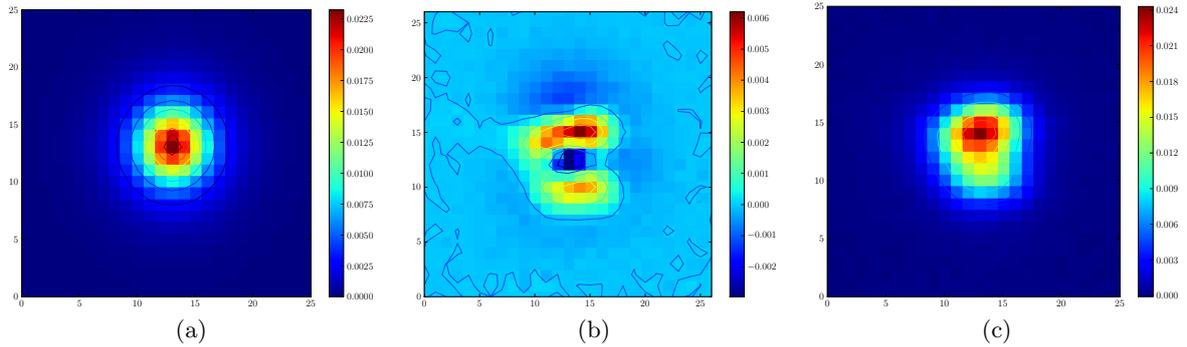
Figure 9.4: PSF model for an F2 observation of a crowded field (EG131, 05_176_091): the final PSF model (of a quite extreme case) (c) is the combination of a Moffat (a) and the residuals (b). The units are expressed in normalized flux – the integral of the PSF model equals 1.

problems of the kernel convolutions when the number of stars is low (mainly in the residual calculation).

9.2.11   Acquisition light curves

A secondary use of the `SnfPhot` pipeline is the creation of supernovæ light curves using the Bessel V filter acquisition images (§ 9.2.1). For this purpose, each of the acquisition exposures is subject to the same pipeline steps which are applied to MF exposures and were described previously. Additionally a final step consisting in the creation of the supernova light curve is performed.

The used procedure is `poloka`'s `make_lightcurve` light curve builder (Fabbro 2001). It is based on a least squares simultaneous fitting of the supernova flux, position (seeded from positions stored in the SNfactory database, corresponding to the target pointing used for the observation) and galactic background. It uses all the pixels of small square vignettes centered on the supernova, and the PSF model of the reference image. The PSF is be propagated throughout all the other images using the convolution kernels (whose estimation, due to the large field-of-view and number of stars, is well constraint and accurate).

For an analysis of the results of this procedure with a number of SNfactory supernovæ *cf.* § 10.

9.3   Quality benchmarking

Due to the importance of the photometric ratios to the flux calibration of SNfactory objects, we have to make sure that the results of the pipeline are consistent, and that any possible systematic errors associated with their determination are under control. Furthermore, the fact that the pipeline has to work on a large range of image quality and field crowding, obliges the use of less-optimal procedures[11] (like the aperture photometry), whose results' quality should be benchmarked.

---

[11]Being `poloka` a tool from SNLS, it is used mostly for large deep field photometry, for which it is more optimized.

9.3.1   Optimal aperture size for photometry

When using aperture photometry, we encounter the problem of which is the "best" aperture radius to use. A typical star's PSF presents a main flux core and wings. These wings may not be completely included inside the chosen aperture for the photometry, leading to the loss of flux in the measurement. This will not be a problem in cases where we are doing differential photometry, comparing the integrated flux of objects of the field, if all of them are measured with the same aperture and have identical PSFs. In our case however, we want to compare fluxes of the same stars in two nights, with different atmospheric conditions (and hence different seeing/PSF). It is clear that an adaptive aperture radius is needed, that is why a seeing dependent aperture is used.

Assuming (*cf.* § 9.3.2) that the seeing is perfectly determined on each night, and that the (not necessarily round) PSF shape does not suffers from extreme field/focus optical distortions on specific nights, each aperture will always measure the same percentage of flux, to a certain precision. Now, to choose one from the 10 used apertures, a few points should be taken into account: it should be big enough to integrate the most flux from the star, yet small enough so that the noise contribution from the background or other sources remains low. Light at very large radius, due to optical effects of the telescope and instrument is expected to be constant over different nights.
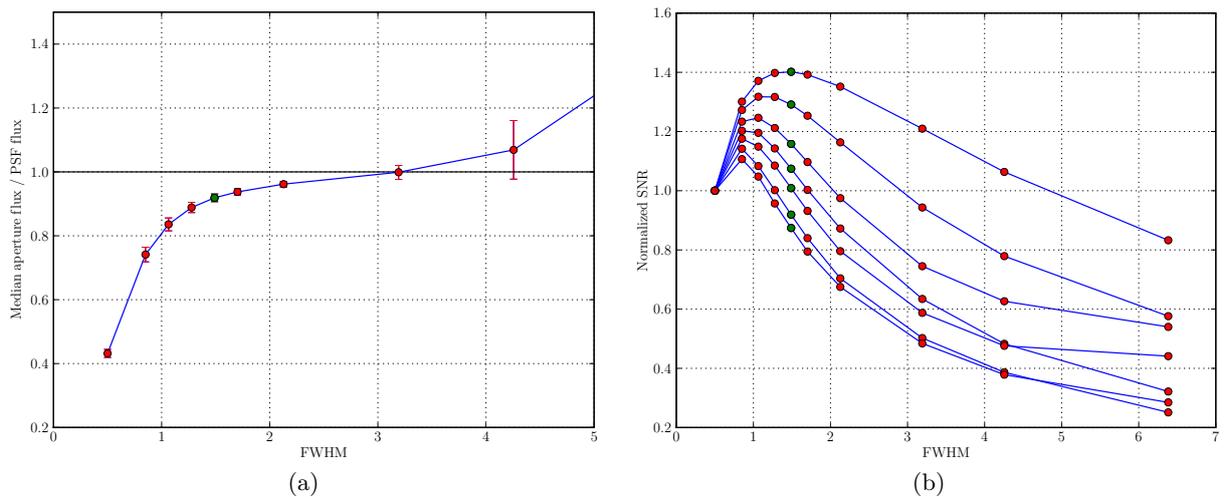
Figure 9.5: (a) Median normalized flux for a total of 61400+ stars on crowded fields, in function of the FWHM (directly related to the chosen aperture); (b) Signal over noise ratio in function of the FWHM, for a set of stars ordered from brighter (top) to fainter (bottom). The chosen aperture is marked in green.

Lost flux per aperture

By using exposures of crowded fields (EG131 and GD71), where we are certain that we can produce a good PSF model, all the stars can be fitted using that optimum model, assumed to account for all the flux of the star, and used to normalize the aperture photometry flux. A total of 777 exposures (with all the sub-filters mixed) were processed, obtaining for each one of them a median normalized aperture flux per radius, for a total of 61400+ stars. The evolution of this median normalized flux *vs.* FWHM can be seen in Fig. 9.5a. The aperture radius that is typically assumed to account for 100% of the flux of a star is ~ 3 FWHM (Howell 2006). On

bigger apertures, the aperture photometry starts to integrate flux coming from nearby stars, so the normalized flux ratio increases continually.

Signal to noise ratio

The signal to noise ratio of the integrated flux will depend of the brightness of the star and the aperture. Fig. 9.5b shows its evolution for a set of stars from the same field, from brighter (top) to fainter (bottom). We can see that for bright stars it is preferable to have a large aperture for better SNR, while that for fainter stars the optimum SNR is obtained with smaller apertures.

The chosen aperture radius to be used for the photometric ratios is the one marked by the green point ($3.5\sigma \simeq 1.5$ FWHM). It is a compromise, accounting for 92% of the total flux, with a normalized median absolute deviation of 1.2% for all the nights used (most probably coming from inaccuracies on the determination of the seeing, or highly distorted PSFs due to focus problems), while having an improvement of over than 20% in the SNR for faint objects, with relation to an aperture closer to the optimal PSF.

9.3.2 Seeing determination

The quality of the seeing determination is important for a consistent comparison of aperture photometry fluxes between nights. The seeing measured from the guide star (GS) for ~ 3500 long SNIFS exposures with airmass lower than 1.3 is shown in Fig. 9.6a. Two distinct seeing determinations per exposure are shown: the one measured on a stack of all the corresponding guiding rasters, thus accounting for guiding drifts, and the instantaneous one, an average seeing of all the individual guiding rasters. The peak instantaneous seeing is $\sim 0.8''$, consistent with the Mauna Kea typical seeing. However if we account for guiding effects, the typical seeing of a SNIFS exposure is $\sim 1''$, with around 9% of observations made at seeings worse then $2''$.

We already saw that the seeing used for the determination of aperture radius is the one calculated using the stars of the specific sub-filter, which is more accurate than the GS one, observed on V. This seeing however will not always be correctly measured, mainly due to the lack of enough objects in the field. In those cases, the pipeline reverts to the GS measured seeing, so we want to know what will be the contribution (if any) of this seeing color discrepancy to the calculated aperture fluxes.

In Fig. 9.6b, the measured seeing during the creation of the aperture catalog is compared to the seeing derived from the guide star, for a group of 200 crowded field exposures (EG131 + GD71), where we are sure that the aperture catalog seeing determination is possible and accurate. A linear fit of the type

$$\mathcal{S}_{\text{aper}} = a \, \mathcal{S}_{\text{GS}} \;, \tag{9.7}$$

was performed, and the results and respective residuals RMS are shown in Table 9.3.

As expected, we see effects from both filter color and relative filter placement in the MF with relation to the guiding CCD. F2 has the smaller residual RMS, since it is the closest one in effective wavelength and position to V, while F3 and F4 (contrary to F5) present an high RMS due to the fact that they are placed near the border of the CCD, where the field curvature is worse. Unless for F4, the different slopes are compatible with zero.

Let's assume a worst case scenario where, in accordance with the observed residuals scatter, there is a $0.1''$ difference between the "real" seeing that we would estimate from measurements on the photometric channel, and the GS seeing used instead. Since our aperture radius is attached

(a)

(b)
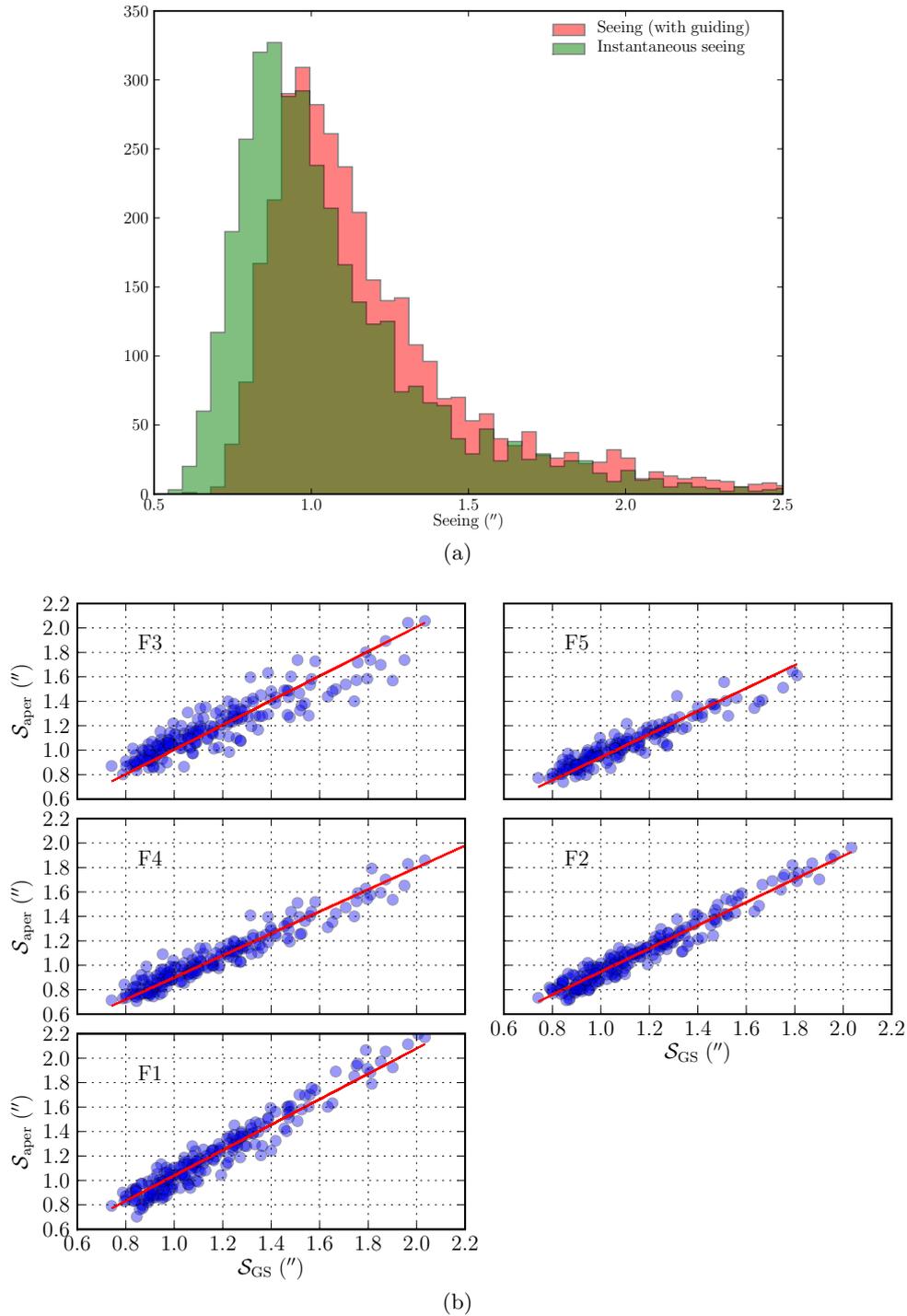
Figure 9.6: (a) Guide star seeing distribution for ~ 3500 SNIFS exposures with airmass lower than 1.3 during the 4 year span. The instantaneous seeing is represented in green, and the seeing accounting for the guiding drifts in red. (b) Relation between the guide star seeing and the seeing measured during the aperture catalog creation, on each specific sub-filter of 200 crowded field exposures. The relative position of the sub-filters plots is the same as their placements on the MF.

Filter	a	RMS ($''$)
F1	1.040 ± 0.059	0.081
F2	0.947 ± 0.059	0.062
F3	1.004 ± 0.061	0.112
F4	0.900 ± 0.059	0.071
F5	0.942 ± 0.073	0.070

Table 9.3: Results of the linear fit between the GS seeing and the aperture catalog calculated seeing, and corresponding residuals RMS.

to the seeing (~ 1.5 FWHM), that difference would amount to having a ~ 1.35 FWHM radius, or from Fig. 9.5a, a $\sim 2\%$ difference in integrated flux.

This exercise shows then the existence of a potential systematic error of 2%, on the photometric ratios issued from aperture photometry on uncrowded fields, due to wrong seeing determinations.

9.3.3 Error estimation

While being an optimal estimator for the photometric ratio between two crowded fields, the convolution kernels have some drawbacks: their usage on fields with a small number of objects[12] is difficult, and the implemented minimization approach does not gives us a statistical error on the integral of the convolution kernel (the photometric ratio). That led to the implementation of the aperture photometric ratios, as a (possibly seeing-biased) comparative measurement.

We will now study the statistical and systematic errors associated to the determination of the ratios using each method.

Statistical errors

As already seen (§ 9.2.8), the photometric ratio determined using the aperture photometry data will have a direct estimate of the statistical error, as a result of the minimization. That is not however the case for the kernel convolution ones, and we will now develop a method to estimate a reasonable approximation for it.

The original usage of the convolution kernel in `poloka` is to perform the subtraction of two images, for outlier objects (supernovæ) identification. The best seeing image will be degraded to the "photometric frame" of the worst seeing one, and subtracted. While this subtracted image is of no primary use to us, it can be used for a study of the subtracted flux residuals, and hence, of the accuracy of the convolution kernel used.

The photometric ratio $\mathcal{P}$ is, in a rough approximation, an average of N stars' (s) fluxes

---

[12]It is not uncommon to find SNfactory fields with less than 10 stars per sub-filter of the MF.

ratios, between the worst image W and the best seeing image B

$$\mathcal{P} = \frac{1}{N} \sum_s^N \frac{W_s}{B_s}$$ (9.8)

$$0 = \frac{1}{N} \sum_s^N \mathcal{P} - \frac{W_s}{B_s}$$

$$0 = \frac{1}{N} \sum_s^N \frac{\mathcal{P} B_s - W_s}{B_s} \; .$$

We can then measure on the data

$$\langle \mathcal{X}_s \rangle = \frac{1}{N} \sum_s^N \underbrace{\frac{\sum_{ij} S_{s_{ij}}}{\sum_{ij} B_{s_{ij}}}}_{\mathcal{X}_s} \; ,$$ (9.9)

where

$$S_s = \mathcal{P} B_s - W_s$$

is the star's residual flux on the subtracted image, and the fluxes are calculated by summing on the ij pixels inside a given aperture (seeing dependent, and where the seeing of S is set as the same of W).

For each pair of images, the distribution of the quantity $\mathcal{X}_s$ for the N stars should have $\langle \mathcal{X}_s \rangle \approx 0$, with $\sigma^2_{\langle \mathcal{X}_s \rangle} = \frac{\sigma^2_{\mathcal{X}_s}}{N}$, and hence we can use the dispersion around the mean $\mathcal{X}_s$ value, to set an upper bound on the statistical error on the photometric ratio

$$\sigma_{\mathcal{P}} \lesssim \frac{\sigma_{\mathcal{X}_s}}{\sqrt{N}} \; ,$$ (9.10)

To further improve the accuracy of this estimation, a weight $\mathcal{W}_s$ is introduced into the mean, in order to mimic the relative weight of each star in function of its flux, inside the kernel computation. (9.9) then becomes

$$\langle \mathcal{X}_s \rangle = \frac{1}{N} \sum_s^N \mathcal{W}_s \mathcal{X}_s \; ,$$ (9.11)

with

$$\mathcal{W}_s = \frac{N}{\sum_s w_s} w_s$$

$$w_s = \sigma^{-2}_{\frac{W_s}{B_s}} \; .$$

Distributions of $\sigma_{\mathcal{P}}$, for kernel convolution and aperture photometry photometric ratios, from ~ 6300 standard star exposures (crowded and uncrowded fields, all filters confounded), as well as their evolution with SNR (signal to noise ratio), are shown in Fig. 9.7. Both distributions peak well below the 1% level (around 0.2%), and the estimated statistical errors on the kernel convolution ratios is compatible (if slightly higher, as expected) with the aperture photometric ones, with a Spearman's rank correlation coefficient of 0.74 between both.

We can then conclude that the developed estimator of the kernel convolution error ($\sigma_{\mathcal{P}}$) produces consistent results, and that the statistical error of the photometric ratios will typically be below the percent level.
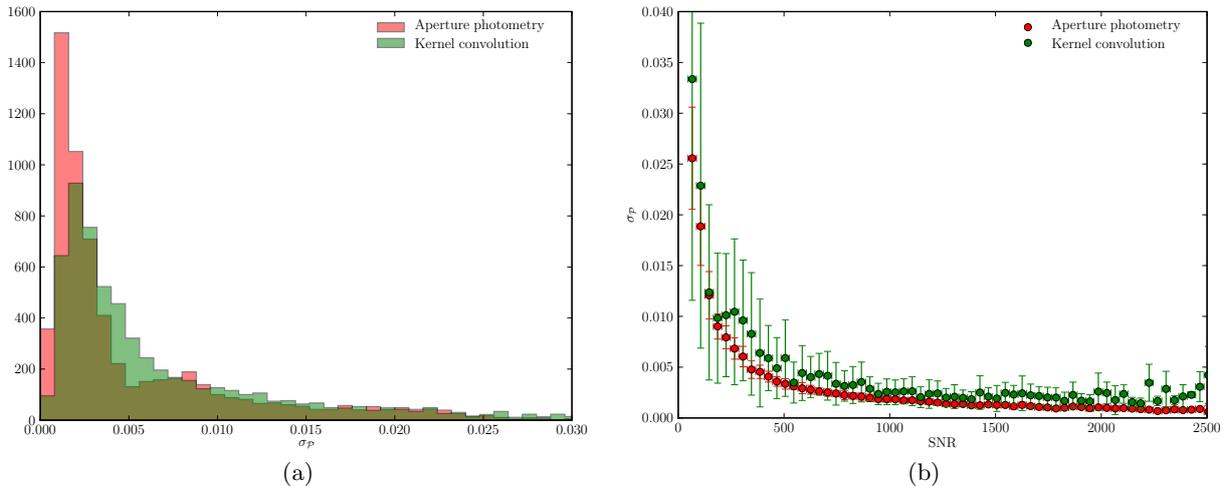
Figure 9.7: (a) Photometric ratios statistical error distribution for both kernel convolution and aperture photometry photometric ratios. (b) Median $\sigma_{\mathcal{P}}$ and nMAD (normalized median absolute deviation, nMAD = 1.4826 MAD) per SNR bin of 40, for both ratios types. $\sim$ 6300 crowded and uncrowded standard star exposures were used for both plots.

Systematic errors – simulation

For the study of possible systematic error on the ratios calculation, we resort to the usage of simulated images.

Pairs of images with the size of F2 were created, using a predefined star position and flux distribution, taken from a EG131 field with exposure time 300s. Both images have an independent PSF model, derived from F2 exposures of EG131. An uniform background is set to 1000 photo-electrons per pixel, and a constant photometric ratio is applied to the fluxes of the worst image. Finally, Poisson shot noise is added per pixel.

For each pair of images, we will perform a Monte-Carlo like procedure: for the full star list with n stars, $n-2$ steps will be run. On each of these s steps, $n-s$ stars will be selected randomly from the best image list and used to calculate the (kernel convolution and aperture photometry) photometric ratios between it and the worst image. This step is repeated a number of times (15 times typically), on each of them selecting a different subset of stars. As an example, Fig. 9.8 shows the resulting photometric ratios of this procedure, for a pair of images with different seeing conditions and a small photometric ratio. In this case, both kernel and photometric aperture ratios are consistent below the percent level, up to a certain total[13] SNR threshold, where the obtained median ratios per SNR bin start to diverge greatly, in function of the used method. To further test this behavior, different PSF/seeing and photometric ratios were used to simulate more images.

Fig. 9.9 shows the median photometric ratio evolution with total SNR, as in the middle panel of Fig. 9.8, for two sets of simulated images, each set with four different photometric ratios. Both sets of data show somewhat similar results: at high SNR, both median photometric ratios are within around 1% of the imposed one, with a clear systematic different between both. The aperture photometry ratio is relatively stable up to low SNR, while on the other hand, the kernel convolution one shows a clear departure from the expected value. Such apparent quantization of the kernel convolution when the SNR is low, or equivalently, when we have a

---

[13]The sum of the SNRs of all the available stars for the calculation.
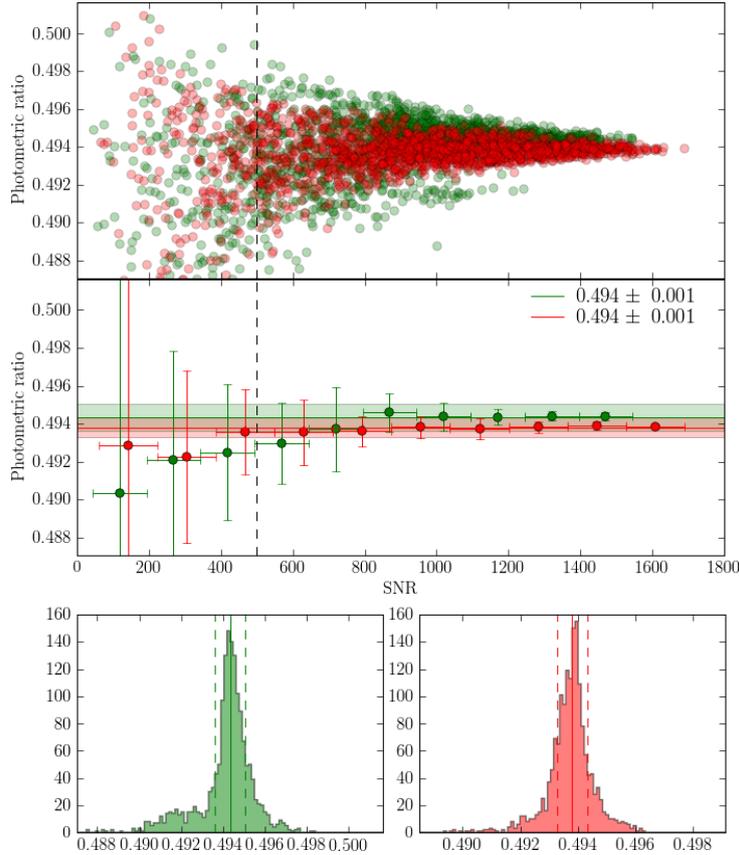
Figure 9.8: Kernel convolution (green) and aperture photometry (red) photometric ratios, obtained from a simulated image pair with 2 independent PSF models. The seeings are respectively $0.8''$ and $0.96''$ for the best and worst images, and have an imposed photometric ratio of 0.5. The top panel represents all the obtained ratios, whose median ratio per SNR bin is represented in the middle panel. The shaded areas represent the nMAD around the median ratio value, for SNR higher than the threshold (dark dashed line). The ratios' histograms are shown in the lower panel, with median and nMAD respectively represented by the full and dashed lines. In this particular case, both median ratios are out by 0.6% of the imposed one.

small number of stars for its computation, led us to the implementation of a double $\mathcal{P}$ approach. Based on the simulations results, an SNR threshold is set at 500. When the summed SNR of all the stars used for the computation of a kernel convolution ratio, is lower than this threshold, we resort to the aperture photometry ratios instead. This transition however may not be "smooth", since both ratios seem to have a systematic offset between them, on which we will develop on the next paragraph.

Using the simulated data, we can then conclude on the existence of a systematic bias of either photometric ratios methods by $\sim 1\%$ from the imposed photometric ratio.

Systematic errors − real data

A distribution of the normalized difference $\frac{\mathcal{P}_{\mathrm{aper}} - \mathcal{P}_{\mathrm{kernel}}}{\mathcal{P}_{\mathrm{kernel}}}$ for ~ 3500 photometric ratios, either from supernovæ or standard stars, with all MF sub-filters confounded, is shown in Fig. 9.10a. The minimum SNR was cutted at 500. We can see clearly a systematic difference between both ratios, with $\mathcal{P}_{\mathrm{aper}}$ higher by $\sim 1.5\%$. Fig. 9.10b shows the median normalized difference per SNR
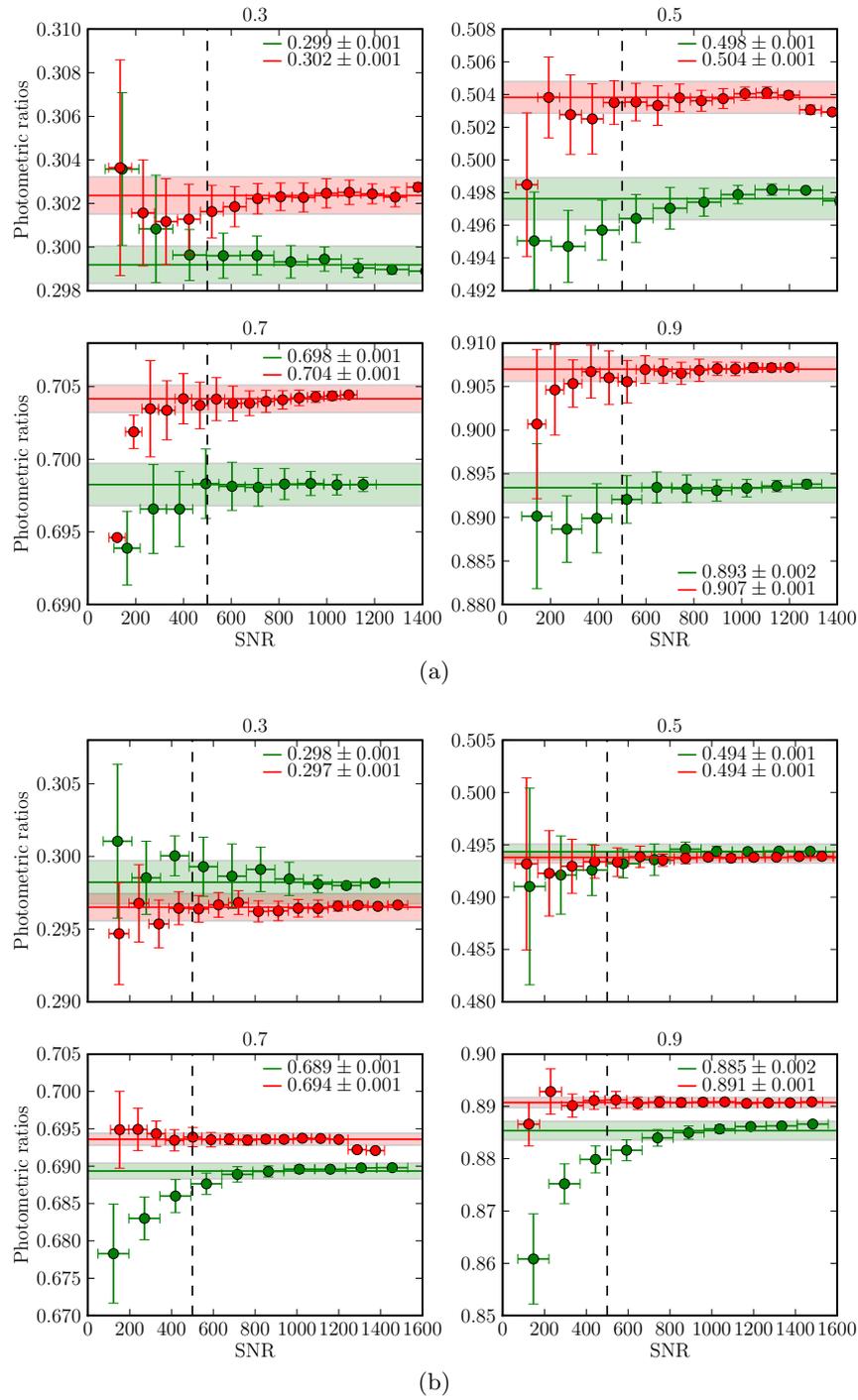
Figure 9.9: Evolution per SNR bin of the median photometric ratio and corresponding nMAD dispersion of all the Monte-Carlo events (kernel convolution in green and aperture photometry one in red), for four different (imposed) photometric ratios: 0.3, 0.5, 0.7 and 0.9. The seeings are respectively for the best and worst images, $0.82''/0.87''$ for (a) and $0.81''/0.97''$ for (b). The shaded areas represent the nMAD around the median ratio value, for SNR higher than the threshold (dark dashed line). In overall, both median ratios are accurate to $\sim 1\%$ of the imposed one.

bin. As seen before, below the SNR threshold the difference increases, due to the inaccuracy of $\mathcal{P}_{\text{kernel}}$ at low flux levels.

(a)   (b)
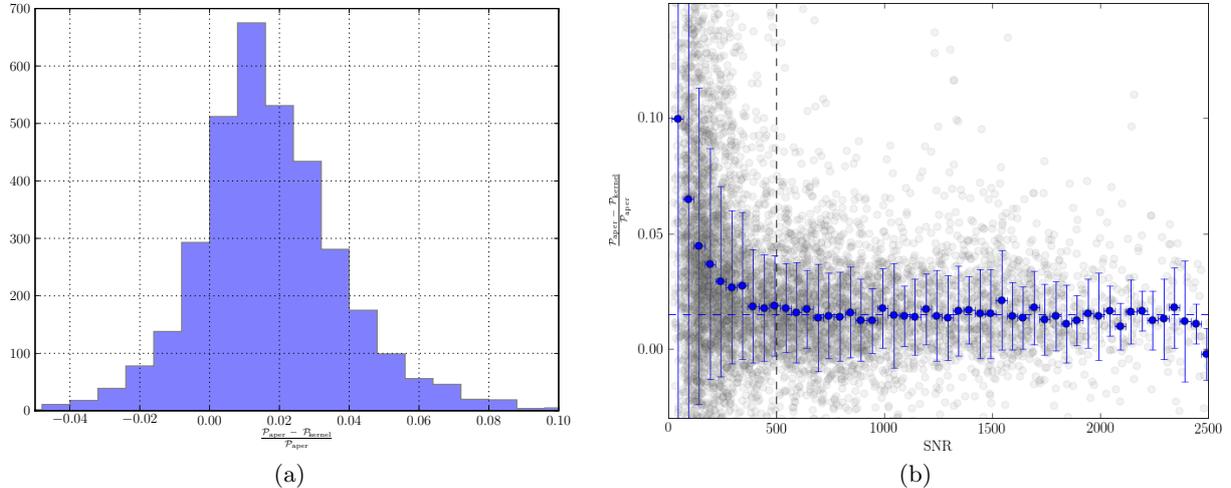
Figure 9.10: (a) Distribution of the normalized difference between photometric ratios for ~ 3500 exposures with SNR > 500. (b) Median normalized difference between photometric ratios and respective nMAD per SNR bin of 50. The vertical dashed line corresponds to the chosen SNR threshold, and the horizontal one to the median normalized difference above this threshold, 0.015.

The origin of this systematic error in unclear. Several tests were done, using supernovæ and standard stars separately, different sub-filters, fields with large numbers of stars only (to prevent seeing miscalculations) and airmass-dependent extinction removal, but in all the cases the systematic bias between $\mathcal{P}_{\text{aper}}$ and $\mathcal{P}_{\text{kern}}$ is present. A further 1.5% systematic error shall then be taken into account.

For the current status of the multi-filter analysis, both systematic errors found using either the simulation and real data, amount to a $\sim 2\%$ systematic error. That error shall then be added quadratically to the statistical error of every photometric ratio calculation.

9.3.4 Ratios statistics and comparison

The distribution of the photometric ratios calculated for 82 targets (supernovæ and standard stars), with 6800+ exposures, is shown in Fig. 9.11a. A median $\mathcal{P}$ of 0.987 is found for this data, which encompasses 4 years of SNIFS observations. 74% of the ratios are within $0.9 < \mathcal{P} < 1.1$, and 52% within $0.95 < \mathcal{P} < 1.05$, which is remarkable: half of the analyzed exposures are attenuated by no more than 5% with relation to a reference night (usually different for all targets), confirming the good observational conditions of Mauna Kea.

During night 06_163, SNIFS was used to follow a standard star (BD+174708) through a wide airmass range, from 1.9 up to 1, from which it took 14 exposures. This night is not photometric, but it is very close: the Skyprobe RMS during all the night is 0.03 mag (vs. the 0.02 mag needed to be considered photometric by the SNfactory standards). We can then use this data to check for the consistency of the calculated photometric ratios. Figs. 9.11b–9.11f show the photometric ratios per sub-filter of the MF, measured for that night. The first exposure (at higher airmass) was taken as the reference one, and each $\mathcal{P}$ is corrected for extinction due solely to the differential airmass between it and the reference one.

It can be seen that due to the small SNR, most of the chosen $\mathcal{P}$ are the aperture photometry ones (in red), which indeed has a consistently smaller dispersion than the kernel convolution ones (in green). All the $\mathcal{P}$ sequences present a similar flux scatter, between 2–3%, which is in accordance with the Skyprobe measured scatter. The similar trend in the attenuation between colors also seems to validate the gray extinction hypothesis (*cf.* § 11.1 for further tests).

We conclude then the photometric ratios section of this document. We explained in detail their importance on the SNfactory flux calibration schema, the calibration of the photometric channel raw images up to the extraction of the $\mathcal{P}$, and their errors estimation.

The full `SnfPhotPipeline` is now plugged and in production. Photometric ratios are periodically generated as new observations are made, or when new targets are observed, and saved on the central SNfactory database, for later usage on the spectra flux calibration, and subsequent creation of spectrophotometric light curves (§ 11).
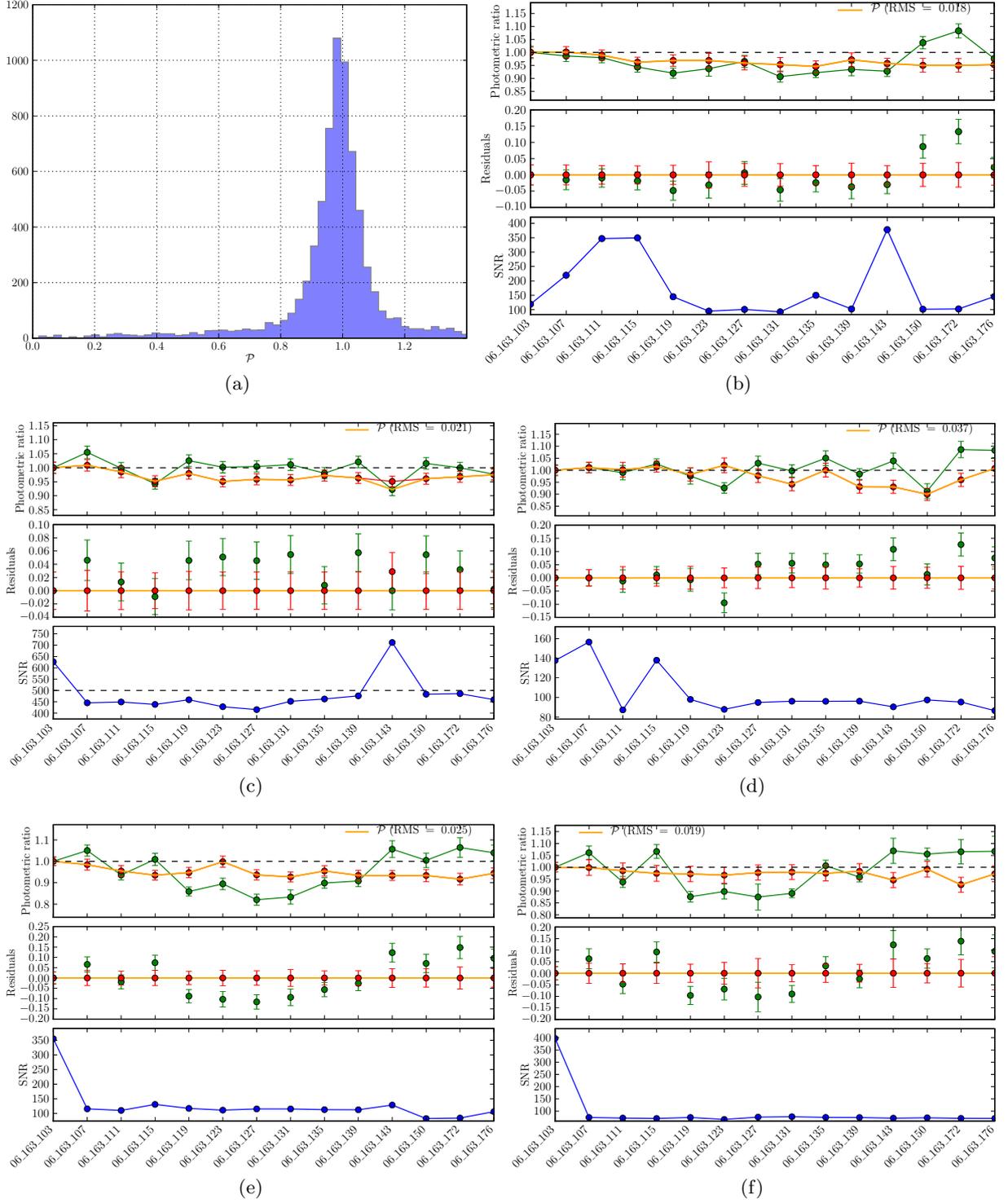
Figure 9.11: (a) $\mathcal{P}$ distribution for 6800+ exposures of 82 targets, all MF sub-filters confounded. 74% of the ratios are within $0.9 < \mathcal{P} < 1.1$. (b)–(f) $\mathcal{P}$ calculated on respectively sub-filter F1 to F5 of the temporal sequence of BD+174708 done on night 06_163. The green dots are $\mathcal{P}_{\mathrm{kernel}}$, the red ones $\mathcal{P}_{\mathrm{aper}}$, and the yellow line represents the final $\mathcal{P}$ chosen, based on the SNR threshold of 500. The middle panel represents the kernel convolution and aperture photometry ratios residuals with relation to $\mathcal{P}$, and the lower panel the SNR evolution. The first exposure is at airmass 1.9 and the last one at airmass 1. The shown $\mathcal{P}$ values were corrected for the extinction due to different airmass between exposures. The quoted error-bars include statistical and systematical errors.

127

Part IV

From bits to light curves - SNfactory's data analysis

Chapter 10

Acquisition exposures' analysis

The acquisition exposures represent an important dataset, which is specific to the photometric channel. Although single filter and with a small exposure time, these exposures are made every time an object is observed, allowing thus the creation of photometric Bessell V light curves (§ 9.2.11).

These light curves can then be used for a first study of the SNfactory sample, notably in terms of phase coverage (by estimation of the date of maximum light) and light curve stretch.

10.1 Bessell V light curves

The photometric pipeline was used to produce the acquisition light curves for all the supernovæ followed by SNIFS with at least 5 exposures. As of the middle of 2008, that sample amounts to 149 targets.

Essential for the creation of "proper" light curves using `poloka`'s simultaneous fitting algorithm, is the existence of reference exposures from the same field without the supernova. These are needed for a proper galactic background subtraction, and are usually taken around one year after the supernova was discovered. While any image can in principle be fed as a reference, it is plain to see that the obtained fluxes will be biased (and hence the fit), if the reference is not completely free of contamination by some flux of the supernova. For this purpose, the available targets were separated into two categories, with (95) and without (54) reference, and were run through `SnfPhot`.

10.1.1 SALT fits

From the 95 objects with reference exposure, 85 were successfully processed by the photometric channel pipeline up to the light curve creation step, and fitted using SALT. From these, a sample of 73 was selected based on the quality of the data and the SALT fit[1], for further study. They are listed in Table 10.1, along with the fitted parameters using SALT and SALT2. A few selected light curves for SNfactory objects are shown in Fig. 10.6.

---

[1]The acquisition images, due to their small exposure time, will be greatly affected on nights where the extinction is high. For this reason, the SALT fit is performed iteratively, with removal of outlier points at more than 3σ from the fit.

Supernova	Redshift	# points	SALT			SALT2			
			Phase	Stretch	RMS	Phase	x_1	Stretch	RMS
SN2004ef	0.0310	11	-8.6 ± 0.21	0.785 ± 0.016	0.090	-8.1 ± 0.47	-2.555 ± 0.541	0.778 ± 0.051	0.082
SN2004gc	0.0321	9	1.1 ± 3.44	0.883 ± 0.073	0.100	1.7 ± 0.17	-1.022 ± 0.496	0.890 ± 0.046	0.103
SN2004gs	0.0274	7	-3.0 ± 0.20	0.638 ± 0.025	0.228	-1.9 ± 0.97	-3.294 ± 0.924	0.737 ± 0.090	0.258
SN2005di	0.0253	13	-11.2 ± 0.03	0.929 ± 0.004	0.027	-11.5 ± 0.12	-0.026 ± 0.197	0.978 ± 0.018	0.025
SN2005el	0.0149	14	-6.4 ± 0.03	0.783 ± 0.001	0.042	-6.4 ± 0.31	-2.144 ± 0.286	0.804 ± 0.027	0.021
SN2005hj	0.0575	9	-1.7 ± 0.16	1.133 ± 0.014	0.021	-2.0 ± 0.68	1.541 ± 0.491	1.126 ± 0.045	0.018
SN2005ki	0.0192	8	-11.2 ± 0.15	0.854 ± 0.013	0.091	-10.8 ± 0.77	-1.809 ± 0.935	0.828 ± 0.087	0.053
SN2006D	0.0085	10	-7.8 ± 0.00	0.760 ± 0.001	0.042	-7.9 ± 0.25	-2.591 ± 0.548	0.775 ± 0.052	0.039
SN2006X	0.0052	10	-12.1 ± 0.02	0.869 ± 0.002	0.079	-12.9 ± 0.17	-0.134 ± 0.204	0.968 ± 0.019	0.074
SN2006ac	0.0231	6	-4.5 ± 0.04	0.967 ± 0.006	0.018	-5.0 ± 0.18	-0.355 ± 0.335	0.948 ± 0.031	0.012
SN2006bk	0.0495	13	2.2 ± 0.19	0.987 ± 0.014	0.092	2.2 ± 0.44	0.857 ± 0.436	1.060 ± 0.040	0.070
SN2006do	0.0284	11	-3.8 ± 0.03	0.800 ± 0.006	0.038	-3.9 ± 0.06	-2.665 ± 0.605	0.771 ± 0.057	0.039
SN2007bc	0.0208	12	-1.0 ± 0.06	0.574 ± 0.008	0.385	0.4 ± 0.78	-4.677 ± 0.718	0.693 ± 0.077	0.325
SN2007bd	0.0310	11	-2.6 ± 0.05	0.901 ± 0.006	0.028	-2.5 ± 0.19	-0.809 ± 0.297	0.908 ± 0.027	0.023
SN2007cq	0.0258	17	-5.4 ± 0.03	0.899 ± 0.004	0.058	-5.5 ± 0.13	-1.054 ± 0.209	0.887 ± 0.019	0.054
SN2007fr	0.0512	15	-3.7 ± 0.00	0.701 ± 0.001	0.062	-2.9 ± 0.50	-3.280 ± 0.475	0.738 ± 0.046	0.147
SNF20050728-000	0.0424	12	-2.4 ± 0.32	1.381 ± 0.033	0.078	-3.9 ± 1.45	5.000 ± 1.223	1.420 ± 0.137	0.109
SNF20050728-006	0.0591	13	-4.9 ± 0.26	1.071 ± 0.029	0.105	-5.7 ± 0.35	0.887 ± 0.455	1.063 ± 0.042	0.108
SNF20050821-007	0.0595	6	-4.0 ± 0.08	1.077 ± 0.012	0.033	-4.9 ± 0.32	0.888 ± 0.445	1.063 ± 0.041	0.027
SNF20050824-002	0.1200	8	-0.8 ± 1.30	1.157 ± 0.054	0.068	0.3 ± 3.01	3.284 ± 2.042	1.287 ± 0.198	0.049
SNF20050826-004	0.0993	5	11.5 ± 2.91	1.093 ± 0.054	0.042	9.6 ± 4.33	0.149 ± 0.570	0.994 ± 0.052	0.018
SNF20050828-001	0.0803	5	0.6 ± 0.19	0.996 ± 0.017	0.033	-0.5 ± 0.51	-0.764 ± 0.441	0.912 ± 0.041	0.025
SNF20050828-003	0.0678	12	1.0 ± 0.25	0.966 ± 0.011	0.030	0.5 ± 0.37	-0.548 ± 0.236	0.931 ± 0.022	0.029
SNF20050829-003	0.0454	8	3.2 ± 0.23	0.801 ± 0.007	0.024	3.8 ± 0.93	-2.175 ± 0.385	0.802 ± 0.036	0.034
SNF20050927-005	0.0407	16	2.1 ± 0.18	1.025 ± 0.007	0.045	0.9 ± 0.35	0.118 ± 0.191	0.991 ± 0.018	0.048
SNF20051003-004	0.0343	21	-10.9 ± 0.01	0.997 ± 0.001	0.114	-11.0 ± 0.13	0.605 ± 0.172	1.036 ± 0.016	0.117
SNF20051113-000	0.0800	7	2.7 ± 0.04	0.835 ± 0.007	0.050	4.4 ± 1.72	-1.187 ± 1.256	0.877 ± 0.116	0.049
SNF20060511-014	0.0476	14	-0.4 ± 0.14	0.689 ± 0.008	0.078	1.8 ± 0.93	-3.319 ± 0.572	0.736 ± 0.056	0.080
SNF20060512-002	0.0510	15	4.5 ± 0.62	0.935 ± 0.016	0.091	2.9 ± 0.56	-0.917 ± 0.256	0.899 ± 0.024	0.086
SNF20060514-003	0.0880	10	14.1 ± 1.17	1.289 ± 0.030	0.067	9.8 ± 0.05	1.863 ± 0.582	1.157 ± 0.054	0.098
SNF20060521-001	0.0670	11	2.7 ± 0.54	0.877 ± 0.021	0.080	3.5 ± 0.88	-1.215 ± 0.358	0.874 ± 0.033	0.077
SNF20060521-008	0.0551	11	4.4 ± 0.58	0.899 ± 0.017	0.049	4.0 ± 0.66	-1.006 ± 0.285	0.891 ± 0.026	0.044
SNF20060526-003	0.0778	15	-6.3 ± 0.16	1.024 ± 0.018	0.111	-7.0 ± 0.19	0.198 ± 0.292	0.998 ± 0.027	0.111
SNF20060530-003	0.0567	16	3.6 ± 0.01	1.123 ± 0.003	0.044	3.3 ± 0.06	1.579 ± 0.345	1.129 ± 0.032	0.046
SNF20060609-002	0.0397	20	-3.3 ± 0.07	0.964 ± 0.006	0.041	-3.7 ± 0.16	-0.231 ± 0.147	0.959 ± 0.013	0.047
SNF20060618-014	0.0638	14	2.1 ± 0.33	1.043 ± 0.013	0.044	1.5 ± 0.55	0.526 ± 0.289	1.029 ± 0.027	0.026
SNF20060618-023	0.1132	13	-7.5 ± 0.20	0.987 ± 0.016	0.079	-8.0 ± 0.22	-0.233 ± 0.241	0.959 ± 0.022	0.074
SNF20060621-012	0.0625	11	5.6 ± 0.01	0.780 ± 0.001	0.074	8.6 ± 1.55	-1.887 ± 0.366	0.822 ± 0.034	0.083
SNF20060621-015	0.0553	14	-2.2 ± 0.17	1.056 ± 0.011	0.035	-2.9 ± 0.44	0.744 ± 0.287	1.050 ± 0.026	0.032
SNF20060624-019	0.0742	14	1.5 ± 1.08	1.008 ± 0.057	0.131	1.5 ± 0.89	0.201 ± 0.626	0.999 ± 0.057	0.127
SNF20060720-042	0.0832	8	-4.9 ± 0.15	1.159 ± 0.033	0.023	-6.2 ± 0.50	1.606 ± 0.924	1.132 ± 0.085	0.013
SNF20060907-000	0.0575	12	-2.8 ± 0.10	0.939 ± 0.008	0.112	-3.6 ± 0.28	-1.147 ± 0.314	0.880 ± 0.029	0.100
SNF20060908-004	0.0500	16	3.0 ± 0.01	1.119 ± 0.000	0.041	0.7 ± 0.51	0.971 ± 0.253	1.071 ± 0.023	0.051
SNF20060911-014	0.0900	12	-2.9 ± 0.30	1.086 ± 0.025	0.129	-3.6 ± 0.51	0.813 ± 0.464	1.056 ± 0.043	0.121

Continued on next page. . .

Table 10.1 – Continued

Supernova	Redshift	# points	SALT			SALT2			
			Phase	Stretch	RMS	Phase	x_1	Stretch	RMS
SNF20060912-000	0.0733	9	-0.2 ± 0.26	0.958 ± 0.027	0.142	-0.4 ± 0.50	-0.868 ± 0.607	0.903 ± 0.056	0.144
SNF20060915-006	0.0892	6	2.3 ± 0.05	1.062 ± 0.010	0.066	5.2 ± 2.26	1.089 ± 0.781	1.083 ± 0.072	0.061
SNF20060919-007	0.0702	5	0.4 ± 0.56	0.964 ± 0.033	0.018	-0.2 ± 1.66	-0.875 ± 0.979	0.903 ± 0.090	0.017
SNF20061011-005	0.0230	13	-2.6 ± 0.03	0.987 ± 0.002	0.025	-3.1 ± 0.23	-0.228 ± 0.169	0.959 ± 0.016	0.051
SNF20061020-000	0.0391	16	-1.4 ± 0.05	0.813 ± 0.005	0.024	-1.3 ± 0.28	-2.184 ± 0.356	0.802 ± 0.033	0.054
SNF20061022-014	0.0414	12	0.5 ± 0.29	0.697 ± 0.018	0.043	2.5 ± 1.17	-3.248 ± 0.852	0.739 ± 0.082	0.040
SNF20061024-000	0.0567	16	-0.0 ± 1.04	0.753 ± 0.075	0.155	1.1 ± 1.39	-2.627 ± 0.923	0.773 ± 0.087	0.144
SNF20061030-010	0.0299	15	-2.3 ± 0.09	0.958 ± 0.006	0.139	-3.0 ± 0.18	-0.417 ± 0.178	0.942 ± 0.016	0.132
SNF20061109-002	0.0433	9	0.5 ± 0.48	0.893 ± 0.026	0.071	0.6 ± 0.65	-1.159 ± 0.452	0.879 ± 0.042	0.062
SNF20070331-014	0.0671	14	2.8 ± 0.74	0.910 ± 0.024	0.095	2.1 ± 0.76	-1.211 ± 0.419	0.875 ± 0.039	0.086
SNF20070331-025	0.0709	13	-4.3 ± 0.72	0.955 ± 0.038	0.123	-4.6 ± 0.70	-1.479 ± 0.560	0.853 ± 0.052	0.090
SNF20070417-002	0.0898	13	0.6 ± 0.04	0.786 ± 0.007	0.121	1.3 ± 0.03	-2.648 ± 0.617	0.772 ± 0.058	0.117
SNF20070420-001	0.0860	13	-1.4 ± 0.35	1.137 ± 0.029	0.050	-2.2 ± 0.82	1.491 ± 0.571	1.121 ± 0.053	0.055
SNF20070424-003	0.0671	19	-8.5 ± 0.12	1.013 ± 0.013	0.054	-8.9 ± 0.16	0.329 ± 0.215	1.011 ± 0.020	0.048
SNF20070427-001	0.0767	15	1.1 ± 0.47	1.080 ± 0.023	0.078	0.3 ± 0.78	0.951 ± 0.437	1.069 ± 0.040	0.083
SNF20070429-000	0.0663	21	2.5 ± 0.57	0.907 ± 0.015	0.080	2.7 ± 0.70	-1.079 ± 0.225	0.885 ± 0.021	0.082
SNF20070506-006	0.0348	27	-15.0 ± 0.02	1.062 ± 0.002	0.046	-15.1 ± 0.10	1.289 ± 0.170	1.102 ± 0.016	0.057
SNF20070528-003	0.1167	15	-7.3 ± 0.19	0.980 ± 0.023	0.093	-7.8 ± 0.22	-0.028 ± 0.372	0.977 ± 0.034	0.083
SNF20070531-011	0.0357	16	1.1 ± 0.17	0.811 ± 0.009	0.038	1.6 ± 0.56	-2.117 ± 0.365	0.806 ± 0.034	0.043
SNF20070617-008	0.0454	14	7.2 ± 0.02	0.804 ± 0.001	0.074	7.8 ± 1.70	-1.886 ± 0.387	0.823 ± 0.036	0.065
SNF20070712-003	0.0770	18	-3.9 ± 0.15	0.955 ± 0.011	0.043	-4.2 ± 0.12	-0.533 ± 0.209	0.932 ± 0.019	0.048
SNF20070714-007	0.0417	17	-1.6 ± 0.17	0.800 ± 0.012	0.118	-0.5 ± 0.36	-1.521 ± 0.293	0.850 ± 0.027	0.103
SNF20070717-003	0.0860	16	-7.5 ± 0.12	0.868 ± 0.015	0.070	-7.7 ± 0.21	-1.466 ± 0.340	0.854 ± 0.031	0.064
SNF20070725-001	0.0679	16	1.9 ± 0.04	1.152 ± 0.004	0.049	1.3 ± 1.18	1.650 ± 0.506	1.136 ± 0.047	0.047
SNF20070727-016	0.0662	15	2.1 ± 0.38	1.040 ± 0.013	0.053	1.4 ± 0.65	0.465 ± 0.261	1.023 ± 0.024	0.047
SNF20070802-000	0.0645	17	-6.0 ± 0.16	0.974 ± 0.016	0.193	-6.5 ± 0.18	-0.319 ± 0.249	0.951 ± 0.023	0.181
SNF20070803-005	0.0314	16	-8.8 ± 0.01	1.015 ± 0.002	0.037	-9.2 ± 0.14	0.756 ± 0.215	1.051 ± 0.020	0.040
SNF20070806-026	0.0451	20	-0.3 ± 0.11	0.765 ± 0.008	0.088	0.6 ± 0.49	-2.568 ± 0.401	0.777 ± 0.038	0.098
SNF20070810-004	0.0835	18	-7.1 ± 0.07	0.962 ± 0.004	0.101	-7.6 ± 0.16	-0.792 ± 0.240	0.910 ± 0.022	0.105

Table 10.1: Fit results using SALT and SALT2 for 73 acquisition (Bessell V) light curves, with reference exposure. Stretch is derived directly from the fit, phase (in days) is calculated using the derived date of maximum and the date of the first spectral exposure for each target, and RMS is the fit residuals RMS in magnitudes. The color parameters are fixed since it is a single color fit.

For easier comparison, the SALT2 x_1 parameter (*cf.* § 2.3.4) is also given in the equivalent SALT stretch, using the approximated transformation derived by Guy et al. (2007)

$$s\,(SALT) = 0.98 + 0.091\,x_1 + 0.003\,x_1^2 - 0.00075\,x_1^3\,. \tag{10.1}$$

The shown phase in days, is calculated using the date of maximum (on a B filter), derived by the fit, and the date of the first spectral exposure of the object taken by SNIFS. No rest-frame B magnitude (also derived by the fit) is show, due to the nonexistence of V filter zero points: the one derived in § 8.7 may be used as a reference one, for getting reasonable light curves (up to ~ 0.2 mag) (Fig. 10.6), however it is not usable as an accurate zero point since we need to take into account the atmospheric transmission of the reference night. That could be accomplished with a similar approach to the spectrum flux calibration, by using acquisition exposures of standard stars observed on a common photometric night with each supernova. However, only 6 of the several standard stars observed by SNIFS are faint enough to not be saturated on a typical acquisition exposure, decreasing the feasibility of this approach. Due to the development deemed necessary to implement such pipeline, the fact that it would not be able to be used on all supernovæ, and since stretch and phase measurements are independent of the zero point, it was hence decided to leave it as low priority, for future updates.

10.2   SNfactory sub-dataset phase and stretch distribution

This sub-dataset represents roughly half of the objects observed by SNIFS, and thus can be used as a representative sample for the study of the phase and stretch distribution of the full SNfactory dataset. Both phase and stretch distributions of the 70 objects with light curve residuals RMS < 0.15 are shown in Fig. 10.1.
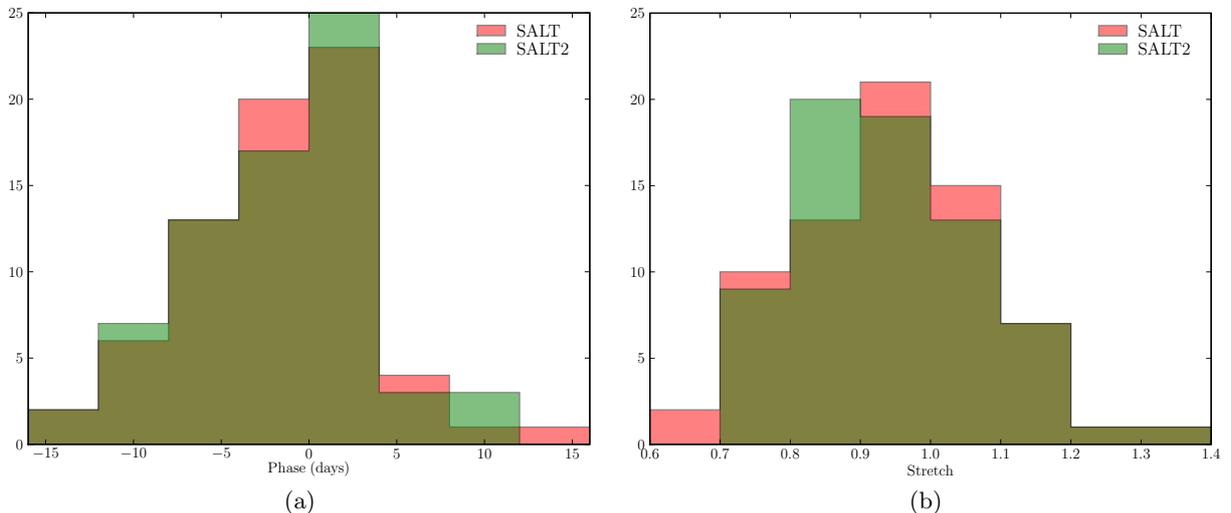
Figure 10.1: Fitted parameters from the acquisition light curves, using SALT and SALT2, for a subsample of 70 objects with reference exposure: (a) phase (date of first observation with relation to maximum B light) distribution per 4 days bin; and (b) stretch distribution per 0.1 bin.

One can notice the slight differences between the results of both fit models, which will be further developed in § 10.3. The bulk of the objects had its first observation earlier than 4 days after maximum, with $\sim 55\%$ of them first observed at pre-maximum phase. The measured

median stretch and corresponding nMAD for this dataset are 0.960 ± 0.139 and 0.931 ± 0.149, using SALT and SALT2 respectively.

We can also use these results and compare them with published data, notably the recent SCP Union compilation. That provides a consistency check of the measured parameters (the acquisition light curves are obviously single color, which may bias the fit results with relation to multi color fits), as well as a first comparison of a (representative) sub-sample of the SNfactory dataset and the nearby dataset currently used for cosmology.

10.2.1 SCP Union compilation comparison

The SCP Union dataset published by Kowalski et al. (2008), is the biggest uniformly analyzed supernovæ compilation to date: the number of supernovæ which passes cuts defined by the authors, for usability on the cosmological analysis, amounts to 307. 67 of the SNfactory objects selected in the last section would also pass the same cuts, which more than doubles the number of nearby ($0.015 < z < 0.1$) supernovæ present in the compilation (51). The full SNfactory dataset alone is 3 times larger and samples all the smooth Hubble flow, as can be seen in Fig. 10.2a, where the redshift distribution for 141 SNfactory supernovæ is compared to the nearby SCP Union ones.
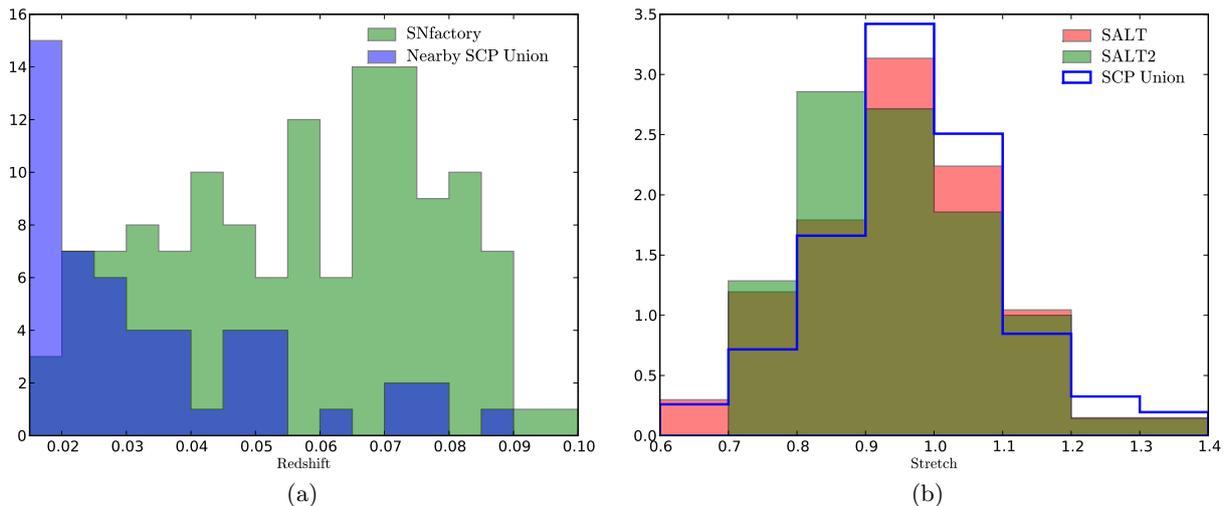
Figure 10.2: (a) Redshift distribution for 141 SNfactory supernovæ and the nearby ($z < 0.1$) SCP Union sample, per 0.01 redshift bins. (b) Normalized stretch distributions for 70 SNfactory objects and the ones from the full SCP Union sample, per 0.1 bin.

Since the light curve fitter used by Kowalski et al. (2008) is SALT, we can easily compare their results, notably the stretch distribution with the one obtained using the SNIFS acquisition light curves. Fig. 10.2b shows the normalized stretch histograms as obtained using SALT and SALT2, compared to the stretchs of the full SCP Union dataset (both for $z > 0.15$). The distributions are fairly similar, especially the one using SALT: a Kolmogorov-Smirnov test of the two samples shows a 85% probability of both being originated from a common distribution. The median and nMAD for the full SCP Union stretch distribution is 0.96 ± 0.119.

Even though originating from single color light curves, the obtained stretchs using SALT are thus remarkably consistent with the ones from the SCP Union. However, that is not the case with SALT2, whose stretchs (derived using the approximation from $x1$) are slightly smaller in average. While it is possible that such difference comes from the way of how each model

deals with single color fits, there is another important factor that may introduce bias into the fitter and may differ from SALT and SALT2: the existence or not of light curve points before maximum light.

10.3 SALT bias

To test the hypothesis of a SALT bias with relation to the presence or not of pre-maximum points, several targets with phase < 0 were chosen from the preceding sample. Each target was fitted twice, using all the available points, and after removal of all pre-maximum points. On Fig. 10.3 and Fig. 10.4 are shown comparisons of the stretch and date of maximum parameters obtained using SALT and SALT2.
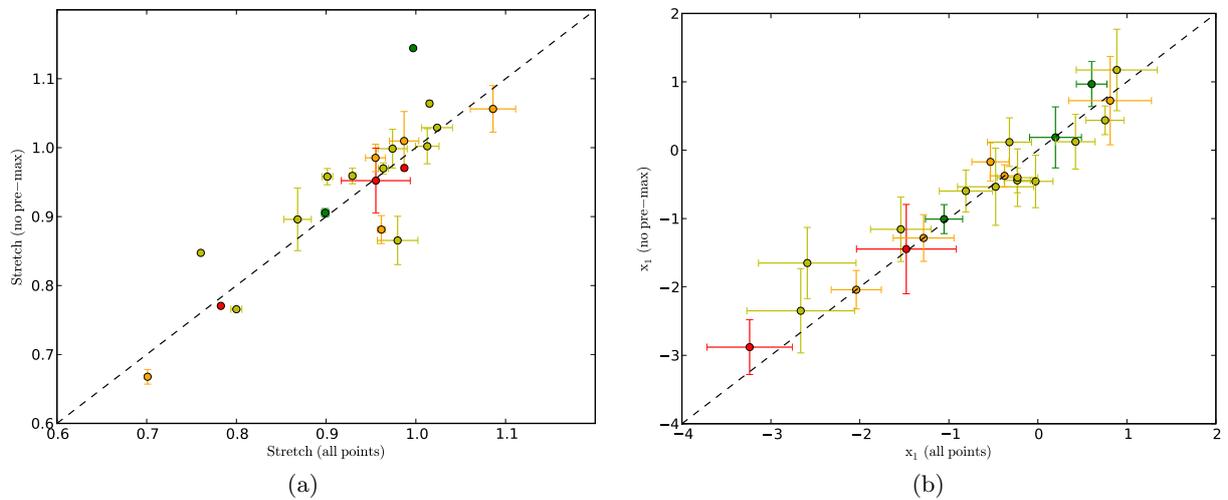
Figure 10.3: (a)–(b) Fitted stretch and x_1 using only post-maximum points *vs.* all the points, for SALT and SALT2 respectively. The colors used represent the number of pre-maximum points per supernova: red - 1 point, orange - 2 points, yellow - 3/4 points, green - > 4 points.

In the case of SALT, a trend emerges where most of the stretchs calculated without pre-maximum points seem over estimated with relation to the ones with the full light curve. On the contrary, the equivalent x_1 parameters fitted using the SALT2 updated model, present a scatter consistent with the estimated errors, rather than a bias. It should be noticed that the shown SALT2 fits account for the diagonal model uncertainties in the χ^2 minimization, and are hence more robust with relation to SALT ones.

In terms of the determination of the date of maximum, both models are consistent, under-estimating it in average by ~ 0.1 days when no pre-maximum points are present. The scatter however is significant for both models (slightly smaller for SALT2), leading to the conclusion that a determination of the date of maximum without pre-maximum points will have a typical ~ 1 day uncertainty.

Concluding, it seems likely that the measured stretchs using SALT are over-estimated for the post-maximum acquisition light curves, with relation to the SALT2 ones. This could explain the small difference in distributions as seen in Fig. 10.1b. For comparison, Fig. 10.5a shows the stretch distributions for the targets with phase < 0, and indeed they are mostly compatible. Fig. 10.5b compares the date of maximum estimated using SALT or SALT2 for the same targets. A median difference of 0.36 days is observed between both estimations, with the SALT2 fit giving
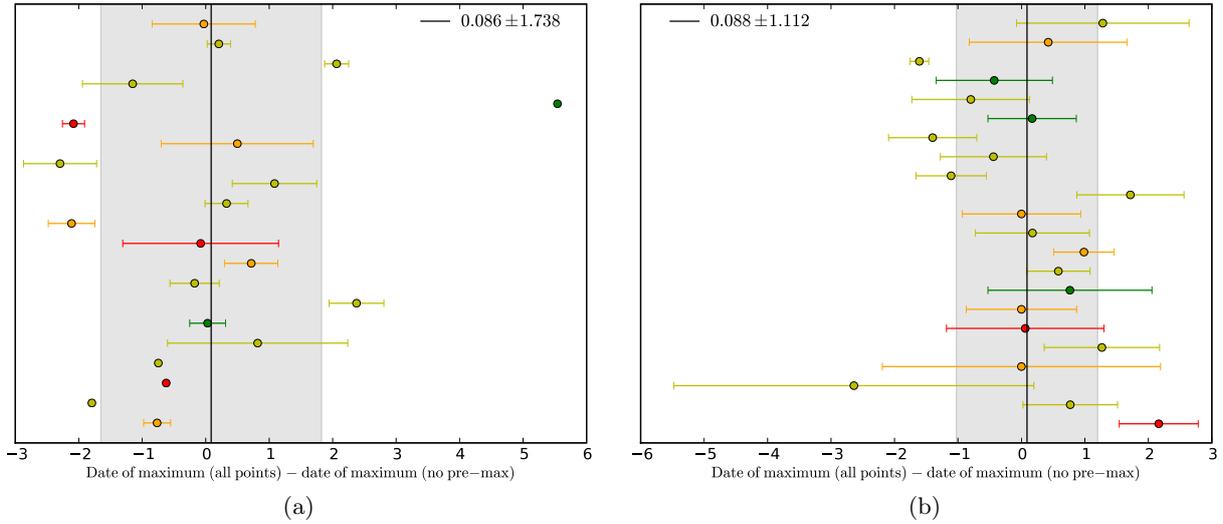
Figure 10.4: (a)–(b) Difference in the date of maximum fitted using all the points and only post-maximum points, for SALT and SALT2. The objects are ordered from bottom to top in increasing stretch. The shaded areas represent the RMS around the mean value. The colors used represent the number of pre-maximum points per supernova: red - 1 point, orange - 2 points, yellow - 3/4 points, green - > 4 points.

larger values.

The shown results are obviously dependent of the fact that we are using single color light curves. It is unclear if similar biases would be observed when comparing post-maximum multi color light curves fitted using SALT and SALT2. Being the fit intrinsically more robust, that is however less likely. Nonetheless, if a small bias exists, targets from the SCP Union compilation (which uses SALT and light curves with phase < 6 days) could have biased estimations of stretch (and possibly color). The authors do not mention the observation of any such bias, and that
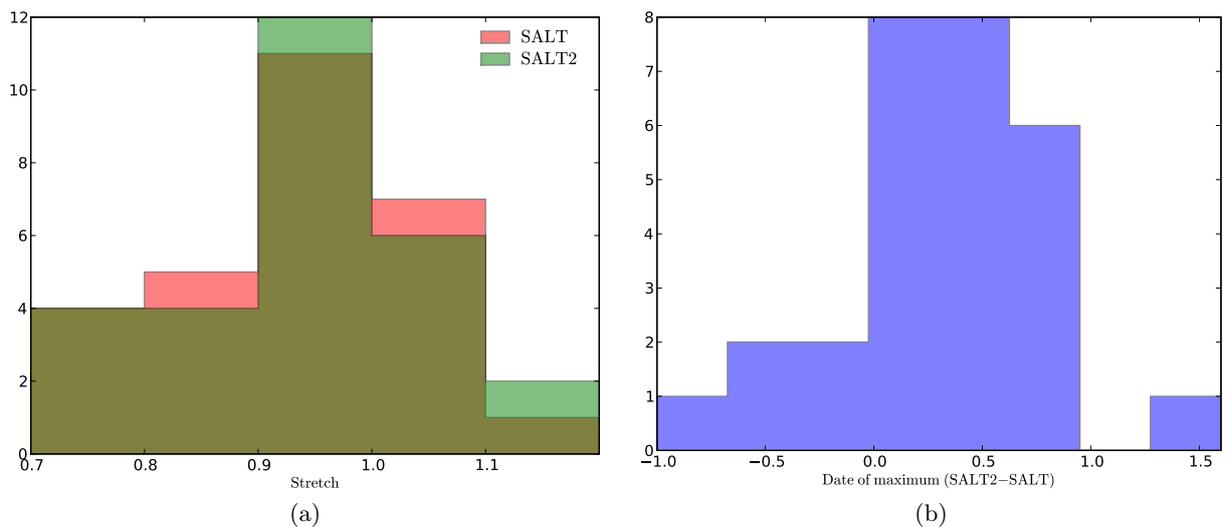
Figure 10.5: (a) Stretch and (b) date of maximum difference distributions, for the objects with pre-maximum light curve points.

137

kind of study is beyond the scope of this exercise.
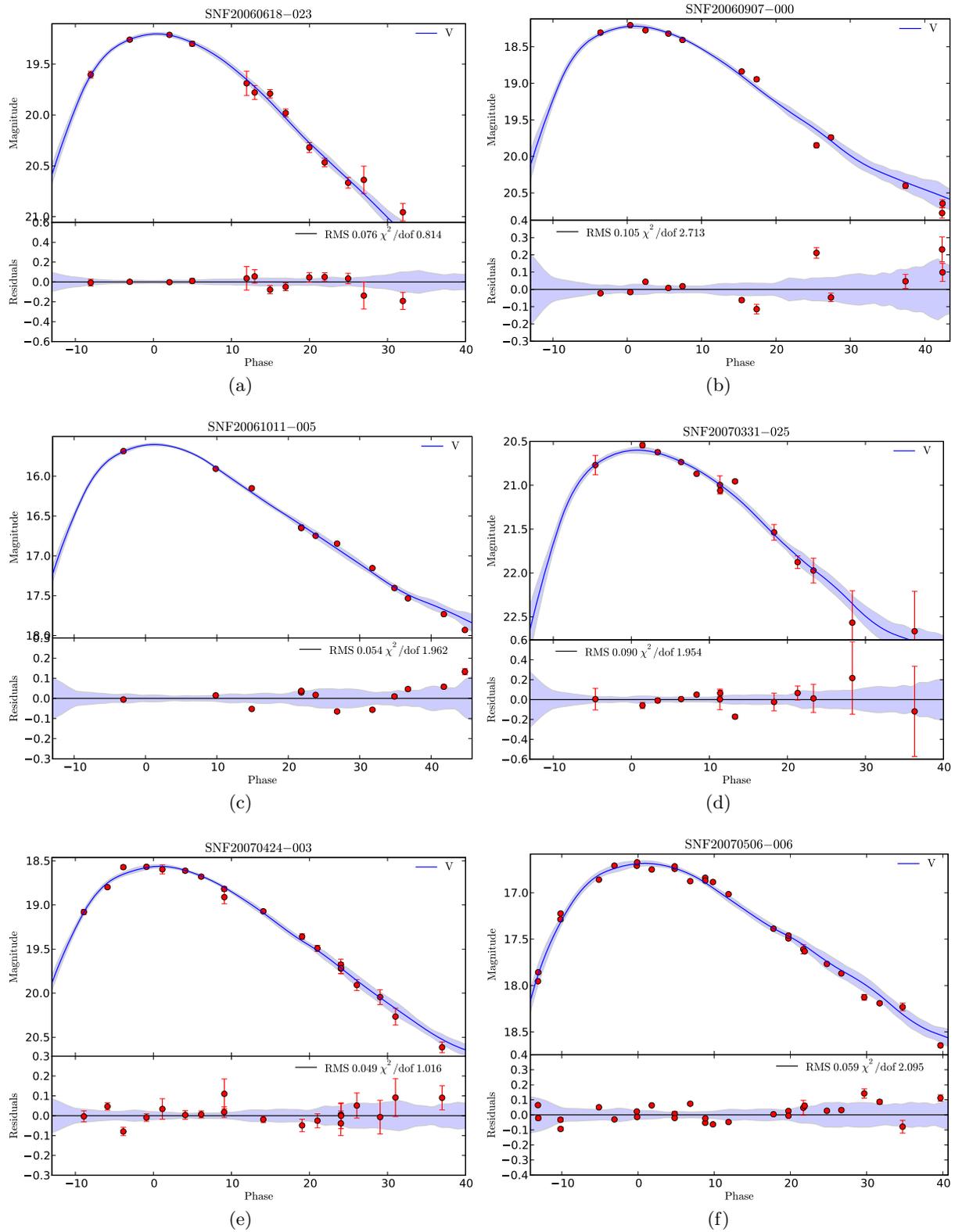
Figure 10.6: Acquisition (Bessell V) light curves, for 6 SNfactory targets with reference exposure and pre-maximum points.

Chapter 11

Spectrophotometric light curves

In Part III of this document, the calibration and determination methods of the photometric ratios ($\mathcal{P}$) were explained in detail. As we saw in § 7, they are essential for the flux calibration of the supernovæ spectra observed by SNIFS on non-photometric nights. Their final purpose is then the construction of spectrophotometric light curves, using the absolutely flux calibrated spectra, which I will present in this chapter.

11.1 Gray extinction hypothesis testing

We've seen in § 7.3.2 that the current SNfactory flux calibration pipeline implementation uses the gray extinction hypothesis. That means that it assumes an *a*chromatic differential atmospheric extinction between nights, that can be approximated by using an extinction template with a scaling parameter, currently F2's photometric ratio. Using the previously calculated photometric ratios we can in principle test that assumption, by comparing $\mathcal{P}$ for different filters for a large number of nights.

A total of 155 exposures from EG131, a standard star with a crowded field, were used. For each exposure, the weighted mean of the five $\mathcal{P}$ from the MF sub-filters (each one corrected to the reference exposure airmass using our average extinction model, Fig. 4.8a), is calculated. Fig. 11.1a shows the evolution of the mean photometric ratio for all the considered exposures. The distribution of each filter's photometric ratio residual, with relation to the average one ($\mathcal{P} - \langle \mathcal{P} \rangle$), are shown in Fig. 11.1b and Table 11.1.

Filter	Median	nMAD
F1	-0.011	0.028
F2	0.004	0.013
F3	0.012	0.020
F4	0.009	0.014
F5	-0.007	0.032

Table 11.1: Median and normalized MAD for the distributions of the residual photometric ratio relative to the average one ($\mathcal{P} - \langle \mathcal{P} \rangle$), for each sub-filter of the MF.

Once again, F2 shows the best behavior of all the filters: its residual $\mathcal{P}$ with relation to the average one show the smaller scatter, of $\sim 1\%$. Both extreme colors, F1 and F5 have the largest variations, which was expected: F1 probes the bluest part of the optical window, where the extinction is most pronounced, due to Rayleigh scattering; and F5 maps a wavelength range full
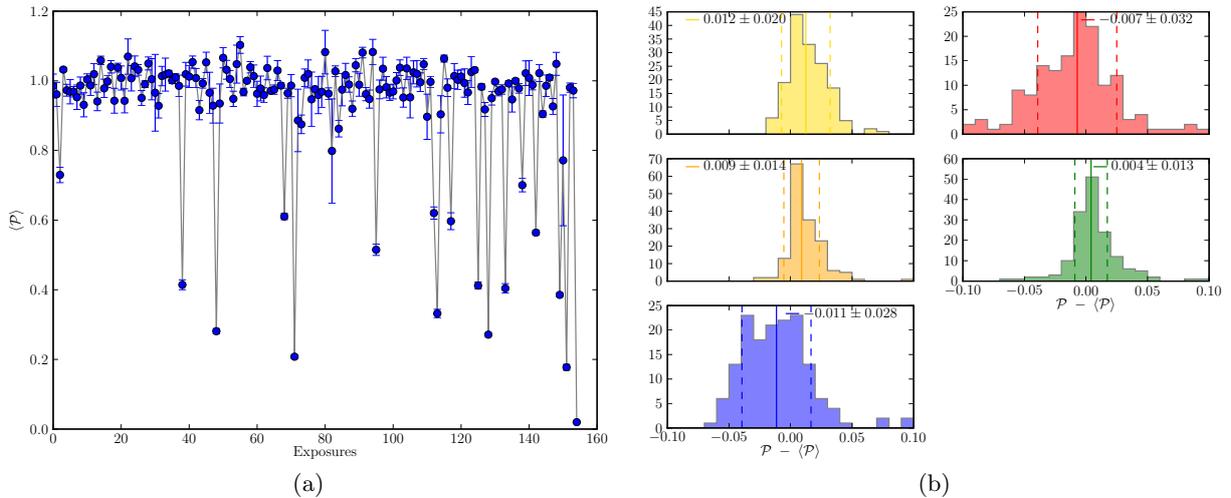
Figure 11.1: (a) Average $\mathcal{P}$ (over all sub-filters) for the 155 EG131 exposures used. The error-bars represent the RMS of the $\mathcal{P}$ from the five sub-filters. (b) Distribution of the residual $\mathcal{P}$ with relation to the one obtained by averaging over all sub-filters of the MF. The relative position of the plots is the same as in the MF: F3, F5, F4, F2 and F1 are placed from left-right, top-bottom. The vertical lines represent the median value and respective nMAD.

of telluric lines due to the water vapor (Fig. 4.8b), which present a large variability and hence will not follow the other filters.

From this study (Table 11.1), we can conclude that in average, our colors are correct at the percent level, since no trend of the median offset of each filter is seen in function of the wavelength. There is however still room for improvements, since the observed dispersion around this gray hypothesis is $\sim 3\%$ for individual nights, bigger than the photometric ratios systematic error. Work under way to compute an extinction template per night (instead of using the average one), and/or the usage of information from all the sub-filters, should help to reduce this effect.

11.2   Fundamental standard calibrators

SNfactory uses an ensemble of spectrophotometric standard stars, for its flux calibration (§ 7). These targets are observed several times during the year, both on photometric and non-photometric nights. We can thus generate synthesized photometric light curves for each one of them, using the flux calibrated spectra, in order to measure the current photometric precision of the SNfactory calibration pipeline. Light curves on Bessell BVR filters, for the 6 SNfactory "favorite" calibrators (from the internal *KANSAS* run) are shown in Fig. 11.2, and the corresponding mean and RMS values for photometric and non-photometric nights are in Table 11.2.

Excepting P177D, which is under investigation at the moment, the tabulated magnitudes are around 1σ of the median synthesized magnitude, but all seem however to be systematically lower than expected. The origin of this 1–2% bias is unclear. It is present both on the photometric and non-photometric night samples, thus can not be due to the photometric ratios. It would rather seem to be a difference in the definition of the filters (Bessell BVR) used in this study to integrate the light curves, and the ones from the published data, or some different zero-point used to convert between filter/photometric systems (our magnitudes are based on the Vega
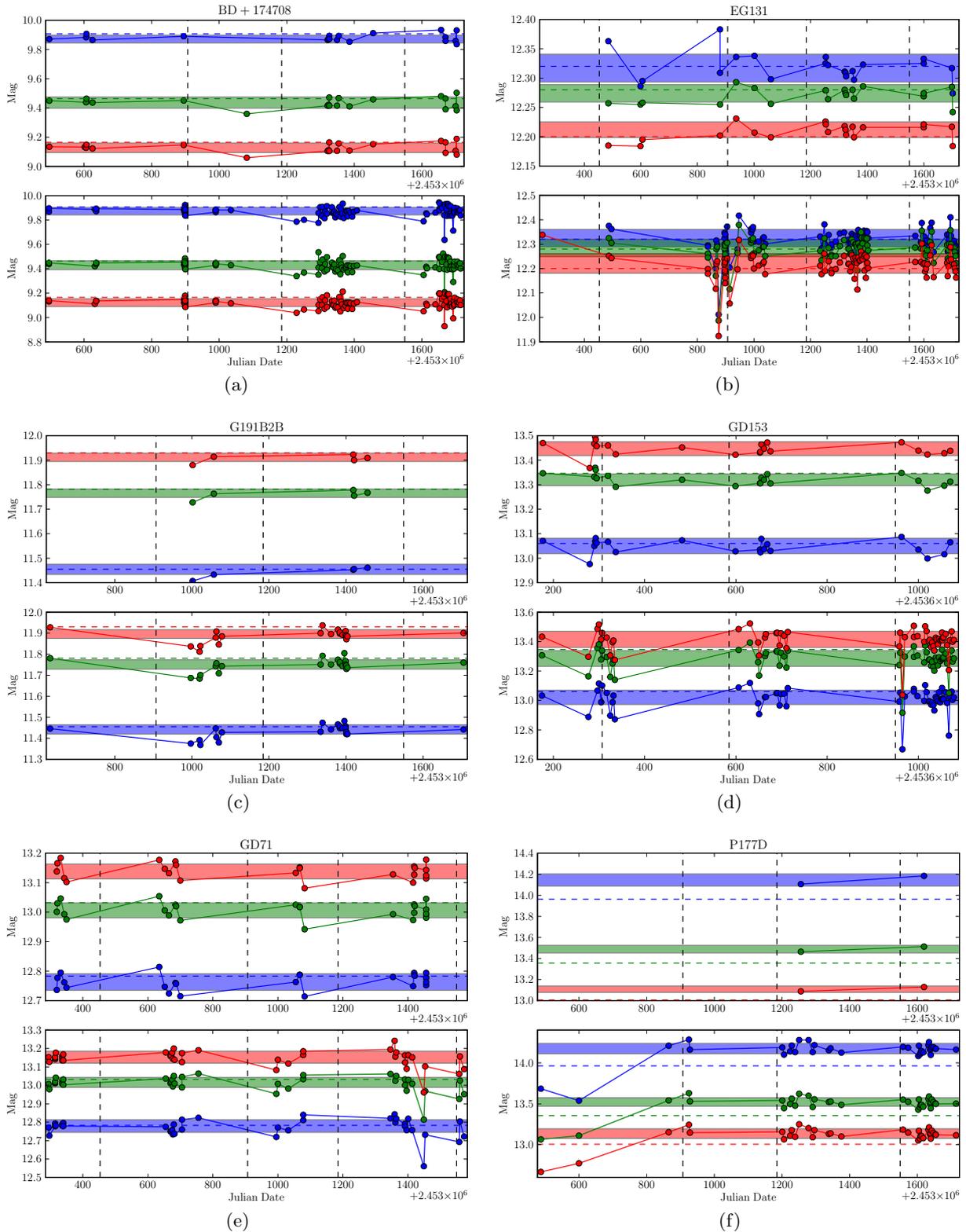
Figure 11.2: Synthesized spectrophotometric light curves on Bessell BVR (blue, green, red), for 6 spectrophotometric standard stars. The top panel corresponds to photometric nights and the lower panel to non-photometric nights. The shaded areas represent the nMAD around the median value (points at $> 3\sigma$ are not shown) and the horizontal dashed line is the tabulated value. The vertical dashed lined represent respectively June 2006, March 2007 and March 2008.

	B		V		R	
Star	Tabulated					
BD+174708[†]	9.907 ± 0.003		9.464 ± 0.003		9.166 ± 0.003	
EG131[‡]	$12.320 \pm -$		$12.280 \pm -$		$12.200 \pm -$	
G191B2B[†]	11.455 ± 0.003		11.781 ± 0.002		11.930 ± 0.003	
GD153[*]	$13.060 \pm -$		$13.346 \pm -$		$- \pm -$	
GD71[*]	$12.783 \pm -$		$13.032 \pm -$		$- \pm -$	
P177D[×]	$13.963 \pm -$		$13.356 \pm -$		$13.006 \pm -$	
	Photometric nights					
	Median	nMAD ($> 3\sigma$)	Median	nMAD ($> 3\sigma$)	Median	nMAD ($> 3\sigma$)
BD+174708	9.871	0.027 (2/21)	9.437	0.039 (1/21)	9.128	0.033 (0/21)
EG131	12.317	0.024 (0/21)	12.274	0.015 (1/21)	12.212	0.013 (1/21)
G191B2B	11.454	0.021 (1/6)	11.765	0.017 (1/6)	11.912	0.017 (1/6)
GD153	13.050	0.031 (0/21)	13.320	0.024 (1/21)	13.447	0.028 (0/21)
GD71	12.763	0.028 (0/25)	13.006	0.025 (0/25)	13.138	0.025 (0/25)
P177D	14.145	0.058 (0/2)	13.489	0.036 (0/2)	13.108	0.030 (0/2)
	Non-photometric nights					
	Median	nMAD ($> 3\sigma$)	Median	nMAD ($> 3\sigma$)	Median	nMAD ($> 3\sigma$)
BD+174708	9.873	0.031 (3/98)	9.430	0.036 (1/98)	9.122	0.032 (3/98)
EG131	12.325	0.036 (3/87)	12.284	0.036 (3/87)	12.221	0.040 (2/87)
G191B2B	11.442	0.022 (1/23)	11.751	0.022 (1/23)	11.896	0.021 (2/23)
GD153	13.021	0.049 (0/57)	13.285	0.053 (0/57)	13.415	0.055 (0/57)
GD71	12.779	0.034 (1/41)	13.016	0.027 (2/41)	13.153	0.033 (1/41)
P177D	14.174	0.064 (2/37)	13.522	0.052 (2/37)	13.136	0.059 (2/37)

[†] Landolt and Uomoto (2007)
[‡] Bessell (1999)
[*] Bohlin et al. (2001)
[×] Casagrande et al. (2006)

Table 11.2: Synthesized photometry on Bessell BVR filters, for 6 spectrophotometric standard stars. The presented values are the median values and respective normalized median absolute deviations, for the light curves made using only points from photometric or non-photometric nights. The number of points from the light curve which present a deviation higher than 3σ of the median value are quoted in parenthesis. For comparison the published values are also shown.

photometric system).

As expected, the scatter is smaller on photometric nights, being typically 2.5–3.5%. On the non-photometric nights, where the photometric ratios are used, it is of the order of 4–5%. This is hence the current photometric precision of the SNfactory photometric pipeline. Such values are still higher than the intended 1%/3% for photometric/non-photometric nights, and the improvement of this precision is the main goal of the SNfactory's calibration team in the near future, which has room for improvements either on the spectra extraction method, the night extinction computation, or the photometric ratios determination.

The color correlations of the synthesized magnitude residuals are shown in Fig. 11.3. The observed high correlation is an indication of the accurate color of the extracted spectra, and of their small flux errors. Specifically, the correlation is still strong when we compare B and R magnitudes, which are integrating parts of the spectra coming from different spectroscopic channels, which confirms that we can be confident in our spectra colors. The tighter correlation comes quite naturally from B and R, which are both observed by the same spectroscopic channel. The overall high correlation is also a product of the very high signal over noise of these standard stars spectra, with uncertainties well below the percent level, an whose examples we can see in Figs. 11.2a–11.3b.

We can then see that the current (worst case) SNfactory photometric calibration accuracy is

(a)

(b)

(c)

(d)

(e)
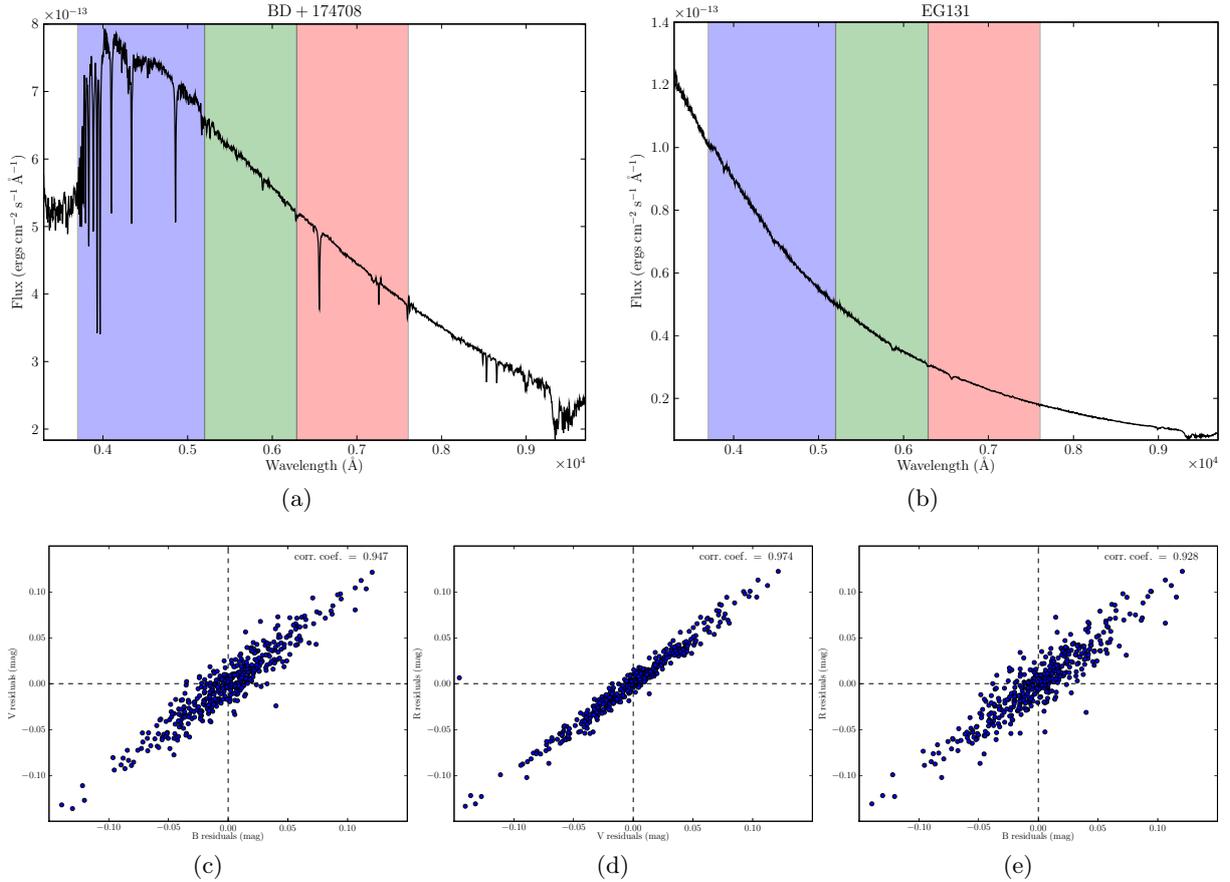
Figure 11.3: (a) BD+174708 and (b) EG131 spectrophotometric standard stars spectra. Residuals' (difference of the synthesized magnitude and the median magnitude per filter) color correlation for the 6 spectrophotometric standard stars, for (c) V *vs.* B, (d) R *vs.* V and (e) R *vs.* B. The correlation coefficients are respectively 0.947, 0.974 and 0.928.

around 3% and 5% for photometric and non-photometric nights respectively. Current work on several fronts aims to further reduce this scatter, but even at this point, our extracted spectra and derived spectrophotometry precision is already below the typical intrinsic scatter of the SNe Ia.

With that in mind, we will now proceed to the calibration of a sub-sample of SNfactory SNe Ia.

11.3 Supernovæ sub-sample

The suite of the analysis presented in this manuscript will use a selection of 30 supernovæ, whose spectra come from a calibration run from the middle of 2008 (the *INDIANA* run). These objects were chosen as the ones which presented the least attrition problems inside the pipeline (which may lead to the loss of some nights for which the internal calibration fails), whose light curves do not present very large outliers, and which are not near their host galaxy core (unless for the ones extracted by DDT(Bongard 2009), a spectrum extractor optimized to deal with large galaxy-induced backgrounds, still under development).

For all the spectral time series, synthetic light curves are generated by convolving pseudo

145

pass-band box filters, with each flux calibrated spectrum, and integrating. The magnitude is in the Vega photometric system, whose spectrum is similarly convolved and integrated to be used as a reference flux.

The SNfactory's filter-set (Table 11.3), along with Bessell's UBVRI filter-set are compared to a typical SN Ia spectrum near maximum, in Fig. 11.5a.

Filter	Wavelength range
B_{SNf}	3700–5200 Å
V_{SNf}	5200–6290 Å
R_{SNf}	6290–7600 Å

Table 11.3: SNfactory filter-set.

The current flux calibration pipeline lacks a full error propagation model from each of its subparts, not accounting *e.g.*, for the errors on the photometric ratios for the non-photometric nights. In this way, the error of the synthesized magnitudes is the photon statistics one, and is surely underestimated (we've seen in the last section that the photometric precision we are capable of attaining is $\sim 5\%$ on non-photometric nights. That is why, before further usage of this data (SALT fitting), the errors of each point of a light curve are scaled (in a conservative way), so that their median value across all the filters is equal to 0.1 mag, the order of magnitude of the SNe Ia absolute magnitudes' intrinsic dispersion (Guy et al. 2007).

The obtained spectrophotometric light curves are then fitted using SALT2 (*cf.* § 2.3.4), for further analysis.

11.3.1 SALT2 fits

SALT's flux model of a supernova is, from equation (2.1) (page 34)

$$F_{SN}(p, \lambda) = x_0 \times [M_0(p, \lambda) + x_1 M_1(p, \lambda) + \ldots] \times \exp\left[c\, CL(\lambda)\right] \;, \qquad (11.1)$$

whose minimization will gives the overall flux normalization x_0 (used in conjunction with the phase estimate to obtain the magnitude at maximum), and the two standardization parameters, x_1 and c, respectively a stretch-like time axis scaling and color, and which are later used on the cosmological fit.

The resulting parameters of the SALT2 fits for the 30 analyzed supernovæ, are shown in Table 11.4, with respective residuals per filter in Table 11.5. To avoid any biased analysis, ongoing SNfactory Hubble diagram fits are being performed using a blinded approach, adding a random value to the magnitude at maximum of each object. In this sense, no m_B values are quoted in the tables. Two examples of the fitted light curves from well sampled objects, can be seen in Fig. 11.4. For all the other light curves, refer to Appendix C.1.
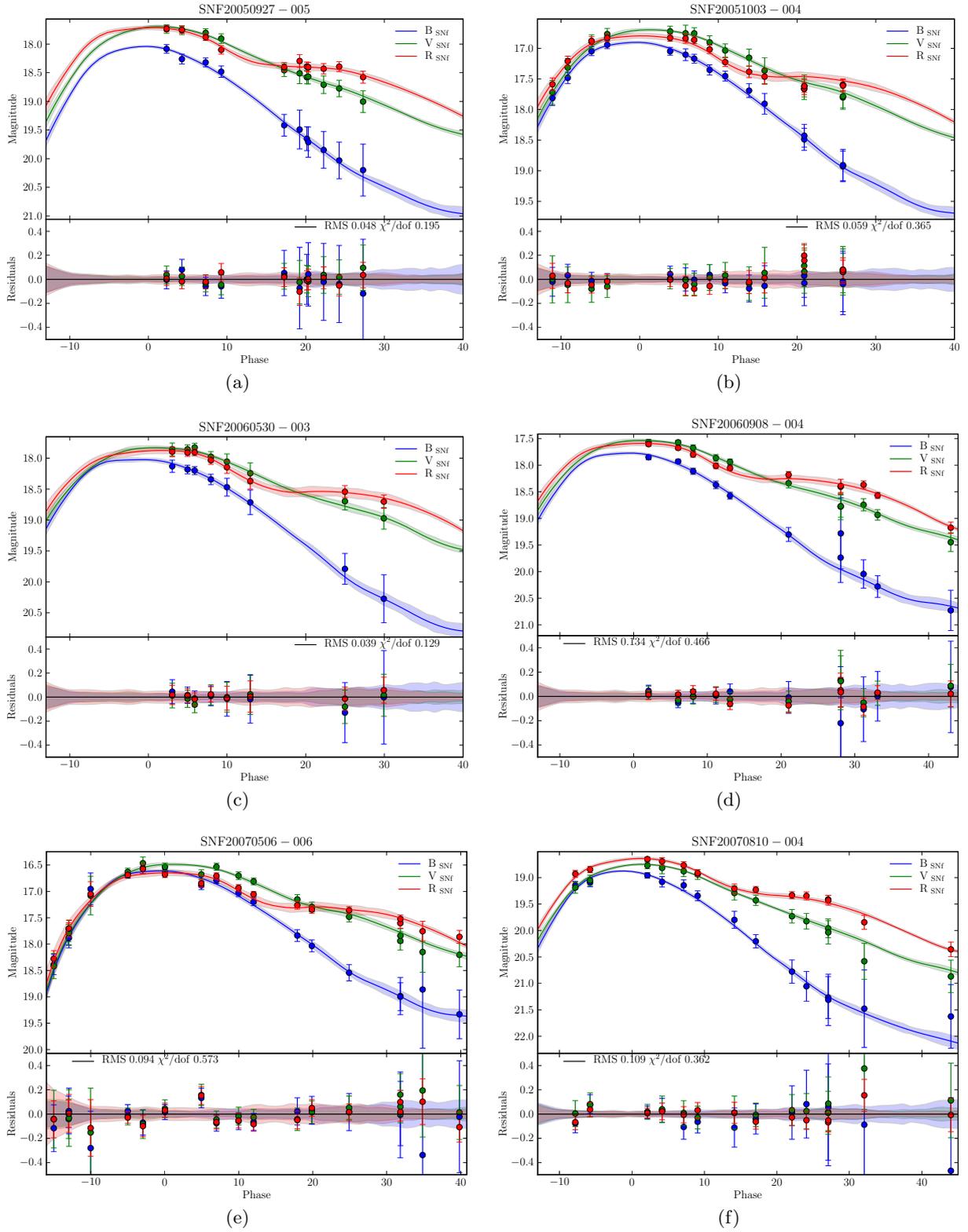
Figure 11.4: Spectrophotometric light curves, fitted using SALT2 for six SNfactory objects. The used filter-set is the SNfactory one. All the light curves are in Appendix C.1.

Supernova	Redshift	# points	Phase	x_1	c	χ^2/dof
SN2005cf	0.0065	10	(-9.69) -9.68 $\pm$ 0.21	-0.190 $\pm$ 0.314	0.071 $\pm$ 0.032	0.293
SN2005el	0.0149	16	(-6.95) -6.92 $\pm$ 0.17	-1.964 $\pm$ 0.151	-0.104 $\pm$ 0.024	0.617
SN2005M	0.0220	22	(-12.87) 2.11 $\pm$ 0.53	0.772 $\pm$ 0.369	0.085 $\pm$ 0.023	0.187
SN2006dm	0.0220	9	(-7.61) -7.60 $\pm$ 0.23	-2.804 $\pm$ 0.465	0.049 $\pm$ 0.036	0.770
SNF20061011-005	0.0230	8	(-3.70) -3.70 $\pm$ 0.49	0.931 $\pm$ 0.336	-0.066 $\pm$ 0.028	0.761
SN2007cq	0.0258	13	(-5.65) -5.65 $\pm$ 0.24	-1.060 $\pm$ 0.302	-0.039 $\pm$ 0.028	0.405
SN2004gs	0.0274	11	(-0.92) 1.04 $\pm$ 0.32	-3.270 $\pm$ 0.243	0.272 $\pm$ 0.019	1.274
SN2004ef	0.0310	9	(-6.64) -1.63 $\pm$ 0.02	-1.444 $\pm$ 0.438	0.211 $\pm$ 0.032	0.604
SNF20070803-005	0.0314	16	(-8.96) -8.96 $\pm$ 0.21	0.823 $\pm$ 0.298	0.026 $\pm$ 0.025	0.246
SNF20051003-004	0.0343	15	(-11.09) -11.09 $\pm$ 0.22	0.344 $\pm$ 0.332	-0.022 $\pm$ 0.025	0.365
SNF20070506-006	0.0348	18	(-14.99) -14.99 $\pm$ 0.17	0.732 $\pm$ 0.197	-0.011 $\pm$ 0.020	0.573
SNF20061020-000	0.0391	11	(-2.45) -2.45 $\pm$ 0.37	-2.100 $\pm$ 0.225	0.112 $\pm$ 0.022	0.571
SNF20060609-002	0.0397	8	(-5.58) -2.62 $\pm$ 0.64	-0.612 $\pm$ 0.488	0.297 $\pm$ 0.034	1.065
SNF20050927-005	0.0407	11	(-0.64) 2.31 $\pm$ 0.02	-0.358 $\pm$ 0.431	0.079 $\pm$ 0.033	0.195
SNF20060511-014	0.0476	9	(1.25) 1.26 $\pm$ 0.92	-1.467 $\pm$ 0.460	-0.008 $\pm$ 0.043	0.128
SNF20060908-004	0.0500	11	(2.03) 2.03 $\pm$ 0.61	0.620 $\pm$ 0.299	0.020 $\pm$ 0.019	0.466
SNF20060521-008	0.0551	8	(3.46) 3.48 $\pm$ 0.04	-2.124 $\pm$ 0.407	0.190 $\pm$ 0.034	0.503
SNF20060621-015	0.0553	12	(-4.34) -4.32 $\pm$ 0.60	0.771 $\pm$ 0.455	-0.031 $\pm$ 0.023	0.860
SNF20060530-003	0.0568	8	(3.02) 3.04 $\pm$ 1.11	1.063 $\pm$ 0.709	0.004 $\pm$ 0.030	0.129
SNF20061021-003	0.0627	14	(-5.68) -5.68 $\pm$ 0.03	-0.417 $\pm$ 0.229	0.108 $\pm$ 0.021	0.512
SNF20060618-014	0.0638	7	(2.21) 2.22 $\pm$ 1.47	0.482 $\pm$ 0.409	0.055 $\pm$ 0.040	0.181
SNF20070817-003	0.0640	13	(-3.30) -3.30 $\pm$ 0.39	-1.313 $\pm$ 0.320	0.000 $\pm$ 0.021	2.196
SNF20070802-000	0.0651	15	(-6.39) -6.39 $\pm$ 0.28	0.214 $\pm$ 0.297	0.157 $\pm$ 0.023	0.580
SNF20050624-000	0.0671	8	(-5.53) -5.53 $\pm$ 0.06	-0.155 $\pm$ 0.931	-0.040 $\pm$ 0.036	0.224
SNF20070725-001	0.0679	15	(-2.14) -0.14 $\pm$ 0.71	0.655 $\pm$ 0.331	-0.070 $\pm$ 0.025	0.201
SNF20070630-006	0.0721	15	(-8.46) -8.45 $\pm$ 0.33	0.458 $\pm$ 0.253	0.037 $\pm$ 0.023	1.137
SNF20070818-001	0.0753	15	(-3.26) -3.26 $\pm$ 0.46	-0.849 $\pm$ 0.300	0.110 $\pm$ 0.028	0.464
SNF20060526-003	0.0779	7	(-8.85) -6.86 $\pm$ 0.40	-0.665 $\pm$ 0.498	0.034 $\pm$ 0.027	0.568
SNF20070403-001	0.0804	13	(-5.39) -2.48 $\pm$ 0.38	-3.348 $\pm$ 0.364	0.011 $\pm$ 0.024	2.105
SNF20070810-004	0.0835	14	(-7.82) -7.82 $\pm$ 0.23	-0.230 $\pm$ 0.293	0.043 $\pm$ 0.022	0.362

† Extracted using DDT

Table 11.4: Fitted SALT2 parameters for 30 SNfactory spectrophotometric light curves, ordered by redshift. The two values shown in the *Phase* column represent the phase of the first spectrum taken by SNIFS (between parenthesis) and the phase of the first point used for the light curve. This difference may be due to failed extractions and unavailable spectra from the used flux calibration run. χ^2/dof is for all the individuals light curves of each supernova together.

Supernova	Redshift	B_{SNf}		V_{SNf}		R_{SNf}		All filters	
		RMS	nMAD	RMS	nMAD	RMS	nMAD	RMS	nMAD
SN2005cf	0.0065	0.051	0.022	0.047	0.043	0.053	0.058	0.055	0.049
SN2005el	0.0149	0.062	0.055	0.048	0.037	0.063	0.053	0.058	0.049
SN2005M	0.0220	0.074	0.030	0.017	0.025	0.056	0.075	0.057	0.034
SN2006dm	0.0220	0.104	0.149	0.085	0.113	0.104	0.081	0.099	0.113
SNF20061011-005	0.0230	0.074	0.072	0.072	0.067	0.056	0.082	0.071	0.081
SN2007cq	0.0258	0.062	0.070	0.067	0.091	0.060	0.065	0.066	0.073
SN2004gs	0.0274	0.127	0.103	0.088	0.069	0.064	0.063	0.100	0.072
SN2004ef	0.0310	0.218	0.028	0.111	0.120	0.102	0.089	0.163	0.079
SNF20070803-005	0.0314	0.061	0.067	0.050	0.049	0.040	0.045	0.056	0.054
SNF20051003-004	0.0343	0.034	0.046	0.055	0.068	0.076	0.068	0.059	0.052
SNF20070506-006	0.0348	0.110	0.041	0.087	0.065	0.075	0.077	0.094	0.066
SNF20061020-000	0.0391	0.194	0.096	0.056	0.035	0.073	0.114	0.136	0.082
SNF20060609-002	0.0397	0.164	0.069	0.072	0.094	0.106	0.113	0.128	0.094
SNF20050927-005	0.0407	0.057	0.079	0.039	0.040	0.041	0.027	0.048	0.050
SNF20060511-014	0.0476	0.037	0.058	0.071	0.051	0.026	0.030	0.049	0.046
SNF20060908-004	0.0500	0.204	0.068	0.062	0.047	0.047	0.052	0.134	0.060
SNF20060521-008	0.0551	0.095	0.124	0.048	0.077	0.068	0.036	0.084	0.081
SNF20060621-015	0.0553	0.080	0.060	0.078	0.051	0.071	0.064	0.077	0.062
SNF20060530-003	0.0568	0.048	0.023	0.037	0.025	0.023	0.022	0.039	0.023
SNF20061021-003	0.0627	0.114	0.178	0.117	0.066	0.059	0.064	0.108	0.089
SNF20060618-014	0.0638	0.062	0.015	0.055	0.051	0.065	0.036	0.062	0.032
SNF20070817-003	0.0640	0.332	0.193	0.151	0.080	0.151	0.134	0.250	0.114
SNF20070802-000	0.0651	0.064	0.070	0.088	0.095	0.062	0.069	0.075	0.077
SNF20050624-000	0.0671	0.041	0.034	0.035	0.052	0.025	0.027	0.040	0.039
SNF20070725-001	0.0679	0.060	0.053	0.043	0.048	0.043	0.047	0.053	0.048
SNF20070630-006	0.0721	0.132	0.084	0.109	0.120	0.106	0.102	0.127	0.102
SNF20070818-001	0.0753	0.606	0.095	0.067	0.049	0.064	0.060	0.328	0.063
SNF20060526-003	0.0779	0.466	0.051	0.107	0.127	0.043	0.062	0.299	0.067
SNF20070403-001	0.0804	0.878	0.368	0.139	0.146	0.124	0.101	0.576	0.145
SNF20070810-004	0.0835	0.134	0.105	0.097	0.040	0.057	0.052	0.109	0.058
All supernovæ points with mag < 20		0.098	0.055	0.072	0.055	0.074	0.060	0.082	0.058

Table 11.5: RMS and normalized MAD (in magnitudes) of the residuals for 30 SNfactory spectrophotometric light curves, fitted using SALT2.

In Fig. 11.5b–11.5c are shown the residuals' *vs.* magnitude and phase of the supernova, and corresponding color correlation on Fig. 11.5d–11.5e. No phase dependence nor magnitude dependence (up to 20) is observed on the synthesized magnitude residuals. For faint fluxes however, there seems to be a slight (opposite) effect on B_{SNf} and V_{SNf}, although the number of events is small to draw a conclusive answer. The used spectrum extractor is known to suffer from small systematic errors in the very low flux limit, and the fact that both colors are measured from spectra coming from different spectroscopic channels, would point to a common culprit, although a fault at the level of both CCDs cannot be excluded.

Contrary to the standard stars, the residuals' color correlation is weak. Other than a systematic error, on a specific color SALT2 fit with relation to the other colors (not observed), this difference is easily explained by the fact that the SNR of the spectra with which we are working here is much smaller than the standard stars one. We are then affected by the noise, especially for spectra issued from the B (blue) channel. Other than that, the different extraction method of the supernovæ, notably the way the background is dealt with (a tilted plane *vs.* a constant plane inside the MLA), may also have its toll in the increased residuals, in case it is wrongly estimated and some galaxy flux is included in the extraction, leading to an increased color noise when comparing spectra from both channels. We would then have a smaller residuals' correlation in the B_{SNf},V_{SNf} and B_{SNf},R_{SNf} cases (which is the case). A further evidence for this issue comes from the fact that, if the correlation coefficient is calculated using only the supernovæ extracted using DDT (Bongard 2009), which is intrinsically more robust to galaxy backgrounds than the standard extraction method, we find 0.45 for the B_{SNf},V_{SNf} residuals' correlation, contrary to 0.21 for all the other supernovæ. DDT is still under development, and is expected to be used for every supernovæ spectrum extraction in the near future.

We can conclude that, up to magnitude 20, the light curve fits are good, and no particular bias are observed on the obtained residuals. Faint flux spectra extraction is still a problem, as well as possible issues with galactic background subtraction. The full normalized median absolute deviation for all the supernovæ points with magnitude small than 20, on all filters confounded, is in the order of 6%, consistent with the individual filter scatters, and with what we had observed on the case of the standard stars.

11.3.2 Comparison with Bessell V light curves

Some of the supernovæ used for this analysis also have an acquisition light curve, among those which were presented on the previous chapter (§ 10). It is thus of interest to compare the SALT2 results for both approaches: synthetic spectrophotometry *vs.* standard photometry, for the identification of possible bias.

We can then do a threefold comparison of the phase and x_1 SALT2 parameters between:

- spectrophotometric multi-color *vs.* single-color synthesized "acquisition light curves" (using the guider Bessell V filter throughput) (Figs.11.6a–11.6b);

- spectrophotometric multi-color *vs.* photometric single-color V light curves (Figs.11.6c–11.6d);

- spectrophotometric single-color synthesized *vs.* photometric single-color V light curves (Figs.11.6e–11.6f).

All the fits results are resumed in Table B.1.

The parameter differences with less scatter are naturally those of light curves created using the same method, that is, the spectrophotometric ones. It is thus basically a measure of the

(a)

(b)　　　　　　　　　　　　　　　　　　　(c)

(d)　　　　　　　　　　(e)　　　　　　　　　　(f)
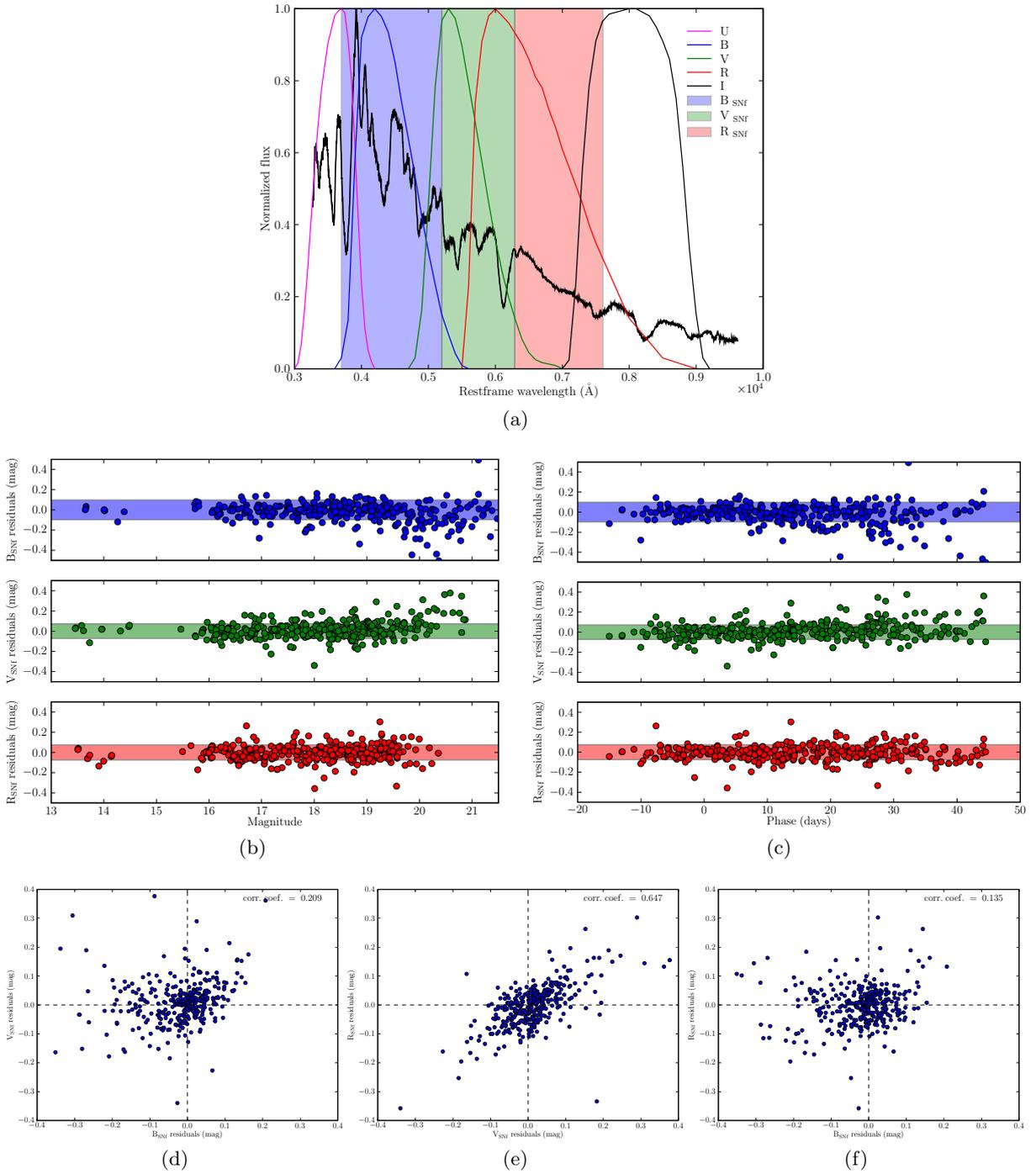
Figure 11.5: (a) SNfactory's filter-set (shaded boxes) compared to Bessell's UBVRI filter-set, and the rest-frame spectrum of a SN Ia near maximum light (SN2006D). It extends from 3700Å to 7600Å. (b)–(c) BVR (blue, green, red) residuals' dependence with magnitude and phase of the supernova. The shaded areas represent the residuals' RMS for the light curve points with mag < 20. (d)–(f) Residuals' color correlation.

consistency of SALT2 when fitting 3 *vs.* 1 color. No redshift correlation is observed, and small biases are observed for either phase or x_1: the synthetic single color fit slightly overestimates the phase and underestimates x_1. The observed dispersion is still consistent with zero.

Comparing parameters from spectrophotometric *vs.* photometric light curves we observe a larger dispersion with a few outliers points, which gets worse when comparing only single color light curves (synthesized V and photometric V). That reveals inconsistencies, mostly on the phase determination using the photometric V light curves, which was already seen (§ 10.3) on the case when we do not have pre-maximum points (no object selection was made in that regard here). The stretch determination (Fig. 11.6d) is consistent between both approaches, which validates the stretch distribution found on the previous chapter using the acquisition light curves.

Concluding, indeed the larger SNR of the spectrophotometric light curves ends up to better SALT2 fits than the photometric ones, that have a smaller exposure time. Still, we have been able to compare in average the results obtained by both approaches, and haven't seen significant differences between the results obtained with the new method, based on spectrophotometric data, and the classical approach based on the photometric imaging of the field.

(a)

(b)

(c)

(d)

(e)

(f)
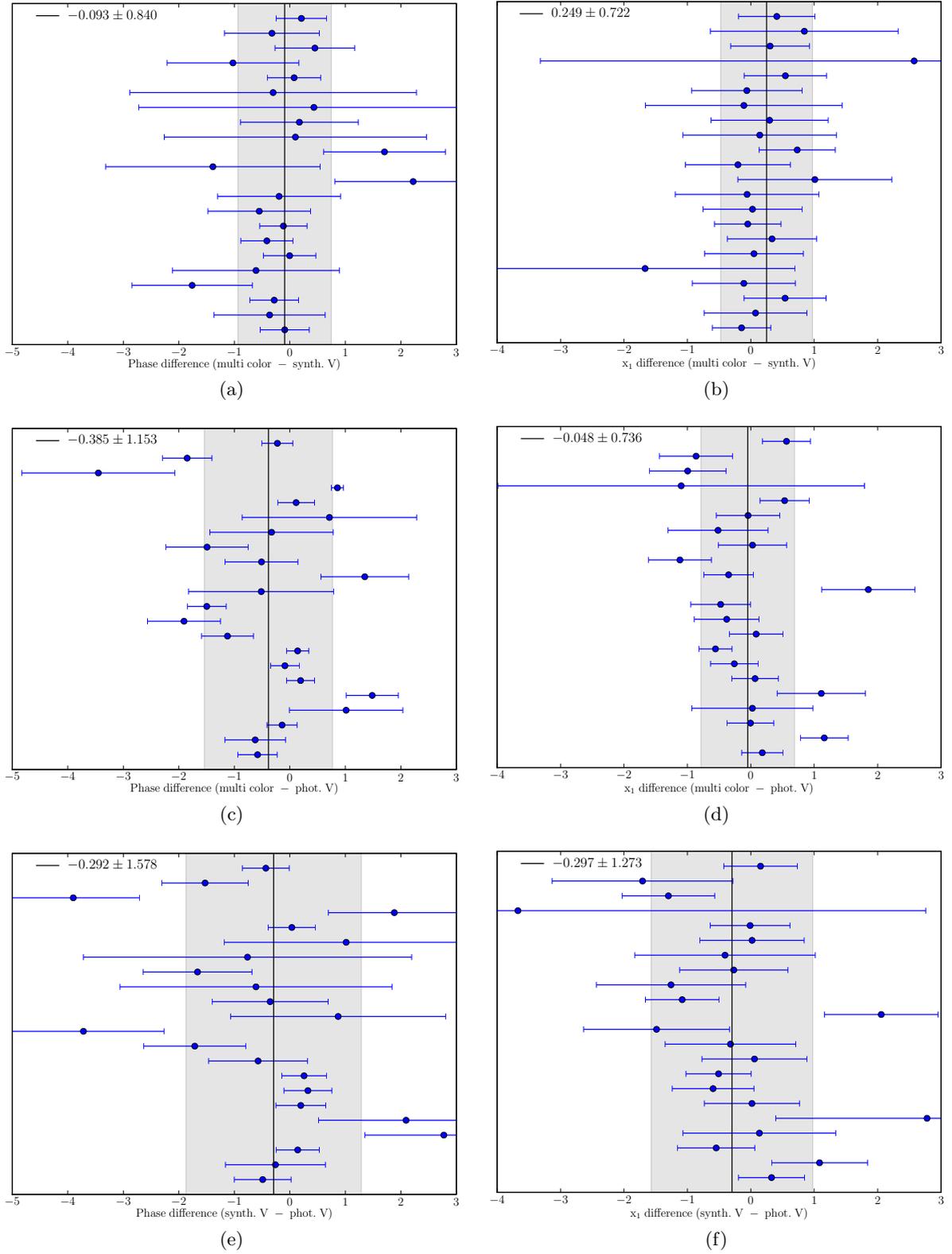
Figure 11.6: SALT2 phase and stretch (x_1) differences for 22 common supernovæ between both acquisition and spectrophotometric light curves datasets, for different light curve creation methods: (a)–(b) spectrophotometric multi-color *vs.* single-color synthesized "acquisition light curves"; (c)–(d) spectrophotometric multi-color *vs.* photometric single-color V; and (e)–(f) spectrophotometric single-color synthesized *vs.* photometric single-color V. The supernovæ are ordered by increasing redshift from bottom to top.

Chapter 12

Hubble diagram

Using the fitted spectrophotometric light curves introduced in the last chapter, we can now proceed to the next step, that is, the construction of a nearby Hubble diagram.

This exercise is not intended to provide (yet) constraints on the cosmological parameters, since for that case a joint fit with high-z supernovæ should be performed[1]. Our intention is rather to illustrate the quality of the spectrophotometric data issued from SNIFS, by studying in detail the Hubble diagram residuals of our data. An absolute calibration of a larger dataset than the presented here, is under way. As seen on the previous chapter, measurements on standard star data confirm that we already control our flux calibration at a level better than the intrinsic SNe Ia flux dispersion, so we can proceed to an Hubble residuals analysis.

12.1 Spectrophotometric nearby Hubble diagram

The SNLS Hubble fitter was used to fit the spectrophotometric light curves to a flat ΛCDM cosmology, with fixed $\Omega_{\mathrm{m}} = 0.24$. It performs a minimization of Eq. (2.3) (page 35)

$$\chi^2 = \sum_i \frac{\left(\mathbf{V}^{\mathrm{T}}\mathbf{X}_i - M - 5\log_{10}(d_L(\theta, z)/10 \text{ pc})\right)^2}{\mathbf{V}^{\mathrm{T}} \mathbf{C}(\mathbf{X}_i) \mathbf{V}} \; , \qquad (12.1)$$

where $\mathbf{X}_i$ includes the SALT2 fits results obtained on the previous chapter, and the fitted parameters are α_x, β (in $\mathbf{V}$) and M, respectively stretch and color factors (for the brighter-slower, brighter-bluer relations), and absolute magnitude. An additional intrinsic dispersion (σ_{int}) of the supernovæ absolute magnitudes is included in the variance of m_B^* (the peak B magnitude), so that $\chi^2/\mathrm{dof} = 1$, as well as an error of the distance modulus due to peculiar velocities, of 300 km.s^{-1}.

One target (SNF20070403-001), was rejected based on its large SALT2 color residuals (nMAD > 0.15). The obtained nearby Hubble diagram and respective residuals are shown in Fig. 12.1, the fitted parameters in Table 12.1, and the detailed residuals per supernova in Table 12.3 (*Hubble diagram* columns). Tables B.4–B.5 (page 183) are equivalent tables, but show the results for an Hubble diagram which uses SALT2 fits of light curves to which the errors were not scaled (*cf.* § 11.3), being directly the spectrum statistical errors.

A few things should be mentioned about this Hubble diagram. First of all, it is the first Hubble diagram ever made with spectrophotometric data only. It is a validation of the SNfactory approach to nearby supernovæ observation, and opens the door to different studies only possible

---

[1]Which implies an accurate cross-calibration between SNfactory's data and *e.g.*, SNLS data.
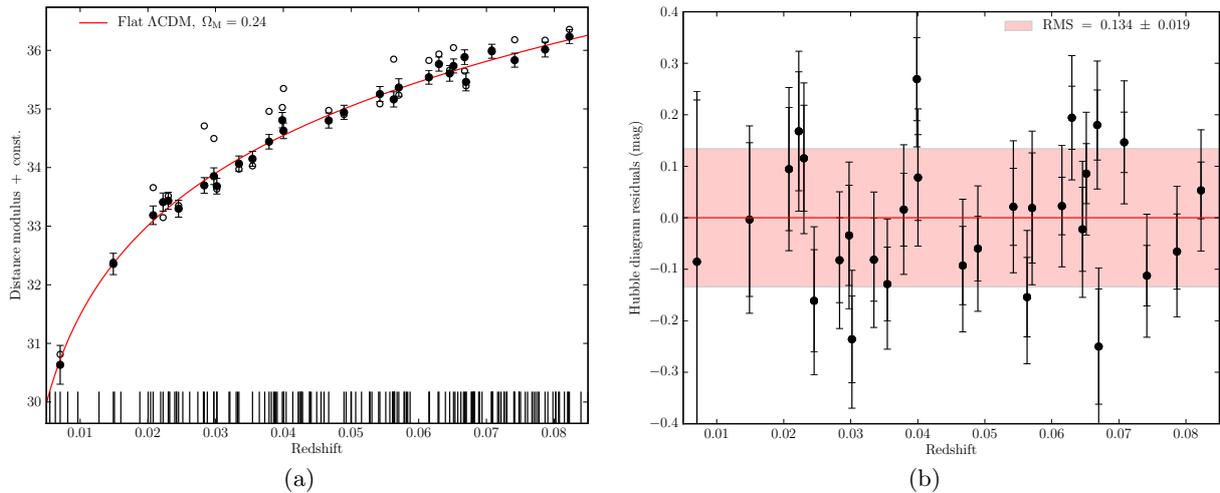
Figure 12.1: (a) Nearby Hubble diagram, derived from SALT2 fitted spectrophotometric light curves, for 29 SNfactory objects. The red line represented the fitted flat ΛCDM cosmology with fixed $\Omega_{\rm M}$. (b) Residuals of the Hubble diagram. The bigger and smaller error bars are respectively with and without $\sigma_{\rm int}$. The shaded area represents the RMS around the Hubble line.

with this kind of data (*cf.* § 12.2). The open points on Fig. 12.1a, represent the distance modulus from the uncorrected peak B magnitudes as measured by SALT2, without any standardization for stretch and color (which is equivalent to using Eq. (2.2) with the parameters α and β set to zero). See Table 12.2 for the detailed Hubble residuals before and after correction. The reduced scatter after standardization, reflects in one hand the remarkable standard candle behavior of SNe Ia, and on the other hand the quality of the standardization performed by SALT. The vertical lines on the redshift axis are the redshifts for 150+ other supernovæ observed by SNfactory on at least 5 epochs, a sample with the potential to greatly improve the nearby Hubble diagram in the near future. Fig. 12.1b shows in more detail the minimized residuals to the Hubble line. Each point presents two error bars, the bigger and the smaller, respectively with and without $\sigma_{\rm int}$. The RMS is calculated using

$$\text{RMS} = \frac{1}{N-3} \sum_i^N r_i^2 \pm \frac{1}{\sqrt{2(N-3)}} \tag{12.2}$$

where r_i is each of the N residuals with relation to the Hubble line, and the $N-3$ degrees of freedom account for the 3 parameters of the fit, α, β and M. No correlation is observed between x_1 or c and the Hubble diagram residuals or redshift (Figs. 12.5b–12.5c).

For comparison, the SALT data from 51 nearby SNe Ia from Kowalski et al. (2008) was fitted using the same fitting conditions. The results are also present on Table 12.1. We can see that the present sample (of 29 objects) already presents a smaller RMS to the Hubble line by $\sim 15\%$ (quadratic), with also reduced $\sigma_{\rm int}$. It is another confirmation of the advantage of having nearby supernovæ data issued from a single telescope/instrument, without inter-calibration problems, as well as a demonstration of the current SNfactory's internal photometric calibration accuracy.

The pull[2] distribution of the Hubble fit residuals, for the case of light curves without error scaling (on Table B.5), is shown in Fig. 12.2. We resort to this pull[3] instead of the one from the

---

[2]pull $= \frac{r_i}{\sigma_{r_i}}$ (without $\sigma_{\rm int}$).

[3]And only to the pull. The residuals' errors and fit results shown in this chapter, all come from the fitted
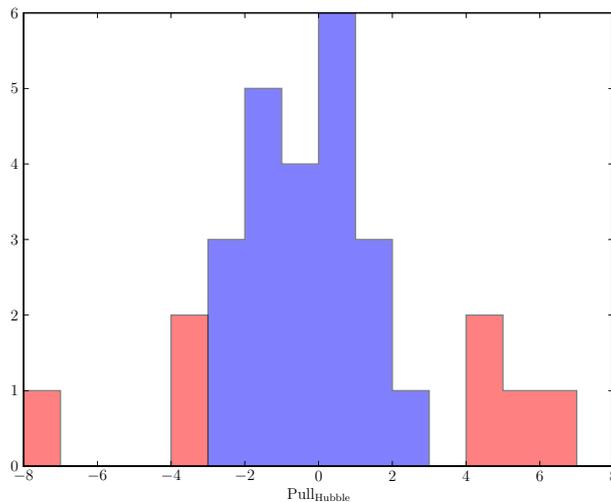
Figure 12.2: Pull distribution per 0.5σ bin of the residuals of the nearby Hubble diagram, from light curves without error scaling. The red bins represent the objects with $|\text{pull}| > 3\sigma$.

light curves with scaled errors, since that with those we are explicitly scaling the experimental errors to the same median value on all supernovæ. While such approach will not affect the SALT2 results, it increases the quoted statistical errors on the fitted parameters, and consequently the uncertainty on the residuals of the Hubble diagram, effectively changing the pull distribution and "drowning" in the SNe Ia intrinsic dispersion, objects that would be significant outliers otherwise. On the other hand, we know that effectively the flux calibration pipeline errors are underestimated, and even if the pull is better, it will not be perfect.

Seven objects deviate $> 3\sigma$ from the Hubble line, even after standardization. We will look succinctly at each one of them, to try to identify the origin of their peculiarity.

12.1.1 "Peculiar" objects

Those objects which SALT2 is unable to properly standardize, may be so due to several reasons: either the synthesized light curve has several outlier points from badly extracted spectra, or incorrect photometric ratios; either the target is faint or suffers from contamination from the host galaxy, and hence has a systematic error effect on the extracted flux and computed magnitudes; either, more interestingly, the object is spectroscopically peculiar, and SALT is not capable of describing it with its average SN Ia model. I recall that all fitted light curves can be seen in Appendix C.1.

SNF20050624-000

This supernova has an high Milky Way extinction (E(B-V)~ 0.37), as is noticeable by the weak flux on the blue part of its spectrum (Fig. 12.3a) and especially its light curve (Fig. C.2f). The spectra are also fairly noisy (it is a faint supernova at $z = 0.067$), which could lead to bad extractions, with a possible additional error due to the SALT2 de-reddening process.

Hubble diagram using SALT2 results with scaled errors.

SNF20050927-005

This object (Fig. 12.3b) is issued from a DDT extraction, and is placed right next to the core of its host galaxy. A look at the extraction residuals show a very big left over flux after the extraction, and the spectra show residual sharp features (~ 5300Å). Its (post-maximum – Fig. C.3a) light curve is good, which confirms the possibility of an overall flux bias on all exposures, which while not creating outlier points, can change dramatically the measured stretch.

SNF20060521-008

There are no particular features on this supernova spectra (Fig. 12.3c), and it is unclear which is the reason for its outlier behavior. We can see clear sky lines in some of the shown spectra, which however do not seem to create outlier points, since its light curve is good (Fig. C.3d).

SNF20070630-006

The SNF20070630-006 is very close to its host galaxy, and some sharp features (Fig. 12.3d) near the dichroic transition point to a possible bad dichroic correction. However, it also presents a very strong Ca II line, a possible indicator of SN1999aa-like supernovæ. It is not clear if that is the case, although that seems unlikely, especially since its light curve (Fig. C.5d) presents some clear outlier points (which may also come from wrong photometric ratios), and the SALT2 fit χ^2/dof is high.

SNF20070725-001

Some sharp features are evident in its spectra (Fig. 12.3e), especially around the dichroic transition, but no outlier points are visible in its light curve (Fig. C.5e). This supernova is off-core, but quite close to its host galaxy, where the tilted plane approach to the background subtraction may fail.

SNF20070803-005

SNF20070803-005 has a large negative residual even after correction using the SALT2 fitted parameters, being overluminous with respect to the other targets. There are no obvious reasons why we should not trust the measured flux, and indeed, we have already seen (§ 5.4) that it is intrinsically peculiar. It is a SN1991T-like supernova, with a very shallow Si II feature, and with a spectrum (Fig. 12.9d) dominated by the Fe III lines.

SNF20070817-003

A quick look at Tables 11.4–11.5 and its light curve (Fig. C.6c), shows that this particular SALT2 fit has the highest χ^2/dof, as well as one of the biggest color residuals' nMAD. That is hence the cause for its big residual on the Hubble fit, a bad SALT2 fit. That may come from the fact that this target redshift measurement has a lesser precision than the other ones, inducing a bias on the fit.

After analysis of this small sample of objects, which present large residuals from the fitted Hubble line, we identified three (10% of the sample) which show clear extraction problems that explain their large pull. Three others are "peculiar" in the sense that no obvious explanation has been found for their behavior, and should be further investigated. One of the outliers, the
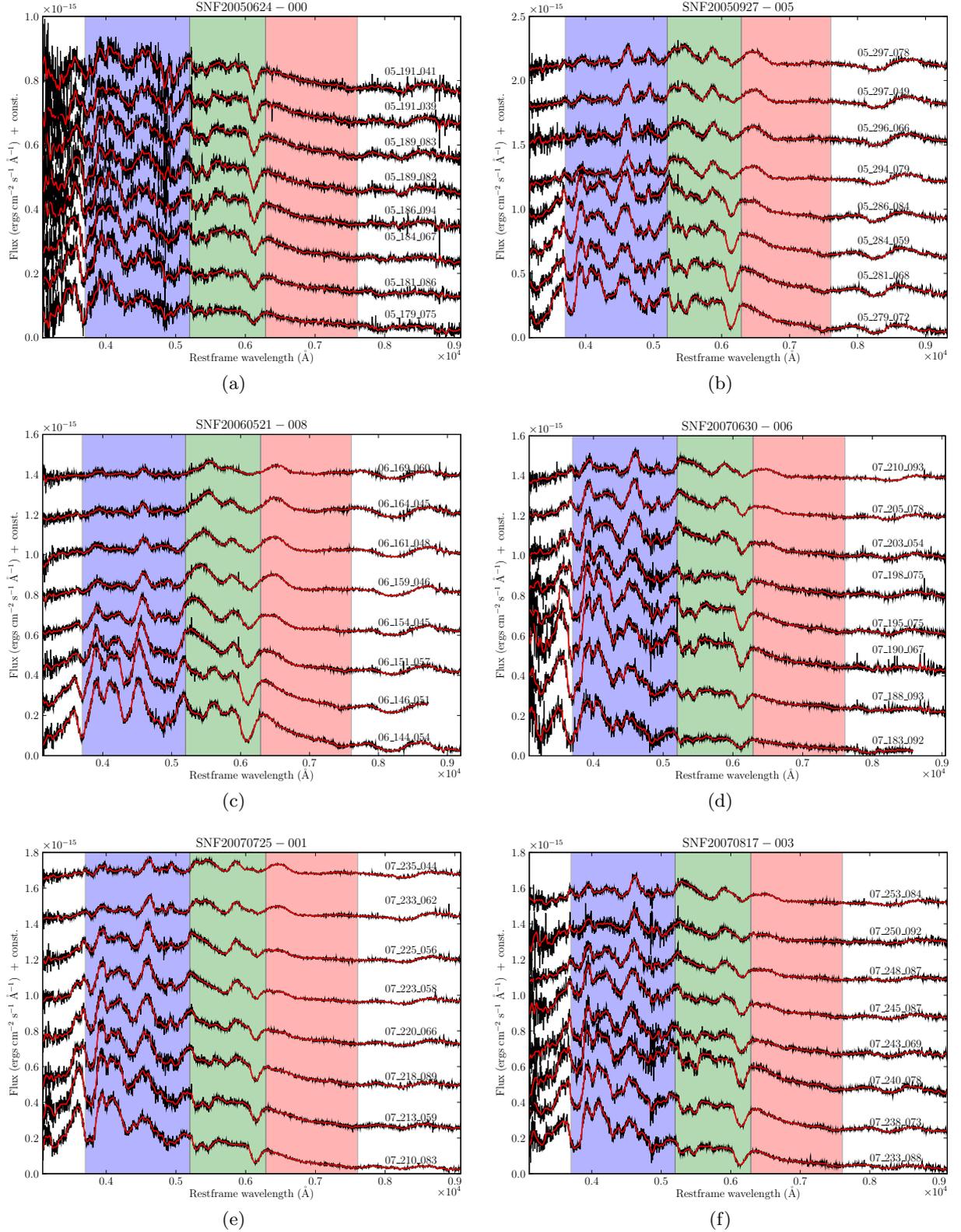
Figure 12.3: Spectral series for some "peculiar" objects. The year, day and run number are noted by each spectrum. For the phase of the first spectrum (the bottom one), see the *Phase* column of Table 11.4. The red line is a gaussian filter smoothing with $\sigma = 5$Å, and the shaded areas are the SNfactory filters, B_{SNf}, V_{SNf} and R_{SNf}. Every spectrum is at rest-frame.

91T-like SNF20070803-005, is clearly a overluminous object, even after the SALT correction. That shows that using SNfactory data with the actual precision, we are already able to peer into the origins of the SNe Ia intrinsic dispersion, namely their spectroscopic diversity. All of these targets, although having a large pull, are within the typical intrinsic scatter of SNe Ia, and do not affect greatly the quality of the Hubble fit, which as was seen, has the lowest scatter of a nearby SNe Ia Hubble diagram to date.

The SNfactory collaboration is currently working on a dataset of ~ 70 flux calibrated SNe Ia, while refining the calibration precision. It is expected to be able to use this data for further improvements of the current dark energy measurement efforts using SNe Ia, during 2009.

12.2 $\mathcal{K}$-correction free nearby Hubble diagram

The unique SNfactory dataset, consisting of absolutely flux calibrated spectral time-series, enables us to perform new studies on the usage of nearby SNe Ia for cosmology. One of such innovative approaches is presented in this section.

Standard SNe Ia photometric light curve fits, such as the approach taken by SALT, introduce a convolution of an average "template" spectral model, redshifted to observer frame – a $\mathcal{K}$-correction. Uncertainties in the template, or a mismatch between the template and an observed SNe Ia SED introduces errors in the $\mathcal{K}$-correction, whose minimization or elimination is key for high-precision SNe Ia cosmology.

Using our spectrophotometric light curves, we are able to recreate rest-frame light curves of each supernova, given its host redshift and synthetic filter throughputs. This effectively eliminates the fitter intrinsic $\mathcal{K}$-correction, in the sense that during the fit, each synthesized light curve point will always be compared to a convolution on the *same* wavelength range of the spectral model, for *any* supernova, and hence we can expect an improvement of the Hubble fit based on those light curves.

(a)   (b)
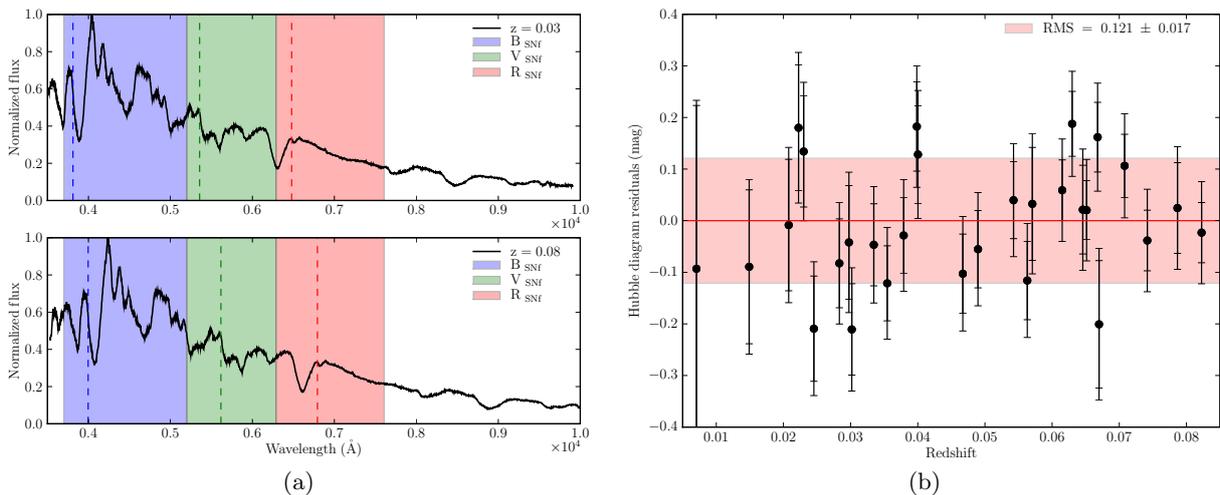
Figure 12.4: (a) Comparison of the spectrum of a SN Ia observed at two different redshifts: 0.03 (upper panel) and 0.08 (lower panel). The shaded areas represent the observer-frame SNfactory filter-set. It is clear that each each filter integrates different spectral features on each one of the cases. The dashed vertical lines represent instead the filter's throughput lower edge, if they are redshifted to the supernova's rest-frame. (b) $\mathcal{K}$-correction free Hubble diagram residuals. The bigger and smaller error bars are respectively with and without σ_{int}. The shaded area represents the RMS around the Hubble line.

The implementation of this method is the following: instead of de-redshifting each supernova spectrum, the base SNfactory filter-set (Table 11.3) is redshifted to the same redshift of the supernova (Fig. 12.4a). Being box filters, that amounts to a simple scaling of their wavelength axis by a $(1 + z)$ factor. Once redshifted, the filters are convolved with the spectrum and integrated as before, synthesizing each light curve point, and the created light curves fitted using SALT2 (Tables B.2–B.3). SALT's code was changed, in order to be able to use always the same base filter-set, so that it is now redshifted on-the-fly, thus avoiding the creating of a specific filter-set per supernova.

Comparing the results of the $\mathcal{K}$-correction free SALT2 fits on tables 11.5–B.3, we can see that the RMS on the color residuals' for the full dataset remains basically the same, with an improved B_{SNf} residuals' RMS but worse for R_{SNf}. This comes probably from the increasing uncertainties of the SALT2 model as we go further redwards: the R_{SNf} filter extends to 7600Å, already higher than the default SALT2 fitting range (7000Å). When redshifting the filters, their wavelength range will go up even further, where the model is worse described, naturally increasing the errors of the fit.

The subsequent Hubble diagram fits are performed as previously, with the SNLS fitter. Its residuals are shown in Fig. 12.4b, and the fit results are also detailed on Tables 12.1–12.3 ($\mathcal{K}$-correction free columns). By using this $\mathcal{K}$-correction free method, one would expect to see an improved Hubble diagram, and that is indeed the case.

We find a smaller quadratic dispersion (by $\sim 5\%$) of the nearby Hubble diagram residuals (*cf.* Fig. 12.5a for a direct comparison) with relation to the standard Hubble diagram, and an equivalently smaller σ_{int} parameter needed for the χ^2 normalization. This improvement comes solely from the reduction of the systematical error introduced by the fitter: SALT2 color-dependent model uncertainties are alone responsible for a 5% scatter on the nearby SNe Ia Hubble diagram, or similarly on the "measured" SNe Ia intrinsic dispersion. As with the standard approach, no x_1 or c correlation with the Hubble diagram residuals or redshift is observed (Figs. 12.5b–12.5c).

Parameter	Hubble diagram	$\mathcal{K}$-correction free	Nearby SCP Union
α	0.130 ± 0.027	0.153 ± 0.022	1.054 ± 0.232
β	2.163 ± 0.337	1.913 ± 0.284	2.812 ± 0.325
M	-19.332 ± 0.030	-19.307 ± 0.028	-19.331 ± 0.035
RMS	0.134 ± 0.019	0.121 ± 0.017	0.195 ± 0.020
σ_{int}	0.104	0.080	0.137

Table 12.1: Parameters of the nearby Hubble diagram fit, for a flat ΛCDM cosmology with fixed $\Omega_m = 0.24$, using 29 SNfactory's spectrophotometric light curves. Both results, for the "standard" Hubble diagram fit and the $\mathcal{K}$-correction free one, are shown.

An analysis of the new pull distribution shows a consistent improvement for the targets previously identified as "peculiars", and a mixed trend for the other ones. These peculiar targets are however not "pulling down" the overall scatter by themselves, since fits without them show a similar RMS reduction. Fig. 12.5d shows the residuals pull variation between the standard Hubble diagram and the $\mathcal{K}$-correction free one, for the ensemble of the targets. Of those, a set of 4 targets detaches themselves: they show the biggest change in Hubble residuals between both fits, and as can be seen in Fig. 12.5e, have all $z > 0.06$, with 3 of them being the top-most targets of the redshift distribution. This is extremely interesting, in the sense that it reinforces our initial supposition: as SNe Ia spectral features get close to the used filter edges for a given redshift range, that induces a systematic $\mathcal{K}$-correction if the used spectral template does not describe them well. To see a larger pull variation between our two fits, for a given redshift

(a)

(b)

(c)

(d)

(e)
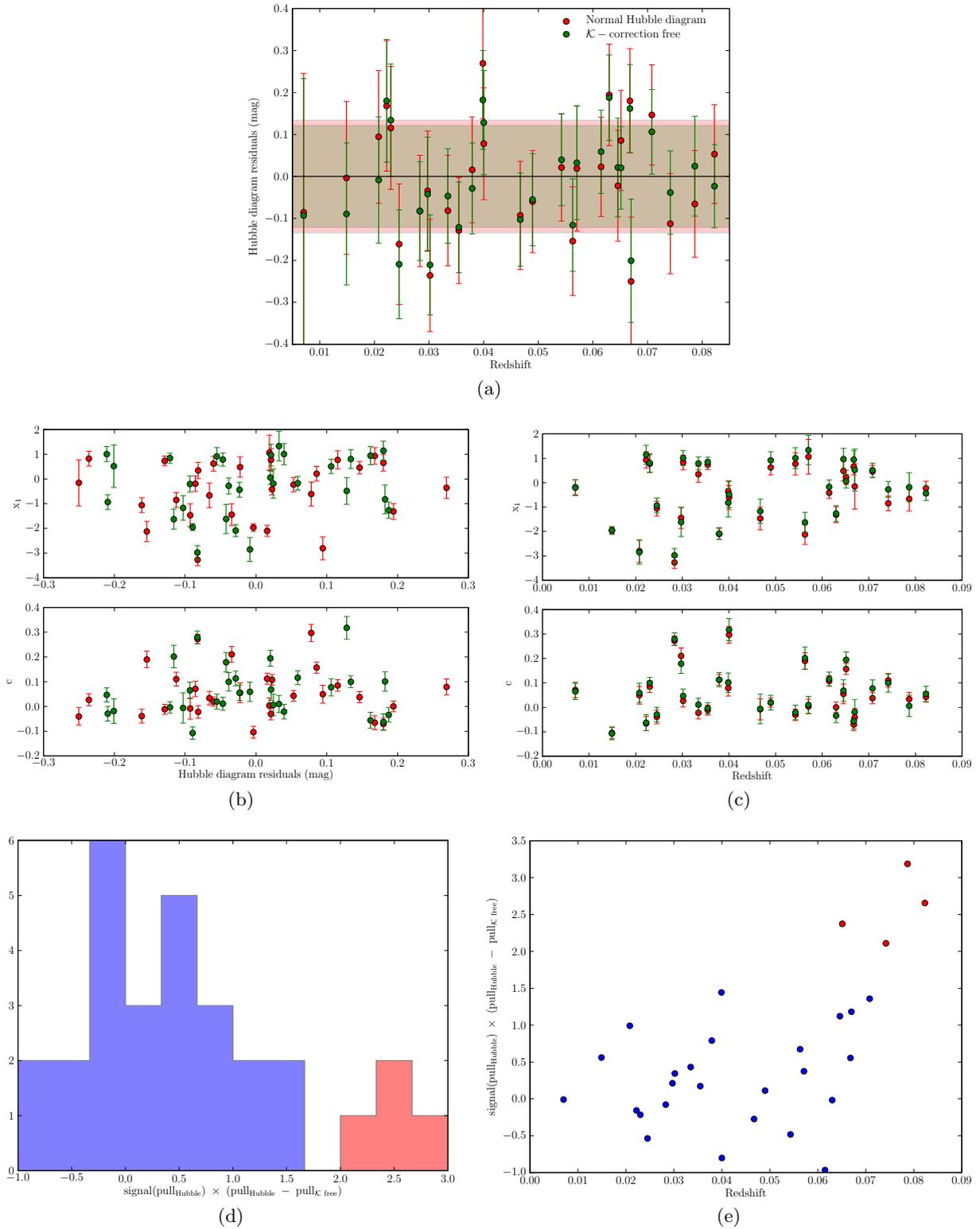
Figure 12.5: (a) Direct comparison between the standard Hubble diagram (red) and the $\mathcal{K}$-correction free one (green) residuals. (b)–(c) x_1 and c dependence on the Hubble fit residuals and redshift respectively. Same colors as in (a). (d) Differential pull distribution between both Hubble diagrams, and (e) correlation with target redshift. The targets whose residuals changed the most are marked in red.

range, is then expected. Of the targets that increased their residual, one in particular should be mentioned: SN2007cq, at $z = 0.0245$. The fact that it shows a overluminous behavior, and since its residual got worse, points to the relative inability of SALT2 to standardize it, confirming its peculiarity, and is in accordance with its SN1999aa-like typing made by Filippenko et al. (2007).

Concluding, we've seen that we are able to reduce the nearby Hubble diagram scatter by a factor of 5%, by minimizing a SALT2 systematic error associated with the model color uncertainties. This is the first time that this sytematic is measured. Up until now, it was buried in the error associated to the SNe Ia diversity/intrinsic dispersion. Even if it is related to the SNe Ia diversity, as shown here, a $\mathcal{K}$-correction fit can avoid it.

Only by using spectrophotometric data are we capable of performing such approach, being that the perfect proof of concept of the SNfactory observational method. There is still however room for improvements. Future iterations with a more appropriate filter-set, avoiding the redder parts of the SALT2 model, where the errors are big, could be able to reduce even more the Hubble residuals scatter.

We will then proceed to another type of analysis specific to our data.

| | | Hubble diagram | | $\mathcal{K}$-correction free | |
Supernova	Redshift	Before	After	Before	After
SN2005cf	0.0070	0.093 ± 0.328	-0.086 ± 0.331	0.063 ± 0.321	-0.093 ± 0.326
SN2005el	0.0149	0.027 ± 0.183	-0.004 ± 0.182	0.004 ± 0.170	-0.089 ± 0.169
SN2006dm	0.0208	0.566 ± 0.154	0.094 ± 0.158	0.543 ± 0.140	-0.008 ± 0.150
SNF20061011-005	0.0222	-0.096 ± 0.148	0.168 ± 0.155	-0.116 ± 0.134	0.180 ± 0.146
SN2005M	0.0230	0.198 ± 0.145	0.115 ± 0.146	0.201 ± 0.129	0.134 ± 0.134
SN2007cq	0.0245	-0.108 ± 0.141	-0.161 ± 0.144	-0.122 ± 0.125	-0.209 ± 0.130
SN2004gs	0.0283	0.932 ± 0.133	-0.082 ± 0.133	0.909 ± 0.117	-0.083 ± 0.118
SN2004ef	0.0297	0.609 ± 0.133	-0.034 ± 0.142	0.548 ± 0.118	-0.042 ± 0.136
SNF20070803-005	0.0302	-0.286 ± 0.131	-0.236 ± 0.134	-0.276 ± 0.114	-0.211 ± 0.119
SNF20051003-004	0.0335	-0.174 ± 0.128	-0.082 ± 0.132	-0.146 ± 0.109	-0.047 ± 0.113
SNF20070506-006	0.0355	-0.249 ± 0.124	-0.129 ± 0.126	-0.258 ± 0.105	-0.121 ± 0.108
SNF20061020-000	0.0379	0.532 ± 0.122	0.016 ± 0.126	0.508 ± 0.105	-0.029 ± 0.108
SNF20050927-005	0.0399	0.486 ± 0.125	0.269 ± 0.132	0.502 ± 0.117	0.182 ± 0.118
SNF20060609-002	0.0400	0.800 ± 0.126	0.078 ± 0.133	0.811 ± 0.115	0.128 ± 0.124
SNF20060511-014	0.0467	0.080 ± 0.137	-0.093 ± 0.129	0.065 ± 0.138	-0.103 ± 0.111
SNF20060908-004	0.0490	-0.098 ± 0.118	-0.060 ± 0.122	-0.158 ± 0.106	-0.055 ± 0.110
SNF20060621-015	0.0543	-0.146 ± 0.115	0.021 ± 0.128	-0.155 ± 0.097	0.040 ± 0.109
SNF20060521-008	0.0563	0.532 ± 0.120	-0.154 ± 0.129	0.520 ± 0.108	-0.116 ± 0.110
SNF20060530-003	0.0571	-0.112 ± 0.125	0.019 ± 0.149	-0.153 ± 0.109	0.033 ± 0.136
SNF20061021-003	0.0615	0.310 ± 0.113	0.023 ± 0.118	0.308 ± 0.094	0.059 ± 0.099
SNF20070817-003	0.0630	0.365 ± 0.113	0.194 ± 0.121	0.317 ± 0.095	0.188 ± 0.102
SNF20060618-014	0.0646	0.034 ± 0.141	-0.022 ± 0.132	0.004 ± 0.119	0.021 ± 0.117
SNF20070802-000	0.0651	0.398 ± 0.113	0.086 ± 0.119	0.384 ± 0.097	0.020 ± 0.098
SNF20070725-001	0.0668	-0.058 ± 0.115	0.180 ± 0.124	-0.090 ± 0.100	0.162 ± 0.105
SNF20050624-000	0.0670	-0.318 ± 0.117	-0.250 ± 0.153	-0.316 ± 0.106	-0.201 ± 0.147
SNF20070630-006	0.0708	0.168 ± 0.113	0.146 ± 0.119	0.176 ± 0.098	0.106 ± 0.101
SNF20070818-001	0.0742	0.237 ± 0.114	-0.113 ± 0.120	0.195 ± 0.099	-0.038 ± 0.099
SNF20060526-003	0.0787	0.093 ± 0.112	-0.066 ± 0.127	0.065 ± 0.099	0.025 ± 0.119
SNF20070810-004	0.0823	0.176 ± 0.111	0.053 ± 0.118	0.149 ± 0.093	-0.023 ± 0.099

Table 12.2: Standard and $\mathcal{K}$-correction free Hubble diagram residuals, before and after correction by SALT2, for the 29 analyzed supernovæ. The quoted redshifts are on the CMB rest-frame (and not on the heliocentric frame, as used for the SALT2 fits).

Supernova	Redshift	# points	Phase	Hubble diagram			$\mathcal{K}$-correction free		
				Residuals	no σ_{int}	Pull	Residuals	no σ_{int}	Pull
SN2005cf	0.0070	10	(-9.69) -9.68 ± 0.21	-0.086 ± 0.331	± 0.314	-0.272	-0.093 ± 0.326	± 0.316	-0.295
SN2005el	0.0149	16	(-6.95) -6.92 ± 0.17	-0.004 ± 0.182	± 0.149	-0.024	-0.089 ± 0.169	± 0.149	-0.599
SN2006dm	0.0208	22	(-12.87) 2.11 ± 0.53	0.094 ± 0.158	± 0.119	0.790	-0.008 ± 0.150	± 0.127	-0.067
SNF20061011-005	0.0222	9	(-7.61) -7.60 ± 0.23	0.168 ± 0.155	± 0.115	1.454	0.180 ± 0.146	± 0.122	1.476
SN2005M	0.0230	8	(-3.70) -3.70 ± 0.49	0.115 ± 0.146	± 0.103	1.121	0.134 ± 0.134	± 0.108	1.246
SN2007cq	0.0245	13	(-5.65) -5.65 ± 0.24	-0.161 ± 0.144	± 0.099	-1.624	-0.209 ± 0.130	± 0.102	-2.053
SN2004gs	0.0283	11	(-0.92) 1.04 ± 0.32	-0.082 ± 0.133	± 0.083	-0.998	-0.083 ± 0.118	± 0.086	-0.960
SN2004ef	0.0297	9	(-6.64) -1.63 ± 0.02	-0.034 ± 0.142	± 0.097	-0.352	-0.042 ± 0.136	± 0.110	-0.383
SNF20070803-005	0.0302	16	(-8.96) -8.96 ± 0.21	-0.236 ± 0.134	± 0.084	-2.799	-0.211 ± 0.119	± 0.089	-2.379
SNF20051003-004	0.0335	15	(-11.09) -11.09 ± 0.22	-0.082 ± 0.132	± 0.080	-1.013	-0.047 ± 0.113	± 0.079	-0.588
SNF20070506-006	0.0355	18	(-14.99) -14.99 ± 0.17	-0.129 ± 0.126	± 0.072	-1.795	-0.121 ± 0.108	± 0.073	-1.670
SNF20061020-000	0.0379	11	(-2.45) -2.45 ± 0.37	0.016 ± 0.126	± 0.071	0.224	-0.029 ± 0.108	± 0.073	-0.391
SNF20050927-005	0.0399	8	(-5.58) -2.62 ± 0.64	0.269 ± 0.132	± 0.081	3.337	0.182 ± 0.118	± 0.086	2.111
SNF20060609-002	0.0400	11	(-0.64) 2.31 ± 0.02	0.078 ± 0.133	± 0.083	0.938	0.128 ± 0.124	± 0.095	1.354
SNF20060511-014	0.0467	9	(1.25) 1.26 ± 0.92	-0.093 ± 0.129	± 0.076	-1.221	-0.103 ± 0.111	± 0.077	-1.339
SNF20060908-004	0.0490	11	(2.03) 2.03 ± 0.61	-0.060 ± 0.122	± 0.063	-0.947	-0.055 ± 0.110	± 0.075	-0.737
SNF20060621-015	0.0543	8	(3.46) 3.48 ± 0.04	0.021 ± 0.128	± 0.075	0.284	0.040 ± 0.109	± 0.074	0.532
SNF20060521-008	0.0563	12	(-4.34) -4.32 ± 0.60	-0.154 ± 0.129	± 0.077	-1.999	-0.116 ± 0.110	± 0.076	-1.528
SNF20060530-003	0.0571	8	(3.02) 3.04 ± 1.11	0.019 ± 0.149	± 0.107	0.178	0.033 ± 0.136	± 0.109	0.297
SNF20061021-003	0.0615	14	(-5.68) -5.68 ± 0.03	0.023 ± 0.118	± 0.056	0.407	0.059 ± 0.099	± 0.059	1.004
SNF20070817-003	0.0630	7	(2.21) 2.22 ± 1.47	0.194 ± 0.121	± 0.061	3.172	0.188 ± 0.102	± 0.063	2.982
SNF20060618-014	0.0646	13	(-3.30) -3.30 ± 0.39	-0.022 ± 0.132	± 0.082	-0.274	0.021 ± 0.117	± 0.086	0.248
SNF20070802-000	0.0651	15	(-6.39) -6.39 ± 0.28	0.086 ± 0.119	± 0.058	1.471	0.020 ± 0.098	± 0.057	0.357
SNF20070725-001	0.0668	8	(-5.53) -5.53 ± 0.06	0.180 ± 0.124	± 0.068	2.649	0.162 ± 0.105	± 0.068	2.397
SNF20050624-000	0.0670	15	(-2.14) -0.14 ± 0.71	-0.250 ± 0.153	± 0.112	-2.235	-0.201 ± 0.147	± 0.123	-1.627
SNF20070630-006	0.0708	15	(-8.46) -8.45 ± 0.33	0.146 ± 0.119	± 0.059	2.497	0.106 ± 0.101	± 0.061	1.736
SNF20070818-001	0.0742	15	(-3.26) -3.26 ± 0.46	-0.113 ± 0.120	± 0.059	-1.913	-0.038 ± 0.099	± 0.059	-0.654
SNF20060526-003	0.0787	7	(-8.85) -6.86 ± 0.40	-0.066 ± 0.127	± 0.073	-0.899	0.025 ± 0.119	± 0.088	0.279
SNF20070810-004	0.0823	14	(-7.82) -7.82 ± 0.23	0.053 ± 0.118	± 0.055	0.965	-0.023 ± 0.099	± 0.058	-0.398

Table 12.3: Standard and $\mathcal{K}$-correction free Hubble diagram residuals, for the 29 analyzed supernovæ. The quoted redshifts are on the CMB rest-frame. The pull is the residual divided by its error without σ_{int}. The two values shown in the *Phase* column represent the phase of the first spectrum taken by SNIFS (between parenthesis) and the phase of the first point used for the light curve. This difference may be due to failed extractions and unavailable spectra from the used flux calibration run.

12.3 Sharp filter light curves

A different usage of the SNfactory data is the creation of synthesized "sharp" filter light curves, that is, using box filters of a few hundreds of Å, centered around specific spectral features.

Being a completely new approach from what is usual done, this is more of an exploratory exercise, made possible to us only with the data from SNfactory. The rationale behind this study is that by focusing on spectral features, known to have different time evolutions on peculiar SNe Ia with relation to typical ones, we may hope that the created light curves will reflect this peculiarity. In that case, those objects will then present an higher residual in a pseudo-Hubble diagram built from SALT2 fits to their light curves, with relation to the standard filter-set.

Filter	Wavelength range
Ca	3360–3860 Å
Si3	3950–4050 Å
Fe	4740–5040 Å
S	5200–5500 Å
Si2	5650–5850 Å
Si	5980–6280 Å

Table 12.4: Defined filter-set for the sharp spectral features study.

The "sharp" filter-set is shown in Table 12.4 and Fig. 12.6. They were mostly chosen to coincide with rest-frame absorption features near maximum light, known to present great variability on peculiar SNe Ia : Ca for the Ca II, Si, $Si2$ and $Si3$ for the three main absorption troughs of Si II and S for S II. Fe maps the Fe II blend area at maximum, and subsequent emission lines at later phases. These are also wavelength ranges typically connected with spectroscopic spectral indices such as $\Re_{Si}$, $\Re_{Ca}$ or $\Re_{SiS}$ (Bongard et al. 2006), which are known to correlate with the supernova absolute magnitude. Different expansion velocities of the supernova shell will naturally change these wavelength ranges, and we will be thus also sensible to those variations.
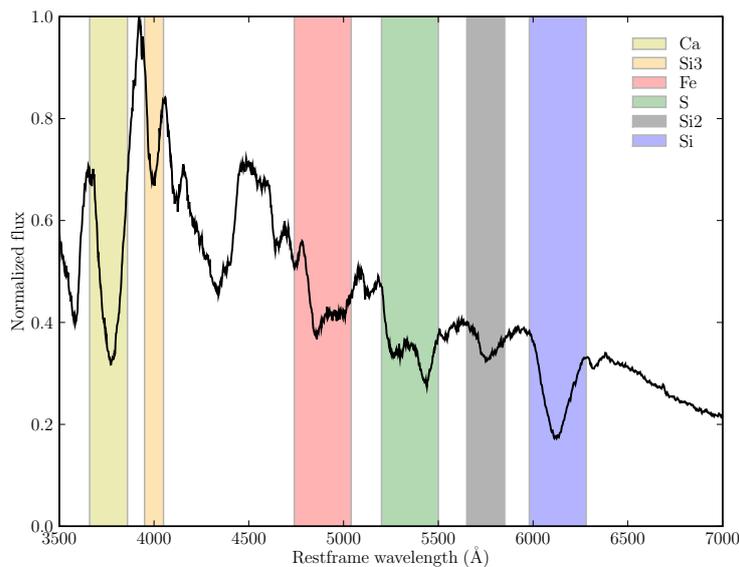

Figure 12.6: Wavelength regions of the 6 filters from the sharp filter-set, with relation to the rest-frame spectrum of a typical SN Ia.

The sheer amount of filter combinations opens a large combinatorial playground, but from these, three were chosen as most representative for the intended study. The combination $\mathcal{X}$ uses light curves from each sharp filter simultaneously, combination $\mathcal{Y}$ uses the three Si II absorption features (two of which are used for $\Re_{Si}$), and combination $\mathcal{Z}$ uses the Ca II range (probed by $\Re_{Ca}$) and the silicon trough at ~ 5700Å. For each combination, light curves for the previously described supernovæ are synthesized, fitted with SALT2 (obviously on the $\mathcal{K}$-correction free/redshifted filters approach), and its results used to create pseudo-Hubble diagram. The light curves for the $\mathcal{Y}$ and $\mathcal{Z}$ filter combinations are in Appendix C.2–C.3.

	$\mathcal{X}^{\dagger}$		$\mathcal{Y}^{\ddagger}$		$\mathcal{Z}^{*}$	
Supernova	Pull	nMAD	Pull	nMAD	Pull	nMAD
SN2005cf	-0.403	0.089	-0.216	0.059	-0.609	0.084
SN2005el	0.578	0.096	0.556	0.088	0.713	0.081
SN2006dm	0.667	0.099	1.074	0.092	(2.243)	0.131
SNF20061011-005	(0.766)	0.129	0.171	0.085	(-1.136)	0.223
SN2005M	1.548	0.084	3.634	0.064	1.946	0.050
SN2007cq	(-2.648)	0.113	(-3.019)	0.100	-1.489	0.086
SN2004gs	(-0.403)	0.176	(0.720)	0.135	(3.856)	0.143
SN2004ef	3.345	0.092	3.064	0.074	5.821	0.072
SNF20070803-005	(-4.345)	0.156	-5.868	0.090	-1.387	0.086
SNF20051003-004	(-2.063)	0.133	(-2.298)	0.111	(-0.145)	0.184
SNF20070506-006	-2.445	0.091	-3.176	0.080	-2.554	0.117
SNF20061020-000	(1.653)	0.111	1.754	0.095	4.298	0.090
SNF20050927-005	4.586	0.063	4.797	0.065	7.030	0.072
SNF20060609-002	(0.994)	0.123	1.022	0.095	2.123	0.077
SNF20060511-014	2.068	0.090	2.237	0.049	(1.828)	0.139
SNF20060908-004	-3.809	0.078	-2.790	0.073	-2.886	0.081
SNF20060621-015	0.425	0.080	0.294	0.086	(-1.427)	0.152
SNF20060521-008	(-5.826)	0.181	-3.427	0.094	-3.383	0.093
SNF20060530-003	(-2.854)	0.116	-5.050	0.045	-9.783	0.058
SNF20061021-003	(0.923)	0.137	(1.431)	0.102	(-3.116)	0.160
SNF20070817-003	(6.892)	0.154	(6.993)	0.113	(0.350)	0.243
SNF20060618-014	(-1.317)	0.109	-2.249	0.069	-1.447	0.107
SNF20070802-000	(2.021)	0.148	4.045	0.080	-0.277	0.073
SNF20070725-001	6.914	0.095	5.765	0.059	(4.902)	0.105
SNF20050624-000	-6.185	0.083	-9.858	0.053	-10.031	0.049
SNF20070630-006	(5.751)	0.202	(4.518)	0.116	(2.638)	0.189
SNF20070818-001	(0.821)	0.147	0.413	0.096	(-0.069)	0.123
SNF20060526-003	(-7.333)	0.115	-8.071	0.074	-6.578	0.109
SNF20070810-004	(1.188)	0.123	4.215	0.099	(-5.987)	0.130

† Ca + Fe + S + Si + Si2 + Si3
‡ Si + Si2 + Si3
* Ca + Si2

Table 12.5: Pull distribution for each pseudo-Hubble fit made with the different sharp filter combinations. The values between parenthesis are the ones for which the SALT2 light curve residuals' nMAD is higher than 0.1.

The pull distribution of the residuals of the pseudo-Hubble diagrams, for each of the three different filter combinations, is presented in Table 12.5. As before, the shown pull values are calculated using non error-scaled SALT2 fits. The nMAD of the SALT2 light curve residuals are also shown, and the objects which have nMAD> 0.1 (the selection applied to the light curves used on the previous section Hubble diagram), have the pull value between parenthesis, for easier identification. This distinction has to be made for the sake of simplicity: while is it clear that a wrong SALT2 fit may be a pointer of an intrinsically peculiar SN Ia, it may also mean that

simply the light curve points are wrong, and we risk of seeing every supernova as a peculiar one.

We'll do a twofold study. First we will look into the pull distribution for each filter combination. Secondly we will start from the already known spectroscopically peculiar object in this dataset, and do a qualitative analysis of their sharp light curves, searching for similarities or differences that correlate with the different peculiar spectral classes.

12.3.1 Pull analysis

The residuals (and associated pull) of the pseudo-Hubble fits, can in principle be used as an estimator of the ability of SALT2 to describe the created light curves. Objects which have a small final residual, were properly corrected, and are hence well described by the SALT average spectral mode. However, while that is true with the broadband filters, such interpretation is more delicate in the case of the sharp filters. Two problems may occur: synthesized magnitudes will have higher uncertainties than in the broader filters case, especially if we have noisy, low SNR spectra. Besides that, SALT was not conceived for fits using such sharp wavelength ranges, and as such, its average model may not be able to describe isolated spectral features, even on a "normal" SNe Ia. Distinguishing a bad SALT2 fit due to these effects, and the one due to a truly peculiar object, will then be a hard task.

A look into Table 12.5 confirms that: even if applying the cut on the SALT2 residuals' nMAD (which as explained before, is a somewhat artificial cut, since we are searching for targets *badly* described by SALT2), a large number of objects are significant outliers. While SALT2 is capable of fitting accurately some of the light curves, as can be seen in Figs. 12.7–12.8, it does not seem capable of producing consistent corrections/standardization values from them, neither of describing the variability of the spectral features at this "sharp" light curve level. That, allied to the existence of a large number of light curves with significant outliers, invalidates this approach, at least until an higher precision is attained, either statistically either on the reduction of systematic errors on the synthesized magnitudes and/or SALT2 model.
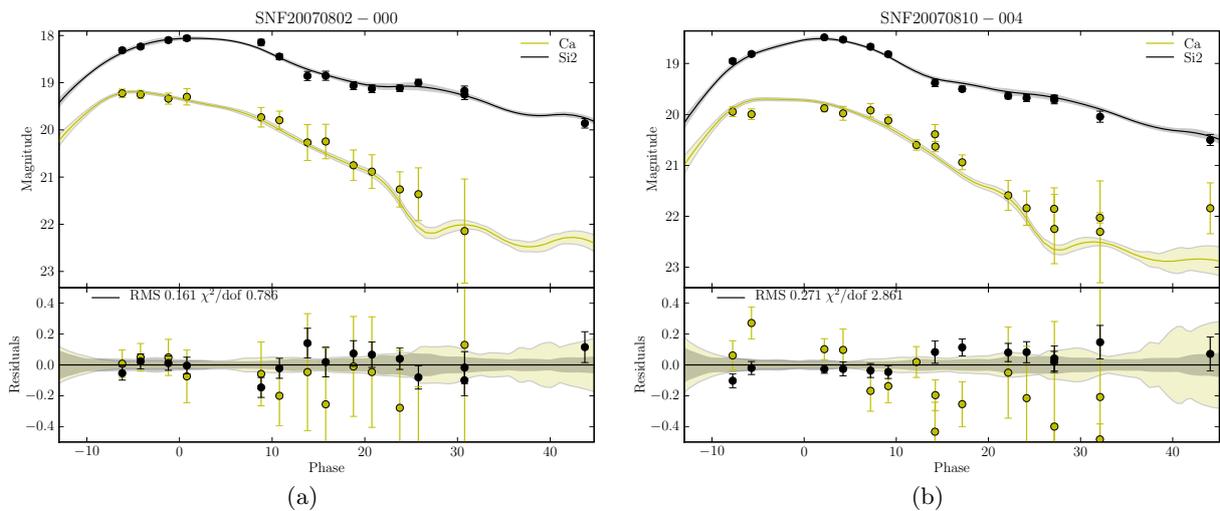

Figure 12.7: (a) SNF20070802-000 and (b) SNF20070810-004 SALT2 fitted light curves, using the sharp $\mathcal{Y}$ filter combination.
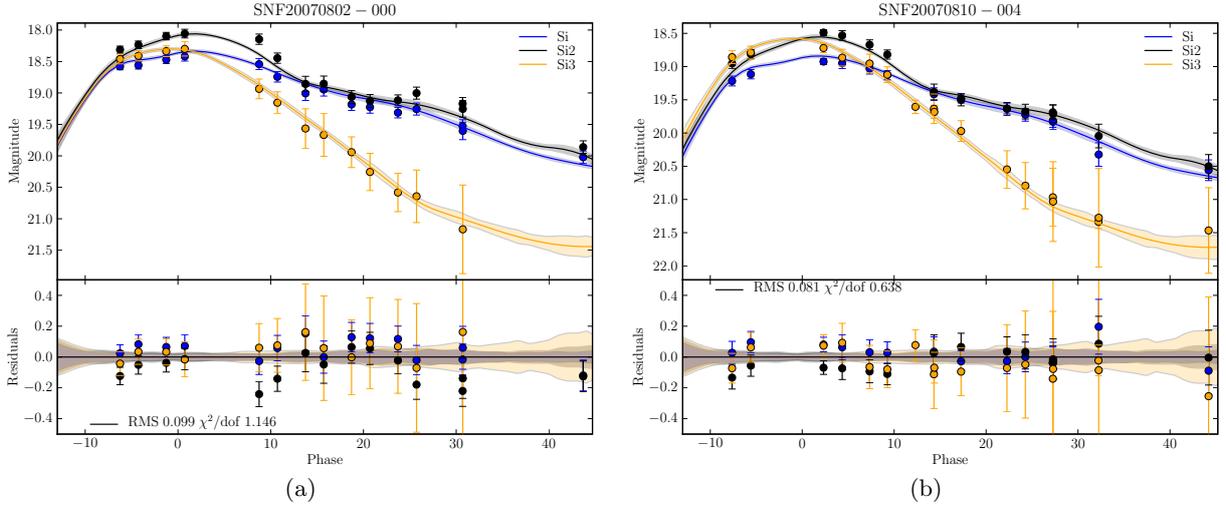
Figure 12.8: (a) SNF20070802-000 and (b) SNF20070810-004 SALT2 fitted light curves, using the $\mathcal{Z}$ sharp filter combination.

12.3.2 91T-like qualitative light curve analysis

Besides the already introduced overluminous SN2007cq and SNF20070803-005, there are two others peculiar objects of similar type in the current sample: SN2005M (Aldering et al. 2005) and SNF20070506-006.

Supernova	Before	After	Spectral type
SN2005M	0.205 ± 0.138	0.110 ± 0.138	91T
SN2007cq	-0.117 ± 0.134	-0.184 ± 0.134	99aa
SNF20070506-006	-0.253 ± 0.118	-0.131 ± 0.118	91T
SNF20070803-005	-0.271 ± 0.124	-0.231 ± 0.124	91T

Table 12.6: $\mathcal{K}$-correction free Hubble diagram residuals, before and after correction with SALT2 with no error-scaling, for 4 overluminous objects.

Of these objects (Fig. 12.9), three are spectroscopically typed as being 91T-like, showing a shallow Si II feature and strong Fe III on the early spectra, and the other one (SN2007cq) as 99aa-like, similar to 91T but with a marked Ca II. Table 12.6 summarizes their $\mathcal{K}$-correction free Hubble diagram residuals, before and after correction by SALT2. Interestingly enough, SN2005M presents a positive residual before correction, contrary to what we would expect from a overluminous supernova. That may come from a wrong flux calibration, and unfortunately, although SNfactory possesses early spectra from it, they are not currently available to the flux calibration pipeline for further testing. It is also worth mentioning that, all 4 targets show a large pull on the $\mathcal{Y}$ sharp filter combination, which was expected: $\mathcal{Y}$ uses the three Si absorptions, known to present a greater difference on overluminous objects, compared to the average SN Ia, and thus a large departure from the SALT2 average spectral model.

A closer look at their $\mathcal{Y}$ light curves (Fig. 12.10), shows some noteworthy results. First of all, these light curves are fundamentally different from equivalent ones from normal SNe Ia, that can be seen in Fig. 12.7 or Appendix C.2: the difference in magnitude near maximum, of the Ca and Si lines is much smaller in the overluminous than the other supernovæ, as would be expected,
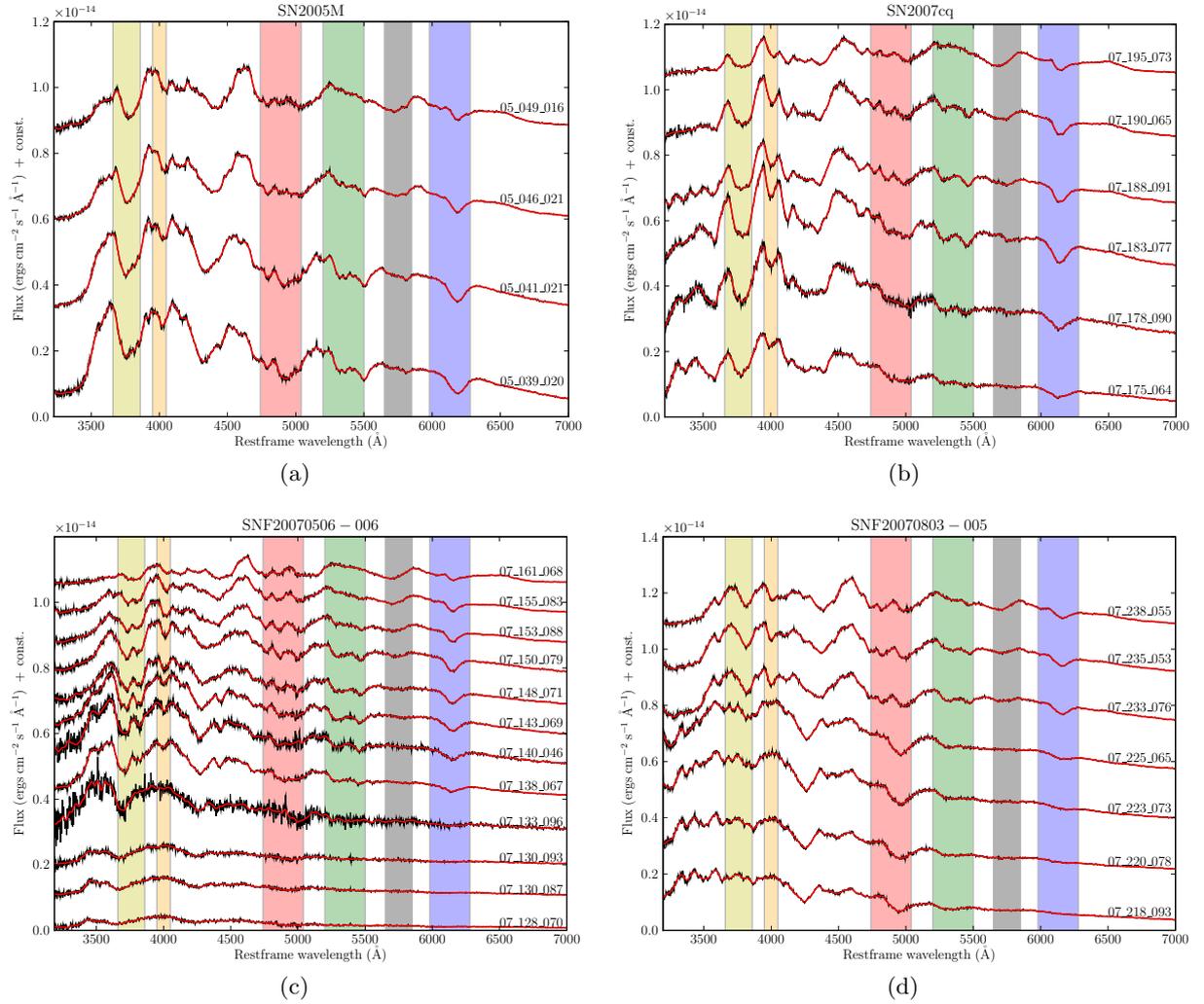
Figure 12.9: Spectral series of overluminous objects. The year, day and run number are noted by each spectrum. For the phase of the first spectrum (the bottom one), see the *Phase* column of Table 11.4. The red line is a gaussian filter smoothing with $\sigma = 5$Å, and the shaded areas are the filters of the sharp filter-set. Every spectrum is at rest-frame.

since a strong Ca II line is one of their defining properties. However, and taking into account the small sample available, there also seems to exist different variabilities of the Ca line inside the overluminous group. While for SN2007cq, which has a different sub-spectral type than the other ones, the Ca light curve does not cross the Si2 one, there is a clear crossing for SNF20070803-005 (which coincidentally is the 91T-like supernova with the smaller SALT2 correction on the Hubble diagram), and a less marked on SNF20070506-006. The SALT2 model seems to indicate a similar crossing for SN2005M, but to confirm it, the early (currently) unavailable spectra will have to be processed. This "crossing" difference between objects, common to the objects of a spectral class, but presenting variability inside that same class, may indicate the existence of other sub-classes of overluminous objects, of which SNF20070803-005 would be part. That however, is an hypothesis that with the available set in hand, and with this simple qualitative approximation, we can not further test.
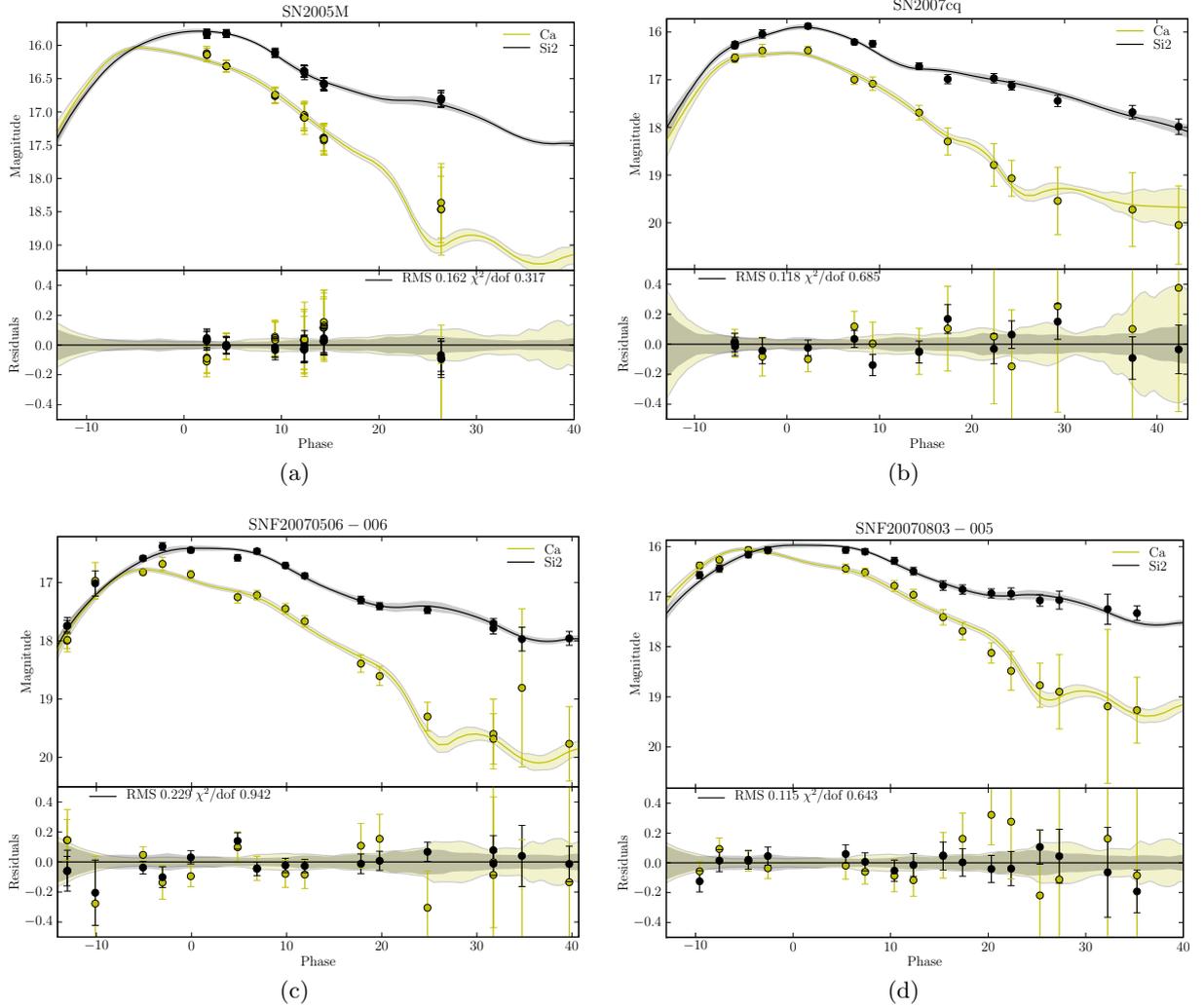
Figure 12.10: $\mathcal{Y}$ (Ca + Si2) sharp filter combination light curves for (a) SN2005M, (b) SN2007cq, (c) SNF20070506-006 and (d) SNF20070803-005.

Concluding, a first exploration of photometric identification of peculiar SNe Ia, using specific sharp bandpass filters, was presented, as well as the first ever light curves for sharp spectral features of SNe Ia. For the moment, we are still very close to the observational noise and the limits of the fitter, for an advanced variability study. For that, one would need a larger sample of optimally extracted spectra, with bigger SNR, and a proper error propagation model. That will be case of SNfactory in the near future, with the current work on advanced spectra deconvolution and the increased sample (the used SNe Ia in this thesis work are roughly 1/5 of the full SNfactory dataset). Even so, we could identify a variability of the Ca II line within the overluminous class, based solely on the sharp filter light curves.

Conclusion & perspectives

Type Ia supernovæ are one of the pillars of modern observational cosmology. It was using them, that 10 years ago the doors to a new era of high precision cosmology were opened, and they are still nowadays one of the main probes of dark energy. Such success is due to their peculiar origin and subsequent similar evolution and explosion conditions, that makes them a particular family of objects, whose brightness at maximum light can be properly standardized (up to an intrinsic dispersion level), in order to use them as good standard candles for distance measurements in the universe.

The cosmological analysis using SNe Ia, requires both high-redshift and low-redshift objects, which act as a lever arm of the Hubble fit. While the higher redshift dataset has been multiplied several times in the recent years, the nearby one has not changed considerably over the last decade, and is nowadays one of the main sources of systematic errors on this analysis.

The work presented in this document is my contribution to one of the projects that searches and follows nearby ($0.03 < z < 0.08$) supernovæ since 2004, the nearby SNfactory. Its particular observational approach, which uses a dedicated integral field spectrograph (SNIFS) to obtain spectral time series of SNe Ia, is unique, and grants the possibility of a broad range of exploratory studies about the observed (small) intrinsic dispersion about the SNe Ia absolute magnitude.

My thesis work can be divided into two main parts: a technical one, dealing with the acquisition, calibration and extraction of specific data from the SNIFS photometric camera; and an analysis where the first spectrophotometric light curves issued from SNIFS were obtained, and used to create the first ever spectrophotometric nearby Hubble diagram.

The photometric channel of SNIFS is used in parallel with the spectrograph, and images the field around the supernova being observed, in order to monitor the atmospheric transmission difference between nights, and as such is essential for an absolute flux calibration of the obtained SNe Ia spectra, on non-photometric conditions. I started with the calibration of the data at the raw level, from the implementation of processes for parasite light handling, up to the characterization of several parameters of the photometric camera. From this, a full pipeline for the extraction of the photometric ratios between nights was built (`SnfPhot+SnfPhotPipeline`) and implemented in the SNfactory central production pipeline. The photometric ratios quality was benchmarked and the systematic errors affecting them are estimated to be below 2%.

A by-product of the photometric channel, the acquisition images, were then used for the creation of single color photometric light curves, and subsequent fitting using SALT. From these, 73 were used for a first study of the phase and stretch distributions of the SNfactory dataset, which shows consistency with published data, and is thus an indication that they are good candidates for a cosmological analysis. A small bias of SALT, when fitting light curves without any pre-maximum points was also seen.

Using the obtained photometric ratios, it was then possible to run the full flux calibration pipeline on the spectra of six spectrophotometric standard stars. The resulting spectrophotometric light curves allowed to determine the current precision of the SNfactory flux calibration

on non-photometric nights, of $\sim 5\%$, and confirm the color consistency of the extracted spectra. Furthermore, the light curves of 30 SNe Ia observed by SNIFS were synthesized and fitted using SALT2, being thus the first SNe Ia light curves issued from spectrophotometric data. No major residuals or flux biases were observed for the fitted light curves.

Finally, all this data was used to create the first ever spectrophotometric nearby Hubble diagram, whose scatter is 15% (quadratically) smaller than the one made using published data. That is a proof of the great improvement in data cross-calibration, by using a single telescope/instrument for the followup of all the objects. The quality of the data also allows us for the first time, to peer into the origins of the supernovæ intrinsic dispersion, namely their spectroscopic variability, as the identification of a spectroscopically peculiar SNe Ia as a clear outlier from the Hubble line confirms. Our unique data allowed to perform the first SNe Ia $\mathcal{K}$-correction free cosmological fit. This fit, insensitive to the interplay between the SNe Ia spectral features and the filters edges in function of the redshift of the objects, showed a 5% quadratic reduction of the Hubble diagram fit residual. We can then conclude that, in the usual cosmological fit, $\mathcal{K}$-correction combined with the current SALT2 description of the SNe Ia spectral variability, induces a dispersion of the same scale. Such dispersion induced by the $\mathcal{K}$-correction, was hidden up until now under the "SNe Ia intrinsic dispersion". A training of SALT2 with the SNfactory spectrophotometric data will certainly allow to reduce this "$\mathcal{K}$-correction" induced dispersion. An exploratory study on the usage of sharp spectral features light curves, for the study of peculiar objects, was also performed. The current extraction quality and statistics does not allow to make a robust outlier rejection method needed for this study, but a qualitative study of the produced sharp light curves showed hints of possible sub-families inside the already peculiar 91T-like SNe Ia family.

After an important technical effort by a small team of people, the analysis of SNfactory data is wrapping up quickly now, and starting to "payback". The study of a dataset more than 2 times bigger than the one used in this thesis, has started this fall. Continuous developments in the data extraction, calibration and analysis methods will allow us to extract even more information from this already invaluable dataset, either from a cosmological fit point of view, either from the physics behind the observed SNe Ia diversity.

Part V

Appendix

Appendix A

SnfPhot pipeline

A.1 Software call

The `SnfPhot` pipeline can be called either from the command line, either as a GUI interface.

```
usage: SnfPhot [options] object [object2 object3 ...]

options:
  --version             show program's version number and exit
  -h, --help            show this help message and exit
  -i INFILE, --infile=INFILE
                        (optional) File with MF exposures
  -f FILTERS, --filters=FILTERS
                        (optional) MF filters to process (default=1,2,3,4,5)
  -a, --acq             Do ACQ instead of MF
  -p PREFIX, --prefix=PREFIX
                        (optional) Prefix for BQS jobname
  -R, --raw             Use raw exposures (Fclass 17) instead of preprocess
                        ones (Fclass 18)
  -l, --lightcurve      Build associated lightcurves (field stars + object)
  -r, --redo            Redo PSF/kernels even if already there (from
                        increment)
  -C, --cosmic          (test) Do cosmic detection (somewhat buggy in poloka)
  -d, --defringe        Apply defringing on all subfilters
  -P, --psf             (test) Creates PSF for _all_ aligned images
  -n, --nomoon          (test) Do not process exposures < 30 deg from Moon
  -I, --increment       Increment hypothetical old processes already in DB
  -A, --apercorr        Use aperture correction for aperture photometry
  -D, --debug           Debug using pdb
  -s, --save            Save results to DB
  -c, --copy            Copy results back to local dir
  -L, --local           Run locally
  -Q, --qsub            Submit created file automatically
  -X                    Use X GUI (Tkinter)
```

A.2 GUI

A simple GUI interface (Fig. A.1) to `SnfPhot` is available using the `-X` flag on the command line. It presents the most used options as tick boxes, and automatically searches the database for matches of the target names inputed by the user.
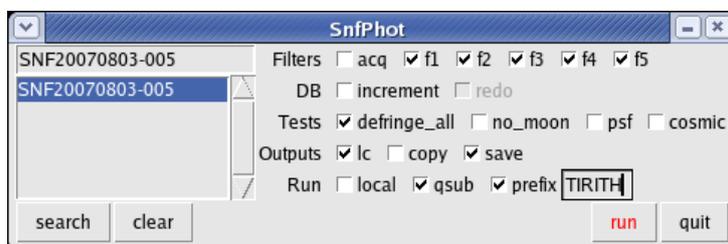

Figure A.1: `SnfPhot` GUI interface.

A.3 Documentation

Full documentation for the `SnfPhotPipeline` package, on which `SnfPhot` is heavily based, can be found at http://snovae.in2p3.fr/pereira/SnfPhotPipeline/.

Appendix B

Extra tables

Some large tables are put together here, in order to unclutter the document.

B.1 Spectrophotometric *vs.* Bessell V light curves

Supernova	Redshift	Phase			x_1		
		Multi-color	Synth. V	Phot. V	Multi-color	Synth. V	Phot. V
SN2005el	0.0149	-6.958 ± 0.172	-6.865 ± 0.407	-6.376 ± 0.310	-1.964 ± 0.151	-1.818 ± 0.436	-2.144 ± 0.286
SNF20061011-005	0.0230	-3.700 ± 0.495	-3.336 ± 0.871	-3.076 ± 0.232	0.931 ± 0.336	0.856 ± 0.737	-0.228 ± 0.169
SN2007cq	0.0258	-5.658 ± 0.238	-5.376 ± 0.368	-5.518 ± 0.131	-1.060 ± 0.302	-1.600 ± 0.572	-1.054 ± 0.209
SN2004gs	0.0274	-0.933 ± 0.323	0.827 ± 1.037	-1.947 ± 0.970	-3.270 ± 0.243	-3.160 ± 0.775	-3.294 ± 0.924
SN2004ef	0.0310	-6.645 ± 0.015	-6.036 ± 1.504	-8.129 ± 0.469	-1.444 ± 0.438	0.222 ± 2.323	-2.555 ± 0.541
SNF20070803-005	0.0314	-8.971 ± 0.206	-8.967 ± 0.425	-9.165 ± 0.144	0.823 ± 0.298	0.773 ± 0.719	0.756 ± 0.215
SNF20051003-004	0.0343	-11.097 ± 0.224	-10.682 ± 0.412	-11.008 ± 0.128	0.344 ± 0.332	0.010 ± 0.621	0.605 ± 0.172
SNF20070506-006	0.0348	-15.000 ± 0.173	-14.884 ± 0.390	-15.141 ± 0.100	0.732 ± 0.197	0.780 ± 0.485	1.289 ± 0.170
SNF20061020-000	0.0391	-2.458 ± 0.374	-1.907 ± 0.846	-1.335 ± 0.281	-2.100 ± 0.225	-2.126 ± 0.748	-2.184 ± 0.356
SNF20060609-002	0.0397	-5.591 ± 0.638	-5.397 ± 0.907	-3.684 ± 0.161	-0.612 ± 0.488	-0.552 ± 1.020	-0.231 ± 0.147
SNF20050927-005	0.0407	-0.646 ± 0.018	-2.868 ± 1.410	0.851 ± 0.350	-0.358 ± 0.431	-1.368 ± 1.135	0.118 ± 0.191
SNF20060511-014	0.0476	1.248 ± 0.920	2.635 ± 1.700	1.764 ± 0.931	-1.467 ± 0.460	-1.263 ± 0.688	-3.319 ± 0.572
SNF20060908-004	0.0500	2.020 ± 0.606	0.314 ± 0.914	0.669 ± 0.507	0.620 ± 0.299	-0.111 ± 0.520	0.971 ± 0.253
SNF20060521-008	0.0551	3.458 ± 0.037	3.357 ± 2.362	3.968 ± 0.655	-2.124 ± 0.407	-2.264 ± 1.142	-1.006 ± 0.285
SNF20060621-015	0.0553	-4.345 ± 0.596	-4.516 ± 0.877	-2.853 ± 0.439	0.771 ± 0.455	0.475 ± 0.804	0.744 ± 0.287
SNF20060530-003	0.0568	3.015 ± 1.110	2.581 ± 2.958	3.344 ± 0.055	1.063 ± 0.709	1.172 ± 1.380	1.579 ± 0.345
SNF20060618-014	0.0638	2.201 ± 1.471	2.503 ± 2.124	1.488 ± 0.554	0.482 ± 0.409	0.545 ± 0.769	0.526 ± 0.289
SNF20070802-000	0.0651	-6.401 ± 0.282	-6.478 ± 0.388	-6.514 ± 0.177	0.214 ± 0.297	-0.331 ± 0.577	-0.319 ± 0.249
SNF20050624-000	0.0671	-5.539 ± 0.061	-4.514 ± 1.186	-6.397 ± 0.090	-0.155 ± 0.931	-2.729 ± 5.818	0.942 ± 2.735
SNF20070725-001	0.0679	-2.146 ± 0.707	-2.597 ± 0.128	1.305 ± 1.184	0.655 ± 0.331	0.351 ± 0.526	1.650 ± 0.506
SNF20060526-003	0.0779	-8.858 ± 0.403	-8.536 ± 0.753	-7.008 ± 0.190	-0.665 ± 0.498	-1.509 ± 1.394	0.198 ± 0.292
SNF20070810-004	0.0835	-7.823 ± 0.230	-8.031 ± 0.393	-7.598 ± 0.156	-0.230 ± 0.293	-0.639 ± 0.528	-0.792 ± 0.240

Table B.1: SALT2 phase and stretch (x_1) for 22 common supernovæ between both acquisition and spectrophotometric light curves datasets, for different light curve creation methods: spectrophotometric multi-color, single-color synthesized "acquisition light curves" and photometric single-color V.

B.2 $\mathcal{K}$-correction free SALT2 fits

Supernova	Redshift	# points	Phase	x_1	c	χ^2/dof
SN2005cf	0.0065	10	(-9.68) -9.67 $\pm$ 0.21	-0.205 $\pm$ 0.325	0.065 $\pm$ 0.033	0.281
SN2005el	0.0149	16	(-6.97) -6.94 $\pm$ 0.18	-1.950 $\pm$ 0.143	-0.108 $\pm$ 0.025	0.505
SN2005M	0.0220	22	(-13.01) 1.96 $\pm$ 0.52	0.806 $\pm$ 0.377	0.099 $\pm$ 0.024	0.186
SN2006dm	0.0220	9	(-7.67) -7.66 $\pm$ 0.24	-2.853 $\pm$ 0.488	0.059 $\pm$ 0.039	0.719
SNF20061011-005	0.0230	8	(-3.38) -3.38 $\pm$ 0.55	1.143 $\pm$ 0.386	-0.063 $\pm$ 0.033	0.668
SN2007cq	0.0258	13	(-5.63) -5.63 $\pm$ 0.25	-0.934 $\pm$ 0.301	-0.029 $\pm$ 0.030	0.437
SN2004gs	0.0274	11	(-0.65) 1.31 $\pm$ 0.41	-2.975 $\pm$ 0.282	0.280 $\pm$ 0.025	1.491
SN2004ef	0.0310	9	(-6.65) -1.64 $\pm$ 0.61	-1.618 $\pm$ 0.589	0.179 $\pm$ 0.039	0.601
SNF20070803-005	0.0314	16	(-9.02) -9.02 $\pm$ 0.23	1.005 $\pm$ 0.306	0.047 $\pm$ 0.028	0.247
SNF20051003-004	0.0343	15	(-11.18) -11.18 $\pm$ 0.04	0.787 $\pm$ 0.264	0.011 $\pm$ 0.026	0.554
SNF20070506-006	0.0348	17	(-15.04) -13.04 $\pm$ 0.17	0.845 $\pm$ 0.199	-0.004 $\pm$ 0.023	0.586
SNF20061020-000	0.0391	11	(-2.32) -2.32 $\pm$ 0.42	-2.087 $\pm$ 0.242	0.113 $\pm$ 0.030	0.437
SNF20060609-002	0.0397	8	(-5.63) -2.67 $\pm$ 0.77	-0.484 $\pm$ 0.538	0.318 $\pm$ 0.046	0.968
SNF20050927-005	0.0407	11	(-1.36) 1.60 $\pm$ 1.09	-0.823 $\pm$ 0.581	0.101 $\pm$ 0.039	0.216
SNF20060511-014	0.0476	9	(1.40) 1.41 $\pm$ 1.17	-1.170 $\pm$ 0.493	-0.006 $\pm$ 0.061	0.137
SNF20060908-004	0.0500	11	(2.94) 2.94 $\pm$ 0.79	0.914 $\pm$ 0.355	0.020 $\pm$ 0.030	0.473
SNF20060521-008	0.0551	8	(3.73) 3.74 $\pm$ 0.04	-1.629 $\pm$ 0.405	0.202 $\pm$ 0.045	0.522
SNF20060621-015	0.0553	12	(-4.21) -4.20 $\pm$ 0.64	1.005 $\pm$ 0.426	-0.021 $\pm$ 0.030	0.936
SNF20060530-003	0.0568	8	(3.47) 3.49 $\pm$ 1.01	1.331 $\pm$ 0.601	0.010 $\pm$ 0.035	0.145
SNF20061021-003	0.0627	14	(-5.40) -5.40 $\pm$ 0.36	-0.172 $\pm$ 0.278	0.116 $\pm$ 0.028	0.651
SNF20060618-014	0.0638	7	(2.83) 2.84 $\pm$ 1.23	0.964 $\pm$ 0.439	0.068 $\pm$ 0.044	0.241
SNF20070817-003	0.0640	13	(-3.33) -3.33 $\pm$ 0.42	-1.265 $\pm$ 0.325	-0.034 $\pm$ 0.029	1.976
SNF20070802-000	0.0651	15	(-6.53) -6.53 $\pm$ 0.09	0.056 $\pm$ 0.277	0.195 $\pm$ 0.032	0.892
SNF20050624-000	0.0671	8	(-5.38) -5.38 $\pm$ 0.60	0.519 $\pm$ 0.860	-0.019 $\pm$ 0.050	0.123
SNF20070725-001	0.0679	15	(-1.48) 0.52 $\pm$ 0.88	0.943 $\pm$ 0.369	-0.056 $\pm$ 0.032	0.529
SNF20070630-006	0.0721	15	(-8.54) -8.53 $\pm$ 0.41	0.509 $\pm$ 0.294	0.077 $\pm$ 0.035	0.988
SNF20070818-001	0.0753	15	(-2.95) -2.95 $\pm$ 0.59	-0.278 $\pm$ 0.322	0.100 $\pm$ 0.037	0.353
SNF20060526-003	0.0779	7	(-8.38) -6.39 $\pm$ 0.60	-0.189 $\pm$ 0.589	0.006 $\pm$ 0.044	0.622
SNF20070403-001	0.0804	13	(-4.79) -1.87 $\pm$ 0.48	-1.957 $\pm$ 0.340	-0.001 $\pm$ 0.031	1.474
SNF20070810-004	0.0835	14	(-7.82) -7.82 $\pm$ 0.26	-0.437 $\pm$ 0.298	0.055 $\pm$ 0.031	0.324

Table B.2: Fitted $\mathcal{K}$-correction free SALT2 parameters for 30 SNfactory spectrophotometric light curves, ordered by redshift.

Supernova	Redshift	B_{SNf}		V_{SNf}		R_{SNf}		All filters	
		RMS	nMAD	RMS	nMAD	RMS	nMAD	RMS	nMAD
SN2005cf	0.0065	0.055	0.026	0.047	0.038	0.053	0.077	0.056	0.049
SN2005el	0.0149	0.067	0.058	0.047	0.028	0.054	0.031	0.057	0.032
SN2005M	0.0220	0.058	0.022	0.019	0.020	0.068	0.062	0.054	0.034
SN2006dm	0.0220	0.111	0.153	0.080	0.091	0.095	0.078	0.097	0.098
SNF20061011-005	0.0230	0.077	0.084	0.064	0.071	0.055	0.079	0.068	0.078
SN2007cq	0.0258	0.067	0.104	0.073	0.088	0.056	0.053	0.068	0.072
SN2004gs	0.0274	0.091	0.103	0.089	0.086	0.088	0.068	0.092	0.093
SN2004ef	0.0310	0.190	0.058	0.100	0.094	0.090	0.087	0.139	0.078
SNF20070803-005	0.0314	0.068	0.059	0.047	0.054	0.058	0.077	0.063	0.063
SNF20051003-004	0.0343	0.033	0.033	0.081	0.097	0.071	0.076	0.066	0.068
SNF20070506-006	0.0348	0.092	0.057	0.087	0.061	0.070	0.062	0.084	0.061
SNF20061020-000	0.0391	0.150	0.082	0.044	0.036	0.071	0.097	0.107	0.075
SNF20060609-002	0.0397	0.111	0.088	0.073	0.107	0.126	0.142	0.113	0.101
SNF20050927-005	0.0407	0.050	0.069	0.026	0.035	0.056	0.059	0.048	0.047
SNF20060511-014	0.0476	0.056	0.043	0.077	0.047	0.027	0.027	0.058	0.043
SNF20060908-004	0.0500	0.123	0.087	0.063	0.054	0.070	0.060	0.094	0.060
SNF20060521-008	0.0551	0.046	0.056	0.073	0.088	0.082	0.082	0.072	0.071
SNF20060621-015	0.0553	0.082	0.086	0.075	0.062	0.090	0.099	0.084	0.091
SNF20060530-003	0.0568	0.029	0.031	0.035	0.044	0.037	0.047	0.034	0.036
SNF20061021-003	0.0627	0.138	0.137	0.094	0.081	0.085	0.125	0.109	0.120
SNF20060618-014	0.0638	0.093	0.032	0.059	0.034	0.050	0.072	0.072	0.036
SNF20070817-003	0.0640	0.177	0.112	0.139	0.071	0.171	0.109	0.170	0.108
SNF20070802-000	0.0651	0.086	0.097	0.069	0.103	0.100	0.137	0.093	0.110
SNF20050624-000	0.0671	0.035	0.046	0.036	0.041	0.022	0.026	0.032	0.037
SNF20070725-001	0.0679	0.046	0.062	0.049	0.060	0.088	0.110	0.069	0.079
SNF20070630-006	0.0721	0.076	0.084	0.106	0.132	0.125	0.113	0.108	0.103
SNF20070818-001	0.0753	0.101	0.023	0.056	0.070	0.076	0.041	0.078	0.046
SNF20060526-003	0.0779	0.338	0.032	0.081	0.137	0.039	0.084	0.215	0.084
SNF20070403-001	0.0804	0.332	0.075	0.126	0.149	0.126	0.115	0.223	0.123
SNF20070810-004	0.0835	0.070	0.090	0.070	0.047	0.061	0.058	0.068	0.061
All supernovæ points with mag < 20		0.080	0.058	0.073	0.059	0.086	0.072	0.080	0.064

Table B.3: RMS and normalized MAD (in magnitudes) of the residuals for 30 SNfactory spectrophotometric light curves, fitted using $\mathcal{K}$-correction free SALT2.

B.3 Hubble diagram results without LC points' error scaling

Parameter	Hubble diagram	$\mathcal{K}$-correction free
α	0.110 ± 0.024	0.136 ± 0.020
β	2.290 ± 0.293	2.058 ± 0.251
M	-19.332 ± 0.029	-19.312 ± 0.026
RMS	0.132 ± 0.018	0.118 ± 0.016
σ_{int}	0.118	0.101

Table B.4: Parameters of the nearby Hubble diagram fit, for a flat ΛCDM cosmology with fixed $\Omega_{\mathrm{m}} = 0.24$, using 29 SNfactory's spectrophotometric light curves.

Supernova	Redshift	Hubble diagram			$\mathcal{K}$-correction free		
		Residuals	no σ_{int}	Pull	Residuals	no σ_{int}	Pull
SN2005cf	0.0070	-0.091 ± 0.330	± 0.308	-0.296	-0.094 ± 0.324	± 0.308	-0.306
SN2005el	0.0149	0.047 ± 0.188	± 0.146	0.324	-0.034 ± 0.177	± 0.146	-0.236
SN2006dm	0.0208	0.142 ± 0.158	± 0.105	1.359	0.038 ± 0.145	± 0.105	0.368
SNF20061011-005	0.0222	0.158 ± 0.153	± 0.098	1.618	0.173 ± 0.141	± 0.098	1.776
SN2005M	0.0230	0.089 ± 0.151	± 0.094	0.948	0.110 ± 0.138	± 0.094	1.164
SN2007cq	0.0245	-0.136 ± 0.148	± 0.089	-1.539	-0.184 ± 0.134	± 0.089	-2.076
SN2004gs	0.0283	-0.054 ± 0.141	± 0.077	-0.705	-0.060 ± 0.127	± 0.077	-0.784
SN2004ef	0.0297	-0.028 ± 0.139	± 0.073	-0.383	-0.013 ± 0.125	± 0.073	-0.172
SNF20070803-005	0.0302	-0.256 ± 0.139	± 0.072	-3.551	-0.231 ± 0.124	± 0.072	-3.207
SNF20051003-004	0.0335	-0.086 ± 0.135	± 0.065	-1.320	-0.058 ± 0.120	± 0.065	-0.889
SNF20070506-006	0.0355	-0.142 ± 0.133	± 0.061	-2.316	-0.131 ± 0.118	± 0.061	-2.144
SNF20061020-000	0.0379	0.031 ± 0.132	± 0.057	0.537	-0.014 ± 0.116	± 0.057	-0.253
SNF20050927-005	0.0399	0.266 ± 0.130	± 0.055	4.872	0.187 ± 0.115	± 0.055	3.429
SNF20060609-002	0.0400	0.052 ± 0.130	± 0.054	0.956	0.096 ± 0.115	± 0.054	1.759
SNF20060511-014	0.0467	-0.064 ± 0.127	± 0.047	-1.370	-0.076 ± 0.111	± 0.047	-1.644
SNF20060908-004	0.0490	-0.075 ± 0.126	± 0.044	-1.683	-0.070 ± 0.111	± 0.044	-1.572
SNF20060621-015	0.0543	0.010 ± 0.125	± 0.040	0.250	0.029 ± 0.109	± 0.040	0.733
SNF20060521-008	0.0563	-0.137 ± 0.125	± 0.039	-3.558	-0.111 ± 0.108	± 0.039	-2.885
SNF20060530-003	0.0571	-0.002 ± 0.124	± 0.038	-0.061	0.012 ± 0.108	± 0.038	0.313
SNF20061021-003	0.0615	0.030 ± 0.124	± 0.035	0.853	0.064 ± 0.107	± 0.035	1.820
SNF20070817-003	0.0630	0.219 ± 0.123	± 0.035	6.334	0.220 ± 0.107	± 0.035	6.352
SNF20060618-014	0.0646	-0.039 ± 0.123	± 0.034	-1.152	-0.001 ± 0.107	± 0.034	-0.031
SNF20070802-000	0.0651	0.074 ± 0.123	± 0.033	2.202	-0.006 ± 0.107	± 0.033	-0.171
SNF20070725-001	0.0668	0.176 ± 0.123	± 0.033	5.391	0.158 ± 0.106	± 0.033	4.837
SNF20050624-000	0.0670	-0.242 ± 0.123	± 0.033	-7.326	-0.203 ± 0.106	± 0.033	-6.145
SNF20070630-006	0.0708	0.133 ± 0.122	± 0.031	4.303	0.091 ± 0.106	± 0.031	2.945
SNF20070818-001	0.0742	-0.068 ± 0.122	± 0.030	-2.288	-0.005 ± 0.105	± 0.030	-0.179
SNF20060526-003	0.0787	-0.057 ± 0.122	± 0.028	-2.054	0.032 ± 0.105	± 0.028	1.133
SNF20070810-004	0.0823	0.052 ± 0.121	± 0.027	1.949	-0.019 ± 0.105	± 0.027	-0.706

Table B.5: Standard and $\mathcal{K}$-correction free Hubble diagram residuals, for the 29 analysed supernovæ, using SALT2 fits of light curves with no error scaling. The quoted redshifts are on the CMB rest-frame (and not on the heliocentric frame, as used for the SALT2 fits). The pull is the residual divided by its error without σ_{int}.

Appendix C

SNe Ia spectrophotometric light curves

In this appendix are put together the spectrophotometric light curves for the 30 SNe Ia fitted using SALT2 and the SNfactory filter-set, and also the "sharp" light curves made using the Ca+Si2 and Si+Si2+Si3 filters.
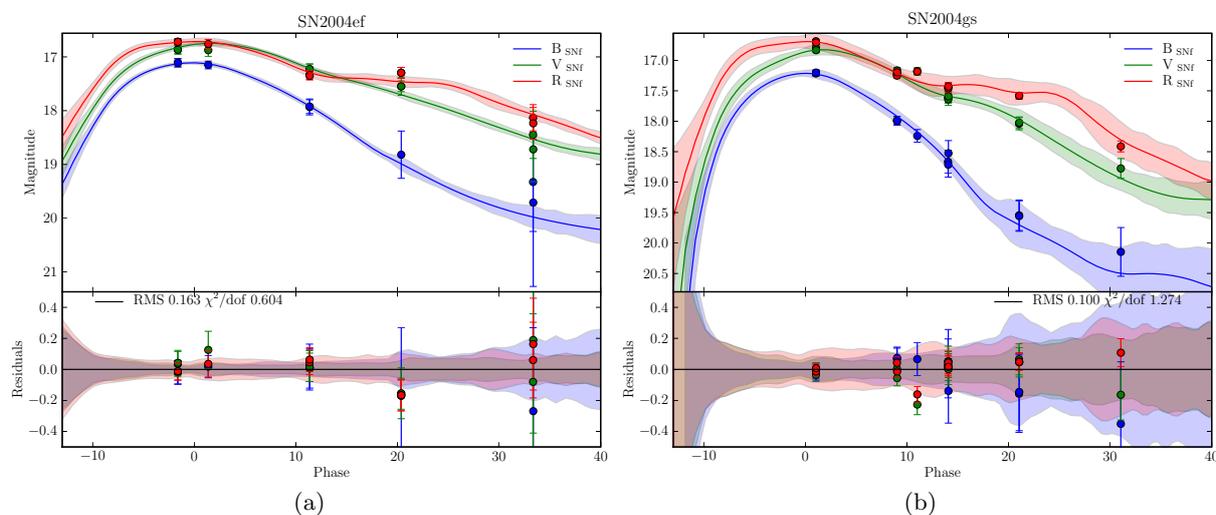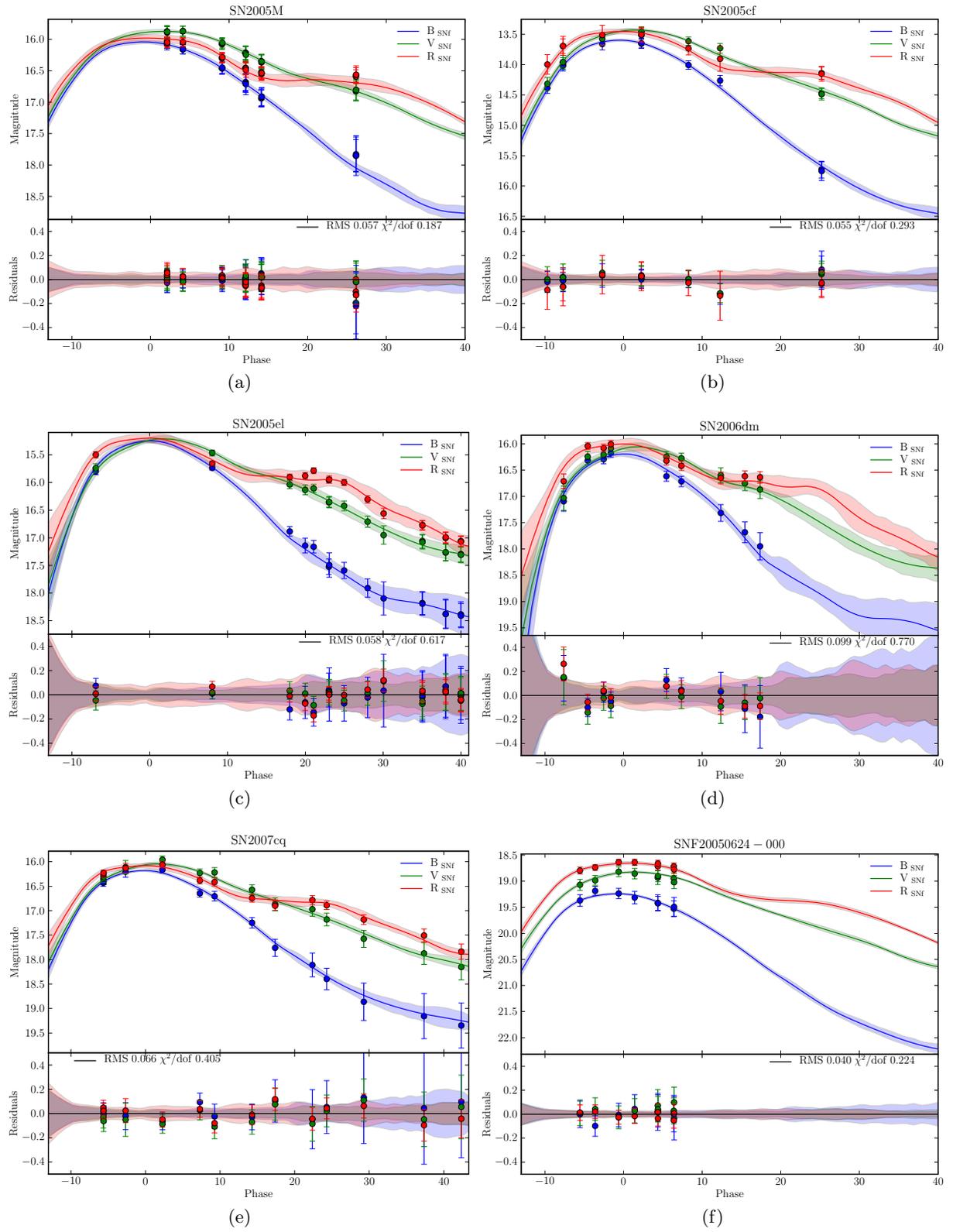
C.1 [BVR]$_{SNf}$ SALT2 fits

Figure C.1: (a) SN2004ef; (b) SN2004

Figure C.2: (a) SN2005M; (b) SN2005cf; (c) SN2005el; (d) SN2006dm; (e) SN2007cq; (f) SNF20050624-000
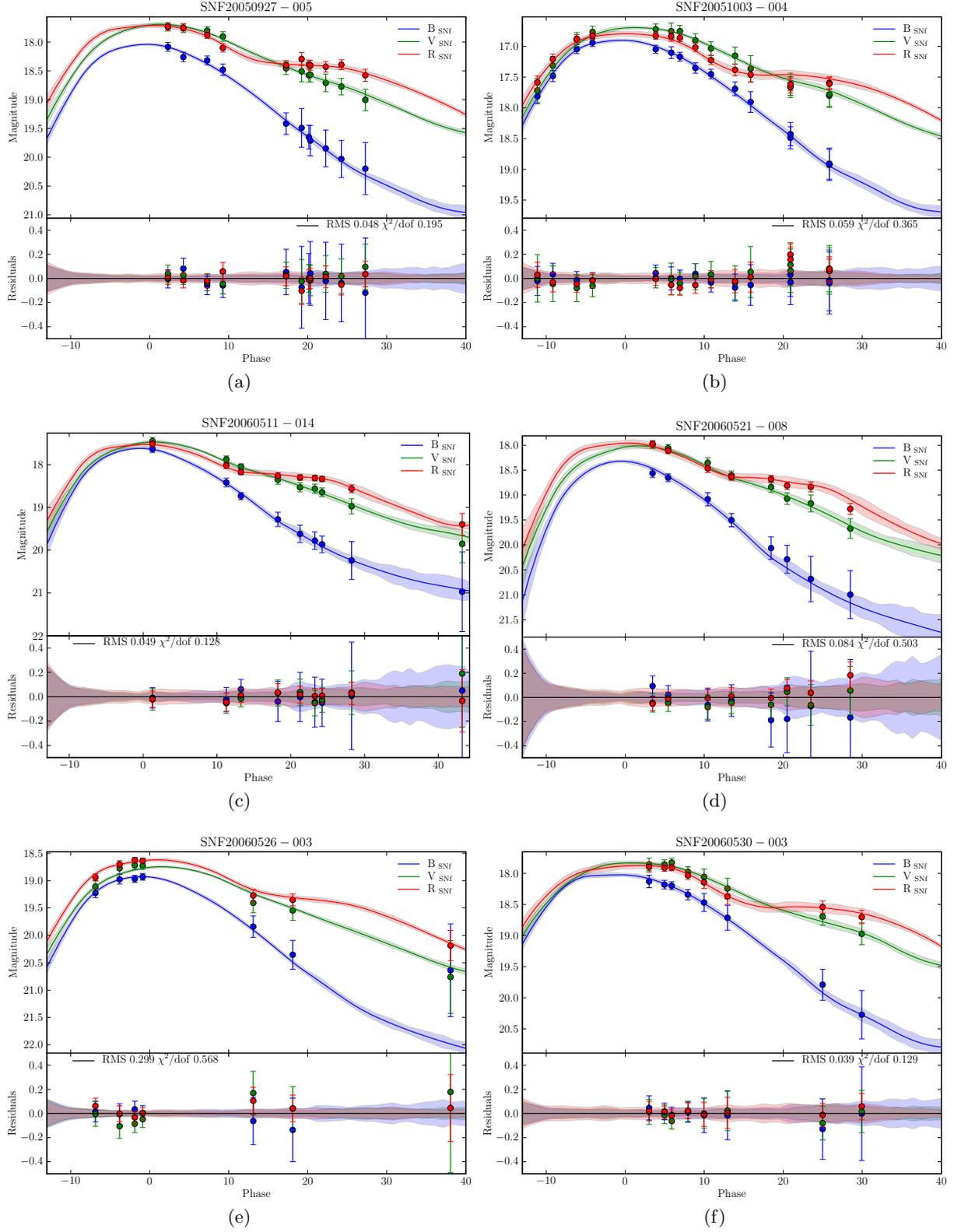
Figure C.3: (a) SNF20050927-005; (b) SNF20051003-004; (c) SNF20060511-014; (d) SNF20060521-008; (e) SNF20060526-003; (f) SNF20060530-003

Figure C.4: (a) SNF20060609-002; (b) SNF20060618-014; (c) SNF20060621-015; (d) SNF20060908-004; (e) SNF20061011-005; (f) SNF20061020-000
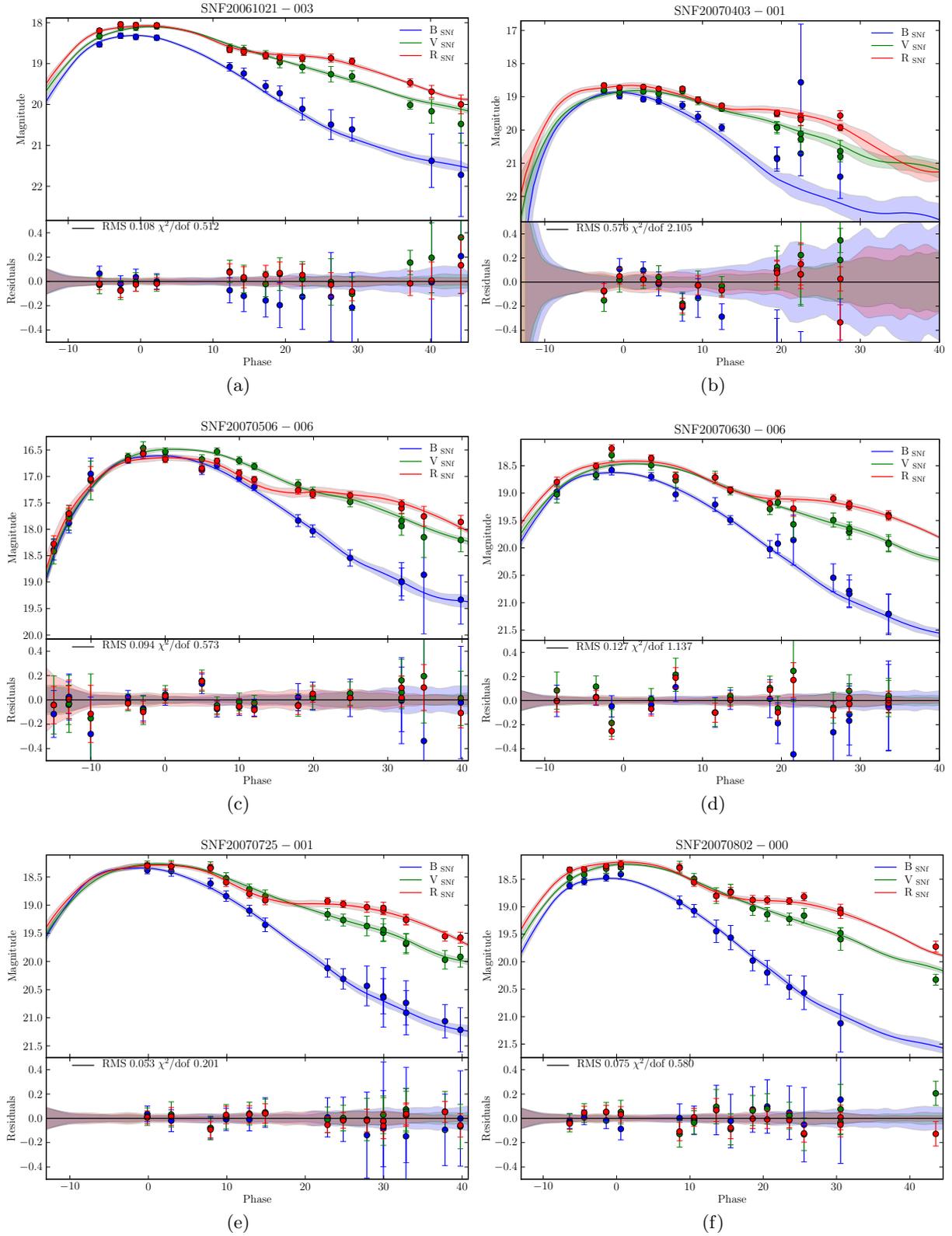
Figure C.5: (a) SNF20061021-003; (b) SNF20070403-001; (c) SNF20070506-006; (d) SNF20070630-006; (e) SNF20070725-001; (f) SNF20070802-000

Figure C.6: (a) SNF20070803-005; (b) SNF20070810-004; (c) SNF20070817-003; (d) SNF20070818-001

C.2   Sharp Ca + Si2 SALT2 fits
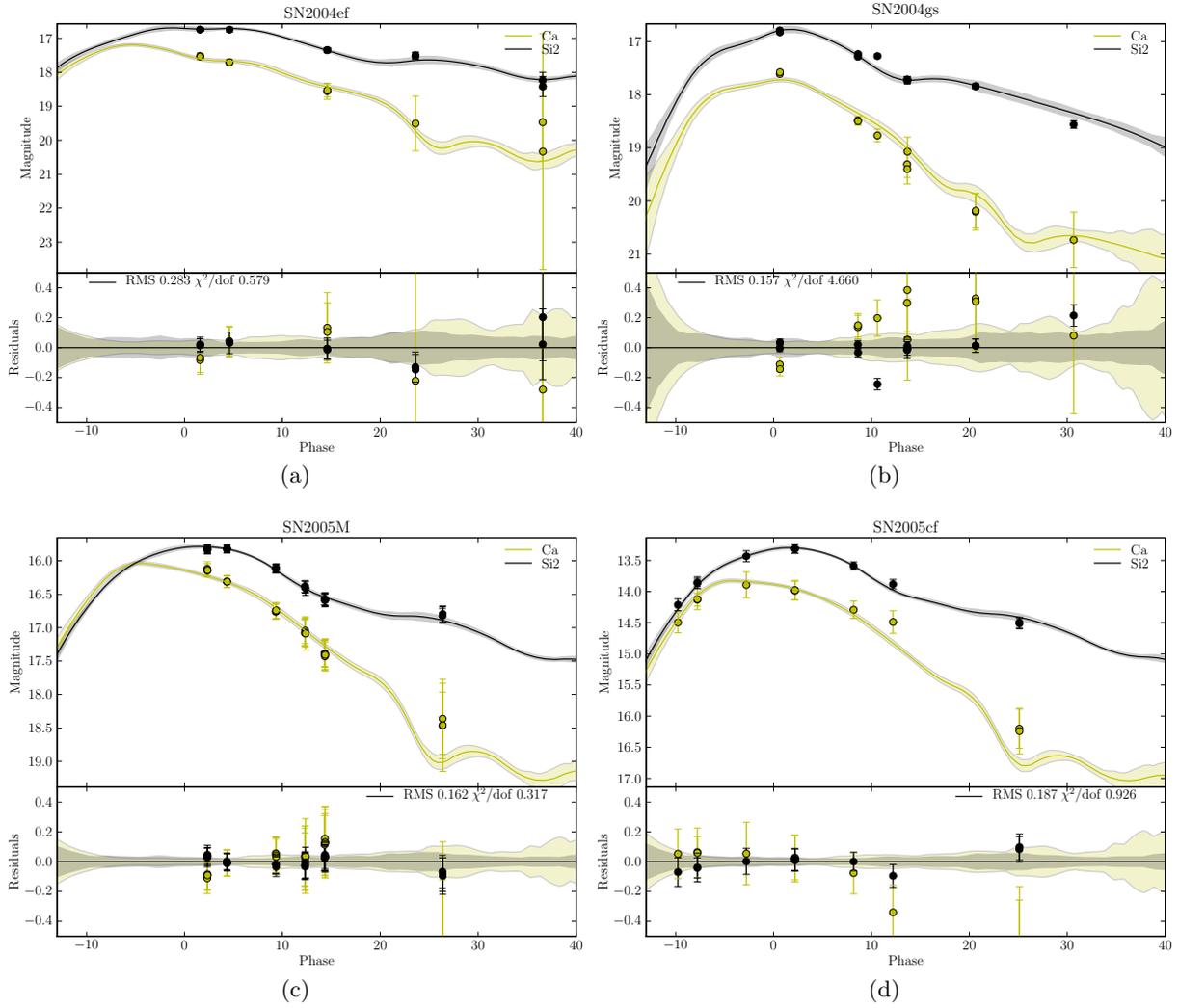
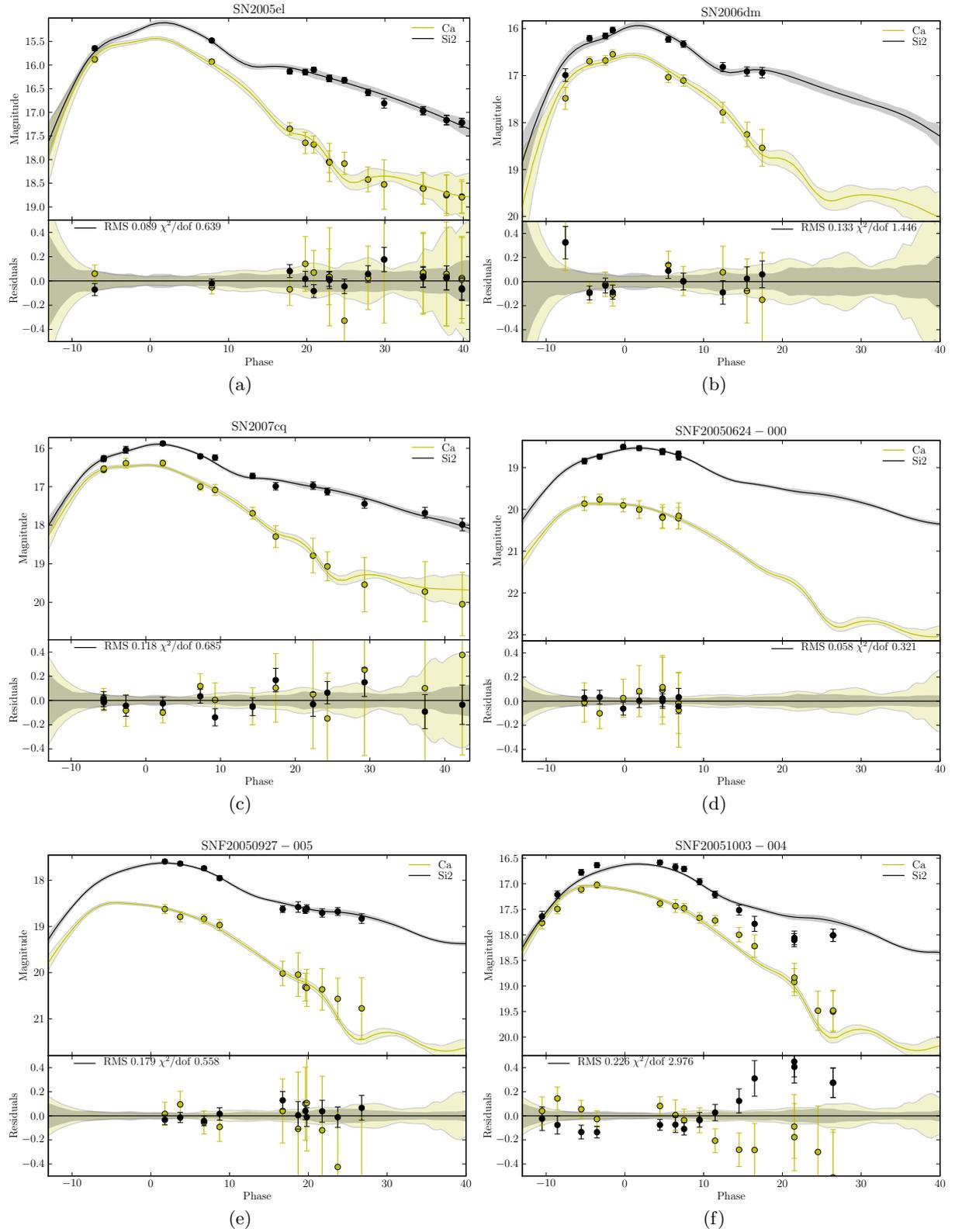Figure C.7: (a) SN2004ef; (b) SN2004gs; (c) SN2005M; (d) SN2005

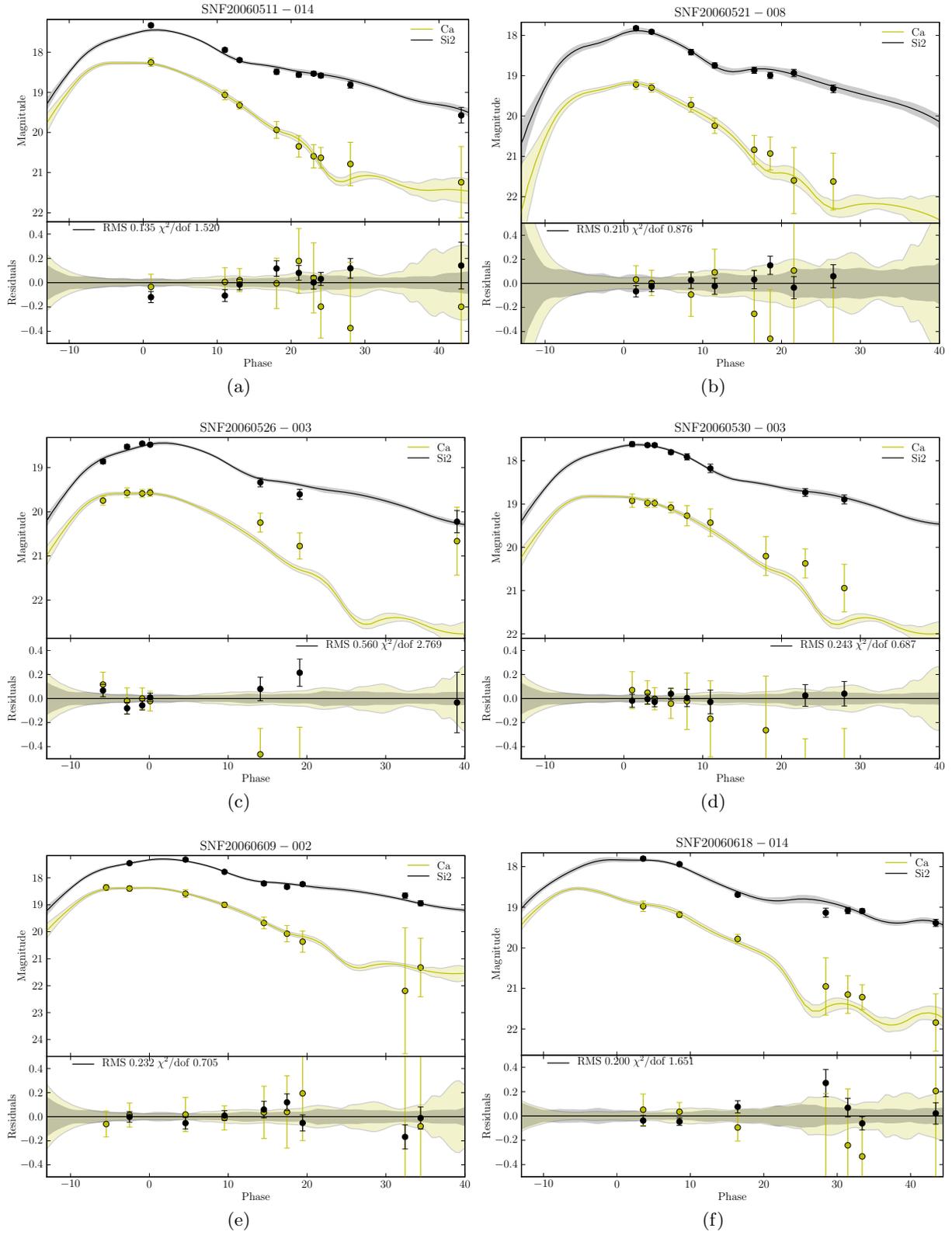Figure C.8: (a) SN2005el; (b) SN2006dm; (c) SN2007cq; (d) SNF20050624-000; (e) SNF20050927-005; (f) SNF20051003-004

Figure C.9: (a) SNF20060511-014; (b) SNF20060521-008; (c) SNF20060526-003; (d) SNF20060530-003; (e) SNF20060609-002; (f) SNF20060618-014
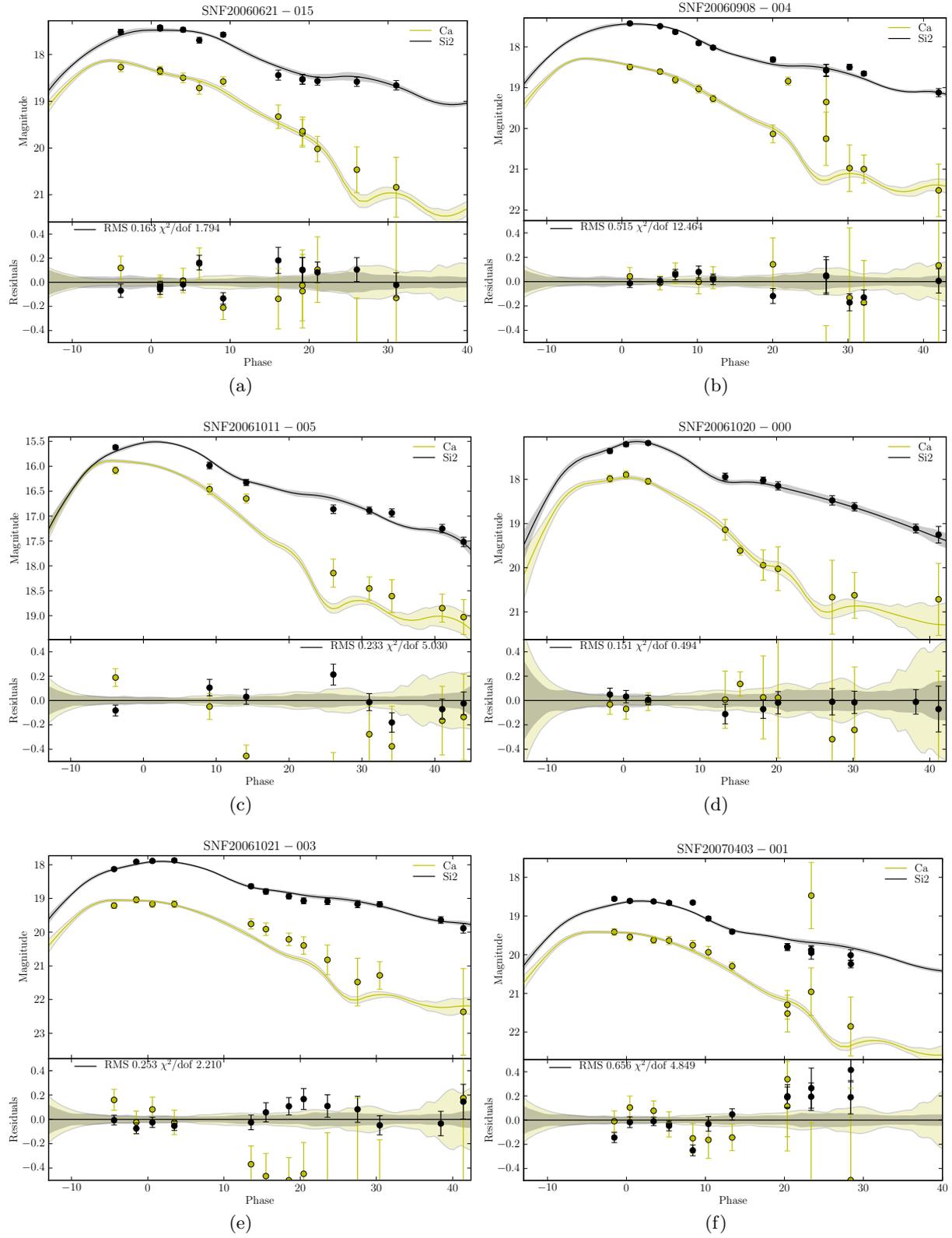
Figure C.10: (a) SNF20060621-015; (b) SNF20060908-004; (c) SNF20061011-005; (d) SNF20061020-000; (e) SNF20061021-003; (f) SNF20070403-001
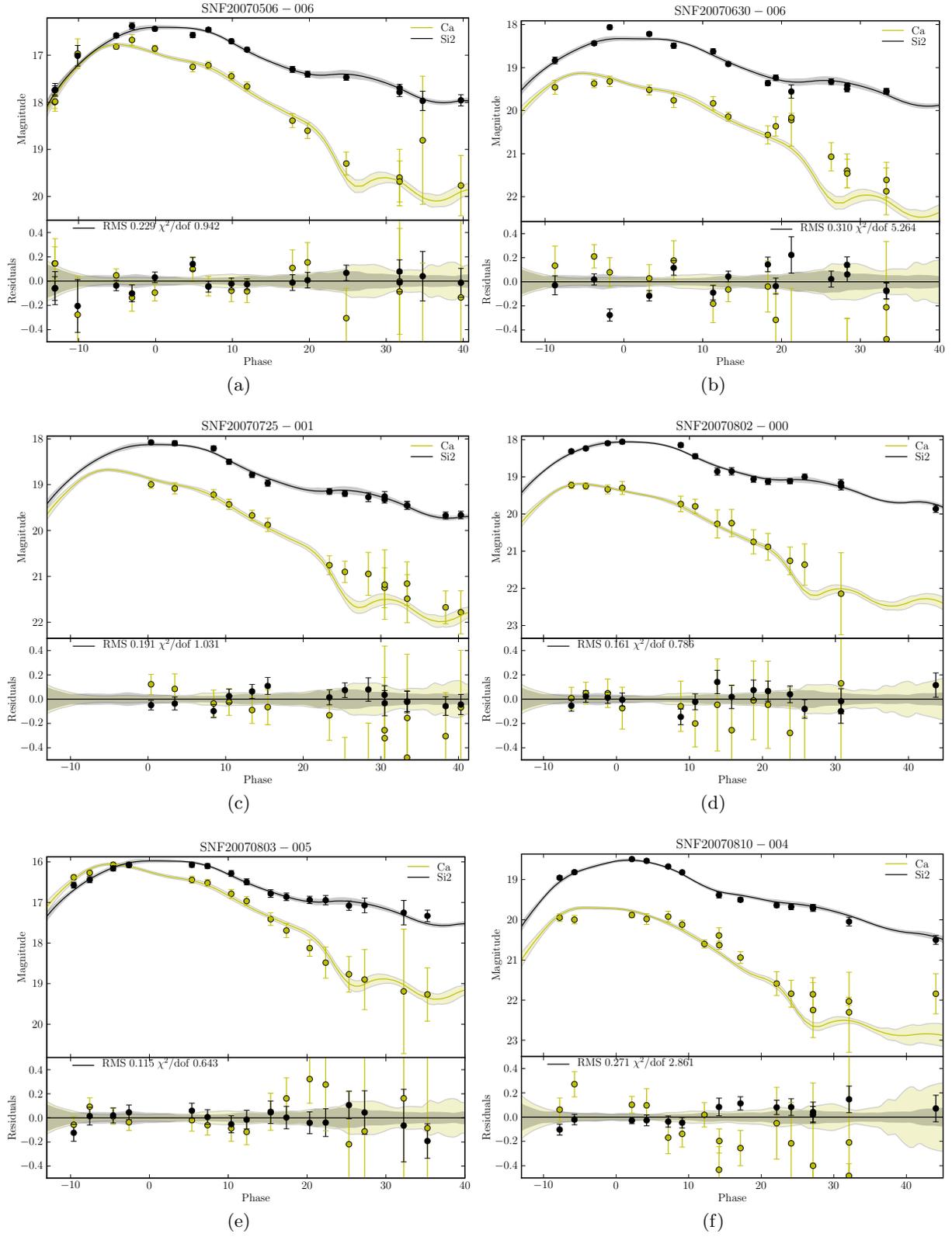
Figure C.11: (a) SNF20070506-006; (b) SNF20070630-006; (c) SNF20070725-001; (d) SNF20070802-000; (e) SNF20070803-005; (f) SNF20070810-004
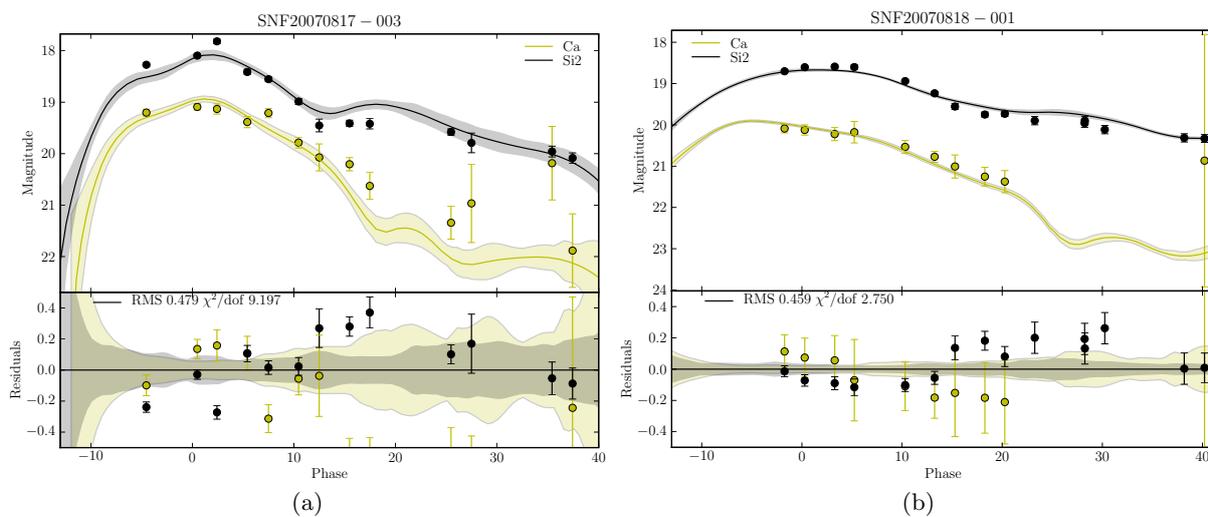
195

Figure C.12: (a) SNF20070817-003; (b) SNF20070818-001

C.3   Sharp Si + Si2 + Si3 SALT2 fits
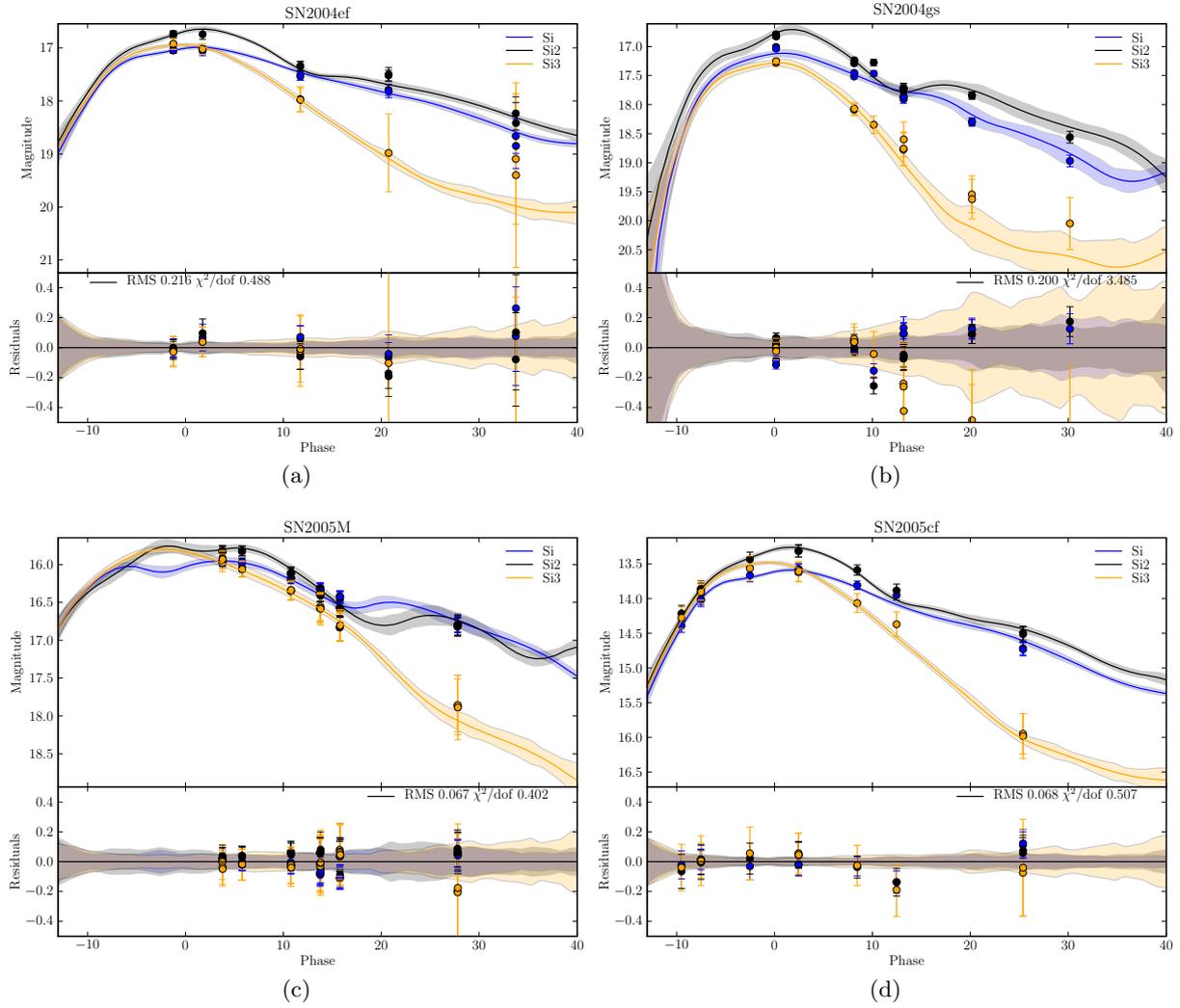
Figure C.13: (a) SN2004ef; (b) SN2004gs; (c) SN2005M; (d) SN2005

Figure C.14: (a) SN2005el; (b) SN2006dm; (c) SN2007cq; (d) SNF20050624-000; (e) SNF20050927-005; (f) SNF20051003-004
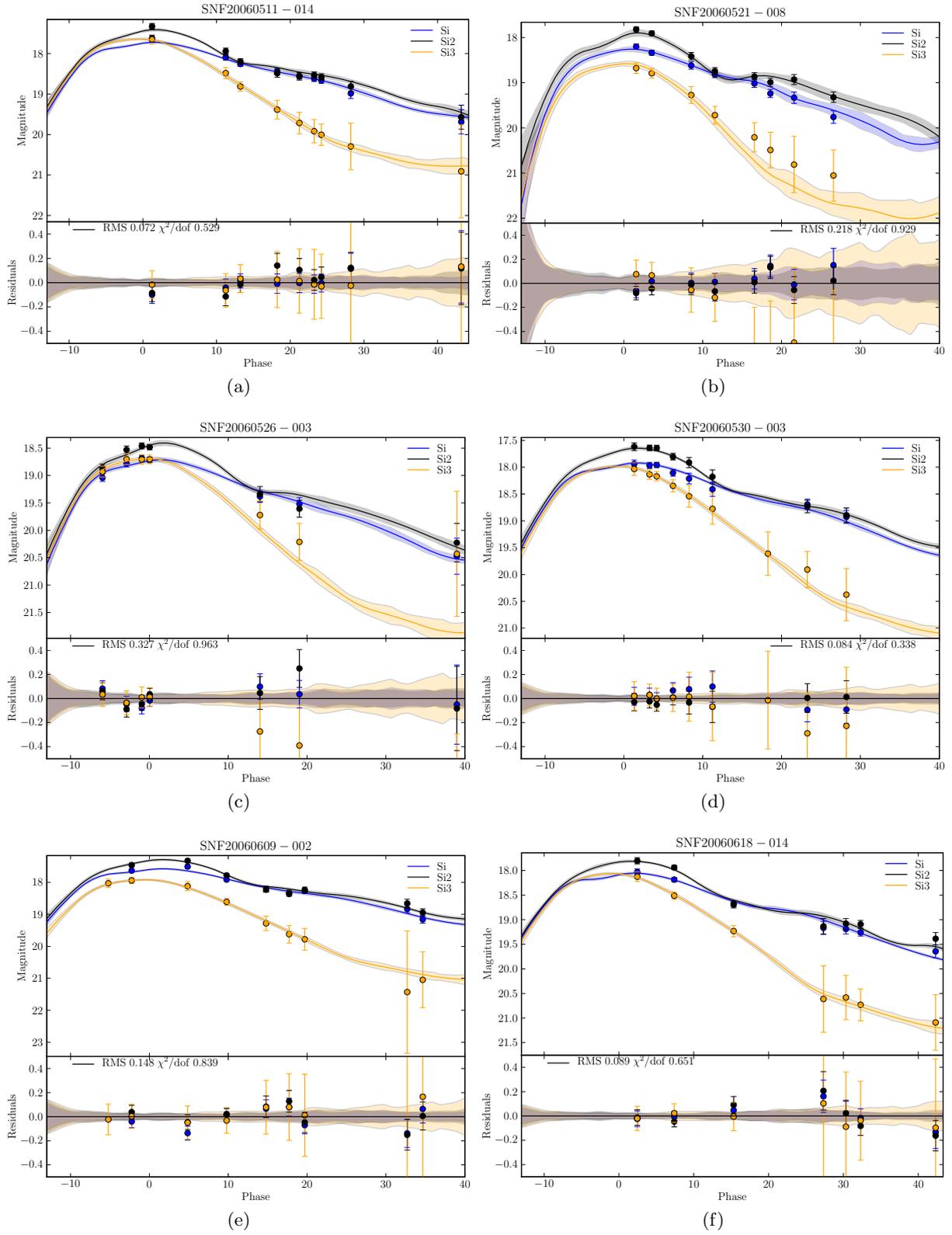
Figure C.15: (a) SNF20060511-014; (b) SNF20060521-008; (c) SNF20060526-003; (d) SNF20060530-003; (e) SNF20060609-002; (f) SNF20060618-014

Figure C.16: (a) SNF20060621-015; (b) SNF20060908-004; (c) SNF20061011-005; (d) SNF20061020-000; (e) SNF20061021-003; (f) SNF20070403-001

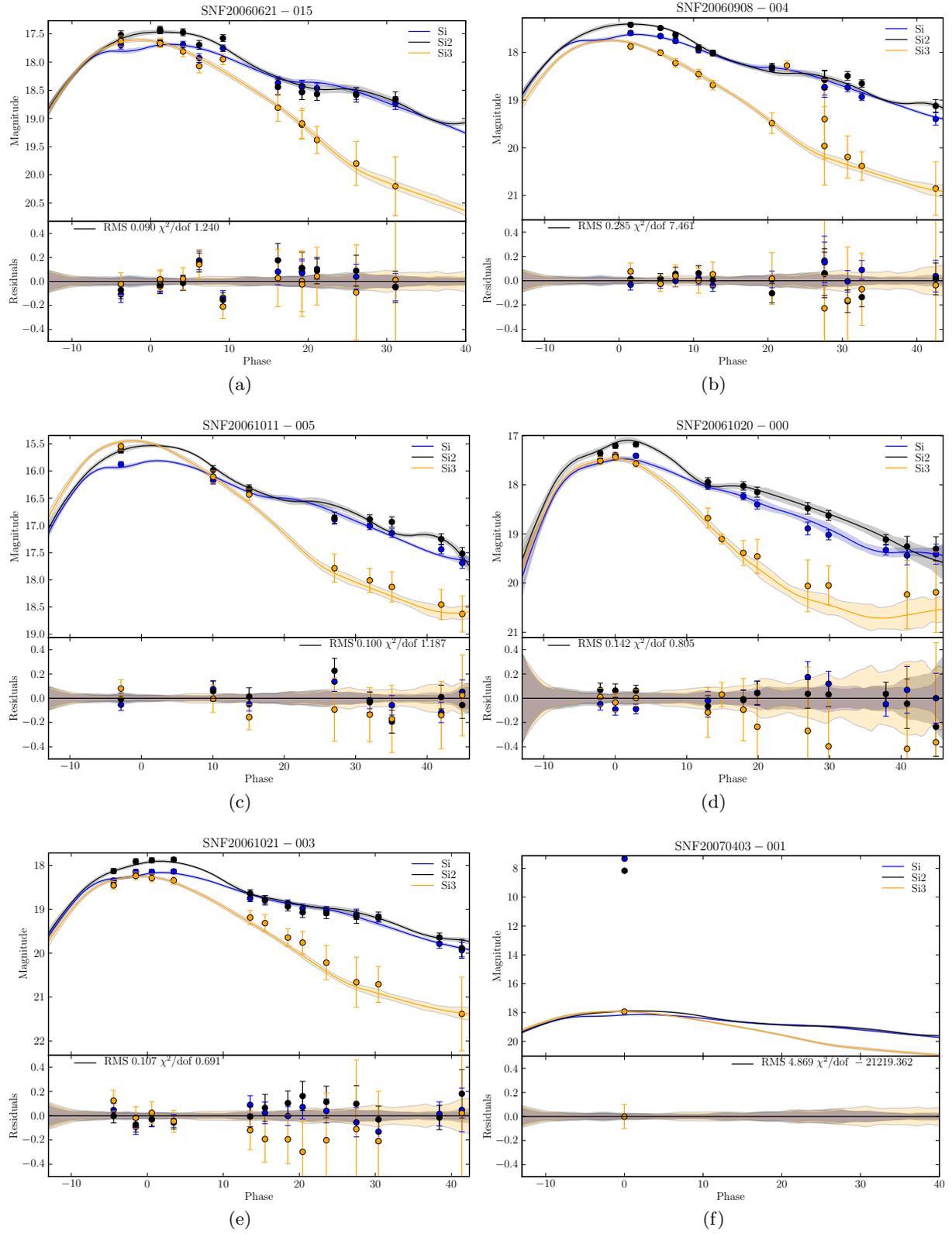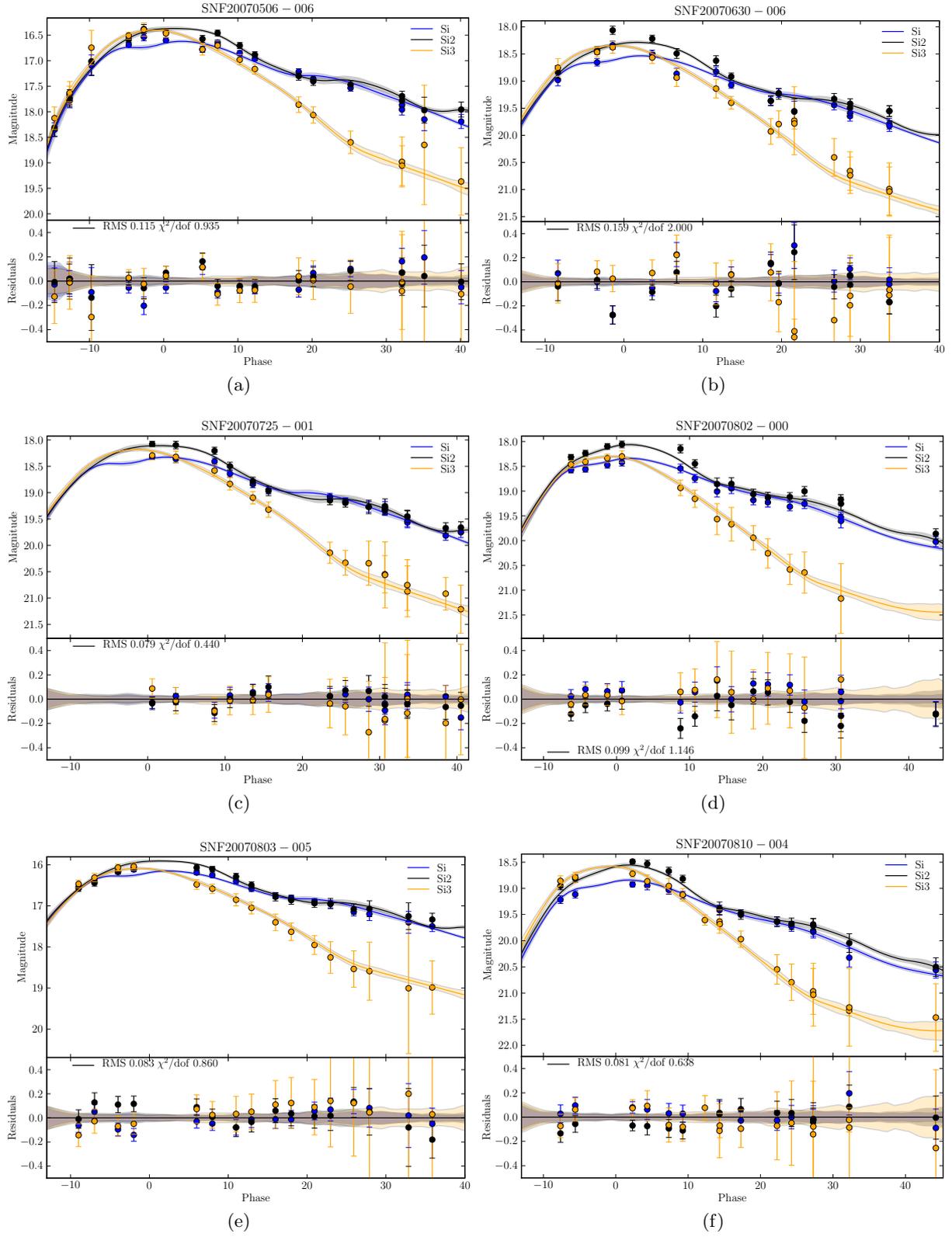Figure C.17: (a) SNF20070506-006; (b) SNF20070630-006; (c) SNF20070725-001; (d) SNF20070802-000; (e) SNF20070803-005; (f) SNF20070810-004
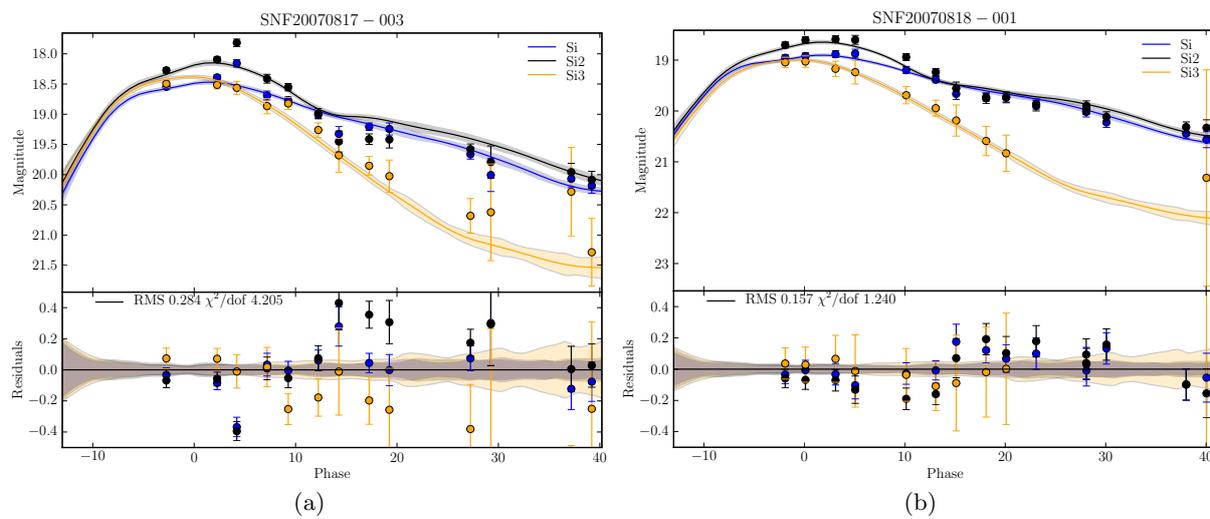
Figure C.18: (a) SNF20070817-003; (b) SNF20070818-001

References

Adelman-McCarthy, J. K., M. A. Agüeros, S. S. Allam, C. Allende Prieto, K. S. J. Anderson, S. F. Anderson, J. Annis, N. A. Bahcall, C. A. L. Bailer-Jones, I. K. Baldry, J. C. Barentine, B. A. Bassett, A. C. Becker, T. C. Beers, E. F. Bell et al. *The Sixth Data Release of the Sloan Digital Sky Survey*. ApJS, 175, 297–313 (**2008**).

Alard, C. *Image subtraction with non-constant kernel solutions*. ArXiv Astrophysics e-prints (**1999**).

Alard, C. and R. H. Lupton. *A Method for Optimal Image Subtraction*. ApJ, 503, 325–+ (**1998**).

Albrecht, A., G. Bernstein, R. Cahn, W. L. Freedman, J. Hewitt, W. Hu, J. Huth, M. Kamionkowski, E. W. Kolb, L. Knox, J. C. Mather, S. Staggs and N. B. Suntzeff. *Report of the Dark Energy Task Force*. ArXiv Astrophysics e-prints (**2006**).

Aldering, G., G. Adam, P. Antilogus, P. Astier, R. Bacon, S. Bongard, C. Bonnaud, Y. Copin, D. Hardin, F. Henault, D. A. Howell, J.-P. Lemonnier, J.-M. Levy, S. C. Loken, P. E. Nugent et al. *Overview of the Nearby Supernova Factory*. In J. A. Tyson and S. Wolff, eds., *Survey and Other Telescope Technologies and Discoveries. Proceedings of the SPIE.*, vol. 4836 of *Presented at the Society of Photo-Optical Instrumentation Engineers (SPIE) Conference*, 61–72 (**2002**).

Aldering, G., B. C. Lee, S. Loken, P. Nugent, S. Perlmutter, J. Siegrist, R. Scalzo, R. C. Thomas, L. Wang, G. Adam, R. Bacon, C. Bonnaud, L. Capoani, D. Dubet, F. Henault et al. *Type determination for SN 2005M*. The Astronomer's Telegram, 396, 1–+ (**2005**).

Aldering, G., P. Antilogus, S. Bailey, C. Baltay, A. Bauer, N. Blanc, S. Bongard, Y. Copin, E. Gangler, S. Gilles, R. Kessler, D. Kocevski, B. C. Lee, S. Loken, P. Nugent et al. *Nearby Supernova Factory Observations of SN 2005gj: Another Type Ia Supernova in a Massive Circumstellar Envelope*. ApJ, 650, 510–527 (**2006**).

Astier, P., J. Guy, N. Regnault, R. Pain, E. Aubourg, D. Balam, S. Basa, R. G. Carlberg, S. Fabbro, D. Fouchez, I. M. Hook, D. A. Howell, H. Lafoux, J. D. Neill, N. Palanque-Delabrouille et al. *The Supernova Legacy Survey: measurement of Ω_M, Ω_Λ and w from the first year data set*. A&A, 447, 31–48 (**2006**).

Bacon, D. J., A. R. Refregier and R. S. Ellis. *Detection of weak gravitational lensing by large-scale structure*. MNRAS, 318, 625–640 (**2000**).

Bacon, R., G. Adam, A. Baranne, G. Courtes, D. Dubet, J. P. Dubois, E. Emsellem, P. Ferruit, Y. Georgelin, G. Monnet, E. Pecontal, A. Rousset and F. Say. *3D spectrography at high spatial resolution. I. Concept and realization of the integral field spectrograph TIGER*. A&AS, 113, 347–+ (**1995**).

Bailey, S., C. Aragon, R. Romano, R. C. Thomas, B. A. Weaver and D. Wong. *How to Find More Supernovae with Less Work: Object Classification Techniques for Difference Imaging.* ApJ, 665, 1246–1253 (**2007**).

Bèland, S., O. Boulade and T. Davidge. *The Extinction Curve at Mauna Kea in the Visible Range.* Bulletin d'information du telescope Canada-France-Hawaii, 19, 16–16 (**1988**).

Bergé, J., F. Pacaud, A. Réfrégier, R. Massey, M. Pierre, A. Amara, M. Birkinshaw, S. Paulin-Henriksson, G. P. Smith and J. Willis. *Combined analysis of weak lensing and X-ray blind surveys.* MNRAS, 385, 695–707 (**2008**).

Bertin, E. and S. Arnouts. *SExtractor: Software for source extraction.* A&AS, 117, 393–404 (**1996**).

Bessell, M. S. *UBVRI passbands.* PASP, 102, 1181–1199 (**1990**).

Bessell, M. S. *Spectrophotometry: Revised Standards and Techniques.* PASP, 111, 1426–1433 (**1999**).

Bessell, M. S. *Standard Photometric Systems.* ARA&A, 43, 293–336 (**2005**).

Bohlin, R. C., M. E. Dickinson and D. Calzetti. *Spectrophotometric Standards from the Far-Ultraviolet to the Near-Infrared: STIS and NICMOS Fluxes.* AJ, 122, 2118–2128 (**2001**).

Bongard, S. *DDT.* In preparation (**2009**).

Bongard, S., E. Baron, G. Smadja, D. Branch and P. H. Hauschildt. *Type Ia Supernova Spectral Line Ratios as Luminosity Indicators.* ApJ, 647, 513–524 (**2006**).

Bousso, R. *The cosmological constant.* General Relativity and Gravitation, 40, 607–637 (**2008**).

Branch, D., L. C. Dang, N. Hall, W. Ketchum, M. Melakayil, J. Parrent, M. A. Troxel, D. Casebeer, D. J. Jeffery and E. Baron. *Comparative Direct Analysis of Type Ia Supernova Spectra. II. Maximum Light.* PASP, 118, 560–571 (**2006**).

Burles, S., K. M. Nollett and M. S. Turner. *Big Bang Nucleosynthesis Predictions for Precision Cosmology.* ApJ, 552, L1–L5 (**2001**).

Buton, C. Ph.D. thesis, Université Claude Bernard - Lyon I (**2009**).

Cappellaro, E., R. Evans and M. Turatto. *A new determination of supernova rates and a comparison with indicators for galactic star formation.* A&A, 351, 459–466 (**1999**).

Carroll, S. M. *The Cosmological Constant.* Living Reviews in Relativity, 4, 1–+ (**2001**).

Casagrande, L., L. Portinari and C. Flynn. *Accurate fundamental parameters for lower main-sequence stars.* MNRAS, 373, 13–44 (**2006**).

Chandrasekhar, S. *The Maximum Mass of Ideal White Dwarfs.* ApJ, 74, 81–+ (**1931**).

Cheng, T.-P. *Relativity, gravitation and cosmology. A basic introduction.* Relativity, gravitation and cosmology / Ta-Pei Cheng. Oxford master series in physics, No. 11, particle physics, astrophysics, and cosmology. Oxford: Oxford University Press, ISBN 19-852956-2, 2005, XIII+339 pp. (**2005**).

Colless, M., B. A. Peterson, C. Jackson, J. A. Peacock, S. Cole, P. Norberg, I. K. Baldry, C. M. Baugh, J. Bland-Hawthorn, T. Bridges, R. Cannon, C. Collins, W. Couch, N. Cross, G. Dalton et al. *The 2dF Galaxy Redshift Survey: Final Data Release.* ArXiv Astrophysics e-prints (**2003**).

Conley, A. J. and Supernova Legacy Survey. *Dark Energy Constraints from the 3rd year Supernova Legacy Survey (SNLS) Dataset*. In *American Astronomical Society Meeting Abstracts*, vol. 211 of *American Astronomical Society Meeting Abstracts*, 28.05–+ (**2007**).

Corasaniti, P. S., M. LoVerde, A. Crotts and C. Blake. *Testing dark energy with the Advanced Liquid-mirror Probe of Asteroids, Cosmology and Astrophysics*. MNRAS, 369, 798–804 (**2006**).

Cuillandre, J.-C., E. A. Magnier, S. Isani, D. Sabin, W. Knight, S. Kras and K. Lai. *CFHT's SkyProbe: a real-time sky-transparency monitor*. In P. J. Quinn, ed., *Observatory Operations to Optimize Scientific Return III. Edited by Quinn, Peter J. Proceedings of the SPIE, Volume 4844, pp. 501-507 (2002).*, vol. 4844 of *Presented at the Society of Photo-Optical Instrumentation Engineers (SPIE) Conference*, 501–507 (**2002**).

Downing, M., D. Baade, P. Sinclaire, S. Deiries and F. Christen. *CCD riddle: a) signal vs time: linear; b) signal vs variance: non-linear*. In *High Energy, Optical, and Infrared Detectors for Astronomy II. Edited by Dorn, David A.; Holland, Andrew D.. Proceedings of the SPIE, Volume 6276, pp. 627609 (2006).*, vol. 6276 of *Presented at the Society of Photo-Optical Instrumentation Engineers (SPIE) Conference* (**2006**).

Einstein, A. *Kosmologische Betrachtungen zur allgemeinen Relativitätstheorie*. Sitzungsberichte der Königlich Preußischen Akademie der Wissenschaften (Berlin), Seite 142-152., 142–152 (**1917**).

Eisenstein, D. J., I. Zehavi, D. W. Hogg, R. Scoccimarro, M. R. Blanton, R. C. Nichol, R. Scranton, H.-J. Seo, M. Tegmark, Z. Zheng, S. F. Anderson, J. Annis, N. Bahcall, J. Brinkmann, S. Burles et al. *Detection of the Baryon Acoustic Peak in the Large-Scale Correlation Function of SDSS Luminous Red Galaxies*. ApJ, 633, 560–574 (**2005**).

Fabbro, S. *Photométrie des supernovæ et applications cosmologiques*. Ph.D. thesis, Université Denis Diderot - Paris VII (**2001**).

Filippenko, A. V. *Optical Spectra of Supernovae*. ARA&A, 35, 309–355 (**1997**).

Filippenko, A. V., M. W. Richmond, D. Branch, M. Gaskell, W. Herbst, C. H. Ford, R. R. Treffers, T. Matheson, L. C. Ho, A. Dey, W. L. W. Sargent, T. A. Small and W. J. M. van Breugel. *The subluminous, spectroscopically peculiar type IA supernova 1991bg in the elliptical galaxy NGC 4374*. AJ, 104, 1543–1556 (**1992**a).

Filippenko, A. V., M. W. Richmond, T. Matheson, J. C. Shields, E. M. Burbidge, R. D. Cohen, M. Dickinson, M. A. Malkan, B. Nelson, J. Pietz, D. Schlegel, P. Schmeer, H. Spinrad, C. C. Steidel, H. D. Tran et al. *The peculiar Type IA SN 1991T - Detonation of a white dwarf?* ApJ, 384, L15–L18 (**1992**b).

Filippenko, A. V., D. S. Wong and M. Ganeshalingam. *Supernova 2007cq*. Central Bureau Electronic Telegrams, 984, 1–+ (**2007**).

Fixsen, D. J., E. S. Cheng, J. M. Gales, J. C. Mather, R. A. Shafer and E. L. Wright. *The Cosmic Microwave Background Spectrum from the Full COBE FIRAS Data Set*. ApJ, 473, 576–+ (**1996**).

Freedman, W. L., B. F. Madore, B. K. Gibson, L. Ferrarese, D. D. Kelson, S. Sakai, J. R. Mould, R. C. Kennicutt, Jr., H. C. Ford, J. A. Graham, J. P. Huchra, S. M. G. Hughes, G. D. Illingworth, L. M. Macri and P. B. Stetson. *Final Results from the Hubble Space Telescope Key Project to Measure the Hubble Constant*. ApJ, 553, 47–72 (**2001**).

Frieman, J., M. Turner and D. Huterer. *Dark Energy and the Accelerating Universe.* ArXiv e-prints, 803 (**2008**a).

Frieman, J. A., B. Bassett, A. Becker, C. Choi, D. Cinabro, F. DeJongh, D. L. Depoy, B. Dilday, M. Doi, P. M. Garnavich, C. J. Hogan, J. Holtzman, M. Im, S. Jha, R. Kessler et al. *The Sloan Digital Sky Survey-II Supernova Survey: Technical Summary.* AJ, 135, 338–347 (**2008**b).

Fu, L., E. Semboloni, H. Hoekstra, M. Kilbinger, L. van Waerbeke, I. Tereno, Y. Mellier, C. Heymans, J. Coupon, K. Benabed, J. Benjamin, E. Bertin, O. Doré, M. J. Hudson, O. Ilbert et al. *Very weak lensing in the CFHTLS wide: cosmology from cosmic shear in the linear regime.* A&A, 479, 9–25 (**2008**).

Fukugita, M., T. Ichikawa, J. E. Gunn, M. Doi, K. Shimasaku and D. P. Schneider. *The Sloan Digital Sky Survey Photometric System.* AJ, 111, 1748–+ (**1996**).

Garcia-Bellido, J. *Cosmology and Astrophysics.* ArXiv Astrophysics e-prints (**2005**).

Gibson, B. K., P. B. Stetson, W. L. Freedman, J. R. Mould, R. C. Kennicutt, Jr., J. P. Huchra, S. Sakai, J. A. Graham, C. I. Fassett, D. D. Kelson, L. Ferrarese, S. M. G. Hughes, G. D. Illingworth, L. M. Macri, B. F. Madore et al. *The Hubble Space Telescope Key Project on the Extragalactic Distance Scale. XXV. A Recalibration of Cepheid Distances to Type IA Supernovae and the Value of the Hubble Constant.* ApJ, 529, 723–744 (**2000**).

Gilles, S. *Spectrophotométrie des supernovæ de type Ia: extraction des données de SNIFS et premiers résultats.* Ph.D. thesis, Université Paris Diderot - Paris VII (**2006**).

Gilliland, R. L., P. E. Nugent and M. M. Phillips. *High-Redshift Supernovae in the Hubble Deep Field.* ApJ, 521, 30–49 (**1999**).

Goldhaber, G., D. E. Groom, A. Kim, G. Aldering, P. Astier, A. Conley, S. E. Deustua, R. Ellis, S. Fabbro, A. S. Fruchter, A. Goobar, I. Hook, M. Irwin, M. Kim, R. A. Knop et al. *Timescale Stretch Parameterization of Type Ia Supernova B-Band Light Curves.* ApJ, 558, 359–368 (**2001**).

Guth, A. H. *Inflation.* In W. L. Freedman, ed., *Measuring and Modeling the Universe*, 31–+ (**2004**).

Guy, J., P. Astier, S. Nobili, N. Regnault and R. Pain. *SALT: a spectral adaptive light curve template for type Ia supernovae.* A&A, 443, 781–791 (**2005**).

Guy, J., P. Astier, S. Baumont, D. Hardin, R. Pain, N. Regnault, S. Basa, R. G. Carlberg, A. Conley, S. Fabbro, D. Fouchez, I. M. Hook, D. A. Howell, K. Perrett, C. J. Pritchet et al. *SALT2: using distant supernovae to improve the use of type Ia supernovae as distance indicators.* A&A, 466, 11–21 (**2007**).

Hachinger, S., P. A. Mazzali and S. Benetti. *Exploring the spectroscopic diversity of Type Ia supernovae.* MNRAS, 370, 299–318 (**2006**).

Hamuy, M., M. M. Phillips, N. B. Suntzeff, R. A. Schommer, J. Maza and R. Aviles. *The Absolute Luminosities of the Calan/Tololo Type IA Supernovae.* AJ, 112, 2391–+ (**1996**).

Hartle, J. B. *Gravity : an introduction to Einstein's general relativity.* Gravity / James B. Hartle. San Francisco, CA, USA: Addison Wesley, ISBN 0-8053-8662-9, 2003, XXII + 582 pp. (**2003**).

Hillebrandt, W. and J. C. Niemeyer. *Type IA Supernova Explosion Models.* ARA&A, 38, 191–230 (**2000**).

Hinshaw, G., J. L. Weiland, R. S. Hill, N. Odegard, D. Larson, C. L. Bennett, J. Dunkley, B. Gold, M. R. Greason, N. Jarosik, E. Komatsu, M. R. Nolta, L. Page, D. N. Spergel, E. Wollack et al. *Five-Year Wilkinson Microwave Anisotropy Probe (WMAP) Observations: Data Processing, Sky Maps, and Basic Results.* ArXiv e-prints, 803 (**2008**).

Hoeflich, P., J. C. Wheeler and F. K. Thielemann. *Type IA Supernovae: Influence of the Initial Composition on the Nucleosynthesis, Light Curves, and Spectra and Consequences for the Determination of Omega M and Lambda.* ApJ, 495, 617–+ (**1998**).

Hoekstra, H., Y. Mellier, L. van Waerbeke, E. Semboloni, L. Fu, M. J. Hudson, L. C. Parker, I. Tereno and K. Benabed. *First Cosmic Shear Results from the Canada-France-Hawaii Telescope Wide Synoptic Legacy Survey.* ApJ, 647, 116–127 (**2006**).

Howell, D. A., M. Sullivan, P. E. Nugent, R. S. Ellis, A. J. Conley, D. Le Borgne, R. G. Carlberg, J. Guy, D. Balam, S. Basa, D. Fouchez, I. M. Hook, E. Y. Hsiao, J. D. Neill, R. Pain et al. *The type Ia supernova SNLS-03D3bb from a super-Chandrasekhar-mass white dwarf star.* Nature, 443, 308–311 (**2006**).

Howell, S. B. *Handbook of CCD astronomy.* Handbook of CCD astronomy, 2nd ed., by S.B. Howell. Cambridge observing handbooks for research astronomers, Vol. 5 Cambridge, UK: Cambridge University Press, 2006 ISBN 0521852153 (**2006**).

Hubble, E. *A Relation between Distance and Radial Velocity among Extra-Galactic Nebulae.* Proceedings of the National Academy of Science, 15, 168–173 (**1929**).

Janesick, J. R. *Scientific charge-coupled devices.* Scientific charge-coupled devices, Bellingham, WA: SPIE Optical Engineering Press, 2001, xvi, 906 p. SPIE Press monograph, PM 83. ISBN 0819436984 (**2001**).

Jansen, R. A., N. R. Collins and R. A. Windhorst. *Autofilet.pro: An Improved Method for Automated Removal of Herring-bone Pattern Noise from CCD Data.* In S. Arribas, A. Koekemoer and B. Whitmore, eds., *The 2002 HST Calibration Workshop : Hubble after the Installation of the ACS and the NICMOS Cooling System, Proceedings of a Workshop held at the Space Telescope Science Institute, Baltimore, Maryland, October 17 and 18, 2002.*, 193–+ (**2002**).

Jha, S., A. G. Riess and R. P. Kirshner. *Improved Distances to Type Ia Supernovae with Multicolor Light-Curve Shapes: MLCS2k2.* ApJ, 659, 122–148 (**2007**).

Jones, W. C., P. A. R. Ade, J. J. Bock, J. R. Bond, J. Borrill, A. Boscaleri, P. Cabella, C. R. Contaldi, B. P. Crill, P. de Bernardis, G. De Gasperis, A. de Oliveira-Costa, G. De Troia, G. di Stefano, E. Hivon et al. *A Measurement of the Angular Power Spectrum of the CMB Temperature Anisotropy from the 2003 Flight of BOOMERANG.* ApJ, 647, 823–832 (**2006**).

Kaiser, N., H. Aussel, B. E. Burke, H. Boesgaard, K. Chambers, M. R. Chun, J. N. Heasley, K.-W. Hodapp, B. Hunt, R. Jedicke, D. Jewitt, R. Kudritzki, G. A. Luppino, M. Maberry, E. Magnier et al. *Pan-STARRS: A Large Synoptic Survey Telescope Array.* In J. A. Tyson and S. Wolff, eds., *Society of Photo-Optical Instrumentation Engineers (SPIE) Conference Series*, vol. 4836 of *Society of Photo-Optical Instrumentation Engineers (SPIE) Conference Series*, 154–164 (**2002**).

Kolb, E. W. *Cosmology and the Unexpected.* ArXiv e-prints, 709 (**2007**).

Komatsu, E., J. Dunkley, M. R. Nolta, C. L. Bennett, B. Gold, G. Hinshaw, N. Jarosik, D. Larson, M. Limon, L. Page, D. N. Spergel, M. Halpern, R. S. Hill, A. Kogut, S. S. Meyer et al. *Five-Year Wilkinson Microwave Anisotropy Probe (WMAP) Observations: Cosmological Interpretation.* ArXiv e-prints, 803 (**2008**).

Kowalski, M., D. Rubin, G. Aldering, R. J. Agostinho, A. Amadon, R. Amanullah, C. Balland, K. Barbary, G. Blanc, P. J. Challis, A. Conley, N. V. Connolly, R. Covarrubias, K. S. Dawson, S. E. Deustua et al. *Improved Cosmological Constraints from New, Old and Combined Supernova Datasets.* ArXiv e-prints, 804 (**2008**).

Landolt, A. U. *UBVRI photometric standard stars in the magnitude range 11.5-16.0 around the celestial equator.* AJ, 104, 340–371 (**1992**).

Landolt, A. U. and A. K. Uomoto. *Optical Multicolor Photometry of Spectrophotometric Standard Stars.* AJ, 133, 768–790 (**2007**).

Lantz, B., G. Aldering, P. Antilogus, C. Bonnaud, L. Capoani, A. Castera, Y. Copin, D. Dubet, E. Gangler, F. Henault, J.-P. Lemonnier, R. Pain, A. Pecontal, E. Pecontal and G. Smadja. *SNIFS: a wideband integral field spectrograph with microlens arrays.* In L. Mazuray, P. J. Rogers and R. Wartmann, eds., *Optical Design and Engineering. Proceedings of the SPIE.*, vol. 5249 of *Presented at the Society of Photo-Optical Instrumentation Engineers (SPIE) Conference*, 146–155 (**2004**).

Li, W., A. V. Filippenko and A. G. Riess. *Monte Carlo Simulations of Type IA Supernova Observations in Supernova Surveys.* ApJ, 546, 719–733 (**2001**).

Liddle, A. R. *An introduction to modern cosmology.* An introduction to modern cosmology, 2nd ed., by Andrew R. Liddle. Chichester, UK: Wiley, 2003, ISBN 0470848340. (**2003**).

Linder, E. V. *Importance of supernovae at $z < 0.1$ for probing dark energy.* Phys. Rev. D, 74(10), 103518–+ (**2006**).

Martin, J. *Quintessence: a mini-review.* ArXiv e-prints, 803 (**2008**).

Matheson, T., R. P. Kirshner, P. Challis, S. Jha, P. M. Garnavich, P. Berlind, M. L. Calkins, S. Blondin, Z. Balog, A. E. Bragg, N. Caldwell, K. Dendy Concannon, E. E. Falco, G. J. M. Graves, J. P. Huchra et al. *Optical Spectroscopy of Type Ia Supernovae.* ArXiv e-prints, 803 (**2008**).

Miknaitis, G., G. Pignata, A. Rest, W. M. Wood-Vasey, S. Blondin, P. Challis, R. C. Smith, C. W. Stubbs, N. B. Suntzeff, R. J. Foley, T. Matheson, J. L. Tonry, C. Aguilera, J. W. Blackman, A. C. Becker et al. *The ESSENCE Supernova Survey: Survey Optimization, Observations, and Supernova Photometry.* ApJ, 666, 674–693 (**2007**).

Minkowski, R. *Spectra of Supernovae.* PASP, 53, 224–+ (**1941**).

Monet, D. G., S. E. Levine, B. Canzian, H. D. Ables, A. R. Bird, C. C. Dahn, H. H. Guetter, H. C. Harris, A. A. Henden, S. K. Leggett, H. F. Levison, C. B. Luginbuhl, J. Martini, A. K. B. Monet, J. A. Munn et al. *The USNO-B Catalog.* AJ, 125, 984–993 (**2003**).

Nolta, M. R., J. Dunkley, R. S. Hill, G. Hinshaw, E. Komatsu, D. Larson, L. Page, D. N. Spergel, C. L. Bennett, B. Gold, N. Jarosik, N. Odegard, J. L. Weiland, E. Wollack, M. Halpern et al. *Five-Year Wilkinson Microwave Anisotropy Probe (WMAP) Observations: Angular Power Spectra.* ArXiv e-prints, 803 (**2008**).

Nugent, P., M. Phillips, E. Baron, D. Branch and P. Hauschildt. *Evidence for a Spectroscopic Sequence among Type 1a Supernovae.* ApJ, 455, L147+ (**1995**).

Nugent, P., A. Kim and S. Perlmutter. *K-Corrections and Extinction Corrections for Type Ia Supernovae*. PASP, 114, 803–819 (**2002**).

Penzias, A. A. and R. W. Wilson. *A Measurement of Excess Antenna Temperature at 4080 Mc/s*. ApJ, 142, 419–421 (**1965**).

Percival, W. J., S. Cole, D. J. Eisenstein, R. C. Nichol, J. A. Peacock, A. C. Pope and A. S. Szalay. *Measuring the Baryon Acoustic Oscillation scale using the Sloan Digital Sky Survey and 2dF Galaxy Redshift Survey*. MNRAS, 381, 1053–1066 (**2007**).

Perlmutter, S., B. Boyle, P. Bunclark, D. Carter, W. Couch, S. Deustua, M. Dopita, R. Ellis, A. V. Filippenko, S. Gabi, K. Glazebrook, G. Goldhaber, A. Goobar, D. Groom, I. Hook et al. *High-redshift supernova discoveries on demand: first results from a new tool for cosmology and bounds on q_0*. Nuclear Physics B Proceedings Supplements, 51, 20–29 (**1996**).

Perlmutter, S., G. Aldering, S. Deustua, S. Fabbro, G. Goldhaber, D. E. Groom, A. G. Kim, M. Y. Kim, R. A. Knop, P. Nugent, C. R. Pennypacker, M. della Valle, R. S. Ellis, R. G. McMahon, N. Walton et al. *Cosmology From Type IA Supernovae: Measurements, Calibration Techniques, and Implications*. In *Bulletin of the American Astronomical Society*, vol. 29 of *Bulletin of the American Astronomical Society*, 1351–+ (**1997**a).

Perlmutter, S., S. Gabi, G. Goldhaber, A. Goobar, D. E. Groom, I. M. Hook, A. G. Kim, M. Y. Kim, J. C. Lee, R. Pain, C. R. Pennypacker, I. A. Small, R. S. Ellis, R. G. McMahon, B. J. Boyle et al. *Measurements of the Cosmological Parameters Omega and Lambda from the First Seven Supernovae at Z ≥ 0.35*. ApJ, 483, 565–+ (**1997**b).

Perlmutter, S., G. Aldering, G. Goldhaber, R. A. Knop, P. Nugent, P. G. Castro, S. Deustua, S. Fabbro, A. Goobar, D. E. Groom, I. M. Hook, A. G. Kim, M. Y. Kim, J. C. Lee, N. J. Nunes et al. *Measurements of Omega and Lambda from 42 High-Redshift Supernovae*. ApJ, 517, 565–586 (**1999**).

Phillips, M. M. *The absolute magnitudes of Type IA supernovae*. ApJ, 413, L105–L108 (**1993**).

Phillips, M. M., P. Lira, N. B. Suntzeff, R. A. Schommer, M. Hamuy and J. Maza. *The Reddening-Free Decline Rate Versus Luminosity Relationship for Type IA Supernovae*. AJ, 118, 1766–1776 (**1999**).

Prieto, J., P. Garnavich, D. Depoy, J. Marshall, J. Eastman and S. Frank. *Supernova 2005gj*. IAU Circ., 8633, 1–+ (**2005**).

Rabinowitz, D., C. Baltay, W. Emmet, T. Hurteau, J. Snyder, P. Andrews, N. Ellman, N. Morgan, A. Bauer, J. Musser, M. Gebhard, G. Adams, G. Djorgovski, A. Mahabal, M. Graham et al. *The Palomar-QUEST large-area CCD camera*. In *Bulletin of the American Astronomical Society*, vol. 35 of *Bulletin of the American Astronomical Society*, 1262–+ (**2003**).

Readhead, A. C. S., B. S. Mason, C. R. Contaldi, T. J. Pearson, J. R. Bond, S. T. Myers, S. Padin, J. L. Sievers, J. K. Cartwright, M. C. Shepherd, D. Pogosyan, S. Prunet, P. Altamirano, R. Bustos, L. Bronfman et al. *Extended Mosaic Observations with the Cosmic Background Imager*. ApJ, 609, 498–512 (**2004**).

Refregier, A., M. Douspis and the DUNE collaboration. *Summary of the DUNE Mission Concept*. ArXiv e-prints (**2008**).

REFERENCES

Reichardt, C. L., P. A. R. Ade, J. J. Bock, J. R. Bond, J. A. Brevik, C. R. Contaldi, M. D. Daub, J. T. Dempsey, J. H. Goldstein, W. L. Holzapfel, C. L. Kuo, A. E. Lange, M. Lueker, M. Newcomb, J. B. Peterson et al. *High resolution CMB power spectrum from the complete ACBAR data set.* ArXiv e-prints, 801 (**2008**).

Richardson, D., R. C. Thomas, D. Casebeer, Z. Blankenship, S. Ratowt, E. Baron and D. Branch. *SUSPECT - The Online Supernova Spectrum Database.* In *Bulletin of the American Astronomical Society*, vol. 33 of *Bulletin of the American Astronomical Society*, 1428–+ (**2001**).

Riess, A. G., W. H. Press and R. P. Kirshner. *A Precise Distance Indicator: Type IA Supernova Multicolor Light-Curve Shapes.* ApJ, 473, 88–+ (**1996**).

Riess, A. G., A. V. Filippenko, P. Challis, A. Clocchiatti, A. Diercks, P. M. Garnavich, R. L. Gilliland, C. J. Hogan, S. Jha, R. P. Kirshner, B. Leibundgut, M. M. Phillips, D. Reiss, B. P. Schmidt, R. A. Schommer et al. *Observational Evidence from Supernovae for an Accelerating Universe and a Cosmological Constant.* AJ, 116, 1009–1038 (**1998**).

Riess, A. G., W. Li, P. B. Stetson, A. V. Filippenko, S. Jha, R. P. Kirshner, P. M. Challis, P. M. Garnavich and R. Chornock. *Cepheid Calibrations from the Hubble Space Telescope of the Luminosity of Two Recent Type Ia Supernovae and a Redetermination of the Hubble Constant.* ApJ, 627, 579–607 (**2005**).

Riess, A. G., L.-G. Strolger, S. Casertano, H. C. Ferguson, B. Mobasher, B. Gold, P. J. Challis, A. V. Filippenko, S. Jha, W. Li, J. Tonry, R. Foley, R. P. Kirshner, M. Dickinson, E. MacDonald et al. *New Hubble Space Telescope Discoveries of Type Ia Supernovae at $z \geq 1$: Narrowing Constraints on the Early Behavior of Dark Energy.* ApJ, 659, 98–121 (**2007**).

Roepke, F. K. *Thermonuclear Supernovae.* ArXiv e-prints, 804 (**2008**).

Roos, M. *Introduction to cosmology.* Introduction to cosmology, 3rd. ed., by Matts Roos. Chichester, UK: Wiley, 2003 (**2003**).

Roos, M. *Expansion of the Universe - Standard Big Bang Model.* ArXiv e-prints, 802 (**2008**).

Sandage, A., G. A. Tammann, A. Saha, B. Reindl, F. D. Macchetto and N. Panagia. *The Hubble Constant: A Summary of the Hubble Space Telescope Program for the Luminosity Calibration of Type Ia Supernovae by Means of Cepheids.* ApJ, 653, 843–860 (**2006**).

Slipher, V. M. *The radial velocity of additional globular star clusters (abstract).* Popular Astronomy, 32, 622–+ (**1924**).

Smith, J. A., D. L. Tucker, S. Kent, M. W. Richmond, M. Fukugita, T. Ichikawa, S.-i. Ichikawa, A. M. Jorgensen, A. Uomoto, J. E. Gunn, M. Hamabe, M. Watanabe, A. Tolea, A. Henden, J. Annis et al. *The u'g'r'i'z' Standard-Star System.* AJ, 123, 2121–2144 (**2002**).

Smoot, G. F., C. L. Bennett, A. Kogut, E. L. Wright, J. Aymon, N. W. Boggess, E. S. Cheng, G. de Amici, S. Gulkis, M. G. Hauser, G. Hinshaw, P. D. Jackson, M. Janssen, E. Kaita, T. Kelsall et al. *Structure in the COBE differential microwave radiometer first-year maps.* ApJ, 396, L1–L5 (**1992**).

SNAP Collaboration: G. Aldering, W. Althouse, R. Amanullah, J. Annis, P. Astier, C. Baltay, E. Barrelet, S. Basa, C. Bebek, L. Bergstrom, G. Bernstein, M. Bester, B. Bigelow, R. Blandford, R. Bohlin et al. *Supernova / Acceleration Probe: A Satellite Experiment to Study the Nature of the Dark Energy*. ArXiv Astrophysics e-prints (**2004**).

Stanishev, V., A. Goobar, S. Benetti, R. Kotak, G. Pignata, H. Navasardyan, P. Mazzali, R. Amanullah, G. Garavini, S. Nobili, Y. Qiu, N. Elias-Rosa, P. Ruiz-Lapuente, J. Mendez, P. Meikle et al. *SN 2003du: 480 days in the life of a normal type Ia supernova*. A&A, 469, 645–661 (**2007**).

Stetson, P. B. *DAOPHOT - A computer program for crowded-field stellar photometry*. PASP, 99, 191–222 (**1987**).

Stetson, P. B. *Homogeneous Photometry for Star Clusters and Resolved Galaxies. II. Photometric Standard Stars*. PASP, 112, 925–931 (**2000**).

Stetson, P. B. *Homogeneous Photometry. IV. On the Standard Sequence in the Globular Cluster NGC 2419*. PASP, 117, 563–588 (**2005**).

Stevenson, C. C. *Penetrating the Fog - Correcting Groundbased CCD Spectroscopy for Telluric Absorption*. MNRAS, 267, 904–+ (**1994**).

The Planck Collaboration. *The Scientific Programme of Planck*. ArXiv Astrophysics e-prints (**2006**).

Thomas, R. C., G. Aldering, P. Antilogus, C. Aragon, S. Bailey, C. Baltay, E. Baron, A. Bauer, C. Buton, S. Bongard, Y. Copin, E. Gangler, S. Gilles, R. Kessler, S. Loken et al. *Nearby Supernova Factory Observations of SN 2006D: On Sporadic Carbon Signatures in Early Type Ia Supernova Spectra*. ApJ, 654, L53–L56 (**2007**).

Timmes, F. X., E. F. Brown and J. W. Truran. *On Variations in the Peak Luminosity of Type Ia Supernovae*. ApJ, 590, L83–L86 (**2003**).

Turatto, M. *Classification of Supernovae*. In K. Weiler, ed., *Supernovae and Gamma-Ray Bursters*, vol. 598 of *Lecture Notes in Physics, Berlin Springer Verlag*, 21–36 (**2003**).

Turner, M. S. and D. Huterer. *Cosmic Acceleration, Dark Energy, and Fundamental Physics*. Journal of the Physical Society of Japan, 76, 1015–+ (**2007**).

Tyson, J. A. *Large Synoptic Survey Telescope: Overview*. In J. A. Tyson and S. Wolff, eds., *Society of Photo-Optical Instrumentation Engineers (SPIE) Conference Series*, vol. 4836 of *Society of Photo-Optical Instrumentation Engineers (SPIE) Conference Series*, 10–20 (**2002**).

van Leeuwen, F., M. W. Feast, P. A. Whitelock and C. D. Laney. *Cepheid parallaxes and the Hubble constant*. MNRAS, 379, 723–737 (**2007**).

Wang, X., L. Wang, X. Zhou, Y.-Q. Lou and Z. Li. *A Novel Color Parameter as a Luminosity Calibrator for Type Ia Supernovae*. ApJ, 620, L87–L90 (**2005**).

Wood-Vasey, W. M., L. Wang and G. Aldering. *Photometry of SN 2002ic and Implications for the Progenitor Mass-Loss History*. ApJ, 616, 339–345 (**2004**).

Wood-Vasey, W. M., G. Miknaitis, C. W. Stubbs, S. Jha, A. G. Riess, P. M. Garnavich, R. P. Kirshner, C. Aguilera, A. C. Becker, J. W. Blackman, S. Blondin, P. Challis, A. Clocchiatti, A. Conley, R. Covarrubias et al. *Observational Constraints on the Nature of Dark Energy: First Cosmological Results from the ESSENCE Supernova Survey*. ApJ, 666, 694–715 (**2007**).

Woosley, S. E. and T. A. Weaver. *The physics of supernova explosions.* ARA&A, 24, 205–253 (**1986**).

Yoon, S.-C. and N. Langer. *On the evolution of rapidly rotating massive white dwarfs towards supernovae or collapses.* A&A, 435, 967–985 (**2005**).

Zel'Dovich, Y. B. *Cosmological Constant and Elementary Particles.* Soviet Journal of Experimental and Theoretical Physics Letters, 6, 316–+ (**1967**).

Résumé

Les supernovæ de type Ia (SNe Ia) sont un des piliers de la cosmologie observationnelle moderne, celles-ci étant de bonnes chandelles standards utilisables pour des mesures de distances dans l'univers. L'analyse cosmologique à partir des SNe Ia s'appuie sur les mesures d'objets à grands et petits décalages vers le rouge (z), et actuellement le faible nombre d'observations de ces derniers constitue une source majeure d'incertitude.

Cette thèse s'inscrit dans le cadre de l'expérience SNfactory, qui a pour objectif l'observation de SNe Ia proches ($0.03 < z < 0.08$) grâce à un spectrographe de champ intégral, SNIFS. Le travail présenté a porté d'une part sur l'étalonnage de la voie photométrique de SNIFS, et d'autre part sur l'analyse des courbes de lumière spectrophotométriques issues des données de SNIFS. Ces études ont abouties à la création du premier diagramme d'Hubble spectrophotométrique pour des SNe Ia proches.

Une chaîne d'extraction de rapports photométriques entre nuits, nécessaires pour l'étalonnage en flux des spectres, a été mise en oeuvre. Les erreurs systématiques de ces rapports ont été estimées comme étant inférieures à 2%, et les courbes de lumière spectrophotométriques d'étoiles standards montrent une précision de 5% pour l'étalonnage absolu en flux dans des conditions non-photométriques. Les résidus du diagramme d'Hubble obtenu présentent une dispersion plus petite que celui fait avec les données disponibles à ce jour. Un ajustement cosmologique sans $\mathcal{K}$-correction montre une réduction supplémentaire de 5%, qui jusqu'à présent était indistinguable de la "dispersion intrinsèque" des SNe Ia.

Abstract

Type Ia supernovæ (SNe Ia) are one of the pillars of modern observational cosmology, since they are good standard candles for distance measurements in the universe. The cosmological analysis using SNe Ia requires the observation of both high and low-redshift objects, and the smaller statistic of events on the latter case represents a major source of uncertainties.

This thesis takes place within the SNfactory project, which aims to study nearby ($0.03 < z < 0.08$) SNe Ia using an integral field spectrograph, SNIFS. The presented work is divided into: a technical part, dealing with the acquisition, calibration and extraction of data from the SNIFS photometric camera; and an analysis where spectrophotometric light curves issued from SNIFS spectra were obtained, and used to create the first spectrophotometric nearby Hubble diagram.

An extraction pipeline of the differential photometric ratios between nights, needed for the flux calibration of the spectra, was built. The systematic errors affecting these ratios are estimated to be below 2%, and spectrophotometric light curves of standard stars show a 5% photometric precision of the full flux calibration on non-photometric conditions. The obtained nearby Hubble diagram presents a smaller residual scatter than the one made using currently available data. A $\mathcal{K}$-correction free cosmological fit shows an additional reduction of 5% on the scatter, until now undistinguishable from the SNe Ia "intrinsic dispersion".